KU LEUVEN

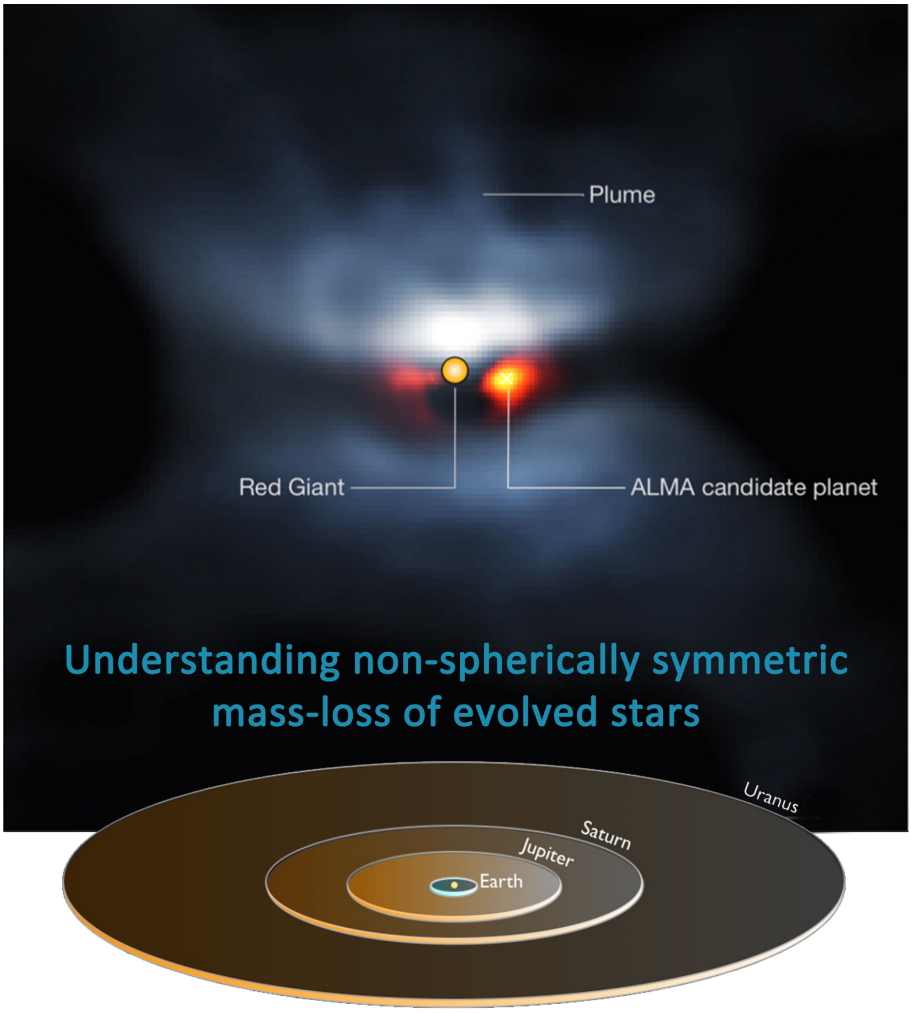

Understanding non-spherically symmetric mass-loss of evolved stars

Ward Homan

Supervisors:
Prof. dr. L. Decin
Prof. dr. A. de Koter

Dissertation presented in partial fulfillment of the requirements for the degree of Doctor of Science (PhD)

May 2017

Understanding non-spherically symmetric mass-loss of evolved stars

Ward HOMAN

Examination committee:
Prof. dr. J. Sundqvist, chair
Prof. dr. L. Decin, supervisor
Prof. dr. A. de Koter, supervisor
Prof. dr. H. Van Winckel
Prof. dr. R. Keppens
Prof. dr. T. Van Riet
Dr. M. Hogerheijde
(Leiden)

Dissertation presented in partial fulfillment of the requirements for the degree of Doctor of Science (PhD): Astronomy and Astrophysics

May 2017

Uitgegeven in eigen beheer, Ward Homan, Celestijnenlaan 200D box 2401, B-3001 Leuven (Belgium)

Abstract

Near the end of their lives, low- and intermediate-mass stars ascend the asymptotic giant branch (AGB) on the Hertzsprung-Russell diagram, where they develop a dense molecular envelope interspersed with (sub-)micron sized dust particles. The rate at which these stars expel their outer envelopes is high, from a few times 10^{-8} to about 10^{-4} solar masses per year. These winds are thought to be driven by a combination of pulsations and radiation pressure on dust grains, although the exact workings of this mass-loss mechanism have turned out to be puzzling.

Until recently, empirical models and hydrodynamic simulations of these outflows have focused mainly on describing isolated AGB stars featuring spherical outflows. This has lead to a detailed understanding on how the observables are influenced by thermal, dynamical and chemical processes in these outflows.

Recent observations with high-resolution telescopes have revealed that these winds harbour a rich spectrum of structural complexities. These include bipolar structures, arcs, shells, clumps, spirals, tori, bubbles and rotating disks. Some of these structures manifest themselves on small scales, others on very large scales. The characteristics of the observables are strongly influenced by the morphological traits of the circumsteller envelope (CSE). Hence, a complex CSE density and/or velocity distribution will have an important effect on the strength and shape of spectral lines. Complex line profile shapes may result from deviations from sphericity. Or, the lines may have shapes resembling the ones created in a spherical flow but strengths that are deviant. The application of spherical models to aspherical CSEs can lead to erroneous determinations of the overall wind properties.

To contribute to bridging the gap between observation and interpretation, we have compiled a database of expected emission characteristics for embedded spiral morphologies and equatorial density enhancements perturbing the inner wind structure. These two morphologies were selected because they are believed to be produced by wind-binary interactions in the inner CSE. Moreover, binary-containing winds form an important class of candidates that may explain the first steps in the morphological

transition to the predominantly bipolar structures found among the descendant of the AGB stars, the post-AGB stars and planetary nebulae. By means of three-dimensional non-local-thermodynamical-equilibrium radiative transfer modelling, the synthetic emission distributions of the analysed morphologies were simulated. These repositories show how the morphologies in question manifest themselves in the spectral lines, but also in the spatially resolved emission distributions and associated position-velocity diagrams. We also discuss what physical and/or geometrical properties of the CSE can be retrieved from the inspection of the observables.

To assess the newly acquired insights, the synthetic models were confronted with real data. The developed techniques and intuition were used to interpret the emission of the inner CSEs of the AGB stars L_2 Puppis and CW Leonis. Both these stars were observed with the ALMA telescope, yielding an unprecedented view on the morphological nature of their closest circumstellar regions. L_2 Puppis was found to possess a rotating disk, the first detection of such a morphology around an AGB star. The star CW Leonis was found to be surrounded by an embedded spiral morphology. After having unambiguously identified these features, both datasets were extensively modelled with 3D radiative transfer techniques, yielding important new constraints on the physical and geometrical properties of the circumstellar morphologies.

Beknopte samenvatting

Wanneer het einde van hun leven nadert volgen lichte en middelzware sterren de asymptotische reuzentak (AGB) in het Hertzsprung-Russell diagram. Tijdens deze fase ontwikkelen ze een dichte enveloppe die bestaat uit gas en (sub)micron stofdeeltjes. Deze enveloppe ontstaat door een zogenaamde sterrenwind, die ervoor zorgt dat de AGB ster het materiaal in haar oppervlaktelagen aan hoog tempo verliest, van 10^{-8} tot 10^{-4} zonsmassa's per jaar. Er wordt vermoed dat oppervlaktepulsaties, gevolgd door stralingsdruk op stofdeeltjes, dit fenomeen teweeg brengen. De precieze oorzaak van dit massaverlies blijkt echter zeer complex te zijn.

Tot hiertoe hebben empirische modellen en hydrodynamische simulaties van dit massaverlies zich voornamelijk gefocust op het begrijpen van geïsoleerde AGB sterren met sferische winden. Dit heeft een zeer gedetailleerd inzicht opgeleverd over de manier waarop thermische, dynamische en chemische processen de waargenomen fenomenen bepalen en beïnvloeden.

Recente observaties met telescopen met hoge ruimtelijke resolutie, zoals de ALMA telescoop, hebben echter aangetoond dat deze sterrenwinden een rijk spectrum aan complexe structuren bevatten zoals bogen, schillen, klompen, spiralen, tori, bellen, bipolaire structuren en roterende schijven. Sommige van deze morfologieën zijn ruimtelijk zeer uitgebreid, terwijl andere zich manifesteren op veel kleinere schaal. Ze hebben een sterke invloed op de waarneming van de circumstellaire omgeving (CSE): een complexe dichtheids- en/of snelheidsverdeling in de wind zal met name een significant effect hebben op sterkte en vorm van de spectraallijnen. Spectraallijnen met een complexe vorm kunnen het gevolg zijn van afwijkingen t.o.v. sferische symmetrie van de CSE. Daarnaast kunnen de lijnen ook een vorm hebben die lijkt op sferisch massaverlies, maar aanzienlijk afwijkende sterktes hebben. Dit betekent dat de toepassing van modellen voor sferische sterrenwinden op niet-sferische CSEs mogelijk foutieve bepalingen oplevert met betrekking tot diens eigenschappen.

Om de kloof tussen observatie en interpretatie te overbruggen, hebben we voor zowel de spiraal als voor de equatoriale dichtheidsverhoging (EDV) een database samengesteld

van de te verwachten observationele karakteristieken.

We hebben deze twee morfologieën gekozen omdat er wordt aangenomen dat ze ontstaan door binaire interacties. Winden die een binair systeem omvatten zijn een belangrijke klasse aan kandidaten waarmee de eerste stappen in de morfologische transitie naar de overwegend bipolaire structuren rond post-AGB sterren en planetaire nevels verklaard kunnen worden. Met behulp van een drie-dimensionaal stralingstransportcode hebben we de synthetische emissieverdelingen van de bovengenoemde morfologieën gesimuleerd. We tonen aan hoe deze zich manifesteren in de spectraallijnen, in de ruimtelijk opgeloste emissieverdelingen, en in de bijhorende positie-snelheid diagrammen. We bespreken tenslotte welke fysische en/of geometrishe eigenschappen van de CSE door middel van visuele analyse kunnen afgeleid worden uit de synthetische waarnemingen.

Om vervolgens de nieuwe inzichten te evalueren hebben we de synthetische modellen geconfronteerd met waarnemingen. De ontwikkelde technieken (in combinatie met een gaandeweg opgebouwde intuïtie) maakten het mogelijk om de emissie van de AGB sterren L_2 Puppis en CW Leonis te interpreteren. Beide sterren werden geobserveerd met de ALMA telescoop, die ons een uniek beeld leverde van de structuur van hun sterrenwind. We detecteerden enerzijds een draaiende schijf rond L_2 Puppis. Dit is de eerste waarneming van dergelijke morfologie rond een AGB ster. Anderzijds troffen we een spiraal rond de ster CW Leonis aan. Nadat ontegensprekelijk was vastgesteld dat de sterrenwinden inderdaad deze structuren bevatten, werden hun respectievelijke datasets onderworpen aan een uitgebreide 3D stralinstransport modellering. Dit leverde een scherper beeld op van de fysische en geometrische eigenschappen van spiralen en EDVs.

Contents

Chapter 1

Introduction

The studies presented in this thesis reside within the field of research aiming to deepen our understanding of the small- and large scale physical, chemical and temporal variations exhibited by the circumstellar environments of evolved stars, focusing mainly on AGB stellar winds. We specifically concentrate on the newly discovered rich morphological complexity of asymptotic giant branch (AGB) envelopes and develop methods to interpret the often complex spatially resolved molecular emission from these morphologies. To illustrate the state of the art, and the difficulties related to this topic, we begin this manuscript with a rather elaborate introduction. In Sect. 1.1 we give a brief overview of the AGB star, and shortly describe its evolutionary origin and characteristics. Subsequently, in Sect. 1.2, we proceed with a discussion on the dynamical nature of the AGB surface, and how this initiates the mass loss mechanism which produces the vast and chemically rich circumstellar AGB envelope. The newly discovered morphological complexities observed within these outflows, and their origins are discussed in Sect. 1.3. We reveal how the characteristics of observations relate to the morphological and physical nature of the wind both for spatially unresolved and spatially resolved data, in Sect. 1.4 and 1.5 respectively. Finally, in Sect. 1.6 we concisely outline the main aims and structural design of this thesis, which is embodied in the following chapters.

1.1 The evolution of solar-like stars

Asymptotic Giant Branch stars are a final phase in the evolution stars that start out their lives with less than 9 solar masses [153]. The longest fraction of the total lifetime of any star is spend in the first phase of evolution, the main-sequence phase, where energy is produced in their cores by converting hydrogen into helium via thermonuclear reactions. Once the core hydrogen reserves are depleted, the star starts H-burning in a shell surrounding the core at a rate that is much higher than during its prior life. To allow for the transport of this energy to the surface, where it is radiated in space, the layers on top of the H-burning shell expand and become convective. The star swells up and its surface cools down; hence, it turns into a red giant. As the temperature of the H burning shell steadily increases, the temperature of the He kernel follows closely. At some point, the temperature of the H-burning shell reaches values of 100 million Kelvin, allowing helium to ignite via the triple-alpha process.

The fusion by-products of He burning, carbon and oxygen, sediment down to the core center, while He continues burning in the bottom layers of a shell surrounding this inert C and O kernel. H, in turn, continues burning in a shell surrounding the He shell. The emergence of this layered core structure signals the beginning of the AGB phase.

The formation of a He-burning shell causes the core to become unstable to temperature perturbations. This is because a small increase in temperature will significantly boost the triple-alpha energy output, causing a runaway thermonuclear event. This mechanism lies at the basis of the most important core instability process in the AGB, called *thermal pulses* (TP).

During the relaxation oeriod following such a thermal pulse, the mantle extends its convection zone inwards, deep down into the He intershell. Whatever fusion products are present in the intershell are essentially dredged-up into the mantle, which subsequently mixes it all the way up to the surface. This means that TP-AGB stars have overall elemental mantle abundances which change with every TP. Most importantly, due to the production of vast amounts of ^{12}C via the triple-alpha fusion process, the mantle gradually turns from being oxygen-rich[1] to being carbon-rich. This process, called the *third dredge-up*, has very important implications for the chemical evolution of AGB stars and their circumstellar environments (CSEs).

Complex surface dynamics provoke the creation of a strong stellar wind, which gradually, but ceaselessly, strips material from the star. This results in the formation of a vast CSE, dominated by intricate dynamical, thermodynamical, chemical and radiative feedback processes. In the next section we give a brief overview of the dynamics

[1] Due to the vast production of oxygen in supernovae [79, 100], oxygen is the third most abundant element in the universe. The universe is therefore predominantly oxygen-rich, and hence the stars which have been formed from supernova remnants also.

governing this mass loss mechanism.

1.2 The dust-driven stellar wind

Most, if not all stars experience mass loss. Our Sun, for example, systematically loses material at an average rate of around 2×10^{-14} Solar masses per year ($M_\odot\ yr^{-1}$). AGB stars lose mass at much higher rates, ranging from 10^{-9} to 10^{-4} $M_\odot\ yr^{-1}$, with typical gas velocities ranging between $5\,km\,s^{-1}$ and $20\,km\,s^{-1}$. This phenomenon is called a *stellar wind*. This outflow of gas and dust creates a dense circumstellar environment (CSE) of vast proportions, with radii up to tens of thousands of AU [33]. The outflows of AGB stars are thought to be driven by radial surface pulsations, which lift material to regions that are sufficiently cold for dust particles to condense. These particles are opaque to the incident stellar light and subsequently initiate a radiation pressure driven wind.

1.2.1 Pulsations

The surface layers of AGB stars are dynamically unstable. They pulsate with periods in the order of a few hundred days. What is believed to be the main cause are the large convective cells in the mantle of the AGB star, which cause large-scale agitation of the surface layers. This agitation is very unpredictable, both spatially and temporally. Yet, averaged-out, these motions translate to patterns of radial pulsation, with the ability to lift up stellar material to high altitudes [58]. In addition, the *kappa-mechanism* is believed to contribute to the pulsation phenomenon [48, 54]. This opacity-driven pulsational instability activates when slight changes in temperature substantially alter the opacity of a gas. Consider a temperature perturbation at the threshold depth where an element of gas is on the brink of ionisation. This perturbation would partially ionise the previously neutral gas, causing a local increase in opacity. The increased rdiation pressure gradually pushes the inonsed material outwards, to regions of lower temperature, where the ions recombine. This reduces the temperature gradient, causing the upper layers to fall back down. For AGB stars, this happens at a threshold depth for He ionisation in the surface layers. Because He is extremely abundant, the opacity is large in the partially ionised zone, and the effect is very strong.

1.2.2 Wind acceleration

The pulsations can lift stellar surface matter to very high altitudes. Measurements of the gas velocities associated with these surface pulsations show that they typically lie

around 15 $\mathrm{km\,s^{-1}}$ [68]. But, for a typical AGB star with a mass of 1 $\mathrm{M_\odot}$ and a radius of 1 AU, the surface escape velocity is approximately 40 $\mathrm{km\,s^{-1}}$. Hence, without an efficient driving force, the matter will remain bound to the star by gravity and will fall back down onto the stellar surface.

As the material is lifted to high altitudes, the conditions become favorable (high densities, lower temperatures) for the formation of large molecules, molecular clusters and dust particles. These dust particles easily interact with photons with wavelengths in the infrared (IR) part of the electromagnetic spectrum. This happens to coincide with the bandwidth where AGB surfaces emit most of their radiation. This results in a strong coupling between the stellar flux and the newly formed dust particles. The absorbed photon energies cause the dust particle to heat up, but more importantly these photons impart their momentum to the dust grains, accelerating them outwards. The outwardly accelerating dust grains collide with the gas particles in their path, bestowing some of their own momentum to the gas, effectively dragging it along. This leads to a global outward migration of material. Because dust is the primary wind acceleration agent, these winds are known as *dust-driven stellar winds*.

The rate of acceleration of the wind decreases with radius, and essentially ceases from a certain radius onward. Attenuation of the radiation field by intervening dust, a decrease in relative total cross-section of the dust as it moves out in the wind, and the decoupling of gas and dust in the low-density outer wind cause the flow to reach a maximum (or terminal) velocity. The gas velocity increase as a function of radius is typically expressed as a *beta law*

$$v(r) = v_0 + (v_\infty - v_0)\left(1 - \frac{R_{\mathrm{dc}}}{r}\right)^\beta, \tag{1.1}$$

with v_∞ the terminal velocity of the gas, R_{dc} the dust condensation radius, and v_0 the velocity of the gas at the dust condensation radius. β is the parameter that sets the acceleration as a function of radius. Assuming the accelerated gas experiences a net outward $1/r^2$ force (simulating an optically thin wind of constant composition, with ideal dust-to-gas momentum coupling) a value of $\beta = 0.5$ can be calculated. However, precise empirical measurements of the gas velocities in the AGB wind acceleration zone span a wide range in β values.

Acceleration in O-rich AGB stars is typically characterised by values of β between 1 and 2 [40]. This suggests a much more moderate radial outward force ($\sim 1/r^{1.5}$). This implies that the acceleration is relatively slow, possibly connected to changing extinction characteristics of the grains as they form, grow, and move out in the flow. Silicate dust grains couple poorly to the stellar radiation. Their absorption opacity could be augmented significantly if they would possess small Fe inclusions. However, this would also significantly increase their temperature, prohibiting a presence in the regions close to the surface where the wind is initiated. Large Fe-free silicate grains can in principle survive in these hot regions, but it is not entirely clear how they can be

produced [91]. The details of O-rich wind acceleration turn out to very very difficult to reproduce.

C-stars show acceleration curves of $\beta < 0.5$ [41]. This relatively rapid acceleration can be explained by the opaqueness of the carbon-rich grains, allowing them to strongly interact with the incident radiation field. The strong chemical bonds with the carbon molecule ensure high structural integrity, making them resistant to the high temperatures they acquire.

During the expansion of the wind many complex phenomena (including photochemistry, gas-grain interactions, grain growth, etc...) contribute the the chemical complexity of the circumstellar matter. Collision of the outflowing wind material with the *interstellar material* generates a sharp zone of extreme pressures and temperatures, known as a *bow shock*. Finally the remaining gas and dust is expelled into the interstellar medium, mixing with the primordial gas and forming vast low-density molecular clouds, which in time can become the cradles for new stars to be born into.

Figure 1.1: The planetary nebulae shown here are NGC 6543, also known as the Cat's Eye, NGC 7662, NGC 7009, and NGC 6826. In each case, X-ray emission from Chandra is colored purple and optical emission from the Hubble Space Telescope is colored red, green and blue. These objects have typical length scales of the order of ~1 lightyear. (source: nasa.gov/mission_pages/chandra/multimedia/planetary_nebula.html)

1.2.3 Final fate and emerging questions

As these winds blow stellar matter outwards, the central star loses mass. Thus, there will be a point in time when it has expelled most of its envelope, exposing its core.

This stellar core is hot and emits copious amount of extreme ultraviolet photons, aiding the interstellar radiation field in dissociating the molecules in the outflow and eroding the solid state component. The circumstellar gas is ionized and a *planetary nebula* is created, of which examples are shown in Fig. 1.1. What immediately catches the eye is that most PNe are not spherical [10]. Yet they are not completely chaotic in morphology either. Extensive documentation of these objects show a wide range of morphologies, with overall bipolarity as a main characteristic, but also including jets and tori [10, 74, 37]. Most PNe exhibit one or multiple axes of symmetry, indicating preferential directions in which the star has lost its material.

As AGB stars are believed to be the progenitor systems of the central stars of PNe, this poses a number of questions: What causes spherical stars to produce a rich morphology of circumstellar environments? Do AGB stars also show a plethora of morphological structures? And if so, what causes these structures and is the root cause of the aspherical PNe structures connected to the mechanism shaping the morphology of AGB outflows?

The research field addressing these questions is relatively new. Studies of AGB outflows have, until relatively recently, operated mainly under the implicit assumption that the general morphology of these winds is smooth and spherically symmetric. Sophisticated instruments able to spatially resolve the dusty AGB CSEs were missing, and so direct observational constraints on their geometrical structure were missing too. From the theoretical perspective, first order physical models usually start off as simple models, which are gradually refined to include additional physics. The initial morphological assumption of sphericity is therefore reasonable.

A major step in observational capabilities was achieved in October 2011 with the first light of the Atacama Large Millimeter/submillimeter Array (ALMA). ALMA is now rapidly revolutionising our understanding of the physics, chemistry and shape of dust-driven stellar winds. It outperforms other telescopes in the 400 μm to 3 mm wavelength range by orders of magnitude in sensitivity and in angular resolution. In combination with the vast amounts of data collected by the Hubble Space Telescope, the Herschel Space Observatory, the Very Large Telescope (VLT) and other ground-based submm telescopes (IRAM, APEX, SMA, etc.), the complementary ALMA data permits unprecedented detailed studies of the physical and chemical structure of these stellar winds, on a wide range of length-scales.

At the present time, the rapid developments in instrumentation and the advent of new observing facilities place us in a situation where observational discoveries precede theoretical developments. But, these observations sometimes show complexities well

beyond our current capabilities to interpret them fully, let alone link them properly to the local physical and chemical conditions. Hence, the field of dust-driven wind morphology is currently in an "age of exploration", with a primary focus on cataloging morphologies, establishing their geometries and their basic properties, as well as establishing the nature and evolutionary state of the AGB star. In the next section we present the different types of known morphologies harboured by these stellar winds, and discuss what is currently believed to be their origin.

1.3 Morphological complexities in the CSEs of evolved stars

Recent observations of the CSEs of AGB stars with high-resolution telescopes have revealed a rich spectrum of structural complexities, of which some examples are shown in Fig. 1.2. These include bipolar structures [11], arcs [39, 33], shells [121], clumps [18], spirals [122, 123, 114, 93], tori [170], bubbles [155] and disks [86]. These morphologies span a wide range of spatial scales, from global features of the order of tens of thousands of AU to highly local structures of the order of fractions of an AU. We discuss the known AGB wind morphologies to some detail in this section.

1.3.1 Structures on large spatial scales

Bow shocks On the largest spatial scales ($\sim 10^4$ AU) gigantic arcs enveloping most of the stellar wind are observed (see panel [iv] in Fig. 1.2). These structures are prominently present around evolved stars, and have been extensively documented by Cox et al. (2012) [33]. They find their origin in the motion of the star relative to the interstellar medium (ISM). The freely expanding AGB wind collides with the ISM, at velocities equal to the wind velocity plus the relative stellar velocity. If this resultant motion is supersonic with respect to the ISM, there will be a point where the internal pressure of the wind will equal that of the ISM. The ISM cannot adapt to the new velocity and pressure caused by the supersonic wind in time. At the resulting discontuinity, the boundary layers become compressed, leading to the formation of a *bow shock* [183]. The conditions in this bow shock can become rater extreme, with temperatures high enough to destroy molecules and dust, and exceptionally high pressures.

Thin detached shells These are thought to be formed during a thermal pulse [114]. The increased core luminosity permeates to the surface, which results in a sudden surge of emitted photons. The increased radiation pressure on the surrounding dust momentarily increases the mass loss rae and the expansion velocity of the wind, resulting in an

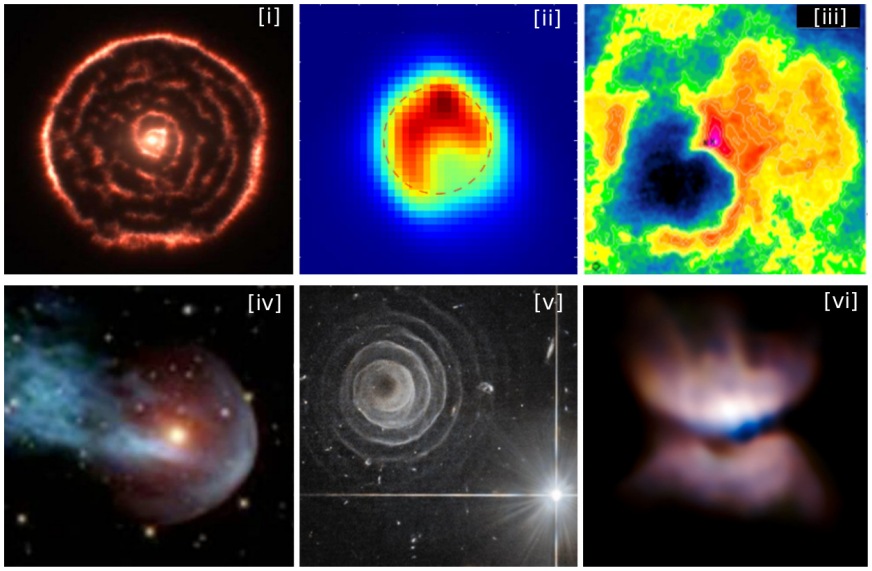

Figure 1.2: Examples of high-resolution AGB star observations clearly showing deviations from spherical symmetry. [i] The wind of the AGB star R Scl [114], showing a bright detached shell surrounding a spiral pattern. [ii] The clumpy dust distribution in the inner wind of the star R Dor [90]. [iii] The inner wind of the binary system Mira AB, showing a hearth-shaped void and a very chaotic emission pattern [155]. [iv] The bow shock of Mira (NASA JPL). [v] The outer wind of the star AFGL 3068, showing a spiral pattern [137]. [vi] A rotating disk in the inner wind of the star L_2 Puppis [87]. The typical length scales of these morphologies range from ~1 AU up to 10^4 AU.

outwardly propagating high-density shell that sweeps up all matter it collides with. Due to their density these shells remain observable up to spatial cales of $\sim 10^3$ AU. They are rare, as the window of opportunity to observe them is very narrow, and they seem to only appear around C-rich AGB stars [148]. Nevertheless, some unmistakable examples have been observed around the AGB stars R Sculptoris [115] (see panel [i] in Fig. 1.2), S Scuti and RT Capricorni [131], and U Hydrae [78].

1.3.2 Structures on Intermediate scales

Molecular shells The presence of nearby hot stars produce appreciable amounts of high-energy ultraviolet radiation, with the power to substantially influence the stellar wind chemistry [107, 106]. *Photodissociation* caused by such photons is an extremely

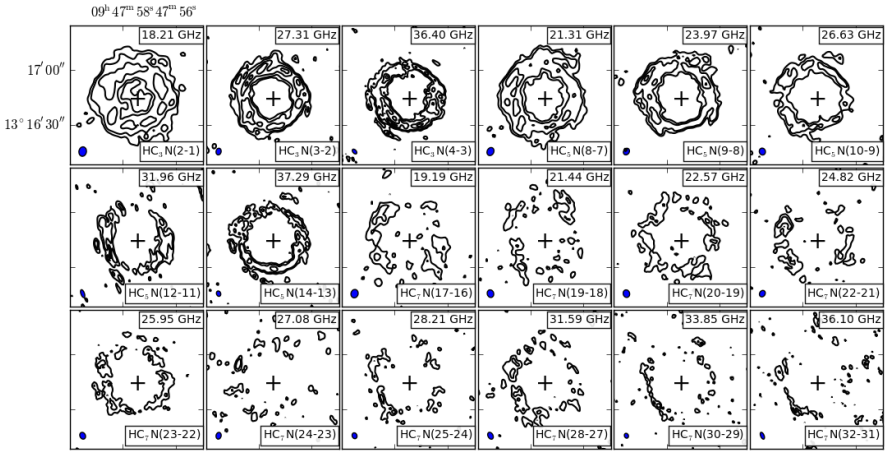

Figure 1.3: Molecular emission of complex carbon chains in the wind of the star CW Leonis (IRC+10216). Figure courtesy of dr. D. Keller.

important contributor to the chemistry, and through it the appearance of the stellar wind. It causes a well defined radial discontinuity in the molecular abundances of the CSE molecules. The location of this boundary depends on the molecular densities, the molecular (photo)chemical reactivity, the velocity of the wind, and the intensity of this UV field. The incoming UV radiation bombards the molecules on the front line, exciting some and destroying others. But because there is a constant molecular replenishment via the stellar outflow, a steady boundary is formed [116]. At this boundary, the molecules shield their companions closer to the AGB star from this destructive fate. This vastly enriches the CSE chemistry, as there exists a constant breaking-up of different molecule species at different locations into reactive radicals that enable new chemistry to take place [107, 132, 106]. Examples of photochemically induced morphologies in an AGB wind are shown in Fig. 1.3. Here, shell-like structures appear due to the presence of both an inner formation radius, and an outer destruction radius. Furthermore, the breaking-up of simpler chains gives rise to the formation of more complex ones. Typical length scales associated with these structures are of the order of 10^2 to 10^3 AU.

Spirals Convincing observational evidence exists on the presence of spirals in AGB outflows [122, 123, 114, 93, 41, 95] (see panels [i] and [v] in Fig. 1.2), leading to theoretical inquiries on their possible formation mechanism [179, 172, 119, 92, 135]. Hydrodynamical simulations show that the influence of a binary companion on its direct surroundings can quite easily form Archimedean spirals embedded in the outflow, along the orbital plane of the system. Local companion-wind interactions cause the

wind material near the companion to be gravitationally funneled into an enhanced density region (a gravity wake) resulting in a flattened (i.e. only barely extending away from the orbital plane) spiral. Additionally, the presence of this binary companion will cause the mass-losing star to wobble around the common center of mass of the binary system. This reflex motion alters the local densities, ultimately forming an Archimedean spiral that is comprised of concentric shells, when observed edge-on [92, 96, 93]. The typical size associated with these structures is of the order of 10 to 10^2 AU, but sometimes even larger. Here, the specific geometrical properties of the resulting spiral have been found to be determined by the strength of the local gravity field with respect to the outflow velocity [96]. Radial models of shocks generated by a pulsating mass-losing source, that are locally enhanced by interaction with a binary companion have shown that not only single, but also multiple spiral branches can form in the CSE [201]. In this case the properties of the spiral depend strongly on the ratio between the pulsation period of the star and the binary period. Finally, if the binary contains two mass-losing stars, the colliding winds at the interaction zone may form a spiral pattern [176, 199, 185]. Here the geometrical properties of the spiral are determined primarily by the velocity of the slower wind and the particular orbital motion of the binary.

Equatorial density enhancements Equatorial density enhancements are a very common astronomical phenomenon, observed in a broad astronomical range. From rings around planets on the smallest scales, to spiral galaxies rotating around supermassive black holes on the largest scales. In the context of stars and stellar evolution, they are caused by either directional loss of material by the central object [70, 31, 181, 83, 104], or by the interplay between conservation of angular momentum and the viscosity of the material orbiting around a strong central source of gravity. This latter scenario ends up forming stable disks, where the balance between the centripetal force and gravity manifests as Keplerian motion. Hence, it takes form as either a non-rotating torus or a rotating disk. These have only very recently been discovered in the evolved stars context, with some clear detections around post-AGB stars [23, 67], and AGB stars [86] (see panel [vi] in Fig. 1.2). Typical disk radii range from around 25 AU around AGB stars up to factors of 10^2 AU around more evolved stars. The mechanism for producing a stable disk around an AGB star is still unknown, and is currently the subject of research. However, yet again, binarity seems to be the most likely explanation. Circumbinary disks around post-AGB stars are believed to be formed as a result of close-binary interactions (1-2 AU), with a possible lower mass main-sequence star as a companion [186, 187]. The protoplanetary community has been studying differentially rotating (protostellar and protoplanetary) disks for decades. Both sample and case studies are being performed with exceptionally detailed models, including but not confined to 3D density and temperature profiles [8, 134, 204], (photo)chemistry [53], dust species and grain size distributions [178, 102], and planet formation [4, 200, 108]. This accumulated knowledge is ripening fast, becoming ever more ready to be adopted by the evolved stars community.

1.3.3 Structures on small scales

Arcs and clumps It has been shown [58, 59] that surface pulsations naturally arise from turbulent convective motions of the stellar mantle, both on very short and on longer timescales. These surface pulsations generate waves, which become increasingly compressed as they propagate through the inner wind, which is dominated by steep radial density gradients. This turns these gentle pulsations into strong and sharp *shock waves*. As the kinetic energy in the wave surpasses the internal energy of the gas, the momentum transfer of the wave to the surrounding gas may become important. Radial velocity measurements of this pulsating and shocked inner CSE material show typical velocity amplitudes of around $15\,\mathrm{km\,s^{-1}}$ [68]. From a comparison of the pulsational kinetic energy with the gravitational potential the radial amplitude can be estimated. For a typical AGB star with a mass of $1\,\mathrm{M_\odot}$ and a radius of one astronomical unit (AU) such velocities translate to substantial radial amplitudes up to $\sim$15 % of the stellar radius. However, in fact these surface pulsations likely describe the average motion of smaller scale surface agitations, caused by the interplay between the convective structure of the AGB mantle and the previously described kappa-mechanism. This chaotic motion of the stellar surface can locally generate small-scale inhomogeneities in the circumstellar environment, which can turn into temporal variations in the mass-loss rate and/or expansion velocity and hence the formation of local density enhancements. These conditions turn out to be optimal for dust formation [208], resulting in non-isotropic mass loss [182] through dusty clumps and arcs (see panel [ii] in Fig. 1.2).

The clear and recurrent detection of the abovementioned morphologies in AGB CSEs fuels a set of important observational questions like “How do these shapes manifest in the observables?” and “How are the observables linked to the local conditions?”. These questions may seem to have obvious answers, but in fact the nature of molecular emission can transform the appearance of these well established shapes into barely recognisable emission patterns. To illustrate the extent to which acquired emission patterns can differ from the expected shapes we dedicate the following section to describing the most important phenomena affecting the distribution of emission.

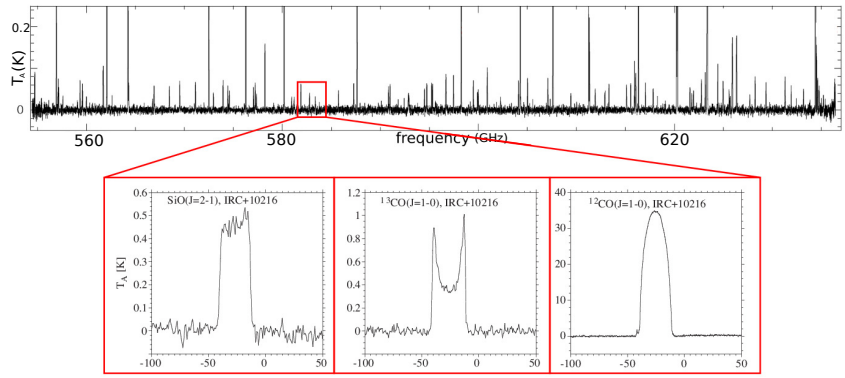

Figure 1.4: *Top panel:* line survey of the star CW Leonis observed with HIFI band 1b. The spectral resolution is poor, and so the spectral lines look, indeed, like lines. [27]. *Bottom panels:* examples of different line shapes that can be expected when observing spherical outflows with high spectral resolution.

1.4 Low spatial resolution observations: Single-dish telescopes

Because the wavelength of IR radiation is much longer than that of visible light, the resolving power of single-dish IR/radiotelescopes is comparatively poor. In fact, typical dish diameters of some 10 meters have main beam opening angles of the order of half an arcminute at typical millimeter-sized wavelengths. At best, large and close-by objects (with sizes up to a few arcminutes) can be barely spatially resolved (with a few pixels over the total wind surface area). But typically these objects are fully engulfed by the telescope's main beam, resulting in the acquisition of a mean emission over the whole spatial extent of the emitting body. The resolution of these devices could in principle be increased by augmenting the diameter of the light-gathering aperture, but practical limits impose a maximum size to these dishes, which most current telescopes operate at.

The gathered light can subsequently be channeled through a *spectrograph* of arbitrary resolution, permitting the detailed exploration of its energy distribution throughout the probed frequencies. Sufficient spectral resolution reveals shapes in the spectral lines, as shown in Fig. 1.4. The interpretation of these shapes can provide a lot of information on the emitting stellar wind, but these shapes also prove to be a major source of ambiguity and uncertainty when used as diagnostics for physical or chemical, local or global stellar wind properties.

1.4.1 Molecular emission - Spectral line shapes

The origin of spectral line shapes can be traced to four fundamental causes. The first, ***line broadening***, relates to all the possible means via which emission is distributed along the spectral domain. The second relates to ***opacity effects***: effects caused by the interaction between the emitted light and the emitting material. Thirdly, ***resolution effects*** arise due to the ability of telescopes to resolve the circumstellar environments. And lastly, the spectral line shapes can be influenced by ***physical morphology***, or by the specific geometrical arrangement of the emitting material. We discuss these here in more detail.

Line broadening

The line broadening mechanisms refer to each and every process that can contribute to the broadening of the spectral lines. They can be classified in three distinct categories.

Quantum Effects The most fundamenal quantum broadening effect is called *natural broadening*. The *Heisenberg uncertainty principle* states that there are certain physical properties of a system that are related such that they unambiguously influence each other. For example, if the position of a particle is well defined, then its momentum is uncertain, and vice versa. Similarly, there is an uncertainty relation between the energy of a system, and its lifetime in that state. Because the spontaneous radiative deexcitation rates are finite, there is a spread on the energies through which decay to a lower level can happen. Thus, the emitted photons are spread-out slightly throughout frequency-space.

A second quantum dominated broadening effect is *collisional broadening*, also known as pressure broadening. As atoms or molecules collide with each other, there is a brief moment where the wavefunctions of the outermost electrons overlap, causing a small shift in the energy levels. Assuming the collision time is short compared to the time between subsequent collisions, then the emitted photons by each collision all have a slightly different wavelength, depending on the energy of the collision, and the orientation and structure of the colliding molecules. The effective result is similar to the natural broadening effect, and is in most cases described by the Lorentz profile

Besides intrinsic quantum effects, the motion of the particles also influences the observed frequency through the *Doppler effect*. Motion towards the observer will result in increased frequencies (called *blue shifted* frequencies), motions away from the observer will result in reduced frequencies (called *red shifted* frequencies). Doppler related broadening effects can be subdivided in microscopic and macroscopic motions.

Microscopic Motions A first subclass of microscopic motions is known as *thermal broadening*. This refers to frequency shifts caused by the thermal motion of the gas particles, whose velocities follow the Maxwell-Boltzmann distribution in the majority of cases.

A second broadening mechanism due to microscopic motions is known as *microturbulent broadening*. This is the broadening effect most often associated with turbulent eddies that have spatial scales that are small compared to the line forming region. Because there exists no complete physical framework for describing turbulent effects, it cannot be quantified by a distribution from basic principles. Assuming turbulent motions are fully random, the corresponding distribution is (like its thermal counterpart) assumed to be Gaussian.

Macroscopic Motions This is the most important broadening effect in the stellar wind context, mainly because the magnitude of the Doppler shifts caused by the global gas velocities are typically much larger than the combined influences of the above mentioned broadening effects. Other sources of macroscopic motion are rotation, pulsations and convective motions on spatial scales that are large compared to the line forming region, though these are mostly associated with the stellar surface, which is typically enshrouded by the dense CSE. The gas velocity in the outflow can cause a significant frequency shift of the transition rest frequency, depending on the orientation of the velocity vector of the emitting particle with respect to the line of sight. This means that the width of a spectral line can be used as a direct measurement of the maximal gas velocities in the observed object.

At each frequency all velocities with a certain projected component are probed. This means that the energy contained in one specific frequency of the spectral line traces the emission along a three-dimensional surface through the stellar wind, whose shape depends on the wind's velocity field. For a radially expanding wind with constant velocity these surfaces are cones, extending from the surface to the center, where their apexes are located. The normal to the base of these cones passing through their apex is always oriented along the line of sight. Thus, as one traces the emission of the spectral line from the blue shifted to the red shifted wing, one is essentially probing the stellar wind emission along these conical surfaces: a very narrow cone with its apex pointing away from the observer (containing the material flowing towards the observer) for the blue-shifted emission, evolving to a flat plane for unshifted emission, proceeding towards a narrow cone with its vertex pointing towards the observer (containing the material flowing away from the observer) for the red-shifted emission. These surfaces are visualised in two dimensions in the leftmost panels of Fig. 1.5.

This constant velocity field is a decent approximation for the low energy spectral lines formed by stable molecules that exist throughout the whole extent of a large and spherically expanding stellar wind. When the transition in question requires higher energies to populate its energy levels, then one is probably probing the more inner

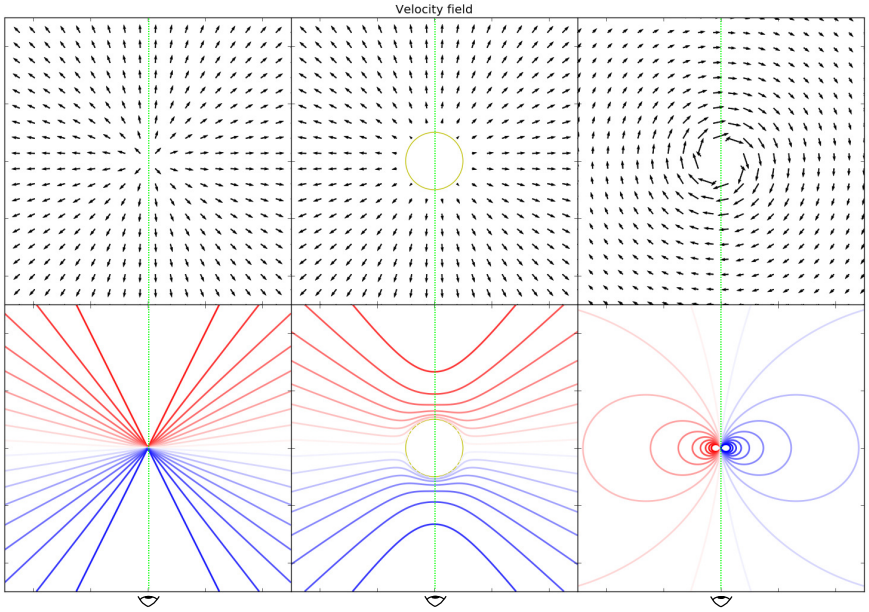

Figure 1.5: Two-dimensional representations of three different velocity fields (*top row*), with the corresponding contours of constant projected velocity along the line of sight for an observer in the plane, looking along the green dashed line (*bottom row*). The colour coding of the contours represents the Doppler shift. *From left to right:* (i) Radial outflow with constant velocity. The resulting contours are (2D projections of) conical surfaces. (ii) Radial outflow with beta law acceleration. The resulting contours are (2D projections of) bowl-like surfaces. (iii) Keplerian rotation. The resulting contours are complex, and probe both the front side and the back side of the space simultaneously.

regions, where temperatures and densities are higher. In this case the approximation of constant velocity may break down, as one enters the realm of the wind acceleration region. Here, still assuming a purely radial outflow, the planes of equal projection of the velocity field along the line of sight change from cones to bowls, and so the spectral line frequencies probe the three-dimensional emission differently. These bowl-like surfaces are visually represented (in 2D) in the two centermost panels of Fig. 1.5. For more complex velocity fields the visualisation of these planes becomes more difficult. For example, for a rotating velocity field with its rotation axis perpendicular to the line of sight the probed regions are inverted compared to the radial outflow. The material with maximally Doppler-shifted frequencies is now located in the plane perpendicular to the line of sight, passing through the center of the field. The unshifted emission now originates from the material located closest and farthest away from the observer. This

is demonstrated by the rightmost panels in Fig. 1.5.

The width of spectral lines originating from stellar winds are thus dictated by three important broadening processes: quantummechanical broadening, Doppler broadening through microscopic motions, and Doppler broadening through bulk motion. However, the mere broadening of the lines cannot explain the different line shapes. We now proceed with the exploration of the sources of peculiar shapes in the spectral lines.

Opacity effects

Some shapes can be traced to effects emerging from the interplay between the emitted light and the light-emitting material. These are generally morphology-dependent. And because we do not wish to elaborate too much on this infinite space of possibilities, we confine the following discussion to possible shapes of spectral lines produced by smooth spherical outflows with constant expansion velocity.

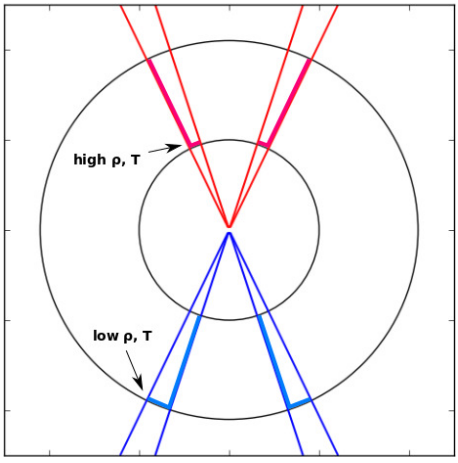

Figure 1.6: A two-dimensional representation of two velocity bins, represented by the area confined by the blue and red contours respectively. In addition, a spherical region is marked, representing the zone in the wind where the densities and temperatures are optimal for the excitation of one particular transition. Due to the optical thickness of the wind, only the emission produced in the surface covering each velocity bin can be observed, shown here as the thick bin edges. Because the red velocity bin probes denser and hotter regions than the blue velocity bin, the blue emission in the line is less pronounced relative to the red shifted emission.

If one divides the spectral line into equally wide portions in frequency-space, then these *frequency bins* correspond to different widths of the cones of constant projected velocity. Due to the geometry of the spherical outflow, the volume enclosed by each of these cones is equal. If the stellar wind is optically thin, then it barely extinguishes any of the light it has produced. This means that the emitted radiation produced by all the material in each cone can be fully observed, and the spectral line will hence be symmetric. And because the volume of each cone is identical, the emitted energy by each cone is also identical. In terms of the spectral line shape, this means that the energy observed in each frequency bin is identical, hence resulting in a *flat-topped* line profile. Such a line is shown in the bottom left panel of Fig. 1.4.

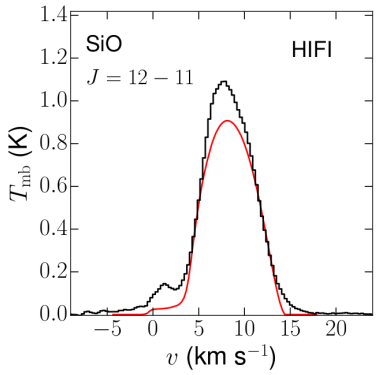

Figure 1.7: Example of a blue wing absorbed line. In black, the SiO J=12-11 spectral line (centered on 7.5 km s^{-1}) exhibits a rather strong asymmetry between the blue shifted and the red shifted side. Furthermore, the small optically thin bump is visible in the far edge of the blue shifted wing. The red line is a synthetic model. (Van de Sande et al. subm.)

Optically thick media interact strongly with the light passing through it, attenuating it substantially. In fact, the observed light emitted by an optically thick medium originates mostly from a thin surface layer. Any light emitted by deeper regions will have been completely absorbed by the medium before making it to the surface. This means that it is the surface, and not the bulk mass of material per cone which dominates the emission. Projected on the plane of the sky, the conical surfaces of constant projected velocity appear as circles. So we expect the highest velocities to only contribute minimally to the profile, as the corresponding cones have small circular projections. Conversely, the lower velocities are expected to contribute substantially more to the line profile, with much larger circular projections. This leads to a parabolic line profile. An example is shown in the bottom right panel of Fig. 1.4.

In optically thick winds, the emission thus completely originates from a thin surface layer covering the portion of the wind where the line is formed. However, if this line formation zone has a significant width, then the surface layer covering the blue-shifted emission zone (as seen from the observer) is located much farther from the central star than the surface layer covering the red-shifted emission zone. Because the temperatures and densities at larger radii are smaller, the blue-shifted part of the spectral line will be less pronounced than

the red-shifted side, causing an asymmetric line profile. This is known as *blue-wing absorption*. An example of a blue wing absorbed spectral line in shown in Fig. 1.7.

In addition, if the wind now also has a substantial broadening component due to microscopic motions, then the spectral line will be broadened beyond the frequencies determined by the outflow. However, in these *line wings*, a peculiar thing can happen. The wind is optically thick to a certain frequency only because of the column of matter that is able to interact with that particular frequency. Microscopic broadening can force a portion of this emission outside of the frequency reach of this sensitive zone, bringing it into optically thin regimes. Thus, the blue wing absorbed emission can sometimes become visible nonetheless as a small bump around the maximum blue-shifted velocities. This small bump then subsides as the frequencies begin to transition into optically thick regimes, to then further proceed with the standard blue-wing absorbed line profile. The small bump that this causes is visible in the blue shifted wing of the spectral line shown in Fig. 1.7.

Spatial resolution effects

The beam size of a single-dish telescope can also affect the spectral line shape. For the sake of simplicity, we continue discussing the spherical outflow. If the telescope beam fully envelops the emission zone inside the stellar wind, then the above mentioned considerations are valid. But when the beam size becomes smaller than this line formation region, the line shapes can undergo an important metamorphosis. Consider an optically thin wind first. Centering the beam on the center of the wind, it will have an angular opening that is smaller than the maximal angular size of the line forming region. And, for well-behaved spherical outflows, this maximal extent corresponds to the material in the cones with maximal projected area. These cones correspond with the lowest projected velocities, and thus with the matter that is moving perpendicular to the line of sight. So, for these velocities (and thus frequencies), the captured emission will be decreased compared to the fully unresolved wind. However, for the higher and lower velocities, the projected cones fit inside the telescope beam, and hence the light gathering at these frequencies remains unaffected. Thus, the line profile will exhibit a central valley, and is called a *double-peaked* line profile. Such a line is shown in the bottom middle panel of Fig. 1.4. The smaller the telescope beam is compared to the full extent of the line forming region, the more outspoken this effect will be.

For optically thick winds the effect is essentially the same. However, the resulting profile will evolve somewhat differently due to its inherently differing shape from the flat-topped optically thin line. The central frequencies will also be diminished by the beam, gradually evolving the parabolic line to a flatter looking line. Only for extreme ratios between the beam size and the size of the line formation zone will the optically thick line also exhibit a double peak.

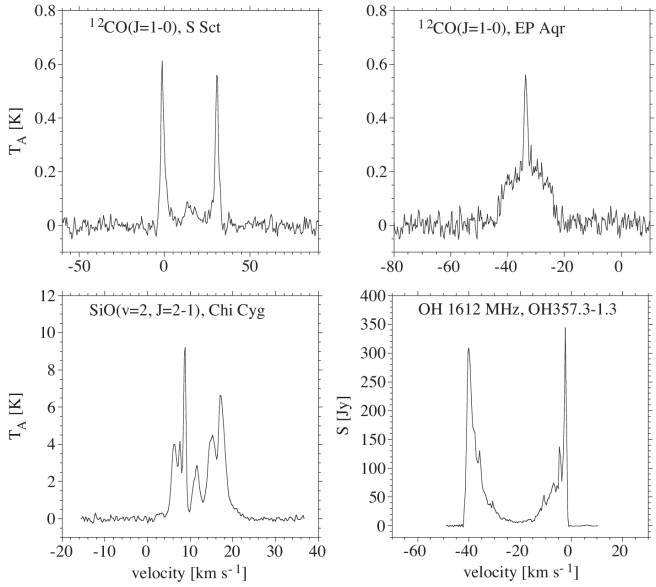

Figure 1.8: Spectral lines with intrinsic shapes that cannot be explained by a smooth spherical outflow.

The beam of the telescope can also be placed off-center. Shifting the beam slightly off-center will primarily reduce the observed emission around zero projected velocity. However, as the beam is moved farther away from the central axis, this impact will propagate to higher velocities, until the highest velocities become excluded from the telescope beam. The highest velocities will then disappear from the line profile and it will become narrower. The width of the line profile will diminish as the beam moves further off-center, until it points completely away from line formation zone hence causing the line to completely disappear.

Morphological effects

For smooth spherical outflows the preceding considerations and descriptions are perfectly valid. The extraordinary capabilities of modern telescopes however permit the detailed probing of the innermost regions of the stellar wind, where the most important deviations from sphericity are observed.

As shown in Sect. 1.2, the realm of CSE morphologies is vast, with virtually infinite variation within each morphological category. Hence, it is impossible to attempt to quantify the impact of each morphology on the resulting spectral lines. Instead, to

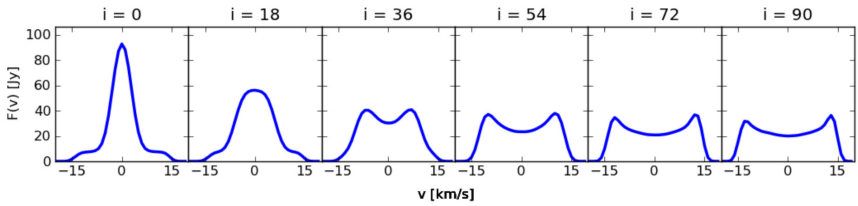

Figure 1.9: Synthetic line shape of a spiral confined to the equatorial plane, embedded in a spherical outflow. The shape changes as a function of inclination angle.[72].

illustrate the importance of morphology, the discussion is held from the vantage point of observations. Seen in Fig. 1.8 are a sequence of line profiles observed by single-dish telescopes. Most appear noticeably different from the above mentioned flat-topped, parabolic or double-peaked line profiles. These are obvious indications that a radially outflowing spherical wind is not a proper model for explaining these lines. We briefly discuss the possible origin of the shapes displayed in Fig. 1.8, from top left to bottom right. (1) Two distinctly separated peaks indicate may that the wind contains a detached shell. Or, it could also reflect an equatorial density enhancement, viewed edge-on. (2) A broad plateau with a narrow peak suggests a cylindrical morphology, like a disk, torus, or equatorial spiral pattern [72, 71]. (3) Chaotic line profiles can be caused by masering molecules, but may also indicate a very chaotic morphology, like randomly distributed clumps or shells. (4) This shape is typically attributed to masers, but could in theory also be an extremely resolved spherical outflow, or even a situation similar to (1).

The lines in Fig. 1.8 strongly suggest the presence of an outflow with a complex morphology. However, not all lines originating from a non-spherical wind exhibit a recognisable deviation from the flat-topped, parabolic or double peaked line shape. In fact, most spectral lines are extremely apt at hiding any morphological information. This is because the spectral lines essentially compress all information about the spatial distribution of the emitting material (for example along the constant projected velocity cones) into a singular point on the frequency axis. This effectively erases the spatial information. Hence, though any deviation from the spherical outflow model will immediately impact the line shape, the effect may be impossible to identify. Only for a few distinct physical set-ups will morphological peculiarity manifest in the spectral line as two or more distinct components. This can be seen in Fig. 1.9, which shows a sequence of synthetic spectral lines emitted by a flat spiral embedded in a spherical outflow, as a function of inclination angle. When seen face-on (i=0), the spectral line exhibits the dual nature of the wind. But when observed edge-on (i=90), the dual nature of the wind is completely hidden. In fact, one may very well misinterpret such a line as being a resolved spherical outflow.

Spatially resolved imaging of the CSE may help to lift this degeneracy. *Interferometry* permits the observation of astronomical sources at extremely high spatial resolution.

1.5 High spatial resolution observations: Interferometry

Intereferometry is the combination of a series of different single dish telescopes into a much more powerful telescope in terms of spatial resolving power. The resolution of the interferometer θ_r is

$$\theta_r \simeq \frac{\lambda}{b_{\max}}, \tag{1.2}$$

where $b_{\max}$ is the largest separation between two individual dishes, i.e. the longest *baseline*. The use of discrete dishes instead of one dish has the advantage that the separation $b_{\max}$ can be made large by placing the outermost ones far from each other, and thus the spatial resolution of the telescope can be made small. One such instrument is the Atacama Large Millimeter-submillimeter Array (ALMA). However, there are also some important drawbacks to such an instrument.

The most important drawback of an interferometric antenna array is, as the name suggests, the inevitable occurrence of interference. The difference in path length the light has to travel from the source to the interferometer dishes will, when combined, produce a very strong and intricate pattern of constructive and destructive interference. This pattern, whose appearance lies very far away from the observed brightness distribution, needs to be 'reverse engineered' in order to reconstruct the original observed emission pattern. This is a difficult task, considering the complexity of the problem.

The limited coverage of the full interferometer 'dish' by the individual antennae results in a good sampling of certain length-scales, compared to a poor sampling of other length-scales. This issue is typically mitigated by performing the observation for extended periods of time. The rotation of the earth makes the dishes trace paths that cause a more complete filling of the 'virtual interferometer dish' area. However, this only partially solves the sampling problem, and thus the recovery of the exact observed brightness distribution can never happen flawlessly. Furthermore, the procedures for the recovery of the brightness distribution of the observed source from the fringe pattern requires a detailed description of the complete instrumental (intrinsic noise) and atmospherical (extrinsic noise) conditions at the moment of observation. These are measured to the highest degree possible, but can sometimes not be completely quantified, and need to be approximated. The consequences of these limitations are that the data recovery procedures often introduce unreal artifacts into the reconstructed

data. It is the scientist's task, when working with such data, to quantify the degree of 'contamination' by such artifacts, and attempt to remove them.

The scientist is left with exceptional fully three dimensional data, one frequency dimension (which relates to the 'depth' dimension through the projected velocity) and two spatial dimensions (which are the coordinates in the plane of the sky, thus 'width' and 'height'). Each emission map at a certain frequency is known as a *channel map*, and the full data block is known as a *data cube*. We discuss the properties and use of these channel maps in the following section.

1.5.1 Molecular emission - Imaging through intensity channel maps

Unlike the low spatial resolution of the data obtained via single-dish measurements, where the beam size is so large that only a mean flux can be measured per frequency, interferometry can provide an actual spatially resolved emission map of the object, per frequency. This concretely means that at each frequency the data consists of a two-dimensional map, showing how the emission is distributed throughout the spatial domain bound by the map. The interpretation of these maps may be complex, as they are flat projections of the three-dimensional emission surface of constant projected velocity along the line of sight (fully determined by a generally unknown velocity field), probing an unknown density distribution.

Consider again the smooth spherical outflow: the energy captured at each frequency bin making up the spectral line originates from a conical zone in the wind. High blue or red shifted velocities correspond to narrow cones pointing away and to the observer. For these cones the projection on the plane of the sky will be a small circle. As one progresses towards the rest frequency of the transition, this circular projection will increase in radius. The radius of this emission pattern reaches a maximum at the rest frequency, after which it steadily decreases. This is the typical progression of the expected frequency dependent spatial emission distribution of the smooth spherical outflow, and is shown in Fig. 1.10.

The smooth spherical outflow is an ideal case. The presence of any density and/or temperature inhomogeneities or enhancements in such a spherical outflow have an impact on the emission distribution. Because the velocity field is unchanged, the traced surfaces are still cones. But, the emission pattern per cone is now spatially dependent. The presence of an outwardly propagating spiral pattern or enseble of clumps clearly manifest in the channel maps, though they may not be immediately recognisable at first sight. We show this in Fig. 1.11, where a dense equatorial spiral pattern is embedded into the model of Fig. 1.10. The spiral is viewed at an inclination

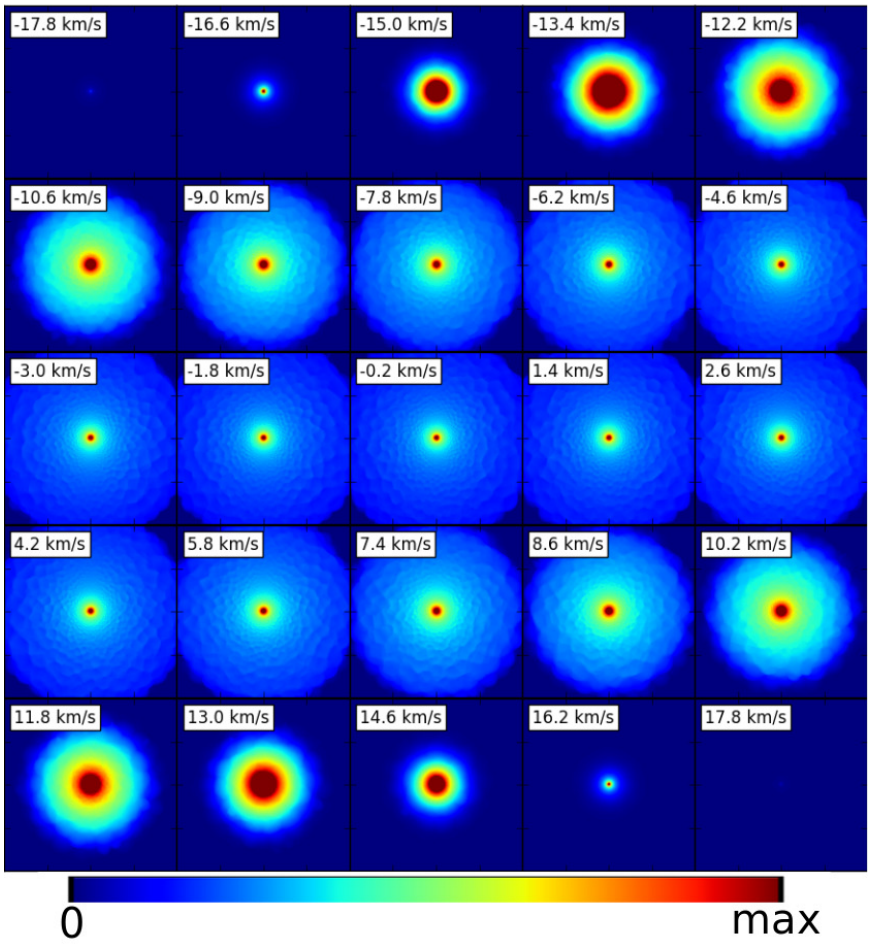

Figure 1.10: Tile plot of resolved synthetic emission (CO rotational transition J =3−2 with LIME, see Chapter E in the appendix) of a spherical outflow. Each tile is a channel map, corresponding with the spatial emission distribution at a certain frequency (or velocity). Here it is clear that the projection of the conical surface of constant velocity along the line of sight is a circle, whose diameter increases as one approaches the natural frequency of the transition. The 'grainy' internal structure present in the channel maps is a numerical artifact. The linear colourbar on the bottom has been used to indicate the intensity, with red being high and blue being low intensity.

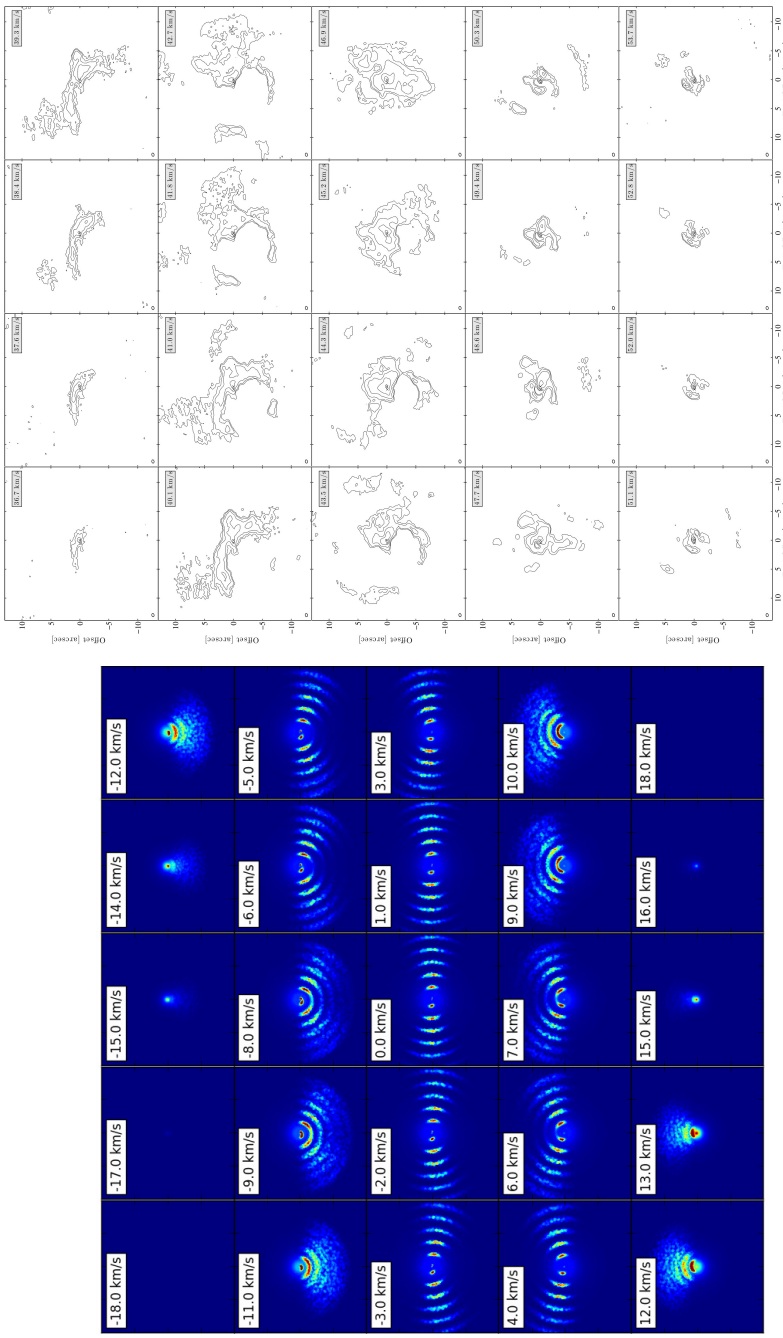

Figure 1.11: *Left Figure:* Same as Fig. 1.10 (including colourmap), but for a spherical outflow with an embedded equatorial spiral morphology, observed at an inclination angle of 54°. The grainy texture of the emission patterns is a numerical artifact. *Right Figure:* Contour channel maps of the CO J =3–2 transition of the inner wind of the Mira AB system. [155]

angle of 54 degrees away from the face-on position. It is not immediately obvious that the viewed morphology is an equatorial spiral pattern.

The high resolution of the newest interferometers permits the detailed imaging of the inner wind and acceleration regions of the AGB CSEs, where we expect intricate density, temperature and velocity features to dominate. Combined, these effects may strongly perturb the local velocity field away from the smooth radial outflow. And, if the velocity field is not constant and/or radial, then the flat channel map projections originate from possibly very complex surfaces. Hence, the task to interpret the images of these regions can quickly become extremely difficult, especially considering that for most objects the local velocity field is unknown. An excellent example of this is shown in Fig. 1.11, where we show the channel maps of ALMA data of the Mira AB system [155]. The mass losing star is accompanied by a binary companion, who stirs up the outflow of the wind, forming extremely complex morphologies that are far from easy to interpret by visual inspection only.

Besides the fact that most high-resolution observations of the inner winds of AGB stars probe unknown velocity fields, real data is often contaminated by instrumental effects, noise, and possibly even reduction artifacts. The recognition, or even the explicit manifestation of typical patterns in the channel maps may be severely hampered by these contaminants. By generating a specific kind of position-velocity diagram we may nonetheless identify 'hidden' emission patterns, if present.

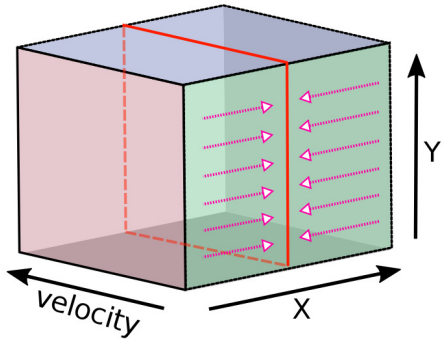

Figure 1.12: Schematic representation of the production of a wide-slit PV diagram. The cube represents the 3D datacube, with two spatial axes (X,Y) and a velocity axis. A slit over the data is selected (red slice), provided the velocity axis remains intact. In this particular case the Y-axis is conserved. Subsequently, all the emission of the 3D data is collapsed onto the slit (purple arrows), by summing up the intensities with idential (Y,v) coordinates.

1.5.2 The position-velocity diagram

3D emission data consists of two linearly independent angular dimensions (representing the two angular coordinates in the plane of the sky), and one (projected) velocity dimension. The position-velocity diagram (PVD) is, in effect, a slice through the 3D data at an arbitrary angular axis in the plane of the sky (thus preserving the velocity axis). It is thus a 2D plot of the emission along this chosen axis versus velocity. If a slice width equal to a singular resolution element is chosen, then only the emission in this narrow spatial range is contained within the PVD. This can be useful to precisely probe the spatial or spectral extent of details in the emission. However, the true power of the PVD as a tool to identify complex or recover hidden morphologies lies in the width of the PVD slice. If the slit has a width larger than one singular resolution pixel, then the emission perpendicular to the chosen spatial axis is collapsed by summing up the emission with identical PV coordinates. And by selecting a slit width that encompasses the whole signal, a condensed overview of the overall wind morphology is obtained, which enhances potentially hidden structural characteristics. It is hence extremely useful to make PVDs with a maximal slit width (namely the full size of the datacube). These will be referred to as wide-slit PVDs. The strength of this visualisation technique has been verified by Decin et al. (2015) [41], where a spiral-shaped structure was detected in the inner wind of the carbon-rich AGB star CW Leonis through PVDs. Because it is a condensed overview of the CSE emission into one or a few images, it is much easier to interpret and analyse than the full datacube, which can easily be made up of hundreds of two-dimensional images. Fig. 1.12 is a schematic representation of the manipulation of the datacube into a PVD.

Based on observations, the typical AGB CSE morphologies can be classified as either predominantly spherical, cylindrical or random. The cylindrical morphologies are of particular interest, as they may point to wind-binary interactions. Thus, it is advantageous to construct two orthogonal wide-slit PV diagrams of the 3D data, choosing any set of linearly independent (thus perpendicular) spatial dimensions oriented such as to maximally exploit the asymmetry of the data. Doing so will permit the scientist to immediately infer the symmetry of the system, an important constraint on the possible mechanism producing the aspherical wind. So, well-chosen wide-slit PV diagrams provide the user with clear correlated structural trends of the complete circumstellar environment, and are hence very powerful tools. We show the power of the orthogonal wide-slit PVDs through a schematic diagram shown in Fig. 1.13

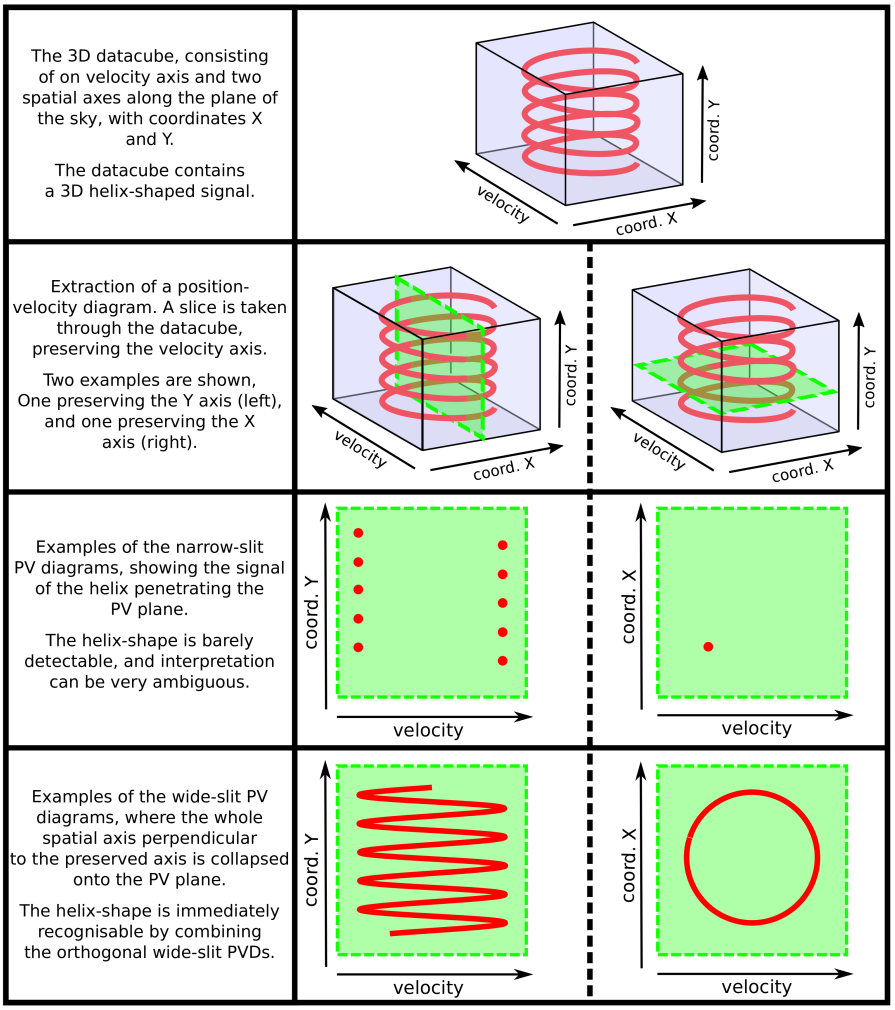

Figure 1.13: Schematic representation of the comparison between a narrow-slit and a wide-slit PV diagram. It shows the power of the wide-slit PVD as diagnostic tool for the identification of correlated structures in the emission.

1.6 This thesis

The complexity associated with the interpretation of the potentially heavily distorted emission patterns in 3D molecular emission lies at the heart of this thesis. Contrary to the detail with which the emission patterns produced by smooth spherical outflows is understood, in this new age of high-resolution observations there existed no repositories of the typical emission patterns produced by complex geometrical and kinematical set-ups, whose characteristics deviate from the smooth spherical outflow. Without these databases, the link between different manifestations of the same morphology (by e.g. a different observation vantage point) may remain enshrouded, and identification analyses need to be performed anew with every new acquired dataset. In addition, intricate correlated emission patterns originating from complex interaction regions may be left completely unidentified. And finally, as has been shown for the smooth spherical outflow, such catalogues would permit the quick estimation of local physics without extensive self-consistent modelling efforts.

Using the channel maps, PV diagrams and spectral lines as main diagnostic tools for understanding the physical and chemical details governing the stellar wind, we have created such databases, presented in Chapters 2 and 5, for the equatorial density enhancement and the embedded spiral structure. The importance of these morphologies originates from the relative occurrence of binarity among the progenitors of AGB stars, which is above 50 percent [154, 49]. Hence binary activity is considered a dominant wind shaping mechanism. This hypothesis is reinforced by the co-detection of cylindrical morphologies and binarity in the PNe and their predecessors, the post-AGB [23, 66, 22, 67]. Any significant secondary gravity source moving on a orbital trajectory confined to the innermost regions of the circumstellar environment will significantly perturb the local matter, giving rise to inhomogeneities with a directional preference, namely the orbital plane of the binary system [92, 96, 93, 29]. These can persist up to very large distances from the central star [137]. Observed binary induced shapes in the CSEs of AGB stars [114, 87, 86] point towards an evolutionary continuity (to the post-AGB and PN stages), with the origin for global morphological evolution being the AGB stage. The most recent modelling results of the rotating disk around the star L_2 Puppis, discussed in Chapters 3 and 4 [86], strongly suggest the presence of a few Jupiter mass planetary companion at the disk's inner rim, further supporting the important role of companions in wind shaping. In addition, planets have been shown to survive up to the star's final moments [169, 38], and may prove to contribute substantially to the shaping of AGB winds. Indeed, if mere planets have the power to fundamentally alter the CSE morphology, then binarity may prove to be a crucial link between the global structure of the AGB wind and the CSE of their progeny.

To simulate the synthetic emission patterns associated with these morphologies, their geometrical and physical properties have been estimated from literature, parametrised in function of their most important geometrical and physical properties, and expressed

analytically. Subsequently, the expected emission produced by these idealised physical set-ups were simulated using the LIME code, which solves the equation of transport of radiation in three dimensions for any morphology of interest in a gas in non-local-thermodynaical equilibrium (see Chapter E in the appendix). Comparing the patterns in the synthetic emission to the input geometry, statements are made about what physical or geometrical information can or cannot be recovered from them. As a final step, some of these models were fed into an observation simulation algorithm, which distorted and transformed the idealised synthetic data to simulate additional instrumental effects expected to come with true observations. Observers can now directly compare these results with real high-resolution data, in order to spot similarities and hence to speed-up the morphology identification process. This repository therefore permits quick first order estimations on the general properties of the observed object, providing a direct shortcut towards gauging the object's true physical properties via more physically consistent modelling endeavours. Of course, this procedure forced us to make certain approximations. However the main aim of this exercise was not to make detailed models, but to provide an intuitive bedrock for the interpretation of future data. Thus, as a summary, these databases serve to (1) be used to speed up the identification of emission patterns found in real data, and (2) directly link features in the emission to the physical conditions in the CSE.

We applied our acquired theoretical methodology to ultra-high resolution ALMA data of the inner wind of the evolved star L_2 Puppis. In previous work, the continuum emission of this star was acquired with SPHERE and showed the star to be surrounded by a compact disk of dust [88]. Subsequent observations with ALMA unambiguously show the presence of a rotating disk of gas and dust in the data. We modelled the data to high detail, probing aspects of the local physics dominating the circumstellar environment (Chapter 4). In addition, a secondary source of emission was observed in the innermost regions of the disk, indicating the possible presence of a planet (Chapter 3). In addition to the L_2 Puppis data, ALMA data acquired during ALMA's cycle 0 on the evolved star CW Leonis was also analysed. A preliminary analysis of the data [41] suggested the presence of an embedded spiral structure. Our full-scale radiative transfer analysis of the object modelling confirms the presence of this large embedded spiral morphology, and further details the nature of the inhomogeneous inner CSE (Chapter 6).

Chapter 2

Simplified models of equatorial density enhancements for interpreting high-resolution data.

(2016A&A...596A..91H)

Ward Homan[1], Jels Boulangier[1], Leen Decin[1], and Alex de Koter[1,2]

[1] Institute of Astronomy, KU Leuven, Celestijnenlaan 200D B2401, 3001 Leuven, Belgium
[2] Sterrenkundig Instituut 'Anton Pannekoek', Science Park 904, 1098 XH Amsterdam, The Netherlands

Abstract: *Equatorial density enhancements (EDEs) are a very common astronomical phenomenon. Studies of the circumstellar environments (CSE) of young stellar objects and of evolved stars have shown that these objects often possess these features. These are believed to originate from different mechanisms, ranging from binary interactions to the gravitational collapse of interstellar material. Quantifying the effect of the presence of this type of EDE on the observables is essential for a correct interpretation of high-resolution data. We seek to investigate the manifestation in the observables of a circumstellar EDE, to assess which properties can be constrained, and to provide an intuitive bedrock on which to compare and interpret upcoming high-resolution data (e.g.* ALMA *data) using 3D models. We develop a simplified analytical parametrised description of a 3D EDE, with a possible substructure such as warps, gaps, and spiral instabilities. In addition, different velocity fields (Keplerian, radial, super-Keplerian, sub-Keplerian and rigid rotation) are considered. The effect of a bipolar outflow is also investigated. The geometrical models are fed into the 3D radiative transfer code* `LIME`*, that produces 3D intensity maps throughout velocity space. We investigate the spectral signature of the J=3−2 up to J=7−6 rotational transitions of CO in the models, as well as the spatial aspect of this emission by means of channel maps, wide-slit position-velocity (PV) diagrams, stereograms, and spectral lines. Additionally, we discuss methods of constraining the geometry of the EDE, the inclination, the mass-contrast between the EDE and the bipolar outflow, and the global velocity field. Finally, we simulated* ALMA *observations to explore the effects of interferometric noise and artifacts on the emission signatures. The effects of the different velocity fields are most evident in the position-velocity diagrams (PVDs). These diagrams also enable us to constrain the EDE height and inclination. A level of degeneracy may occur in the shapes of individual PVDs for different global velocity fields. The orthogonal PVDs may completely eliminate this ambiguity. Information on the EDE substructure is evident in the channel maps, but cannot be recovered from the PVDs, nor from the spectral lines. However, stereograms enable the detection of warping. For most inclinations the spectral lines are relatively broad, making it difficult to distinguish from an eventual superposed bipolar outflow component. Only under low inclination angles can one distinguish between these structures. Simulations of synthetic ALMA observations show how emission is affected when the largest angular scale of an antenna configuration is exceeded. For a rotating EDE, the emission around zero velocity will first fade because of filtering of the interferometer of large spatial scales.*

Contribution to the article: *The flared Keplerian disk models have been constructed and modelled in a joint effort with Jels Boulangier in the context of his Master thesis. All other work scientific work discussed below, as well as the composition of the article was carried out solitarily, with the exception of regular consulatation with my supervisors.*

2.1 Introduction

We compare the intrinsic emission signatures of different analytical EDE models to provide the reader with an insight on how these objects manifest in the observables to aid the interpretation and analysis of future data. In particular, we focus on the effect of the velocity structure in the EDE, the combined emission signal of a Keplerian rotating disk with a bipolar outflow, and a density substructure within the EDE.

This chapter is organised as follows: In Sect. 2.2 we provide a detailed description of the mathematical expressions generating the desired morphologies, followed by the physical and numerical setup of our models (Sect. 2.3). Section 2.4 presents the results of the radiative transfer calculations in the form of channel maps, PVDs, and integrated spectra. In Sect. 2.5, we link the calculated intensities to intrinsic geometrical properties and discuss the use of stereograms. Section 2.6 shows the effect of the *ALMA* 'eye' on the characteristics of the intrinsic emission. Finally, a summary of the findings is given in Sect. 2.7.

2.2 Morphological models and scientific motivation

2.2.1 General assumptions of the EDE

Spherical coordinates are defined as

$$r_{xyz} = \sqrt{x^2 + y^2 + z^2}, \tag{2.1}$$

$$\theta = \arccos\left(\frac{z}{r_{\mathrm{xyz}}}\right), \tag{2.2}$$

$$\phi = \arctan\left(\frac{y}{x}\right), \tag{2.3}$$

representing radial distance, and vertical and equatorial angle respectively. Cylindrical coordinates are defined as

$$r_{xy} = \sqrt{x^2 + y^2}, \tag{2.4}$$

$$\phi = \arctan\left(\frac{y}{x}\right), \tag{2.5}$$

$$z = z, \tag{2.6}$$

representing radial distance, and equatorial angle, and vertical height (with respect to the equatorial plane) respectively.

The shape of an analytical EDE is, in principle, comprised of three major spatial dependencies. One radial component (R), one component describing any possible equatorial variations (Φ), and a final constituent describing its height (Z). Each of these can be dependent on any of the cylindrical coordinates. In dimensionless units we express this as

$$D(r_{xy}, \phi, z) = R(r_{xy}, \phi, z)\ \Phi(r_{xy}, \phi, z)\ Z(r_{xy}, \phi, z), \tag{2.7}$$

where D is the physical property that is being described.

To describe the physical properties of the EDE, one needs to specify temperature, density and velocity. We assume a power-law temperature dependence for the gas constituting the EDE,

$$T_{EDE}(r_{xy}) = T_* \left(\frac{r_{xy}}{R_*} \right)^{-\epsilon}, \tag{2.8}$$

with T_* the stellar temperature, R_* the stellar radius, and ϵ the temperature power-law index. We note that the assumed temperature profile is independent of the vertical height coordinate z. This is inconsistent with optically thick EDEs, since for a fixed radial distance these types of EDEs would have relatively hot surface layers and a relatively cool mid-plane zone [150]. As these obscured mid-plane regions are mostly unobservable at the (infrared and submillimeter) line frequencies investigated here, they will only marginally affect our results.

A universal turbulent velocity $v_{\rm turb}$ is present in the entire spatial domain of the numerical model.

Since we aim to understand different density structures and velocity fields, different prescriptions will be analysed. We detail the physical assumptions and analytical formulations in Sect. 2.2.2 and 2.2.3, respectively. As EDEs are often accompanied by a bipolar outflow, we also study the effect of a bipolar outflow on the observables. A mathematical description is given in Sect. 2.2.4.

2.2.2 Density structure

Flared EDE

We construct a simple EDE with no substructure by setting $R(r_{xy}, \phi, z) = R(r_{xy})$, $\Phi(r_{xy}, \phi, z) = 1$ and $Z(r_{xy}, \phi, z) = Z(r_{xy}, z)$, shown in Fig. 2.1. The radial component of the EDE density is assumed to decay as a power law. Vertically, a simple Gaussian distribution is assumed. This is consistent with the previously made assumption of a flat, non-self-gravitating, vertically isothermal disk. In addition we define a critical radius r_c within which the density of the EDE has been set to zero, to simulate its inner

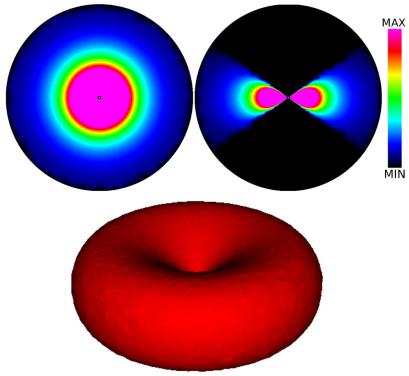

Figure 2.1: Visualisation of the EDE density model. The top left image shows a cut through the equatorial plane, the top right image shows a cut through a meridional plane. MIN represents the minimum density in the models (in this case zero), and MAX has been chosen such as to enhance the visual appearance of the image. The bottom image shows a three-dimensional contour plot of the red regions in the top images of this figure.

radius. Mathematically, this translates to an EDE density represented by

$$\rho_{EDE}(r_{xy}, \phi, z) = \rho_0 \left(\frac{r_{xy}}{r_c} \right)^{-p} \exp\left[\frac{-z^2}{2H(r_{xy})^2} \right], \tag{2.9}$$

where ρ_0 represents the density at $r_{xy} = r_c$ and $z = 0$, p describes the rate at which the density decays radially, and $H(r_{xy})$ represents the one-sigma Gaussian height of the EDE. Adopting the solution of a disk in vertical hydrostatic equilibrium we express the Gaussian height $H(r_{xy})$ as

$$H(r_{xy}) = H_c \left(\frac{r_{xy}}{r_c} \right)^h, \tag{2.10}$$

where H_c represents the initial one-sigma height at $r_{xy} = r_c$ and $z = 0$, and the exponent h represents the characteristical course with which the EDE height changes as a function of radius. By adopting $h > 1$, which ensures the aspect ratio $H(r_{xy})/r_{xy}$ keeps increasing, we can refer to this property as the flaring of the EDE.

Warped EDE

Warped EDEs have been observed [140], and are believed to arise when a strong non-axisymmetrical force is acting on the EDE. It is theorised that compact, high-mass objects may bring about such a force [141, 136, 145]. AGB stars and their descendants

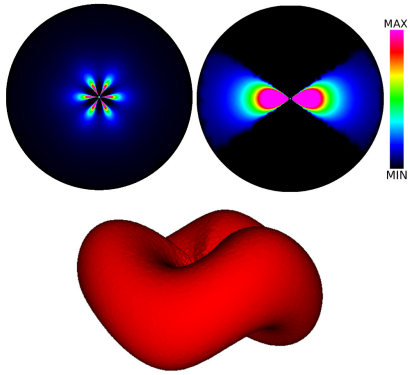

Figure 2.2: Visualisation of the density model of the warped EDE with three undulations. The top left image shows a cut through the equatorial plane, the top right image shows a cut through a meridional plane. The meaning of the colours is clarified by the linear colourbar on the right. MIN represents the minimum density in the models (in this case zero), and MAX has been chosen such as to enhance the visual appearance of the image. The bottom image shows a three-dimensional contour plot of the model.

are often accompanied by a binary companion [154, 49]. If the system acquires an EDE, and the companion is massive enough, the EDE may result in acquiring a warp. Though presently not well understood, warped EDEs have also been observed around solar-type (pre-) main sequence stars [15], and may somehow be related to planet formation [24].

The density of our warped EDE is represented by

$$\rho_d(r_{xy}, \phi, z) = \rho_0 \left(\frac{r_{xy}}{r_c} \right)^{-p} \exp \left[\frac{-(z - A \sin(N\phi))^2}{2H(r_{xy})^2} \right], \tag{2.11}$$

where A is the amplitude of the warping, and N the number of undulations. $H(r_{xy})$ is as described in Eq. 10. A visual representation of a warped EDE with three undulations can be found in Fig. 2.2.

Spiral-shaped density model

Spiral-shaped instabilities arise when the attracting force of the primary source of gravity has a magnitude large enough to overcome both the internal pressure gradient of the gas (i.e. Jeans criterion) and the centrifugal forces, and also to halt the relative motion between different portions of the differentially rotating object [180]. Recent

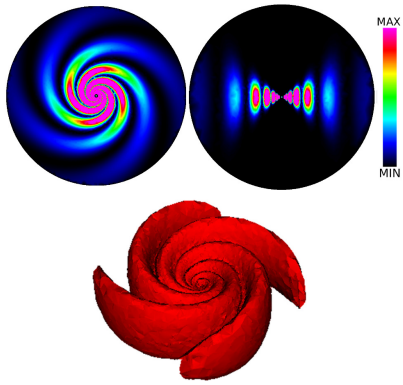

Figure 2.3: Visualisation of the density model of the spiral-shaped density model. The panels have the same meaning as in Fig. 2.2.

high-resolution observations of the CSE of young stars have clearly identified spiral-shaped instabilities [32], which have lead to an extensive study of their detectability (in continuum emission) via *ALMA* simulations [44]. Theoretical work on their formation and on the consequences of their presence is currently underway [45, 81, 110]. It is believed that massive planets inside protoplanetary EDEs may also cause such patterns [47, 212].

We model EDE containing spiral-shaped instabilities as

$$\rho_d(r_{xy}, \phi, z) = \rho_0 \sin(L\phi + \omega(r_{x,y})) \left(\frac{r_{xy}}{r_c}\right)^{-p} \exp\left[\frac{-z^2}{2H(r_{xy})^2}\right], \tag{2.12}$$

where L is the number of spiral arms and $\omega(r_{xy})$ is a radial dependent phase factor. We find that a phase factor which depends logarithmically on the radius $\omega(r_{xy}) \sim \log(r_{x,y})$ produces spiral shapes which, in visual appearance, closely resemble the instabilities generated by hydrodynamical simulations of young stellar objects and protostellar systems [110, 197]. $H(r_{xy})$ is as described in Eq. 10. Fig. 2.3 contains a visual representation of the density model.

EDE with annular gap

The primary cause for the formation of an annular gap in an EDE would be the growth of a (proto) planet from the rotating EDE-material. Recent high-resolution imaging has proven able to resolve such gaps, which are the direct consequences on EDEs of planets in the making [55]. These discoveries have also lead to a theoretical development of the mechanics behind the formation of these gaps in protoplanetary systems [105].

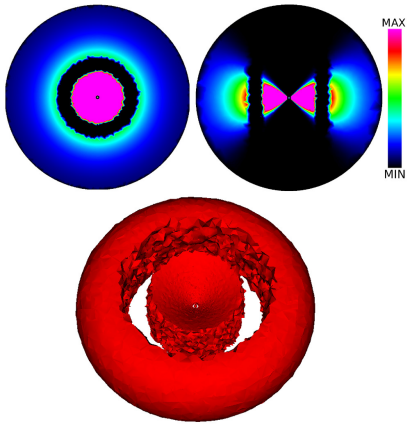

Figure 2.4: Visualisation of the density model of the EDE containing an annular gap. The panels have the same meaning as in Fig. 2.2. The coarseness of the gap edges is purely a resolution effect.

The annular gap in the EDE is achieved by setting a fixed radius-range in which the EDE density is substantially reduced. The images in Fig. 2.4 show a three-dimensional contour plot of this geometry, and slices through such an EDE.

Table 2.1: The different combinations of previously described morphological properties we explore in this chapter. The last column refers to the section where the specific combination is discussed.

EDE Density	EDE Velocity	Extra feature	Section
Flared	Keplerian		2.4.1
Flared	Radial		2.4.2
Flared	Super-Keplerian		2.4.2
Flared	Sub-Keplerian		2.4.2
Flared	Rigid rotation		2.4.2
Warped	Keplerian		2.4.3
Annular gap	Keplerian		2.4.3
Spiral instabilities	Keplerian		2.4.3
		Bipolar outflow	2.4.4
Flared	Keplerian	Bipolar outflow	2.4.4

2.2.3 Velocity field

We also appraise five global velocity fields: Keplerian, super-Keplerian, sub-Keplerian, rigid rotation and radially outflowing.

- **Keplerian field:** An EDE can be assumed to rotate in a Keplerian way by simply assuming a zero net force on an orbiting test-particle. This is the most basic of the chosen velocity fields. This field has an exclusively tangential velocity component of the following magnitude

$$v_{EDE} = v_{EDE,\perp}(r_{xy}) = \sqrt{\frac{GM_*}{r_{xy}}}, \tag{2.13}$$

  where M_* is the mass of the central object to which the EDE is gravitationally bound.

- **Super-Keplerian field:** Super-Keplerian EDEs, i.e. differentially rotating EDEs with a positive radial velocity component, are believed to exist around rapidly rotating stars, and are the result of material reaching the critical velocity for mass-loss from the equatorial regions [104]. Super-Keplerian EDEs have also been used to model EDEs surrounding the central regions of post-AGB stars [20]. An increased rotation rate, or an augmented tangential velocity component of the field will result in the centripetal force on a test-particle to surpass the graviational attraction, resulting in the test-particle slowly travelling outward. It must be noted that in such a case the tangential velocity structure of the differential rotation field would be somewhat different from Keplerian. However, because we do not possess a clear analytical description of such a rotational field, we approximate it by modelling a Keplerian field superposed by an outward radial velocity field $v_{\rm out}$. The temporal stability of such a field is guaranteed only if $v_{\rm out}$ is much smaller than the mean tangential Keplerian velocity.

- **Sub-Keplerian field:** Accretion of elliptically orbiting material onto EDEs, and the subsequent mixing with the EDE material, can exert a torque on the system which is great enough to slow the rotation down to sub-Keplerian regimes, pushing the material in towards the central star [25, 196]. We refer to this scenario as the sub-Keplerian case, where an inward velocity $v_{\rm in}$ has been superposed on top of a differentially rotating field. A particle travelling in this field will slowly spiral inward. Following the same argumentation as for the super-Keplerian field, we approximate the perturbed rotating field by a Keplerian velocity field superposed by an inward radial velocity field $v_{\rm in}$. The condition for the temporal stability of this field is identical to the super-Keplerian case.

- **Rigid rotation:** The presence of a strong magnetic field can generate the required torque to force a rigid rotation. Simulations of protoplanetary EDEs with

magneto-rotational instabilities can generate self-correcting (thus stable) rigid rotators [83]. In addition, MHD (magneto-hydrodynamics) has shown the periodical formation of a rigidly rotating EDE in a line-driven wind of a rotating star with a properly aligned dipole surface field [181]. We model this rigid rotation (which is rotating with a constant angular velocity) by setting a maximum tangential velocity v_{tan} at the boundary of the model.

- **Radial field:** Radially outflowing EDEs have been frequently observed around post-AGB stars [70, 31] and possibly also around AGB stars [87]. We model our radially outflowing EDE by assuming a constant outflow velocity v_{rad}.

2.2.4 Bipolar outflow

Finally, we briefly discuss the emission characteristics of a bipolar outflow. We do this because we expect, due to the geometrical boundary conditions, EDEs and bipolar outflows to be commonly observed together in the evolved stars regime. If an EDE forms around an evolved star which is producing a wind, the EDE will obstruct the motion of the gas through its densest regions, and naturally collimate the outflow. Quantifying the appearance of bipolar outflow emission is therefore essential when studying cylindrically symmetrical morphologies of evolved star CSEs.

Velocity $v_{\rm bo}$:
We assume the bipolar outflow to have an exclusively radial velocity field, expressed as

$$v_{\rm bo}(r_{xyz}) = v_\infty \left(1 - \frac{r_c}{r_{xyz}}\right)^\beta, \tag{2.14}$$

where v_∞ is the terminal wind velocity, and where β is the parameter controlling the rate of acceleration of the flow.

Density $\rho_{\rm bo}$:
The density of the bipolar outflow is exclusively radial, and given by

$$\rho_{\rm bo}(r_{xyz}) = \frac{\dot{M}}{\Omega r_{xyz}^2 v_{\rm bo}(r_{xyz})}, \tag{2.15}$$

where $\dot{M}$ is the mass loss rate of the central star through the bipolar outflow, Ω is the total solid angle taken up by the bipolar outflow, and $v_{\rm bo}(r_{xyz})$ is the radial velocity of the outflow. For an un-obscured wind, $\Omega = 4\pi$. When the radial wind is obscured by an EDE, the solid angle of the bipolar outflow is limited by the boundary between the two structures, the description which is given in Sect. 2.4.4.

Temperature $T_{\rm bo}$:
For the temperature structure we adopt the same power-law profile as for the EDE (Eq. 8), albeit using the spherical radial coordinate,

$$T_{\rm bo}(r_{xyz}) = T_* \left(\frac{r_{xyz}}{R_*} \right)^{-\gamma}, \tag{2.16}$$

with T_* the stellar temperature, R_* the stellar radius, and γ the temperature power-law index.

2.3 Radiative transfer models and numerical methods

2.3.1 Parameter space

In this section we describe the models we examine, as well as the model parameters of each specific combination of density and velocity field. Table 2.1 presents the combinations of specific morphological models we explore. We also present a listing of both the general parameters (Table 2.2), and of the specific physical and morphological parameters of the investigated geometries (Table 2.3).

Table 2.2: General situational parameter values of every radiative transfer model.

Stellar Parameters	
T_*	2500 K
L_*	10000 $L_\odot$
M_*	2 $M_\odot$
Distance	150 pc
$[CO/H_2]$	5.0×10^{-4}
Dust Parameters	
Amorphous Carbon	53%
Silicon Carbide	25%
Magnesium Sulfide	22%
Gas/Dust by mass	100

The choice for the stellar and dust parameters are based on estimations of the system properties of the carbon-rich AGB star CW Leo (See Homan et al. (2015) [72] for details).

The overview presented in Table 2.3 is chosen such as to narrow-down the total explorable parameter space. The EDE parameters are based on values which are

Table 2.3: Parameter values of the EDE and bipolar outflow models.

EDE density parameters		
p	2.25	
H_c	2.0 AU	
h	1.25	
$M_{\rm EDE}$	$10^{-3}\,{\rm M}_\odot$	
EDE velocity parameters		
$v_{\rm out}$	$2.0\,{\rm km\,s^{-1}}$	(super-Keplerian)
$v_{\rm in}$	$-2.0\,{\rm km\,s^{-1}}$	(sub-Keplerian)
$v_{\rm rad}$	$10.0\,{\rm km\,s^{-1}}$	(radial)
$v_{\rm tan}$	$10.0\,{\rm km\,s^{-1}}$	(rigid rotation)
$v_{\rm turb}$	$1.0\,{\rm km\,s^{-1}}$	
EDE temperature parameters		
ϵ	0.5	
Bipolar outflow parameters		
v_∞	$10.0\,{\rm km\,s^{-1}}$	
$v_{\rm turb}$	$1.0\,{\rm km\,s^{-1}}$	
β	0.5	
r_c	10.0 AU	
γ	0.5	
$M_{\rm bipolar}$	$10^{-3}\,{\rm M}_\odot$	

bound by theory, and whose numerical values have been confirmed by modelling of observations. Hydrostatic equilibrium for a non-self-gravitating Keplerian disk requires that $h = -\epsilon/2 + 3/2$. The parameter ϵ (see Eq. 8) adopts a value of 0.75 for the flat disk limit, and 0.5 for a more complex flaring disk [84]. Chianh et al. (1997) [30] and Hartmann et al. (1998) [65] show the latter to be more consistent with reality, resulting in a flaring coefficient h of 1.25. Expressing the disk midplane density as a function of its surface density (defined as the integral of the mass volume density ρ over the vertical disk height z) one comes to the relation $p = f + h$, where f is the power of the rate with which the surface density drops with radius. Generally, f is found to have a value between 0 and 1 [205, 99, 5]. Andrews et al. (2009,2010) [6, 7] found a mean value of $< f > \sim 1$ for a sizable sample of disks. Adopting this value for the radial surface density decay rate and the previously adopted value for the flaring exponent, the value of $p = 2.25$ is obtained. This value also happens to coincide with typical density decay rates found in EDEs around post-AGB stars and planetary nebulae [20, 23, 22]. The bipolar outflow parameters correspond to typical expected values of dust-driven winds generated by evolved stars.

At this point we wish to emphasise that the main aim of this work is to provide the reader with a basic intuition on how EDEs might manifest in the observables. The

numerics involved in calculating the transport of radiation for such a vast set of cases is very CPU-intensive. Thus, in order to circumvent hydrodynamics calculations and thus mitigate calculation times no effort has been committed to ensuring the adopted expressions are physically self-consistent. However, a very low degree of consistency has been implemented using analytical first-order approximations of disk morphologies. In addition, besides having made such reasonable assumptions, it must be noted that these assumptions are only valid for simple, non-self-gravitating, hydrostatically stable Keplerian disks. The assumption that the previously described physical distributions, and parameter values are universally valid for each case presented in Table 2.1 is therefore substantial. Nevertheless, we believe these simplifications to be valid first-order approximations, and therefore use them universally throughout this chapter. The same can be said of the velocity fields, and especially of the sub- and super-Keplerian cases. These are both approximated by a regular Keplerian field, with a superposed radial component. While one would also expect the tangential velocity structure of such a steady-state to be different from the simple Keplerian field, the Keplerian field should still be a good first-order approximation of a differentially rotating field with its highest tangential velocities close to the central star.

2.3.2 Radiative transfer

To generate the 3D intensity channel maps of simulated emission of the above models, the Non-Local-Thermodynamical-Equilibrium (NLTE) full-3D, submillimeter and infrared (IR) radiative transfer code `LIME` was used. For a technical overview of the inner workings of the code, see Chapter E in the appendix, or Brinch et al.(2010) [19].

We focused mainly on the emission of the CO J=3−2 rotational transition (unless otherwise stated), for which the spectroscopic CO data of the LAMDA database [165] were used. The collisional rates were taken from Yang et al. (2010) [210]. We have chosen this transition as the primary reference transition because the line formation zone encompasses most of the morphological structure, yet does not extend into the region where photodissociation effects must be taken into account.

All models have been sampled with approximately 7×10^5 tetrahedral cells, whose size and position have been weighted by the density in the model.

2.3.3 Synthetic ALMA simulations

To produce simulations of *ALMA* observations of the emission of the spiral wind models we used the Common Astronomy Software Applications, `CASA`, post-processing package [126]. It consists of a collection of `C++` tools, managed by a `python` wrapper code.

The specific tools used to simulate the observations are the 'simobserve' and 'clean' functions. The simobserve task converts any model image (corresponding to the true sky brightness distribution) into virtual observations. For that it is necessary to specify quantities such as integration time, antenna configuration, frequency, and astrometrical and atmospherical parameters. These are used to calculate the noise contributions in uv-space. Subsequently, the task creates the Fourier transform of the model image and projects this onto this grid. The clean task converts your visibilities from uv-space back into real coordinates, to simulate how *ALMA* would see the input model. Finally, it performs a deconvolution of this 'dirty image' to get rid of the sidelobe structure, yielding a 3D datacube of a synthetical *ALMA* observation of the intrinsic 3D emission.

2.3.4 The wide-slit position-velocity diagram

As discussed in Sect. 1.5.2, it is advantageous to construct two orthogonal wide-slit PVDs of the 3D data, choosing any set of linearly independent (thus perpendicular) angular dimensions oriented such as to maximally exploit the asymmetry of the data. In the case of disk-like structures, one slit should be oriented along (or parallel to) the equatorial axis, and the other along (or parallel to) the polar axis of the structure.We note that these orientations cease to have meaning when the structure is viewed face-on. The axes along which the asymmetry of the models appears strongest will be labeled as X and Y. X and Y are thus by no means fixed spatial coordinates, but are rather chosen entirely as a function of the geometrical properties of the observed system. All PVDs presented in this chapter have been constructed following these instructions, with X being the polar axis, and Y being the equatorial axis (for non-face-on views). In all the following sections, the PVDs which maximally exhibit the asymmetry of the data (along X and Y) will be referred to as PV1 and PV2 respectively. Each PVD is centered on $v = 0\,\mathrm{km\,s^{-1}}$ and zero offset.

2.4 Radiative transfer results

In this section we describe the properties of the intrinsic emission in both the intensity channel maps and the spectral lines. The colour-coding used in all images below follows from the linear colourbars shown in Fig. 2.5. The colours are always scaled to the emission in the individual image, unless otherwise stated. We note that the quality of most images shown below is strongly enhanced when viewed on screen. The emission from above mentioned models will be viewed at six evenly spaced inclination angles between zero degrees (face-on) and ninety degrees (edge-on). The field of view consists of 500 pixels per dimension. The modelled disks have a radius of 500 AU, which encompasses the whole field of view. The spectral resolution is $0.5\ \mathrm{km\,s^{-1}}$.

We have opted to omit the scales in all figures because due to the nature of the geometrical set-up, these systems are arbitrarily scalable in size and in absolute emission strength. Any absolute evaluation of correspondent angular or length scales is entirely model-dependent, and therefore meaningless. All results are continuum subtracted.

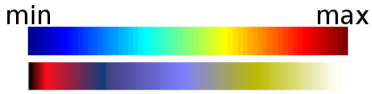

Figure 2.5: The top linear colourmap is used in all images of PVDs below. The bottom linear colourmap is used in all images of channel maps. Both colourmaps represent the strength of the pixel intensities in the image. The colours are always scaled to the emission in the individual image, unless otherwise stated.

We begin with an in depth discussion of the emission features of the channel maps and the position-velocity diagrams of the flared Keplerian disk (Sect. 2.4.1). Subsequently, in Sect. 2.4.2, we focus on the effect of the different velocity fields, and compare them with the results from Sect. 2.4.1. In Sect. 2.4.3, we discuss how density substructure affects the emission patterns. We finish with a description of the bipolar outflow and its influence on the global emission features when combined with a flared disk (Sect. 2.4.4).

2.4.1 The Keplerian disk

Looking through the channel maps

The most straightforward way to investigate three-dimensional emission data is by looking at the channel maps, i.e. images of the Doppler-shifted emission at different velocities (The channel maps of all calculated models are presented in Appendix A). If the data is of high quality and of high enough spatial and spectral resolution, an exploratory investigation of the channel maps should reveal all the data has to offer.

In order to illustrate this we discuss the properties of the channel maps of the Keplerian disk, seen under an inclination angle of $i = 54°$ (shown in Fig. 2.6). We choose this particular inclination because one is most likely to observe objects with cylindrical symmetry under such or comparable inclination angles. Additionally, the main properties of the emission features are very similar for all other inclination angles which do not approach $i = 0°$ or $i = 90°$. The emission generated by the center of the EDE is found to be maximally Doppler-shifted, because it contains the highest speeds in the differentially rotating EDE. The right side of the EDE contains blue-shifted

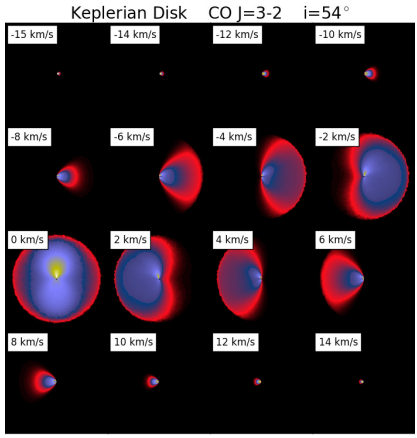

Figure 2.6: Example of a matrix of channel maps of the Keplerian flared EDE model, seen under an inclination angle of $i = 54°$. Appendix A contains an overview of the channel maps of all calculated models.

emission, and the left side red shifted emission, allowing for a direct deduction of the direction of rotation. As velocities approach the central velocity, the emission zone increases. This is due to the geometry of the EDE which, being flared, contains the material with lower projected velocities (along the line of sight) in a bigger volume. Around zero velocity a small asymmetry is seen in the intensities along the vertical offset axis. This is due to the geometrical implications of penetrating any inclined EDE with parallels to the line of sight. These parallels will probe different density regions for identical, but opposite, vertical offsets. The fact that the highest emission has a positive vertical offset indicates that this is the side of the EDE closest to the observer. The inclination orientation can thus be deduced from this difference in emission.

The Keplerian disk in the PVDs

When the data is noisy and/or when the embedded morphology is perturbed by local dynamics, position-velocity (PV) diagrams may be a better suited tool to analyse the three-dimensional data. Fig. 2.7 shows the PVDs of the Keplerian EDE model as a function of inclination. Seen face-on ($i = 0°$), the EDE produces a narrow vertical emission band around the central velocity. This is due to the velocity field of the EDE. Being Keplerian, this means that there is no component of the velocity along the line of sight. The width of the signal is exclusively a manifestation of the turbulent velocity component of the velocity field. Because the face-on EDE model is perfectly

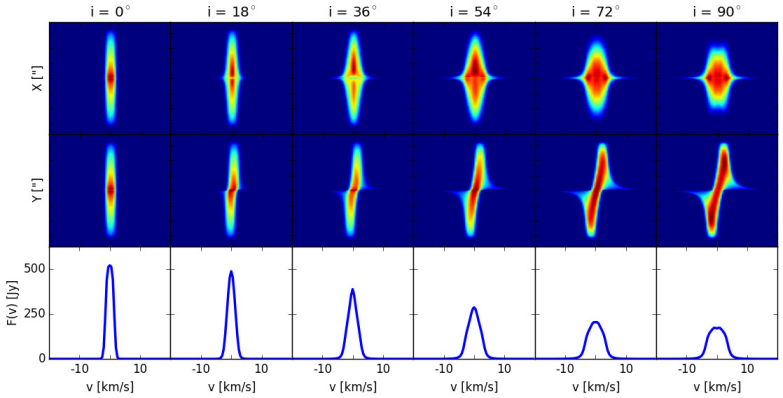

Figure 2.7: Dependence on inclination of the PVDs (*top two rows*) and the spectral lines (*bottom row*) of the Keplerian EDE model.

symmetrical, both PVDs are identical. As the inclination increases towards an edge-on vantage point, the behaviour of the two PVDs diverges. The EDE emission in PV1 broadens, and its vertical size diminishes substantially. This can be explained by the elliptical aspect of a tilted EDE, projected on a plane perpendicular to the line of sight. If the object is not observed edge-on or face-on, the inclination direction can be deduced from the difference in emission between the positive and the negative offset side in PV1. The side with the higher emission is probing denser and hotter regions, meaning that this is the side which is oriented towards the observer. The inclination dependence of PV2 is different. The EDE contribution does not contract vertically, but slowly shifts in velocity space. The emission with positive offset shifts towards the red, while the emission with negative offset shifts to the blue. This shift originates in the rotation direction of the inclined EDE. Additionally, some EDE emission around zero offset gets stretched throughout the entire velocity space. This is created by the material with a very high tangential velocity, which resides very close to the center of the EDE.

Fig. 2.7 also displays the spectral lines corresponding to each inclination angle. These show a very narrow and bright peak around zero velocity for the face-on EDE. As the inclination increases, the strength of the line decreases, while its width gradually increases. The spectral lines provide very limited information on the specific geometric details of the observed object. This conclusion repeats itself throughout this chapter.

2.4.2 Effect of the velocity field on the emission

In this section we will quantify the effect of modifying the global nature of the velocity field on the molecular emission patterns, addressing the cases of the radial field, the super-Keplerian field, the sub-Keplerian field and the rigid rotator. For the sake of simplicity, we use the same geometrical setup of the simple flared disk for each case. The effect of the different velocity fields on the emission redistribution is extremely pronounced. In fact, we confine the discussion only to the PVDs because they enable us to deduce all the information contained in the channel maps (which can be found in Appendix A).

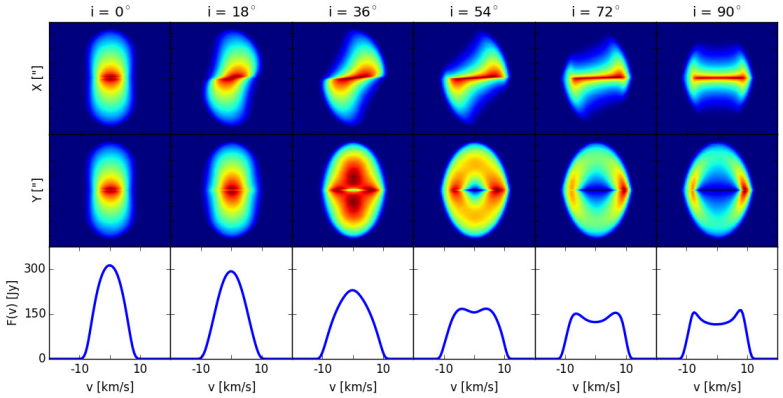

Figure 2.8: Dependence on inclination of the PVDs (*top two rows*) and the spectral lines (*bottom row*) of the EDE model with a constant radial velocity.

Radial EDE velocity

We have simulated an expanding EDE, of which the PVDs and spectral lines are shown in Fig. 2.8. Here, the expansion velocity of the EDE is 10 $\mathrm{km\,s^{-1}}$. The overall morphology of the PVDs is very different from the Keplerian EDE. Seen face-on, the PVDs show a much broader central feature, which arises from the fact that the EDE emission region now contains a greater range of projected velocities along the line of sight. With increasing inclination PV1 shows a transition of the top half of the emission towards the red-shifted side, and the bottom side of the emission towards the blue-shifted side. This shift is caused by the orientation of the tilted EDE. Additionally, the emission is compressed vertically. Like for the Keplerian EDE, this is because the projected height of the cylindrical EDE diminishes as its orientation approaches a more edge-on position. Finally, in the edge-on view, the EDE appears as a strong and narrow

emission feature centered around zero offset, extending over the whole of velocity space. In PV2 the emission rapidly stretches out towards terminal velocity, with an eye-shaped opening appearing in its center. This eye-shaped feature increases in size, whilst the highest emission zones migrate to the highest velocity regions. The resulting edge-on emission morphology in PV2 becomes progressively ring-like. This ring-like pattern is caused by a combination of the flaring of the EDE and the line-forming region, which both have the tendency to enhance the emission in specific regions of the EDE. Regarding the spectral lines, when viewed face-on, this expanding EDE generates a parabolic spectral feature, with a width which remains slightly more narrow than the 10 $\mathrm{km\,s^{-1}}$ input expansion velocity. This feature flattens and broadens with increasing inclination angle turning increasingly double-peaked.

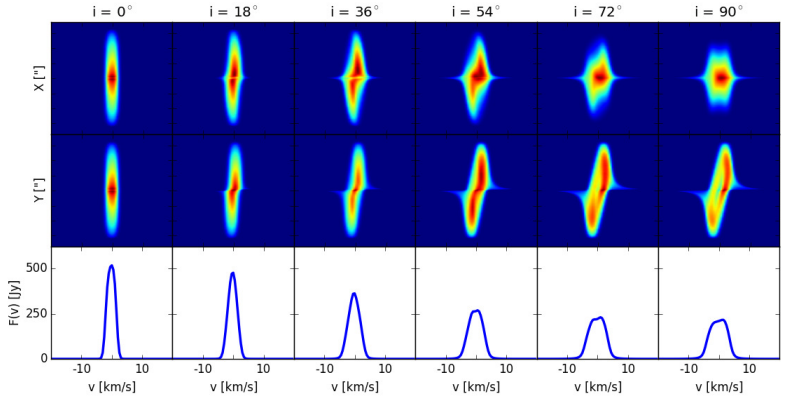

Figure 2.9: Dependence on inclination of the PVDs (*top two rows*) and the spectral lines (*bottom row*) of the super-Keplerian EDE model.

Super-Keplerian rotation

The morphology of the molecular emission for the super-Keplerian EDE (Fig. 2.9) is similar to the emission signatures of the Keplerian disk. This is not surprising, because our velocity field is dominated by the differentially rotating component. However, the effect of the weaker radial component does not go unnoticed in the PVDs. The behaviour of PV1 as a function of inclination is comparable to the EDE with the Keplerian velocity field. However, due to the weaker velocity components of the radial field, the emission is slightly redistributed. The emission with a positive offset is moved into the red-shifted side of the diagram, and vice versa. The general morphology of PV2 is also similar to the morphology of PV2 in Fig. 2.7. In fact, because the emission redistribution in PV2 in Fig. 2.8 only becomes very characteristic for high

inclination angles, the PV2 in Fig. 2.9 is indistinguishable from the PV2 in Fig. 2.7 for low inclination angles. The highest inclination angles clearly show some 'internal substructure', with a central decreased emission, which is not present in the Keplerian PVDs. Due to the relatively low magnitude of the radial velocity component, the small amount of high-velocity emission, generated by the most inner regions of the EDE, where the Keplerian field dominates, is unchanged. The spectral lines are comparable to the spectral lines of the EDE with a Keplerian velocity field. This is because the rotating velocity field dominates over the radial field throughout most of velocity space. In the regions in velocity space where the emission is strongest, both velocity components are of comparable magnitude, with a combined effect.

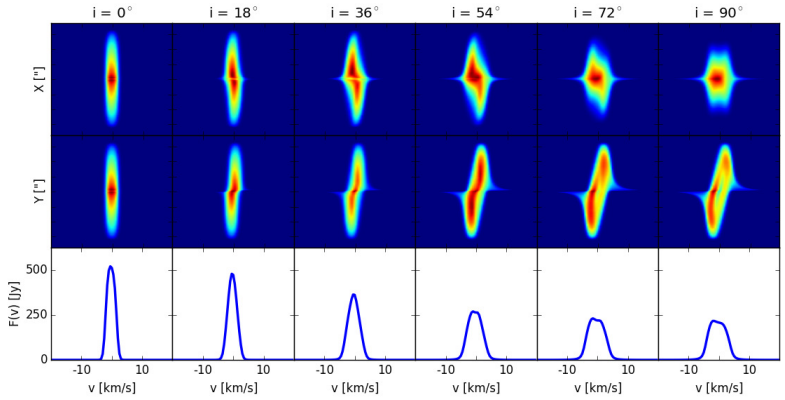

Figure 2.10: Dependence on inclination of the PVDs (*top two rows*) and the spectral lines (*bottom row*) of the sub-Keplerian EDE model.

Sub-Keplerian rotation

The emission signature of an accretion EDE is shown in Fig. 2.10. Comparing these emission signatures with the super-Keplerian case some strong similarities are immediately noticable. In fact, the PV2 diagrams are identical point-reflected versions of each-other, and for the PV1 the shape of the emission is mirrored around zero velocity. This is because the projected components of a global negative radial velocity component are, in essence, visually completely equivalent to the super-Keplerian case with an inverted rotation direction. Essentially, the blue-shifted emission of the super-Keplerian case is transformed to red-shifted emission here, and vice-versa, by the introduction of this negative radial velocity component. The effect on the line profiles is negligible compared to the lines in Fig. 2.9, for the same reasons as outlined for the super-Keplerian velocity field. This is to be expected, because the line profiles in the

super-Keplerian case are symmetrical, therefore any mirroring around zero velocity leaves them unchanged.

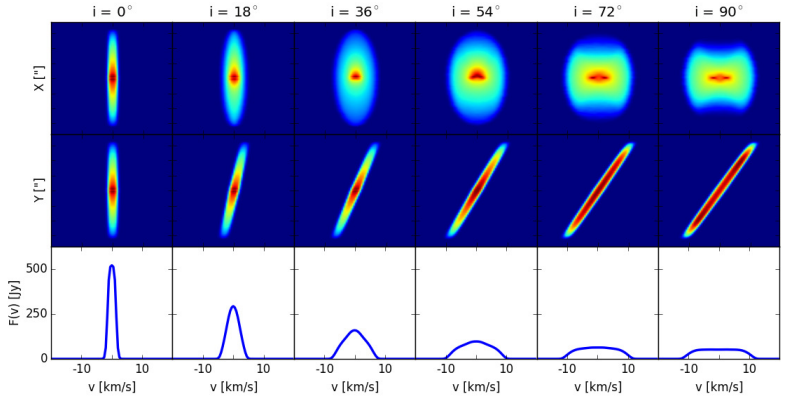

Figure 2.11: Dependence on inclination of the PVDs (*top two rows*) and the spectral lines (*bottom row*) of the rigidly rotating EDE model.

Rigid rotation

We present the spectral results of a rigidly rotating EDE, rotating with a constant angular velocity, and a tangential velocity of 10 $\mathrm{km\,s^{-1}}$ at the outer edge of the model in Fig. 2.11. Face-on the PVDs do not differ from the Keplerian EDE. In PV1, an increasing inclination angle broadens the strong emission feature of the EDE and compresses it vertically. Again, this is a direct consequence of the flatter appearance of an inclined circular object projected onto a plane perpendicular to the line of sight. The effect of inclination on PV2 is strong, and results in an effective clockwise rotation of the narrow vertical emission feature (for the face-on EDE) to an equally narrow feature, rotated by a 45° angle when viewed edge-on. This is essentially caused by the fact that the velocity increase with radius exactly cancels out the projection effects. The projected velocities of the outer regions of the EDE are identical to the projected velocities of all the material along the same line of sight. The effect on the spectral lines is pronounced, compared to the models above. Face-on, the spectral line does not differ from the Keplerian disk. However, as the inclination angle increases, the peak strength becomes substantially smaller, the line broadens and flattens, until (when edge-on) it becomes an outspoken flat-topped profile.

2.4.3 Effect of EDE substructure

In this section, we investigate the influence of additional density substructure on the emission patterns. In order to put reasonable limits on the available parameter space, we confine the discussion to the Keplerian EDE. We investigate the effect of EDE warping, annular gaps and spiral-shaped instabilities in the EDE on the molecular emission patterns. We discuss the channel maps here, but (in order to avoid the repetition of figures) refer the reader to Appendix A, where all channel maps are shown. A strong general characteristic of the channel maps of all three cases is the strong domination of the Keplerian velocity field. This is recognised by the strong overall morphological similarities between the channel maps of the EDEs with substructure and the Keplerian EDE without any. We discuss the effect of the substructure on the channel maps and on the PVDs per individual case. However, we have found that the resulting signatures in the PVDs are minimal, and are simply non-existent in the spectral lines. This is mainly due to the fact that the spectral lines and the wide-slit PVDs reprocess the spatial axes, which leads to a concealment of the substructure due to intensity-averaging. Only if the data is of high enough quality will the substructure be immediately apparent from the channel maps.

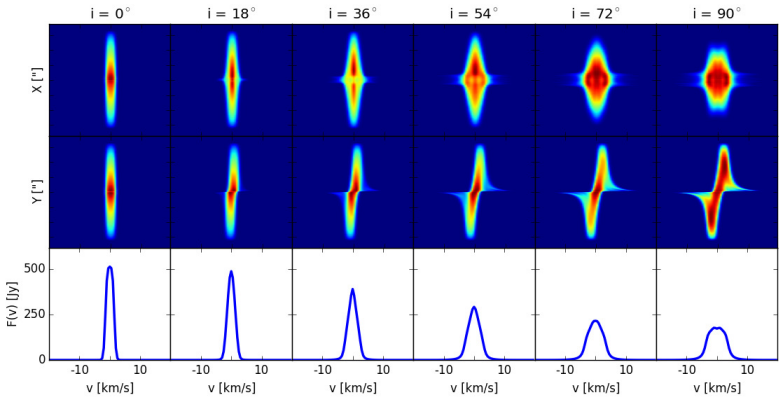

Figure 2.12: Dependence on inclination of the PVDs (*top two rows*) and the spectral lines (*bottom row*) of the Keplerian EDE model containing a warp.

Warped EDE

Introducing a warping of the EDE does not radically alter the appearance of the channel maps. Here, we discuss an EDE with L=3 undulations, and with an amplitude A of one eighth of its radius. We do not consider the L = 1 case because it is equivalent to a

regular disk whose normal on the equatorial plane is tilted with respect to the axis of totation. These objects are beyond the scope of this work. The lack of a clear warping signature in the channel maps (see Fig. A.3) seems at first sight surprising. But this result can be easily explained by a combination of projection effects. The projected velocity of the EDE along the line of sight completely masks the warping for objects with an uneven number of undulations, when their inclination deviates from a face-on view. This is because the peaks of the warping of the blue-shifted side of the EDE have the same projected velocity as the valleys of the red-shifted side of the EDE, and vice versa. The warped EDE thus appears as a thicker unwarped EDE in the 3D datacube. EDEs with a warp consisting of an even number of undulations may not suffer this fate. However, this is only the case when the equatorial orientation of the EDE is such that the blue-shifted valleys coincide perfectly with red-shifted valleys (and the same for the peaks). In this case the 3D data will exhibit a wave-like pattern in the EDE emission. It is, however, much more likely to observe a warped EDE with an even number of undulations under an equatorial orientation which does not perfectly coincide with this condition. In that case (and thus in most cases) warped EDEs are thus more likely to manifest as a broader and unwarped in the emission.

When constructing a wide-slit PVD all the emission at the chosen position-velocity coordinate is summed, and any previously present pattern is lost, as shown in Fig. 2.12. In both the evenly and unevenly warped EDE the resulting emission feature in the PVDs is thus wider than the feature expected from an unwarped EDE. This can clearly be seen by comparing (the not face-on) PV1 of the warped EDE with the equivalent PVD of the Keplerian disk model (Fig. 2.7). Some small features can be found to differ between this morphological model and the Keplerian EDE. However, these differences are so small we expect them to be undetectable in real data. Again, like for the other morphologies, the presence of warping is not noticable in the spatially unresolved case. We refer to the Keplerian disk (Fig. 2.7) for a discussion of the spectral lines.

EDE with an annular gap

In Fig. A.4 we exhibit the effect of introducing an annular gap into the Keplerian disk model on the velocity channel maps. The gap has a width of 15% of the EDE radius, and is located at a distance of 25% of the EDE radius from the center. The effect of the gap is predictable. The gap generates an annular zone void of emission, clearly visible in the channel maps of the $i = 0°$ case. Focusing on the $v = 0\,\mathrm{km\,s^{-1}}$ channel, we find that as the inclination increases, the projected gap size diminishes along the inclination axis, until the gap signal is completely hidden by the material which is located between the gap and the observer. However, the gap reappears at higher velocities (in this specific case around $v = \pm 6 - 8\,\mathrm{km\,s^{-1}}$) as it disappears at lower velocities. The emission gap is thus always present in the channel maps, and taking into account the inclination an estimation of its size can be readily performed.

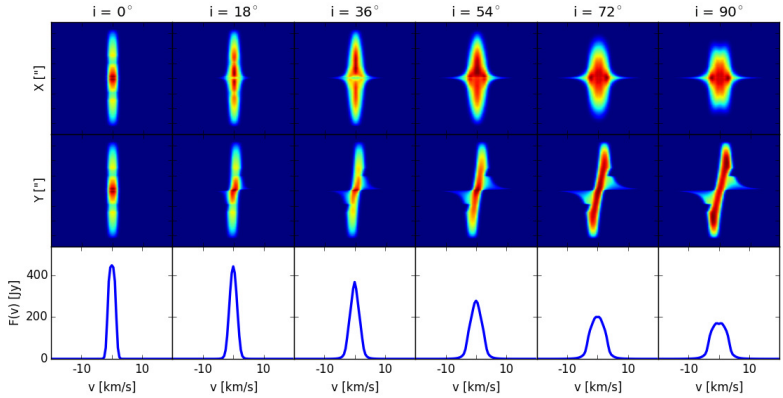

Figure 2.13: Dependence on inclination of the PVDs (*top two rows*) and the spectral lines (*bottom row*) of the Keplerian EDE model containing an annular gap.

The overall morphology of the PVDs is nearly unaltered by the introduction of a gap (Fig. 2.13). The PVDs of the face-on EDE nicely show a discontinuity in the emission at the offset at which the gap is located. As inclination increases, this discontinuity turns into a wedge of 'missing emission' in PV2. Higher inclination angles effectively erase any effect of the gap on the morphology of PV1. The annular gap has no noticable effect on the shape of the spectral lines. There is, however, a decrease in flux in the EDE contribution, as expected. If the probed rotational transition just so happens to be mainly produced in the region of the gap, this decrease may be substantial. However, such a spectral line would be morphologically indistinguishable from a gapless EDE, with an adapted mass.

EDE with spiral-shaped instabilities

Fig. A.5 shows the channel maps for the EDE with spiral-shaped density-enhancements, as a function of inclination. For low inclination angles the presence of the spiral is very clear. As inclination increases, the spiral in itself becomes less pronounced. In fact, for the highest inclination angles the spiral may very well be misintepreted as a series of narrow annular gaps. The only indication that it may be a logarithmic spiral is the rate at which the gaps appear as a function of offset. This conclusion propagates through to the PVDs.

In Fig. 2.14 the PVDs are shown. PV2 shows a sequence of enhanced emission zones for low inclination angles, which turn into wedge-like cuts on the outside of the EDE emission for higher inclinations. In fact, the observed effect of introducing

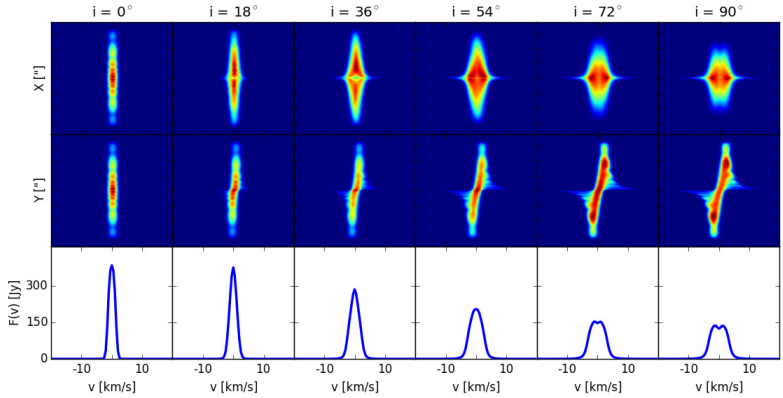

Figure 2.14: Dependence on inclination of the PVDs (*top two rows*) and the spectral lines (*bottom row*) of the Keplerian EDE model with added spiral-shaped instabilities.

spiral-shaped density enhancements to the EDE is indistiguishable from introducing annular gaps at different radii, for any inclination angle. However, in the case of a logarithmic spiral, it can be seen that the angular size of the enhanced emission (in the low-inclination PVDs) or of the wedges (for the higher-inclination PVDs) decreases towards zero offset. Additionally, the rate at which these features appear increases towards zero offset. This can either be interpreted as a sequence of annular gaps, which decrease in frequency but increase in size with radius, or as logarithmic spiral-instabilities. The latter thus indicates the likely presence of spiral shapes. The effects on the spectral lines of introducing logarithmic spiral-instabilities in the EDE are comparable to these of annular gap.

2.4.4 The emission of the bipolar outflow

The bipolar outflow (without EDE)

Fig. 2.15 shows the channel maps of the intrinsic emission of a bipolar outflow, observed under an inclination angle of $i = 54°$. The reasoning behind this specific choice of angle follows the same argumentation as in Sect. 2.3.1. At high velocities the emission is strong, but the emission area is minimal. Only material with exclusively positive or negative offset is visible. As velocities approach zero, the channel maps present the portion of the bipolar outflow which is oriented towards the observer. In this case it is the portion of the outflow with a positive vertical offset which contains the blue-shifted emission, and the portion with the negative vertical offset which contains

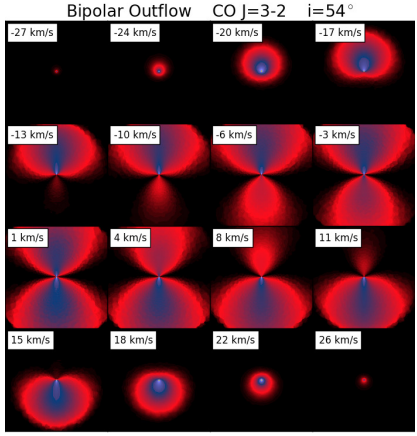

Figure 2.15: Example of a matrix of channel maps of the bipolar outflow model, seen under an inclination angle of $i = 54°$. Appendix A contains an overview of the channel maps of all calculated models.

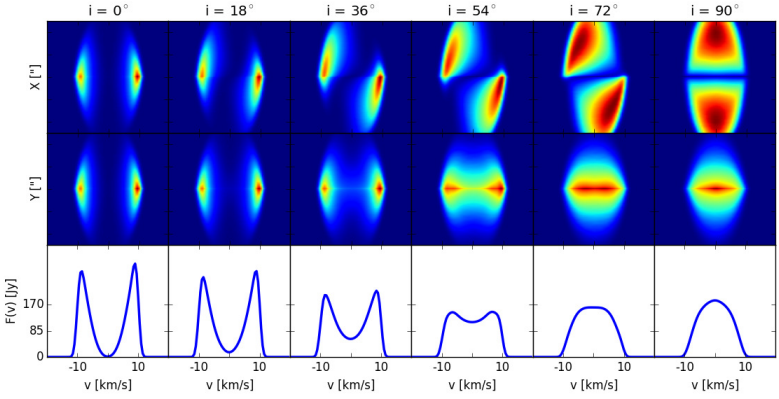

Figure 2.16: Dependence on inclination of the PVDs (*top two rows*) and the spectral lines (*bottom row*) of the bipolar outflow model.

the red-shifted emission, clearly showing the orientation of the inclined hourglass. Around central velocity the bipolar outflow is symmetrical.

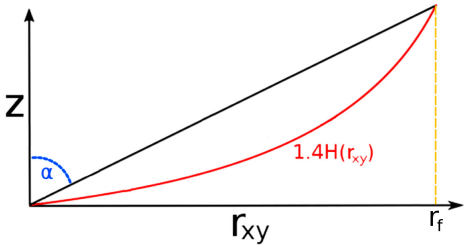

Figure 2.17: Visual representation of the boundary conditions.

Fig. 2.16 shows the PVDs of the bipolar outflow model as a function of inclination. Seen face-on ($i = 0°$), the bipolar outflow produces two emission features at high velocities. Along the velocity axis, a region void of emission resides between these two components, which is easily explained by the lack of material in the equatorial regions. Of course, because the face-on bipolar outflow is perfectly symmetrical, both PVDs are identical. As the inclination increases towards the $i = 90°$ vantage point, the behaviour of the two PVDs diverges. The emission in PV1 rotates around the center of the image, filling up the velocity-gap, and preserving point reflection symmetry. This is caused by the intrinsic correlation between Doppler-shift, and orientation of the hourglass-shape. The inclination dependence of PV2 is different. The emission of the bipolar outflow in PV2 gets stretched-out horizontally towards zero, producing a large feature with a strongly enhanced central bar at $i = 90°$. The spectral lines of the outflow start-off as a pronounced double-peaked profile at $i = 0°$, after which its peaks slowly diminish in strength. As one approaches the $i = 90°$ vantage point, the relative emission contribution of the central velocity regions augments until these regions dominate the spectral lines, ultimately forming a parabolic line profile which is slightly narrower than the $i = 0°$ profile. This decrease in line width is explained by the decreased maximum-projected-velocity-component for the fully inclined outflow.

Keplerian disk + bipolar ouflow

As mentioned previously, EDEs and bipolar outflows quite often go hand-in-hand in the evolved stars context. We therefore believe a discussion on their combined emission to be paramount for the completeness of this chapter. When combining both the EDE and the bipolar outflow in a single radiative transfer model, we require a condition by which we can numerically differentiate between these components. One straightforward criterion is by defining the boundary as the spatial coordinates where the density of the EDE and the density of the bipolar outflow are identical. However, this introduces numerical anomalies for certain contrasts between outflow mass and EDE mass. We have therefore opted to separate both components by a geometrical

criterion. We place the boundary at an angle

$$\alpha = \arctan\left(\frac{\mathrm{r_f}}{1.4\mathrm{H}(\mathrm{r_f})}\right), \tag{2.17}$$

with r_f the edge of the considered numerical domain, and where H is given by Eq. 10. Cutting off the EDE by confining it within this wedge does not strongly affect its flaring because the higher density flare curve systematically lies below this line. This can be visualised in Fig. 2.17. It does, however, discard the lowest density outer regions of the EDE, accounting for 5.7% of the total EDE mass for the chosen 1.4 prefactor of the denominator. This value has been empirically determined to best resemble the density criterion for the cases where no complications arise. We believe this not to be an issue because, for EDE's with a bipolar outflow, one may expect the outer layers of the rotating EDE to strongly interact with the radial outflow (generating thermodynamical instabilities at the boundary zone), and possibly even the outflow to blow away the outer low-density regions of the EDE. However, due to the complexities associated with defining and modelling such detail, we have opted not to include them.

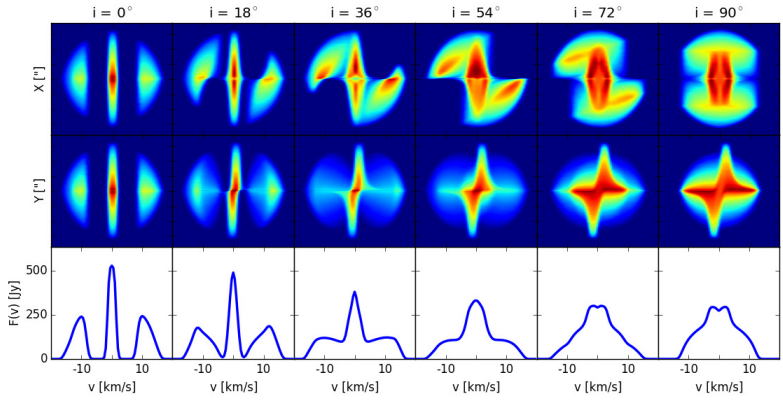

Figure 2.18: Dependence on inclination of the PVDs (*top two rows*) and the spectral lines (*bottom row*) of the bipolar outflow model.

Fig. 2.18 shows the PVDs of the combined Keplerian disk + bipolar outflow model. Around $i = 0°$ the emission signature of the disk is clearly recognisable. This is because it is well separated (in velocity space) from the bipolar outflow emission features. This gap is caused by the previously described boundary condition criterion, which does not ensure continuity in velocity space. At the interface between the outflow and the disk, the velocity field abruptly transitions from radial to tangential. In reality we may expect this boundary to harbour some (thermo)dynamical instabilities, like turbulent Kelvin-Helmholtz mixing zones at the shearing interface between the disk and the

outflow. Due to the separate behaviour of both the disk and the outflow the combined PVDs evolve in a very predictable way. However, as one approaches $i = 90°$, the signatures begin to overlap, creating emission patterns which may not be so easily disentangled. In PV2 the Keplerian disk signature is still recognisable, but now the addition of the bipolar outflow strongly enhances the regions around zero offset. This generates a much more horizontally elongated emission pattern. In PV1 the vertical size of the disk feature can hardly be recognised to diminish in size. In addition, the two emission features of the bipolar outflow now melt together with the central disk feature, forming a resultant emission distribution that may not be easily recognised as a direct combination of the disk and outflow features. The evolution of the spectral lines is generally more predictable. The lines can simply be recognised as a direct morphological combination of both the disk and the bipolar outflow lines. The dual nature of the combined object can be clearly recognised in all the lines.

General findings on the combining of geometrically separate emission

Because we assume the bipolar outflow and any EDE to be geometrically separate, it is very easy to simulate their combined emission patterns to a good first order approximation (for any of the above mentioned models). If both the EDE and the bipolar wind are optically thin, then the resulting intensity pattern is simply the sum of both individual components. If the EDE is optically thick, and the wind is not, then the emission of the wind originating behind the EDE (along the line of sight) will be obscured, and therefore only the EDE emission should be considered in the overlap regions. Conversely, when the EDE is optically thin, and the outflow optically thick, the emission originating in the portions of the EDE oriented towards the observer can simply be added on top of the emission of the outflow. The emission from the portions of the EDE obscured by the outflow can simply be discarded. The only areas where some non-trivial optical depth effects may take place is right at the edges between the EDE emission and the outflow emission. However, these regions are very small compared to the global intensity map, and thus only minimally impact the global shapes present in the PVDs. We thus argue that non-trivial optical depth effects (in PVDs) are only of marginal importance when interpreting emission of combined EDE and bipolar outflow objects.

2.5 Discussion

2.5.1 Model sensitivity to input parameters and distributions

Because we wish to limit this study to a qualitative investigation of the overall morphological emission trends we have not researched the impact of each parameter on the emission. Nevertheless, we reserve this section for a short discussion on the impact of the model parameters.

The models are most sensitive to the parameters which directly impact the distribution of emission throughout the three dimensions (velocity, X and Y) which make up the datacube. This translates concretely to the global velocity field, and to the overall geometry of the morphology. Assuming a fixed velocity field and geometrical set-up, the general shape of the emission edges (as a function of velocity) will always remain unchanged, both in the channel maps and in the PVDs. This means that changes to the internal properties of the system only manifest as a redistribution of the internal (confined by the edges) emission of the data. The most important of these internal properties are the density distribution, the temperature field and/or the molecular abundance (henceforth referred to as DTA). A very important point to address here is that DTA are fully degenerate when modelling CO emission. This is because the molecule has an extremely low electric dipole moment, causing the excitation of the CO energy levels to be primarily stimulated by collisions. Hence, its energy level populations are fully thermalised, with the temperature of the gas determining the energy level populations. Increases in both density and abundance increase the total mass of the emitting molecule, and hence the total emission. Their effect on the resulting emission can thus impossibly be disentangled, or discussed separately. An in depth investigation of the available parameter space would therefore result in a virtually infinite discussion. The low electric dipole of the CO molecule also implies that the level populations are insensitive to the radiation field of the central star and/or of the dust, and to the relative abundance and composition of the circumstellar dust.

We can, however, briefly describe the ‘predictable’ qualitative effect of modifying the rate with which any of the simplified radial power-laws describing any of the DTA fields changes the PV emission, by means of two examples. (1) An increased radial decay rate of one of the DTA distributions (whilst leaving the others unchanged) will result in an increased emission contrast between the material at zero offset compared to the material at greater offsets. This increased contrast can be undone by decreasing the rate at which any one of the other DTA distributions decreases radially, due to the above mentioned degeneracy issue. (2) More substantial morphological emission differences may arise when the DTA distributions are organised such that cool and dense material makes up the outer regions of the EDE. Such a scenario will cause absorption of the emission originating from hotter gas located further along the line-of-sight, which may

result in concealed (or missing) portions of the expected intrinsic emission distribution at certain velocities.

Regarding the velocity parameters; M_*, v_{rad} and v_{tan} will simply stretch the PV signature throughout velocity-space. The effect of $v_{\rm in}$ and $v_{\rm out}$ is less trivial. Increasing their absolute value will open-up a bigger portion of the velocity-space to be influenced by the radial-velocity emission redistribution. As the values increase, the PV signatures will resemble the exclusively radial field more closely. However, the underlying Keplerian field will maintain its influence in the relevant portion of velocity-space, most strongly manifested as a tilt of the 'radial signature'.

2.5.2 Considering extra transitions of CO

In addition to the J=3−2 rotational transition in the lowest vibrational energy level of CO, we have considered the 4 subsequent rotational transitions for the Keplerian model, all the way up to the highest transition that can be observed with *ALMA* (J=7−6). We have not modelled the two lowest rotational transitions to avoid having to make assumptions on the onset of photodissociation far from the central source. The results are shown in Fig. 2.19. Higher J transitions are formed in hotter regions, and thus probe the denser inner regions of the model. In this particular case the chosen temperature profile and EDE size are such that the higher energy levels of CO are more effectively populated. We therefore measure an increased emission for these higher J transitions. When viewed face-on, the projected velocities all tend toward zero, leaving the turbulent velocity as the only broadening mechanism. This explains why the velocity range within which the lines of the face-on EDE are formed is unaffected.

The formation of the double peak can be attributed to optical depth effects. For a Keplerian disk seen face-on there are no systematic velocities in the line of sight, leaving only the turbulent velocity as broadening mechanism. At line center, where the extinction is maximal, one reaches optical depth unity high up in the disk surface where for a given line-of-sight the temperature is lower than it is at the point where the beam crosses the mid-plane (see Eq. 11, which is a function of r_{xyz} and not r_{xy}). In the line wings (which probe the wings of the Gaussian turbulent velocity distribution) the depth of the $\tau \sim 1$ layer is deeper in the disk, effectively increasing the volume of the emission zone. In addition, the increased optical depth probes higher temperatures (and thus an increased source function). These effects combined result in a slightly increased emission in the line wings, causing the double-peaked line shape. This double peak is not visible for the lower J transitions because the main line-forming region is beyond the radial distance probed in these models. Hence optical depth differences between the line core and wings are not as pronounced as for the higher J lines, consequently the difference between the source functions is much smaller, suppressing the double-peaked shape.

At high inclinations the higher transitions show a sharp peak around zero velocity. This peak is caused by the substantially larger volume of optically thinner emitting material around zero velocity, compared to the optically thick dense regions at high velocities. Also, compared to the lower transitions, this peak is more pronounced. This is due to the low excitation of the population of the lower levels, resulting in emission which is generally optically thin (throughout the whole of velocity space), leading to a more even emission profile.

The ratios between the integrated flux of each line compared to the integrated flux of the J=3−2 transition is independent of inclination, as shown in Table 2.4. This indicates that (at least for the rotational transitions of CO where *ALMA* is sensitive, and if the temperature profile is known) the density profile can be properly probed, independent of its orientation with respect to the observer.

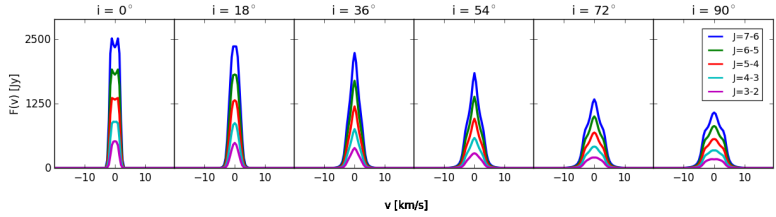

Figure 2.19: CO transition lines of the Keplerian EDE model, as a function of inclination.

As expected because of simple scaling arguments, no significant morphological effects are seen in the channel maps and PVDs of the higher J transitions of CO. Therefore we refrain from showing them in this work.

	i=0°	i=18°	i=36°	i=54°	i=72°	i=90°
J=3−2	1.00	1.00	1.00	1.00	1.00	1.00
J=4−3	2.61	2.61	2.62	2.62	2.62	2.60
J=5−4	5.27	5.27	5.29	5.30	5.30	5.26
J=6−5	9.16	9.15	9.19	9.20	9.19	9.09
J=7−6	14.36	14.33	14.38	14.37	14.30	14.10

Table 2.4: Ratios of the integrated flux of the higher rotational transitions of CO compared to the J=3−2 transition, per inclination angle.

2.5.3 Constraining the geometry

Approximating an EDE by a cylinder of diameter $\sqrt{x^2 + y^2} = d$ and height $z = h$, it is trivial to calculate its projected dimensions as a function of inclination angle i. Obviously, the projected width d' does not change, which is why the maximum offset of the EDE emission in PV2 does not change with inclination angle. Thus $d' = d$. The projected height h' of the emission zone of the chosen spectral line changes with inclination angle as follows

$$h' = \frac{h \tan i + d}{\sqrt{\tan^2 i + 1}}. \tag{2.18}$$

Having knowledge of either h or i can thus provide insight into the value of the other. Estimating a value for i, by comparison with the emission models above or with the channel maps shown in Appendix A, will permit the calculation of an estimated value for h.

2.5.4 Constraining the velocity field

Consider the following PVDs:

- Fig. 2.7, PV2 at i=54°-90°.
- Fig. 2.8, PV1 at i=36°-54°.
- Fig. 2.9, all diagrams except i=0° and PV1 at i=90°.
- Fig. 2.10, all diagrams except i=0° and PV1 at i=90°.

Clearly, there is possible ambiguity when comparing the above mentioned PVDs, as they all have a very similar morphology. The importance of constructing orthogonal wide-slit PVDs is yet again emphasised at this point. The morphology of the orthogonal PVD looks very different in the four cases, which would make it a vital diagnostic in determining the overall type of velocity field. As PVDs are becoming a very important method of analysing and evaluating the observed morphology [70, 31], the orthogonal PVD method can be used as an additional technique to acquire more constraints on the properties of the system.

2.5.5 The use of stereograms as tool to identify substructure

Next to wide-slit PVDs, it is in some cases also useful to plot integrated emission for a specific user-chosen velocity range. This means dividing the 3D datacube into

portions along the velocity axis, and summing up the intensities with identical spatial coordinates for each portion. Essentially, it is simply a channel map with a wide velocity width. We refer to such diagrams as stereograms. They are especially useful to investigate relative velocities between emission zones.

We proceed with the stereograms shown in Fig. 2.20, where we have collapsed the exclusively red-shifted, blue-shifted, and central velocities of the 3D datacube of the edge-on Keplerian disk model with a bipolar outflow. It can immediately be seen that the bipolar outflow contains both approaching and receding emission. Also, the EDE can be recognised. The approaching and receding sides are mirrored, as expected from a rotating object. The central velocities, shown as the black contours, show the maximal height of the EDE.

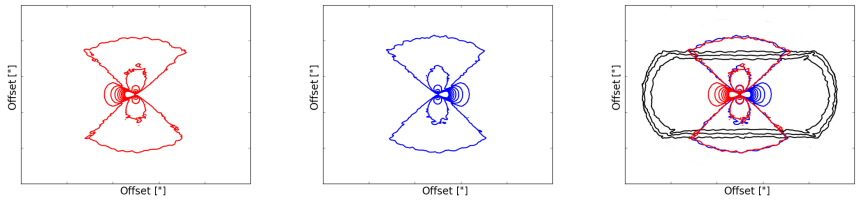

Figure 2.20: Stereograms of the Keplerian disk model with a bipolar outflow. The receding (red contours) and approaching (blue contours) sides have been constructed with the outermost 49% of the velocity channels. The remaining two percent, the material with hardly any projected velocity along the line of sight, corresponds to the black contours.

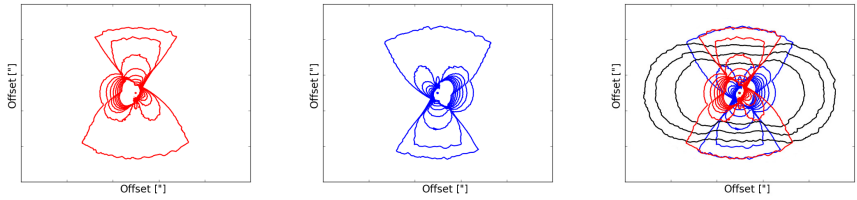

Figure 2.21: Stereograms of the warped EDE + bipolar outflow model. The receding (red contours) and approaching (blue contours) sides have been constructed with the outermost 49% of the velocity channels. The remaining two percent, the material with hardly any projected velocity along the line of sight, correspond to the black contours.

Because the stereogram does not reprocess the spatial axes of the datacube, it is a powerful tool to analyse emission from objects containing spatial asymmetries. For the considered models in this chapter, its use is best demonstrated by focusing on the

warped EDE, which was the only considered case where neither channel maps, PVDs nor spectral lines have proved able to detect any warping signatures. Fig. 2.21 shows the velocity-bias of the emission of the warped EDE + bipolar outflow model, and in comparison the stereogram of the EDE with no substructure (Fig. 2.20). Some clear differences can be seen. The most striking difference arises from the portions of the bipolar outflow which are unobstructed by the warped EDE, leading to the appearance of petals in the higher-density contours of the stereogram. In this particular case three petals appear both in the red and in the blue emission. The petals in the red emission consist of one petal facing up, and two facing down. The opposite is found for the blue emission. The petals are created by the undulations, i.e. how many times the bipolar outflow penetrates through the orbital plane of the EDE. Also visible is the EDE itself, manifested as an asymmetrical bulge around the central horizontal axis of the stereograms. The appearance in the red component is mirrored in the blue component. The asymmetry of the EDE feature originates in its combination with the contours of the bipolar wind petals.

2.6 Simulation of observations

2.6.1 Single-dish telescopes

Simulating single-dish observations of the gas emission of a rotating EDE can be done by applying a Gaussian mask of variable width over the intrinsic 3D data. However, due to the symmetry of the modelled system, and its invariance to scale, the centering of any Gaussian filter (with an angular diameter comparable to the size of the object) over the 3D data will yield nearly identical line shapes, containing less flux. Depending on the relative densities, one can expect the proportions of the emission contributions of both EDE and wind components to vary with the width of the Gaussian filter.
Low spectral resolution data may conceal the intrinsic shape of the lines. Determining line strengths may be the only viable option to retrieve information from the molecular emission.

It is important to be prudent when dealing with such data, as the potential for misinterpretation is significant. For instance, erroneously assuming a spherically symmetrical outflow for a source which is intrinsically EDE-like, or has both a radial outflow and an EDE-like component, may result in serious deviations on the estimations of the physical properties of the system. This has been shown by e.g. Homan et al. (2015) [72]. The authors outline and quantify the uncertainties related to a misinterpretation of embedded spiral shapes in stellar winds. Their conclusions on the uncertainties, related to falsely interpreting the emission from a narrow spiral (which is effectively a kind of equatorial density enhancement) as originating from a simple spherically outflowing stellar wind, are also applicable here.

2.6.2 *ALMA*

Using CASA we have simulated *ALMA* observations of the Keplerian disk model with a bipolar outflow. Since the considered radiative transfer model has no substructure, there is no reason to explore the effect of angular resolution. Its effect will only be of importance if the aim is to properly resolve the inner EDE, the edges of the EDE or the EDE-wind boundary. We have opted to show the effect of exceeding the chosen configuration's largest angular scale (LAS), determined by the shortest baseline of the interferometer, on the emission distribution in the PVDs of the Keplerian disk model with a bipolar outflow.

Simulation Parameters	
Pixel size of original data	0.015”
Field size of original data	7.5”
Peak flux	Taken from LIME output
Transition	CO 3-2 (345.76599 GHz)
Pointing	Single
Channel width	1.15MHz, centred on rest freq.
PWV	0.913 mm
Thermal noise	standard
Temperature	269 K
Integration time	10 min on-source

Table 2.5: The *ALMA* observation simulation specifications.

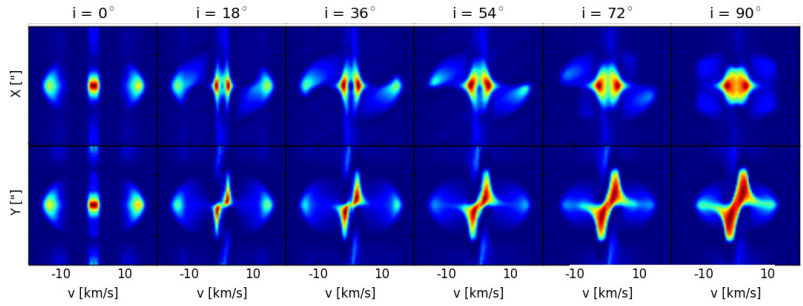

Figure 2.22: Synthetic *ALMA* observation simulation of the Keplerian disk model (with a bipolar outflow) with the C36-1 antenna configuration (res=1.5”, LAS=11”).

A synthetic observation is shown in Fig. 2.22, for which the main SIMOBSERVE parameters are presented in Table 6.1. To obtain the results in Fig. 2.22 we have simulated an observation with the most compact of the extended configurations, C36-1. This configuration has an angular resolution of 1.5” and a largest angular scale of 11”.

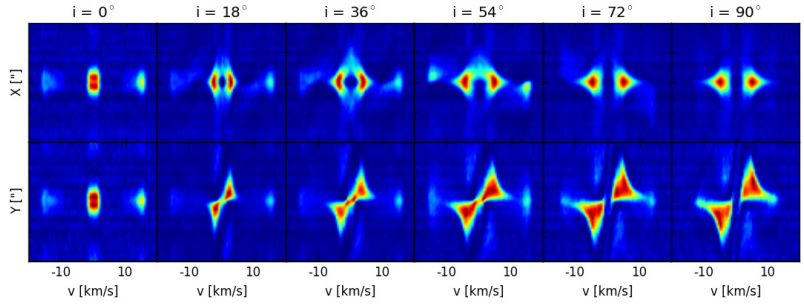

Figure 2.23: Synthetic *ALMA* observation simulation of the Keplerian disk model (with a bipolar outflow) with the C36-1 antenna configuration (res=1.5”, LAS=11”), for which the original model has been rescaled to a size 3.5 times greater than it was in Fig. 2.22. The effect of the largest angular scale being exceeded can be seen around zero velocity.

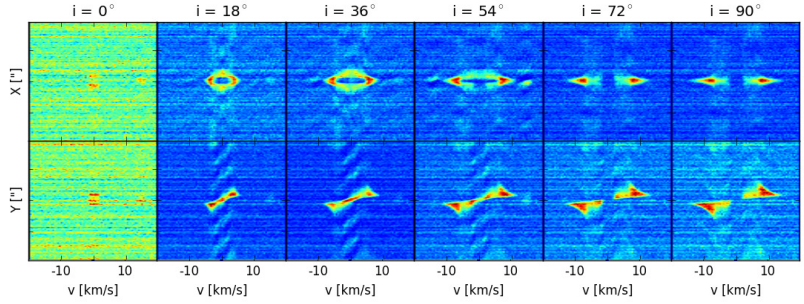

Figure 2.24: Synthetic *ALMA* observation simulation of the Keplerian disk model (with a bipolar outflow) with the C36-1 antenna configuration (res=1.5”, LAS=11”), for which the original model has been rescaled to a size 18 times greater than it was in Fig. 2.22. The effect of the largest angular scale being exceeded dominates the image. Most emission is resolved out.

To properly show the effect of a decent observation, we have rescaled the pixel size to artificially place the object at the minimal distance for no EDE flux to be lost. Morphologically, the intrinsic emission and the emission in Fig. 2.22 are very similar, as expected. The sheer number of antennae available for cycle 3 ensures even for modest integration times a decent filling of the UV-plane. The high inclination models show that even though the signature of the EDE is barely unaltered, the bipolar wind emission has exceeded the LAS of the antenna configuration around zero velocity. Some of the flux of the wind is thus lost. Because our models are confined to a numerical region, and bipolar outflows are not expected to exhibit such abrupt edges, this effect is expected to be more pronounced in real physical objects.

If the antenna configuration is chosen such that some EDE flux is lost, then this effect will target the features with the largest angular size first, which, in this case, is the emission around the rest frequency. In order to show this effect we have simulated two additional observations, shown in Fig. 2.23 and Fig. 2.24. Both figures show synthetic observations of the same model as Fig. 2.22, but with a rescaled pixel size to simulate the object being even closer to the observer. This has been done to ensure the emission around zero velocity exceeds the LAS of the configuration to different degrees. As seen in Fig. 2.23, some substantial differences with the intrinsic emission have arisen. The only remaining features of the bipolar wind are the high emission blobs at maximum velocity, which even disappear at high inclinations. The remaining wind emission is resolved out. The face-on model only shows the inner emission of the EDE, which remains under the LAS of the configuration. As inclination increases, the emission around the central velocity systematically exceeds the LAS, resulting in a characteristical emission deficit. In this case, however, the general morphology of the PVDs is not too strongly altered. The features in the PVDs can thus still be identified as being a rotating Keplerian EDE. Substantially reducing the LAS with respect to the pixel size augments this effect, to the point where most of the EDE emission is resolved out. Such a case can be seen in Fig. 2.24, where the object has been placed even closer. The bipolar wind is undetected, and the EDE emission is observed only at the highest tangential velocities. Also, due to the weak detection, the `CASA` CLEAN function seems to have difficulties reducing the synthetic data, resulting in a noisier datacube.

2.7 Summary

In this study we present 3D NLTE radiative transfer models of the rotational CO emission from 3D equatorial density enhancements (EDEs) with and without substructure and a variety of assumptions regarding the velocity fields in these EDEs. We have modelled five distinct velocity fields in the EDE: a Keplerian, a super-Keplerian, a sub-Keplerian EDE, a radially outflowing field, and rigid rotation. We have also modelled four distinct spatial morphologies: an axisymmetric flared EDE,

one with spiral-shaped instabilities, an axisymmetric one with an annular gap, and a warped structure. We have also discussed the emission properties of a bipolar outflow, as these phenomena are strongly connected to the presence of EDEs around evolved stars.

- For each model we have constructed channel maps, wide-slit position-velocity diagrams and spectral lines of the intrinsic emission. The velocity field has a strong effect on the PV morphology. PVDs enable us to constrain EDE height and inclination. Some degeneracy exists in the shapes of individual PVDs for different global velocity fields. Making use of the orthogonal PVDs may completely eliminate this ambiguity, and facilitates the identification of the nature of the global velocity field.

- Having introduced substructure (warps, spiral instabilities and annular gaps) into the models we found that the orthogonal wide-slit PVDs prove quasi-unable to recover and identify these peculiarities. Gaps and spirals are readily detected in the channel maps. The warped EDE is undetectable in either channel maps, PVDs or spectral lines, unless the warp consists of an even number of undulations and the EDE is oriented such that the height is constant along the line-of-sight. However, a substantial morphological difference is found between the stereogram of the simple EDE and the warped EDE, providing a method to identify warping.

- Generally, the spectral lines are unaffected by the introduction of density substructure in the EDE. When considering different velocity fields, we conclude that for most inclinations the EDEs produce spectral lines which are relatively broad, making it difficult to distinguish from a possible superposed bipolar outflow component. When the velocity fields contains a strong radial velocity component, these could even be misinterpreted as spherical outflows. Only when observed under low inclination angles can the EDE be distinguished from the bipolar outflow. In this case the dual nature of the observed object may be recognised in the spectral lines as a narrow central spike on top of the broader emission feature of the outflow.

- We found that the optically thick rotational transitions of the ground vibrational state of CO form J=3−2 up to J=7−6 have relative line strengths which are independent of inclination, resulting in a robust way of probing the radial density profile of the EDE.

- Simulations of synthetic ALMA observations show how the visual aspect of the emission signatures can change when the largest angular scale (imposed by the smallest baseline of the interferometer) is exceeded. For a rotating EDE the emission around zero velocity will be first to be discarded by the destructive interference.

Chapter 3

ALMA observations of the nearby AGB star L_2 Puppis: I. Mass of the central star and detection of a candidate planet

(2016A&A...596A..92K)

Pierre Kervella[1,2], Ward Homan[3], Anita M. S. Richards[4], Leen Decin[3], Iain McDonald[4], Miguel Montarges[5], and Keiichi Ohnaka[6]

[1] Unidad Mixta Internacional Franco-Chilena de Astronomía (CNRS UMI 3386), Departamento de Astronomía, Universidad de Chile, Camino El Observatorio 1515, Las Condes, Santiago, Chile
[2] LESIA (UMR 8109), Observatoire de Paris, PSL Research University, CNRS, UPMC, Univ. Paris-Diderot, 5 Place Jules Janssen, 92195 Meudon, France
[3] Institute of Astronomy, KU Leuven, Celestijnenlaan 200D B2401, 3001 Leuven, Belgium
[4] JBCA, Department Physics and Astronomy, University of Manchester, Manchester M13 9PL, United Kingdom

[5] Institut de Radioastronomie Millimétrique, 300 rue de la Piscine, 38406, Saint Martin d'Hères, France
[6] Universidad Católica del Norte, Instituto de Astronomía, Avenida Angamos 0610, Antofagasta, Chile

Abstract: *Six billion years from now, while evolving on the asymptotic giant branch (AGB), the Sun will metamorphose from a red giant into a beautiful planetary nebula. This spectacular evolution will impact the solar system planets, but observational confirmations of the predictions of evolution models are still elusive as no planet orbiting an AGB star has yet been discovered. The nearby AGB red giant L_2 Puppis ($d = 64\,pc$) is surrounded by an almost edge-on circumstellar dust disk. We report new observations with ALMA at very high angular resolution ($18 \times 15\,mas$) in band 7 ($\nu \approx 350\,GHz$) that allow us to resolve the velocity profile of the molecular disk. We establish that the gas velocity profile is Keplerian within the central cavity of the dust disk, allowing us to derive the mass of the central star L_2 Pup A, $m_A = 0.659 \pm 0.011 \pm 0.041\,M_\odot$ (±6.6%). From evolutionary models, we determine that L_2 Pup A had a near-solar main-sequence mass, and is therefore a close analog of the future Sun in 5 to 6 Gyr. The continuum map reveals a secondary source (B) at a radius of 2 AU contributing $f_B/f_A = 1.3 \pm 0.1\%$ of the flux of the AGB star. L_2 Pup B is also detected in CO emission lines at a radial velocity of $v_B = 12.2 \pm 1.0\,km\,s^{-1}$. The close coincidence of the center of rotation of the gaseous disk with the position of the continuum emission from the AGB star allows us to constrain the mass of the companion to $m_B = 12 \pm 16\,M_{\rm Jup}$. L_2 Pup B is most likely a planet or low-mass brown dwarf with an orbital period of about five years. Its continuum brightness and molecular emission suggest that it may be surrounded by an extended molecular atmosphere or an accretion disk. L_2 Pup therefore emerges as a promising vantage point on the distant future of our solar system.*

Contribution to the article: *The kinematical analysis of the rotation of the gas disk, as well as the fitting of the PVD curves.*

3.1 Introduction

Planets are ubiquitous at all stages of stellar evolution: from young stellar objects [34], main-sequence stars [124], red giants [63], up to white dwarfs and neutron stars [209]. The asymptotic giant branch (AGB) designates the brief phase of the evolution of low- and intermediate-mass stars during which they metamorphose from red giants into compact stellar remnants, experiencing intense mass loss and extreme changes in their brightness and temperature. This directly affects their planetary systems, in the most dramatic way since their formation. Their fate during the final stellar evolution stages has been the subject of several recent works [190, 174, 192, 166, 194, 189]. However, as AGB star planets are embedded in complex circumstellar envelopes and are vastly outshone by their parent star, the observation of this critical phase presents considerable and yet unsolved challenges. As a result, there currently exists only indirect evidence of planets orbiting AGB stars [203].

At a distance of 64 ± 4 pc ($\pi = 15.61 \pm 0.99$ mas, [184]) L_2 Puppis (HD 56096, HIP 34922, HR 2748, 2MASS J07133229-4438233) is the second nearest AGB star behind R Doradus ($\pi = 18.31 \pm 0.99$ mas), and it is $\approx 30\%$ closer than Mira. L_2 Pup is a semi-regular pulsating variable ($P \approx 140$ days, [89, 12]). An asymmetric resolved environment around L_2 Pup was first identified by Ireland et al. (2004) [77] using aperture masking in the optical and near-infrared. Kervella et al. (2014) [88] observed L_2 Pup in 2013 using the VLT/NACO adaptive optics (AO) between 1.0 and 4.0 μm, detecting an edge-on circumstellar dust disk. As the scattering of the stellar light by the dust is more efficient at shorter wavelengths, the central source appeared obscured by a dark band up to $\lambda \approx 1.2\,\mu$m (J band). At longer wavelengths, the scattering becomes less efficient and the transparent dust lets the thermal emission from the hot (≈ 1000 K) inner rim of the dust disk pass. In the L band ($\lambda = 4\,\mu$m), the thermal emission from a loop extending to ≈ 10 AU was also observed. From NACO aperture masking and long-baseline interferometry, Lykou et al. (2015) [113] and Ohnaka et al. (2015) [147] confirmed the overall geometry and extension of the disk. Kervella et al. (2015) [87] identified the polarimetric signature of the circumstellar disk and detected bipolar "hourglass" cones in L_2 Pup's envelope using the VLT/SPHERE AO imaging polarimeter. They also discovered streamers in the bipolar cones and two thin, tightly collimated plumes. These structures make L_2 Pup a promising candidate for hosting a low-mass companion, as circumstellar disks and bipolar cones are classically predicted by hydrodynamical models of binary objects [142]. Chen et al. (2016) [29] presented the results of a 3D hydrodynamical simulation of L_2 Pup as a binary object that reproduces the spectral energy distribution and morphology of the disk.

Knowing the mass of the central star in L_2 Pup is essential to constrain its age and evolutionary state. Indirect estimates vary considerably in the literature: from $0.5 \pm 0.2\,M_\odot$ by Ohnaka et al. (2014) [146], $0.7\,M_\odot$ by Lykou et al. (2015) [113], and $1.7\,M_\odot$ by Dumm et al. (1998) [52] to $2\,M_\odot$ by Kervella et al. (2014) [88]. With

the goal of precisely determining the mass of the AGB star, we obtained very high angular resolution observations in ALMA's band 7 (330 – 360 GHz), covering several molecular lines and the continuum (Sect. 3.2). The simultaneous high spatial and spectral resolution provided by ALMA allows us to map the kinematics of its molecular envelope and derive its mass (Sect. 3.3). We also detect a secondary source located at a projected separation of 2 AU from the primary. We discuss the evolutionary state of the AGB star and the nature of the companion source in Sect. 3.4.

3.2 Observations and data reduction

L_2 Pup was observed on 5 November 2015 at UT08:39:25 (epoch 2015.8448, MJD = 57331.361) by ALMA for project code 2015.1.00141.S. Forty-five antennae were present for most of the observations, providing baselines from 0.09 to 16 km and resulting in an angular resolution better than 15 mas. The coverage of the (u, v) plane inside 350 m is sparse, giving a maximum angular scale of about 200 mas for reliable imaging, which is a good match to the extension of the disk surrounding L_2 Pup. The total field of view to the half-power primary beam is approximately 15". The observations used spectral windows (spw) placed as described in Table 3.1. Two identical executions of the high-resolution band 7 science goal were performed in succession. The observing frequency of each spw, corrected for the Earth's motion with respect to the Local Standard of Rest (LSR) and the VLSR of L_2 Pup (33.0 km s^{-1}) was calculated for the start of each execution and then held fixed. The target was observed for a total of 84 min, alternating with the phase reference with a cadence of 90 s / 18 s; the total cycle time was 2-3 min allowing for system temperature and water vapor radiometry measurements and occasional scans on the check source. The precipitable water vapor was very low during observations, at 0.40 – 0.45 mm. Standard human-steered ALMA data reduction scripts were used [164]. The main stages are to apply the instrumental calibration, to flag edge channels and other bad data, and to use the astrophysical calibrators to derive the bandpass corrections, flux scale and time-dependent phase and amplitude corrections. These were applied to L_2 Pup and to the check source.

The compact QSOs J0538-4405, J0701-4634 and J0726-4728 were used to establish the flux scale and derive bandpass corrections as the phase reference source and as the check source, respectively. L_2 Pup and J0726-4728 have separations of 2.85° and 4.33° from the phase-reference J0701-4634. The flux density of J0538-4405 was taken as 1.04488 Jy at 338.994438 GHz, spectral index −0.596, based on fortnightly ALMA flux monitoring derived from planetary standards, with 5% accuracy at band 7 frequency. The derived flux densities of J0701-4634 and J0726-4728 were 0.396 ± 0.002 Jy and 0.145 ± 0.007 Jy. Assuming that the flux scale transfer to L_2 Pup is of similar accuracy to that of the check source, the overall flux scale accuracy is 7%.

Table 3.1: Selected ALMA spectral windows (spw). The sky frequencies assume a source radial velocity of $v = 33.0\,\mathrm{km\,s^{-1}}$.

Baseband	Objective	Rest ν (GHz)	Sky ν (GHz)	Number of channels	Channel width (MHz)	spw width (MHz)	Velocity res. ($\mathrm{km\,s^{-1}}$)
1	^{12}CO	345.79599	345.75793	3840	0.122073	469	0.106
2	^{29}SiO	342.98085	342.94309	960	0.488292	469	0.427
	HC^{15}N	344.20011	344.16222	480	0.488292	234	0.426
3	^{13}CO	330.58797	330.55158	1920	0.244146	469	0.222
4	Continuum	331.60000	331.56350	128	15.625350	2000	14.136

After applying the phase-reference and other calibrations to L_2 Pup, the corrected target data were split out and each spectral window adjusted to fixed velocity with respect to the LSR. Obvious spectral lines were identified in the visibility data, leaving 2.5 GHz of line-free continuum. A copy of the data with all channels averaged to the coarsest resolution was made to speed up continuum imaging. The continuum image (made with natural weighting) has a synthesized beam size 17.7×14.5 mas at position angle (PA) 73°.

The position of the continuum peak was located at α = 07:13:32.47687, δ = −44:38:17.8443 with an absolute position uncertainty of ±7 mas. The clean components of this image were used as a model for phase self-calibration, and iterative cycles of phase and amplitude self-calibration were performed. Multi-frequency synthesis was used with a linear position-dependent spectral index as a free parameter; although the spectral index is not reliable except for the brightest emission over the relatively narrow, unevenly sampled bandwidth, this improves the image fidelity. A 2.5 mas pixel size and a field of view of 2.56" were used for all images unless otherwise stated.

3.3 Analysis

3.3.1 Continuum emission

The ALMA continuum emission map at $\nu = 338 \pm 16$ GHz (Fig. 3.1, left panel) shows thermal emission from the AGB star and the dust disk at a resolution corresponding to 0.9 AU at L_2 Pup. The east-west elongation of the diffuse emission is consistent with the major axis of the dust disk observed by Kervella et al. (2014) [88], Lykou et al. (2015) [113], Ohnaka et al. (2015) [147] and Kervella et al. (2015) [87] at infrared and visible wavelengths. The visible image of L_2 Pup from Kervella et al. (2015) [87] is shown at the same scale as the ALMA maps for comparison.

Flux from L_2 Pup A

The total flux density at the location of the AGB star including the contribution from the dust thermal emission is: $f_A + f_{\rm dust} = 78.6 \pm 0.03$ mJy beam^{-1}. We estimate the dust emission at the location of the AGB star from the mean continuum flux measured in the disk plane away from the stellar emission peak, as was done by Kervella et al. (2014) [88] in the infrared. We obtain $f_{\rm dust} = 1.4$ mJy beam^{-1}, for which we adopt an arbitrary uncertainty of ±0.3 mJy beam^{-1} to account for possible variations in the local dust emission over the disk. The flux from the L_2 Pup A is then

$$f_A = 77.2 \pm 0.3 \text{ mJy beam}^{-1}. \tag{3.1}$$

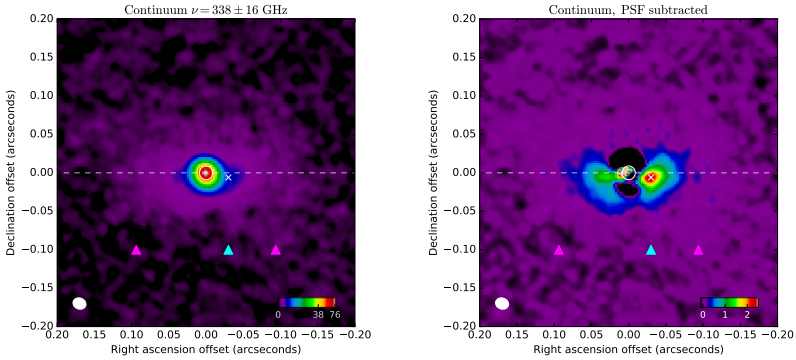

Figure 3.1: *Left panel:* Continuum emission from L_2 Pup at $\nu = 338 \pm 16$ GHz. *Right panel:* PSF-subtracted continuum emission map. The color scales are a function of the square root of the intensity in mJy beam^{-1} km s^{-1}. The white cross marks the position of the secondary source in the PSF-subtracted ALMA image. The triangular symbols are pointers to the inner rim of the dust disk (6 AU, magenta) and of the secondary source detected in the visible by Kervella et al. (2015) [87] (cyan), shifted by -0.1" in declination. The position of source B from ALMA is marked with a white cross, and the size of the photosphere of the star is shown as a white circle. The 17.7×14.5 mas beam is represented in the lower left corner of the images.

The angular diameter of the photosphere of L_2 Pup A has been measured by Kervella et al. (2014) [88] using near-infrared interferometry at $\theta_{\rm LD} = 17.9 \pm 1.6$ mas (see also [147]). The major axis of the central source in the ALMA continuum map is 20.8 mas at a position angle of 51° ($N = 0°$, $E = 90°$, and the minor axis 18.9 mas. These values are slightly higher than the ALMA beam size (17.7×14.5 mas at PA = 73°) and consistent with a partial resolution of the stellar photosphere.

As a consistency check, we verified that the measured flux from the central AGB star f_A is close to the emission of $f = 92$ mJy expected for a blackbody at $T_{\rm eff} = 3500$ K and with an angular diameter of $\theta = 18$ mas. The AAVSO light curve[1] of L_2 Pup at visible wavelengths presented in Fig. 3.3 shows that our ALMA observations were obtained approximately one month after the expected maximum light, during the decreasing flux phase of the cycle of L_2 Pup. During this phase, the star is cooler and fainter, which could explain part of the 20% flux deficit compared to the expected value. The photometric curve also shows that L_2 Pup went through a particularly long minimum around $m_V = 8.0$ during the second half of 2015, including during our ALMA observations. The deficit in flux could also be enhanced by this special minimum. The small amplitude peak flux shortly before the ALMA epoch could indicate that the

[1] `https://www.aavso.org`

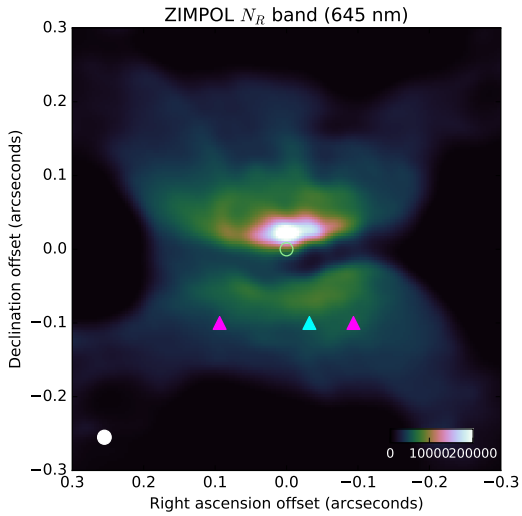

Figure 3.2: Visible image of L_2 Pup from Kervella et al. (2015) [87] for comparison with the ALMA maps, at the same scale. The beam size is represented by the ellipse in the lower left corner of the image. The radius of the inner rim (6 AU) and the radius of the companion of L_2 Pup are shown with magenta and cyan triangles, respectively.

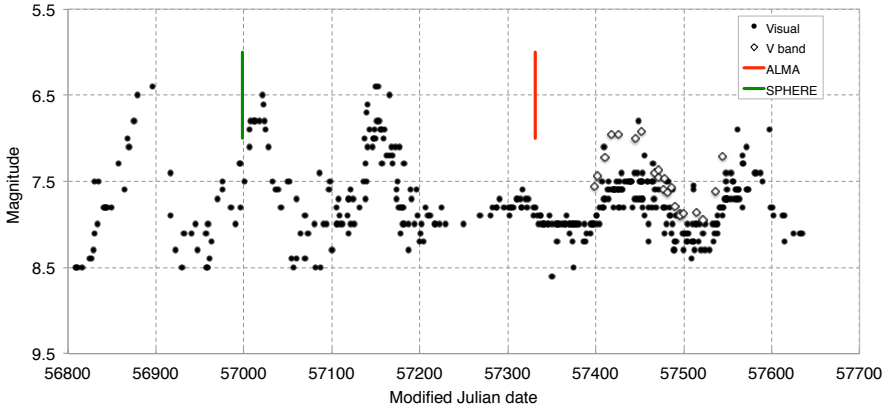

Figure 3.3: Photometric curve of L_2 Pup in the visible from the AAVSO database, from 23 May 2014 to 2 September 2016. The vertical color segments represent the epochs of the SPHERE observations (green) by Kervella et al. (2015) [87] and the present ALMA band 7 observation (red).

obscuration of the star by dust became particularly strong and compensated for the increase in flux of the AGB star. The regular pulsational variability resumed in early 2016, although with a smaller amplitude than in 2014.

Secondary source L_2 Pup B

As shown in Fig. 3.1 (left panel), the west wing (to the right of the image) of the disk emission appears brighter than the east side. To isolate this asymmetry, we estimated the contribution of the central star by fitting a two-dimensional elliptical Gaussian to the central source and we subtracted it from the continuum image. The result of the PSF subtraction is presented in the right panel of Fig. 3.1. The red wing of the disk (West) clearly generates significantly more flux than the blue wing. A secondary source (hereafter source B, or L_2 Pup B) is observed in the subtracted image at a relative position of $\Delta\alpha = -30.0 \pm 2.5$ mas and $\Delta\delta = -6.0 \pm 2.5$ mas with respect to the central object. Source B appears superimposed on the emission from the disk, and is unresolved angularly. The observed position corresponds to a projected separation of $\rho = 30.6 \pm 2.5$ mas, which is equivalent to a linear radius of $R_0 = 1.96 \pm 0.16$ AU. The relative position of source B with respect to A is closely coincident with that of the companion detected by Kervella et al. (2015) [87] at visible wavelengths.

The flux density at the location of source B is $f = 2.33 \pm 0.05\,\mathrm{mJy\,beam^{-1}}$. The uncertainty takes into account the standard deviation of the background noise of the reconstructed image and of the PSF subtraction. As for L_2 Pup A, the measured flux includes the emission from B plus the thermal emission of the surrounding dust. We estimate the dust contribution from a point in the disk located symmetrically to B with respect to the central star, where we find $f_{\mathrm{dust}} = 1.34 \pm 0.10\,\mathrm{mJy\,beam^{-1}}$. The error bar includes a provision for a possible variability in the local dust emission in the disk. The net flux from source B is then

$$f_B = 0.99 \pm 0.11\ \mathrm{mJy\,beam^{-1}}, \tag{3.2}$$

and the flux contrast between sources A and B at $\nu = 338\,\mathrm{GHz}$ ($\lambda = 887\,\mu\mathrm{m}$) is

$$f_B/f_A = 1.28 \pm 0.13\%. \tag{3.3}$$

This relative flux is considerable in absolute terms because of the very high brightness of the AGB star. At visible wavelengths, the contribution of B is even higher in relative terms, as Kervella et al. (2015) [87] found $f_B/f_A[V] = 24 \pm 10\%$ in the V band ($\lambda = 554\,\mathrm{nm}$) and $f_B/f_A[N_R] = 19 \pm 10\%$ in the N_R filter ($\lambda = 646\,\mathrm{nm}$). The flux at visible wavelengths is most likely dominated by scattered light above the disk plane, that biases the color toward the blue (where scattering is more efficient). Moreover, as a result of inhomogeneities in the dust disk, the flux of the central star and source B are potentially affected by differential absorption, which is particularly strong in the visible.

3.3.2 Molecular emission

We focus our analysis on the gas velocity field as derived from the ^{29}SiO($\Delta v = 0, J = 8 - 7$) molecular line. The molecular disk is centered on the star (which is visible in the continuum images presented in Fig. 3.1). The central dark 'hole' is due to line absorption by the molecular gas located in front of the star.We also present in Appendix B the images and position-velocity diagrams (hereafter PVDs, see Sect. 1.5.2 for more information) of the detected ^{12}CO, ^{13}CO, SO_2, SO and SiS lines that are also observed at high spectral resolution and high signal-to-noise ratio in the ALMA data. A summary of the detected lines is presented in Table 3.2.

Position velocity diagrams

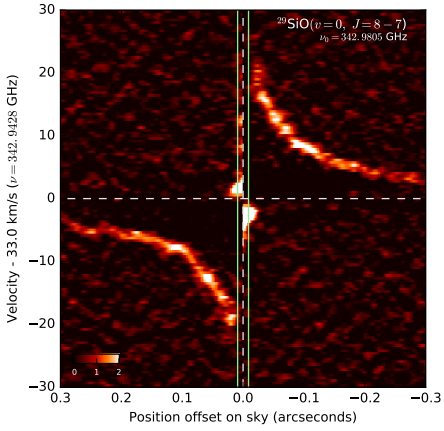

Figure 3.4: Derivative along position of the PVD of the ^{29}SiO($\Delta v = 0, J = 8 - 7$) line. The color scale in Jy arcsec^{-1}. The corresponding PVD is presented in Fig. 3.6.

We computed PVDs (see Sect. 1.5.2) for each emission line from the reconstructed ALMA image cubes using a virtual slit of 20 mas oriented in the east-west direction (position angle $PA = 90°$ with respect to north $= 0°$), that is, along the plane of the circumstellar disk. To constrain the value of the central mass from the orbital motion of the circumstellar gas, we estimated the maximum velocity as a function of the radius. Several techniques have been employed in the literature to derive masses from PVD velocities (e.g. [168, 138]). We adopted the innovative approach to compute the derivative of the PVD along the radial direction to determine the radius of maximum variation slope. Compared to the use of a fixed flux detection threshold, for instance, this technique has the advantage to be less sensitive to the angular resolution of the observation (as long as the disk itself remains resolved). An example of derivative of the PVD along the position axis is presented in Fig. 3.4 for the ^{29}SiO($\Delta v = 0, J = 8 - 7$) line (see also Fig. 3.6 for the corresponding PVD). The edge of the velocity profile is clearly defined and easily measurable.

Using this technique, the determination of the spatial position of the point of inflection of the PVD is largely insensitive to biases. Whether Keplerian or non-Keplerian, the

Table 3.2: Molecular emission lines detected in L_2 Puppis.

Molecule	Quantum numbers		Sky freq. ν (GHz)	Rest freq. ν_0 (GHz)	Upper-state energy (K)
	Vibrational	Rotational			
Unidentified			330.437	330.477	
^{13}CO	$\Delta v = 0$	$3 - 2$	330.552	330.588	31.732
H_2O	$\Delta v_2 = 2$	$3(2,1) - 4(1,4)$	331.08	331.12	
^{30}SiO ?	$\Delta v = 3$	$8 - 7$	331.93	331.97	
Unidentified			331.99	332.03	
SO_2	$\Delta v = 0$	$21(2,20) - 21(1,21)$	332.055	332.091	219.525
SO_2	$\Delta v = 0$	$34(3,31) - 34(2,32)$	342.724	342.762	581.919
^{29}SiO	$\Delta v = 0$	$8 - 7$	342.943	342.981	74.077
SiS	$\Delta v = 1$	$19 - 18$	343.063	343.101	1235.828
SO 3Σ	$\Delta v = 0$	$8(8) - 7(7)$	344.272	344.311	87.482
^{12}CO	$\Delta v = 0$	$3 - 2$	345.758	345.796	33.192

pure rotation profile of the gas itself is theoretically sharp (i.e. a Heaviside function). There may be an intrinsic dispersion of the velocity in the disk due to turbulence, for example. In this case, we would expect for the velocity profile to observe a convolution of the Heaviside function by a Gaussian-like function, and a broadening of the profile extension in radius for a given velocity. But this operation would not change the position of the point of inflection, as the convolution of the Heaviside function already smoothed by a Gaussian by a second Gaussian (the angular resolution of the array) would not shift the point of inflection. It would only reduce the maximum slope, hence the accuracy of the determination of its position. This measurement technique is valid when the instrumental beam is smaller than the true width of the profile itself in a given spectral channel. As a consequence, it does not work properly for the highest velocities, which exhibit a point-like flux distribution on the images and are located very close to the star. The inner cavity (within 6 AU from the star), however, is approximately 0.1" in radius, and therefore very well resolved by ALMA.

Mass of the central object

The first moment of the ^{29}SiO($\Delta v = 0, J = 8 - 7$) line velocity (Fig. 3.5) and the PVD (Fig. 3.6) point unambiguously at a rotating gaseous disk, as shown in Chapter 2 [72]. The point of inflection of the PVD along the position axis for each velocity bin is represented with a light green or orange dot for the east and west sides of the disk, respectively. They correspond to the peak positions visible in Fig. 3.4. The size of the stellar photosphere ($\theta_{\rm LD} = 17.9 \pm 1.6$ mas; [88]) is shown with light green lines. Color markings indicate the positions of the inner rim of the dust disk (magenta) and of the companion of L_2 Pup (cyan) as observed by Kervella et al. (2015) [87]. The yellow curve in Fig. 3.6 represents the best-fit Keplerian velocity profile to the inflection points, adjusted between radii of 2.5 and 4.5 AU. The velocity field over this radius domain is Keplerian as shown in the right panel of Fig. 3.6, with a power law dependence of the velocity in $R^{-1/2}$. The radial position uncertainty in the point of inflection is fixed in the fit at ±2.5 mas (one reconstructed image pixel), and the velocity uncertainty to $\pm 0.5\,{\rm km\,s^{-1}}$. This fit gives us the total mass enclosed within a radius of 2.5 AU,

$$m_{2.5\,\rm AU} \sin(i) = 0.653 \pm 0.011 \pm 0.041\ M_\odot, \tag{3.4}$$

where i is the inclination of the rotating Keplerian disk on the line of sight. The determined mass is linearly proportional to the parallax. The corresponding systematic uncertainty (±6.3%) dominates the error budget and is listed separately in Eq. 3.4. It should be noted that this mass estimate includes any additional mass contributor within the inner radius. This implies that the mass contribution of the secondary source L_2 Pup B presented in Sect. 3.3.1 is included in this mass estimate. However, we have essentially an upper limit for the mass of this secondary source (Sect. 3.4.2) that could be very low. We therefore did not correct for its contribution and refer in the following to the mass $m_{2.5\,\rm AU}$ as the mass of L_2 Pup A (m_A).

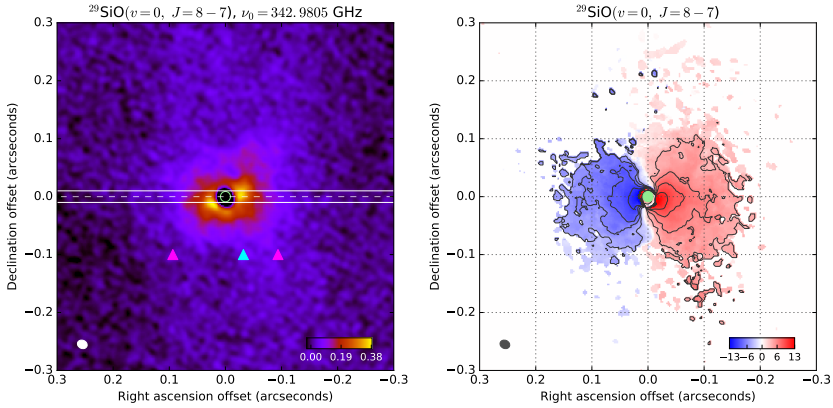

Figure 3.5: *Left panel:* Map of the emission from L_2 Pup in the ^{29}SiO($\Delta v = 0, J = 8-7$) line (left), integrated between radial velocities −30 and +30 km s^{-1} around the systemic velocity (v_0 = 33 km s^{-1}). The pseudo-slit used to compute the position-velocity diagrams is represented with solid white lines. The linear color scale in Jy beam^{-1} km s^{-1} is shown in the bottom right corner, and the beam size is represented by the ellipse in the lower left corner of the image. The radius of the inner rim (6 AU) and the radius of the companion of L_2 Pup are shown with magenta and cyan triangles, respectively. *Right panel:* Map of the first moment emission of the velocity (the color scale is in km s^{-1}). The contours are drawn between 4 and 10 km s^{-1} with a 2 km s^{-1} step, and the size of the photosphere is shown with a light green disk.

The position angle of the gaseous disk rotation plane is oriented almost perfectly east-west, within ±3°. We determined this angle through a maximization of the PVD velocity amplitude, but the exact position angle within this range has a negligible influence on the determined mass. The inclination i of the circumstellar disk of L_2 Pup on the line of sight has been estimated by Kervella et al. (2014) [88] to $i = 84°$ and slightly revised by Kervella et al. (2015) [87] to $i = 82°$. Ohnaka et al. (2015) [147] also concluded a high inclination from the partial obscuration of the stellar disk by the edge of the dust disk. We therefore adopt a value of $i = 82 \pm 5°$., and obtain the mass enclosed within 2.5 AU in radius, identified as the mass of L_2 Pup A,

$$m_A = 0.659 \pm 0.043\ M_\odot\ (\pm 6.6\%). \tag{3.5}$$

Sub-Keplerian disk rotation

Figure 3.6 shows that the rotation velocity of the gaseous disk changes from the purely Keplerian regime in the central cavity ($v \approx R^{-1/2}$) to a markedly sub-Keplerian regime

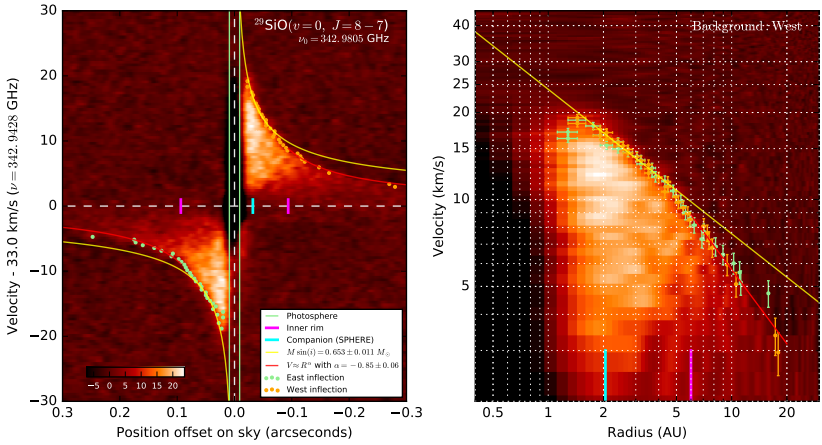

Figure 3.6: Position-velocity diagram with Cartesian coordinate axes (left) and with logarithmic coordinates (right) to show the Keplerian and non-Keplerian domains of the disk rotation velocity profile more clearly. The yellow curve is a Keplerian fit to the inner cavity, and the red curve is a power law fit to the non-Keplerian radius domain. The color scale is in mJy beam^{-1}.

beyond the inner rim of the dust disk (6 AU). The adjustment of a power law to the observed profile in the sub-Keplerian domain ($6 < R < 20$ AU) gives the following radial dependence of the orbital velocity:

$$v = (40.7 \pm 5.5) \times R^{(-0.853 \pm 0.059)} \text{ km s}^{-1} \tag{3.6}$$

with R expressed in astronomical units. This velocity profile is represented with a red curve in Fig. 3.6. We qualitatively interpret the deceleration beyond 6 AU as being caused by the friction of the gas with the sub-Keplerian dust in the disk. The dust grains are subject to the strong radiative pressure from the central star's radiation, and the effect of this radial force on the dust grains is equivalent to a reduction of the effective gravity. This results in a reduced orbital velocity at a given radius compared to the Keplerian regime. As the inner cavity has a low dust content, this effect is absent below a radius of $R \approx 5$ AU, justifying our choice of the radial domain from 2.5 to 4.5 AU (where the rotation is Keplerian) for the determination of the mass of the central object. A detailed discussion of the sub-Keplerian rotation profile and structure of the disk is presented in Chapter 4.

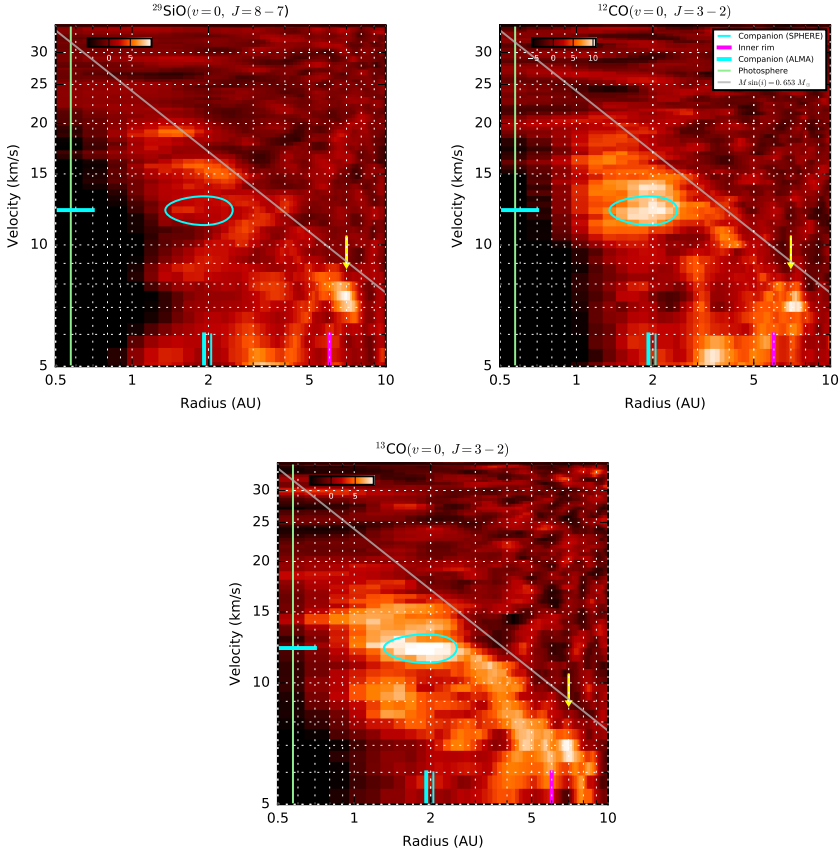

Figure 3.7: Position-velocity diagrams of the ^{29}SiO($\Delta v = 0, J = 8 - 7$), ^{12}CO($\Delta v = 0, J = 3 - 2$) and ^{13}CO($\Delta v = 0, J = 3 - 2$) lines for the west part of the gaseous disk from which the east part of the PVD has been subtracted. The cyan ellipse is centered on the position of B, with a radial extension corresponding to the beam size and a velocity range of $12.2 \pm 1.0\,\mathrm{km\,s^{-1}}$. The yellow arrow indicates the position of the notch at 7 AU in the gaseous disk. The color scale is in $\mathrm{mJy\,beam^{-1}}$.

Molecular emission from L_2 Pup B

Figure 3.7 shows the result of subtracting the eastern part of the PVD from the western part for the ^{29}SiO, ^{12}CO and ^{13}CO lines. We observe an excess molecular emission at the location of source B in the PVDs of ^{12}CO and ^{13}CO, but not in that of ^{29}SiO. We applied a global multiplicative factor of 0.8 to the east PVD as the emission is stronger in average (possibly due to absorption from dust), and we smoothed it using a moving median box of 7.5 mas $\times$ 1.2 km s^{-1} to improve the signal-to-noise ratio. The emission at the radius of source B is observed at a radial velocity of $v_0 = +12.2 \pm 1.0$ km s^{-1}, represented with a blue ellipse in Fig. 3.7. As a remark, an excess emission is also present in the ^{29}SiO PVD (Fig. 3.6) at the same radial velocity, but it is essentially symmetrical between the east and west wings and therefore cancels out in the subtraction. We also observe an excess emission at the radius of source B and around 12 km s^{-1} velocity in the PVD of the SO 3Σ ($\Delta v = 0, 8(8) - 7(7)$) that is presented in Appendix B. The frequency coverage of the opposite wing of the disk is incomplete, however, and does not permit the same subtraction as for the other lines.

A compact emission is also identified at a radius of 7 AU and a velocity of 7.0 ± 0.5 km s^{-1} in the three subtracted PVDs (yellow arrows in Fig. 3.7). In contrast to the emission identified at 2 AU, it corresponds to a deficit of the east part of the PVD (i.e. opposite to the companion) rather than an excess emission in the west. This notch is visible in the non-subtracted PVDs (e.g. Fig. 3.6) in the east, at a radius of 7 AU, that is, slightly beyond the inner rim of the dust disk. The origin of this notch is unknown, but it could indicate a furrow in the disk. It is located at a similar radius as the origin of plume #1 observed by Kervella et al. (2015) [87] (see also Sect. 3.4.3).

3.4 Discussion

3.4.1 Mass and evolutionary state of L_2 Pup A

We compared the measured parameters of the star listed in Table 3.3 (left columns) to the database of PARSEC+COLIBRI models of thermally pulsating AGB stars (TP-AGB) developed by Marigo et al. (2008,2013) [118, 117] in version PR16 [160]. The pre-AGB evolution was computed using the PARSEC code [28]. Based on its Galactic space velocity, Jura et al. (2002) [82] proposed that L_2 Pup belongs to the thick-disk population of the Galaxy (i.e. is a low-metallicity star). This is consistent with the low-mass we measure, and we therefore adopted a sub-solar metallicity of $Z = 0.008$. We retrieved the isochrones from the CMD 2.8 web site[1]. We chose to not interpolate them as the correlations between parameters are potentially complex. A comparison

[1] http://stev.oapd.inaf.it/cgi-bin/cmd

of selected L_2 Pup parameters compared to the COLIBRI isochrone predictions is presented in Fig. 3.8.

The closest COLIBRI model to the observed properties of the star has the parameters listed in Table 3.3 (right columns). Thanks to our knowledge of the mass and pulsation period, the model properties are well constrained and non-degenerate. The agreement between the model and observed parameters is very good.

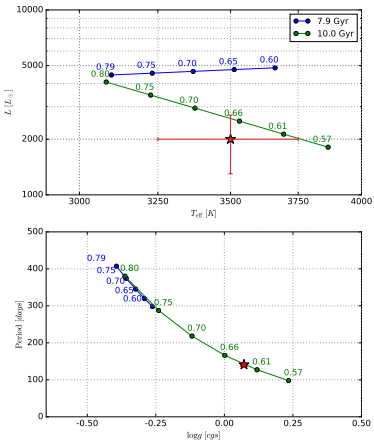

Figure 3.8: Position of L_2 Pup compared to isochrones from the evolutionary models by Marigo et al. (2008,2013) [118, 117]. The mass of the star at the age of the isochrone is indicated as labels of each curve. *Top panel:* Hertzsprung-Russell diagram. *Bottom panel:* Pulsation period vs. log g.

The measured effective gravity ($\log g$) was derived from the angular diameter measured by Kervella et al. (2014) [88] using near-infrared interferometry, combined with the *Hipparcos* parallax and the mass m_A determined in the present work. The difference in $\log g$ with the observed value is well within the error bar, although no correction was made for the pulsation phase of the star. The pulsation period predicted by the model (141.5 days) is very close to the observed period (138 ± 1.7 days). As expected for this evolved star, the fraction of helium in the core is very high, close to 90% in mass. The mass loss predicted by the COLIBRI model $\dot{M} = 3 \times 10^{-8}\, M_\odot\ \mathrm{yr}^{-1}$ is lower than the values estimated by Winters et al. (2002) [206], Bedding et al. (2002) [13] and Jura et al. (2002) [82] by about an order of magnitude. This parameter is particularly difficult to model, and the agreement is still relatively satisfactory. To explain the discrepancy, we could speculate that the mass loss of L_2 Pup is currently enhanced compared to its medium-term average value (over a millenium, for example). In this context, Chen et al. (2016) [29] proposed that the formation of the dust disk could be the result of a recent, maybe still ongoing, enhanced mass-loss event. The influence of the companion on the mass loss is also uncertain. The lifetime of L_2 Pup in the TP-AGB phase is expected to be only on the order of 0.5 Myr [159] which is very short and makes the proximity of this star particularly remarkable from a statistical point of view.

In summary, L_2 Pup's current evolutionary state is a thermally pulsating AGB star, which is a brief stage of its evolution. Its initial mass on the main sequence was very

Table 3.3: Observed properties of L_2 Pup and best COLIBRI model parameters.

Parameter	Observed	Ref.	Model	$\Delta[\sigma]^a$
Current mass $M_{\rm act}$ $[M_\odot]$	0.659 ± 0.043	K16	0.63	−0.6
Initial mass $(M_\odot)$ $M_{\rm ini}$			0.98	-
Radius R $[R_\odot]$	123 ± 14	K14	121	−0.1
Effective gravity $\log g$ [cgs]	0.078 ± 0.027	K16	0.072	+0.2
Luminosity L $[L_\odot]$	2000 ± 700	K14	2347	+0.6
Effective temperature $T_{\rm eff}$ [K]	3500 ± 250	K14	3629	+0.5
Pulsation period P [days]	138.3 ± 1.7	B02	141.5	+1.9
Pulsation mode order			0	-
Metallicity Z			0.008	-
Carbon-to-oxygen ratio C/O			0.46	-
Mass of helium core $M_{\rm He}$ $[M_\odot]$			0.55	-
Mass-loss rate $\dot{M}$ $[M_\odot\,{\rm yr}^{-1}]$	5×10^{-7}	B02	3×10^{-8}	-

close to solar, and its age is approximately twice that of our star. L_2 Pup thus provides a remarkable analog of the Sun when it will enter the final phases of its evolution, shortly before metamorphosing from a red giant into a planetary nebula and becoming a white dwarf.

3.4.2 Physical properties of L_2 Pup B

Mass from molecular disk dynamics

The velocity profile of the disk and the position of the central AGB star allow us to estimate the mass of L_2 Pup B. As the molecular disk revolves around the barycenter G of the enclosed mass, we can constrain the mass of source B from the difference in position between the AGB star's photocenter Ph (taken as a proxy of the center of mass of the star) and the geometrical center of rotation G of the gaseous disk.

We measured the position of G by matching the Keplerian velocities on each side of the PVD (east and west) of the ^{29}SiO($\Delta v = 0, J = 8 - 7$) line (Fig. 3.6). Thanks to the very high signal-to-noise ratio, we measured the position of G with an accuracy of ±0.2 pix (±0.5 mas). We shifted all images (line and continuum) to define this position as the zero of the relative coordinate grid. The position Ph of the photocenter of the AGB star is derived from a bidimensional Gaussian fit over the central part of the continuum emission. The possibility exists that a position shift is introduced by an asymmetric masking of the stellar photosphere by the northern edge of the dust disk [147]. This photocenter displacement is expected to be of smaller amplitude

at millimeter wavelengths than in the visible or near-infrared because of the higher transparency of the dust, but we conservatively adopt a systematic uncertainty of ±0.2 pix (±0.5 mas) on the measurement.

We therefore obtain a relative position in right ascension of *Ph* with respect to *G* of

$$\Delta\alpha[Ph - G] = +0.22 \pm 0.30\,\mathrm{pix} = +0.55 \pm 0.75\,\mathrm{mas} \tag{3.7}$$

This difference is positive as *Ph* is located slightly to the east of *G*. The agreement between the positions of *G* and *Ph* is therefore very good and statistically compatible with zero.

Considering the observed position offset in right ascension $\Delta\alpha[BA] = +30.0 \pm 2.5$ mas between L_2 Pup B and the AGB star, we conclude that the mass of B is

$$m_B = \frac{\Delta\alpha[Ph - G]}{\Delta\alpha[BA] - \Delta\alpha[Ph - G]} \times m_A \tag{3.8}$$

We therefore derive

$$m_B = 0.019 \pm 0.025 \times m_A \tag{3.9}$$

$$= 0.012 \pm 0.016\,M_\odot \tag{3.10}$$

$$= 12 \pm 16\,M_{\mathrm{Jup}}. \tag{3.11}$$

We assumed in this reasoning that only one companion source is present in addition to the central star A. The presence of other sources could induce a different combined shift of the barycenter that might bias the mass estimate.

Orbital period and radius

For simple geometrical reasons (see e.g. Fig. 3.10), the observed velocity v_0 of source B is sub-Keplerian at the observed projected separation R_0 and corresponds to the projected component of the orbital velocity v of source B. Its orbital radius R_B is necessarily larger than its currently observed radius R_0 from A, and is given by the expression:

$$R_B = \left(\frac{R_0}{v_0}\sqrt{G\,m_A}\right)^{2/3} \tag{3.12}$$

where $m_A = 0.659 \pm 0.043\ M_\odot$, $R_0 = 1.92 \pm 0.12\ R_\odot$ and $v_0 = 12.2 \pm 1.0\,\mathrm{km\,s^{-1}}$. We assumed that the orbit of B is circular and coplanar with the disk. This may not be perfectly true in reality as the position of source B in the continuum appears slightly south of the plane of the disk. The actual orbital plane of B may therefore be moderately

tilted with respect to the plane of the disk. Under the assumption that the molecular emission does come from source B, the orbital radius is therefore $R_B = 2.43 \pm 0.16$ AU corresponding to a maximum angular separation of $\rho_B = 38 \pm 3$ mas. The orbital velocity (circular orbit) is $v_{\rm orb} = 15.4 \pm 1.0\,{\rm km\,s^{-1}}$. From Kepler's third law, the orbital period is $P_{\rm orb} = 4.69 \pm 0.45$ years. As shown in Fig. 3.10, this period is consistent with the small observed astrometric displacement of source B between the ZIMPOL (2014.93) and ALMA (2015.84) epochs that are separated by 0.91 years. The two epochs would then correspond to almost symmetric phases with respect to the maximum elongation (−33° and +38° for ZIMPOL and ALMA, respectively). The ephemeris of the separation $\Delta\alpha_{[B-A]}$ in right ascension between source B and L_2 Pup A is therefore

$$\Delta\alpha_{[B-A]}(T) = -\rho_B \cos\left[2\pi\,\phi(T)\right] \tag{3.13}$$

with $\phi(T) = (T - T_0)/P_{\rm orb}$, and the ephemeris of the radial component $v(T)$ of the orbital velocity is given by:

$$v(T) = v_{\rm orb} \cos\left[2\pi\,\phi(T)\right] \tag{3.14}$$

where T is the observing date expressed as decimal year and $T_0 = 2015.1$ the epoch of maximum elongation to the west. If the orbital motion ephemeris we determine is correct, the maximum elongation of source B to the east of L_2 Pup A should occur around June 2017. The radial velocity would then be approximately $v_{\rm rad} = -15\,{\rm km\,s^{-1}}$.

3.4.3 Nature of L_2 Pup B

Considering our uncertainty domain on the mass of L_2 Pup B ($m_B = 12 \pm 16\,M_{\rm Jup}$), we can exclude that it is a very low-mass star at a 4σ level. We are left with three hypotheses, ordered by increasing mass, that we critically discuss in the following paragraphs:

1. a dense, coreless aggregate of gas and dust,
2. a planet ($m_B \leq 12\,M_{\rm Jup}$),
3. a low-mass brown dwarf ($12\,M_{\rm Jup} < m_B < 30\,M_{\rm Jup}$).

For simplification, we address the planet and low-mass brown dwarf hypotheses together, using the same "compact body" term.

Continuum and molecular emission

The continuum flux contribution of B is considerable in absolute terms ($f_B = 1.03 \pm 0.05$ mJy assuming it is unresolved), and its molecular emission is also very strong in

the CO lines. These two characteristics can be explained by the emission of a dense aggregate of dust and gas, but the thermal emission of a planet or brown dwarf is clearly insufficient. However, L_2 Pup B evolves in a particular environment, that is hot, rich in molecules and possibly also contains refractory dust that condensed in the AGB star wind. Assuming that B is a compact body, it is therefore located in a very favorable position to accrete material. The emission from the accreted material, either from an extended atmosphere or an accretion disk, could strongly outshine the thermal emission from the planet itself. An approximate computation using the formulae by Paczynski et al. (1971) [149] shows that the Roche lobe of a $12\,M_{\rm Jup}$ companion located at 2.5 AU from a $0.65\,M_{\odot}$ star has a radius of $r_{\rm Roche} = 0.3$ AU. A detailed model of the system is beyond the scope of the present work, but we speculate that the accretion of the AGB wind by source B fills the Roche lobe of the companion with a sufficient quantity of material to produce the observed continuum and line emission. If confirmed, this configuration would provide valuable constraints for hydrodynamical models of star-planet interactions at the late stages of stellar evolution (see e.g. [174, 202]).

We conclude that the high observed continuum and molecular emission of L_2 Pup B is compatible with the object being either a core-less aggregate or a compact body.

Persistence over time

L_2 Pup B has been detected at both the ZIMPOL (2014.93, [87]) and ALMA (2015.84) epochs separated by 0.91 years. From hydrodynamical simulations, gas clumps in an idealized radial outflow typically do not survive for long periods of time, mainly because of the internal pressure gradient. The predicted lifetimes are on the order of weeks or months (depending on the size of the clump, temperature gradient, density gradient, etc.). The dust (both small and large grains) is almost unaffected, as it is not subject to internal pressure. The only influence of the outflow on the dust is a gradual elongation of the clump perpendicular to the local radial velocity vector field. In a rotating medium as observed around L_2 Pup, the gas would not survive as a clump because of the intense shear originating from the Keplerian rotation, and would be quickly dissolved. These predictions are difficult to reconcile with the observed molecular emission enhancement in the CO lines (Sect. 3.3.2). Moreover, as a result of the strong radiative pressure, a fluffy clump of dusty material would most likely be quickly blown away from the star and incorporated in the dust disk. Overall, the observed asymmetry between the west and east wings of the disk is difficult to explain by simple inhomogeneity of the disk structure, since the turbulence in, and the viscosity of the medium would conspire against its development.

The persistence of source B over a period of one year favors the hypothesis of a compact object over a core-less aggregate.

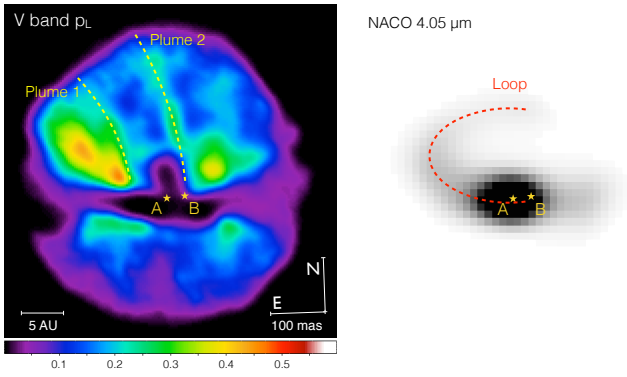

Figure 3.9: *Left panel:* Map of the degree of polarization in the nebula of L_2 Pup showing plume #2 (from [87]). *Right panel:* Intensity image at $\lambda = 4.05\,\mu$m showing the loop (from [88]). The angular scale and orientation of the two panels are identical.

Relation with the nebular features

From visible polarimetric imaging, two plumes (labeled #1 and #2) were identified by Kervella et al. (2015) [87] in the envelope of L_2 Pup at visible wavelengths. An extended loop was also detected in the thermal infrared ($\lambda = 4\,\mu$m), starting from the western wing of the disk and developing toward the northeast. The location of these features is presented in Fig. 3.9 (see also Fig. 3.2). Both plumes appear to originate in the plane of the disk, and the position of L_2 Pup B coincides with the origin of plume #2. Plume #1 is less extended and more irregular than plume #2, and could be related to the notch in the SiO disk observed at 7 AU (Sect. 3.3.2). The polarimetric signature of plume #2 shows that it contains dust, and the high degree of linear polarization ($p_L \approx 30\%$) is characteristic of a large scattering angle, probably around 50°. It is unresolved spatially in the SPHERE/ZIMPOL images, implying that it is less than ≈ 1 AU across, but its extension perpendicularly to the plane of the disk reaches at least 15 AU. Assuming that source B is at the origin of the generation of plume #2, this very strong focusing is difficult to explain if B is simply a clump of gas and dust. As a side note, we observe a signature of plume #2 also in the ^{29}SiO emission map presented in Fig. 3.5 (left panel), as an elongated north-south emission emerging from the disk at a radius of 2 AU. The accretion of the AGB star wind and dust on a compact body appears as a plausible explanation for the origin of the plume and its coincidence with L_2 Pup B. Jets are a typical signature of accretion in vastly different objects, from young stars [157, 112] to active galactic nuclei [46]. Our proposed geometry of the plume with respect to the disk and source B is presented in Fig. 3.10. We speculate that the plume is created by an accretion disk around source B, and launched perpendicularly to the dust disk plane. Considering the expected size of the Roche lobe of L_2 Pup B,

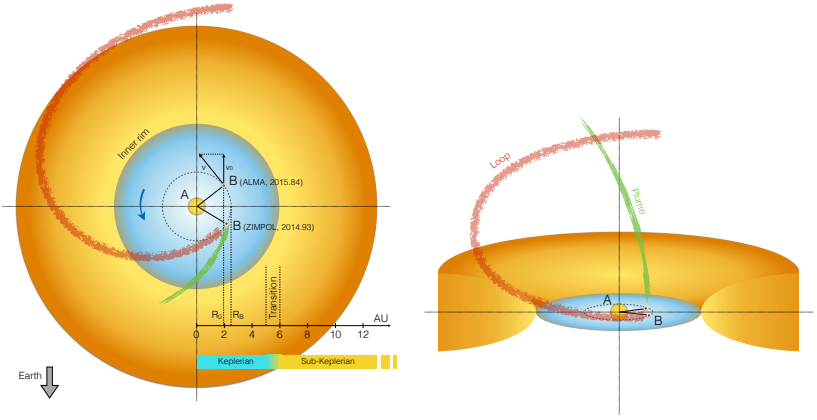

Figure 3.10: Schematic view of the environment of L_2 Pup as seen from the north pole of the disk (left panel) and close to the plane (right panel). The dust component is shown in yellow-orange, and the median plane of the inner gaseous disk is represented in blue. The position of source B is represented for the ZIMPOL and ALMA epochs. The components are shown to scale.

the radius of this accretion disk is probably smaller than 0.3 AU, that is, 5 mas in radius. It is therefore unresolved in our ALMA observations in band 7, as observed in the subtracted PVD profiles in the CO lines (Fig. 3.7). However, future observations with ALMA in band 9 or 10 could reach a sufficient angular resolution ($\approx$ 5 mas) to resolve this putative accretion disk around L_2 Pup B.

The loop is the dominant feature in the envelope of L_2 Pup in the thermal infrared domain. It extends radially up to the eastern edge of the dust disk and expands vertically to the north up to approximately 10 AU above the disk plane as a streamer. We propose that the development of the loop is linked to the presence of source B, and that it follows the geometry represented in Fig. 3.10. A possible mechanism for the formation of the dust is that it condenses in the shadow of source B, where the lower temperature would be more favorable to the survival of dust grains [130]. A relatively dense accretion disk around L_2 Pup B could also favor the formation of dust. The dust would then be blown away by the wind and radiation pressure of the AGB star, creating a planar spiral. The three-dimensional development of the spiral into a streamer may be caused by the focusing of the wind by the flared disk along the polar axis, or by polar wind emitted by the disk itself.

Relation with the disk and bipolar structure

The overall morphology of the nebula of L_2 Pup consists in an equatorial disk and bipolar cones [87]. Nordhaus et al. (2006) [142] showed that a low-mass companion in the envelope of a mass-losing star can lead to the formation of a disk and is likely to generate polar outflows. Mastrodemos et al. (1999) [119] constructed three-dimensional hydrodynamical models of the dusty wind geometry in binary systems. They obtained a range of envelope geometries from spherical to bipolar, including with internal spiral shock structures created by the orbital motion of the companion. Specifically focused on L_2 Pup, the simulations by Chen et al. (2016) [29] also indicate that an orbiting companion can result in the formation of an equatorial disk. Possible traces of the interaction of the companion with the disk and bipolar cones can be observed in the visible images of L_2 Pup as spirals and streamers (Fig. 3.2; [87]). This means that the general morphology of the envelope of L_2 Pup is compatible with the expected signatures of a compact companion.

Owing to its near-Keplerian rotation and axial symmetry, the disk surrounding L_2 Pup holds a considerable angular momentum. The origin of this momentum cannot be explained by the current rotational velocity of the star, however, which is most likely very slow because of its strong inflation on the red giant branch [127]. As discussed by Chen et al. (2016) [29], a planetary mass or brown dwarf companion can inject angular momentum into the circumstellar disk and shape the wind of the star. The compact body thus provides a simple explanation to the angular momentum of the disk, while a fluffy aggregate of gas and dust does not.

3.4.4 Scenarios for the formation and evolution of L_2 Pup B

L_2 Pup B could be an old planet that formed together with the star, or alternatively a second-generation body recently formed in the disk [76]. Its uncertain mass is compatible with a low-mass rocky object that could have formed relatively quickly in the circumstellar disk, even though its estimated total dust mass is relatively low ([87] estimated a few $10^{-7}\,M_{\odot}$). Bonsor et al. (2013,2014) [17, 16] reported debris disks around subgiants, which may provide seeds for the formation of second-generation planetary bodies. A circumbinary dust disk and probably also planets orbiting the post-common envelope binary NN Ser was reported by Hardy et al. (2016) [64] (see also Veras et al. (2016) [189]). This strengthens the credibility of the scenario of second-generation planet formation.

The dynamical evolution of L_2 Pup B is essentially conditioned by its mass, the mass of the central star, the stellar mass-loss rate and tidal interactions. An overview of the two-body mass-loss problem is presented in Veras et al. (2011) [193]. If the mass of L_2 Pup B is in the gaseous giant or brown dwarf regime, the large convective envelope

of the AGB star induces strong tidal forces. Mustill et al. (2012) [139] predicted that these forces will pull the planet inside the envelope of the AGB star if their initial orbital radius is shorter than 3 AU. This has also been the conclusion of Villaver et al. (2007) [194]. The tidal stability of any exoplanetary system strongly depends on the tidal quality factor Q [125], which is poorly calibrated for main-sequence-star – Jupiter-mass systems, and essentially unconstrained for evolved systems. With a current orbital radius of 2.4 AU, L_2 Pup B may currently be migrating toward the star. Nordhaus et al. (2010) [144] predicted that once engulfed, Jupiter-mass companions will be destroyed during the common-envelope phase and therefore will not remain in orbit around the final white dwarf. Lower mass planets are more likely to survive as their orbital radius will expand as the star loses mass. Accretion onto the companion or evaporation [195], anisotropic mass loss or jets [191] and viscous interaction with the disk [109] will also influence the companion's orbital evolution. While tidal factors should circularize the orbit relatively quickly, eccentricity pumping of the companion's orbit through interactions with the disk are likely to have a destabilizing influence. The signature of such interactions may be apparent both in the orbital parameters of L_2 Pup B (in particular eccentricity and inclination with respect to the disk plane) and in the disk structure (warp).

Considering L_2 Pup as an analog of the future Sun, the present properties of L_2 Pup indicate that Mercury and Venus will very likely be engulfed in the Sun's envelope as they orbit within or very close to the present radius of the AGB star (0.6 AU). Assuming that the orbital energy of L_2 Pup B remained constant since its formation, its orbital radius while component A was on the main sequence (when $m_A \approx 1\,M_\odot$) was around 1.6 AU, that is, comparable to the present orbit of Mars around the Sun. The presence of L_2 Pup B is thus consistent with the minimum radius of 1.15 AU inferred by Schroder et al. (2008) [166] for the survival of planets orbiting the Sun. The orbital interactions between the planets will play a major role in determining their survival. For instance, an inward migration of Jupiter would naturally have a major impact on the inner planets. The fate of Earth also strongly depends on the detail of how the RGB and AGB phases progress, particularly with regard to asphericities in the stellar wind and the timing and efficiency of RGB/AGB mass loss. Different models prescribe different outcomes Earth, and L_2 Pup could provide important indications to distinguish between its engulfment in the central star and its survival as a white dwarf planet.

3.5 Conclusion

From the Keplerian rotation of ^{29}SiO molecular gas observed with ALMA, we determined that the mass of the central object of L_2 Pup is $m_A = 0.659 \pm 0.011 \pm 0.041\,M_\odot$. The error budget (±6.6%) is fully dominated by the uncertainty of the *Hipparcos* parallax, which will soon be improved by *Gaia*. This accurate mass

combined with the other observed properties of the AGB star (pulsation period, radius luminosity, etc.) allowed us to conclude from evolutionary models that the mass of L_2 Pup A when it was on the main sequence is close to solar, and that its current age is approximately 10 Gyr. This age is consistent with the Galactic space velocity of the star, which indicates that it is probably a member of the thick-disk population.

We also identified a secondary source of continuum and molecular emission, located at a projected radius of $\approx$ 2 AU. This position corresponds to the location of the companion L_2 Pup B reported by Kervella et al. (2015) [87]. From its estimated mass of $12 \pm 16\,M_{\rm Jup}$ and observed emission, we argue that source B is either a planet or a low-mass brown dwarf accreting the wind of the AGB star. While it could formally be a dense clump of dust and molecules, its persistence over one year, its coincidence with remarkable nebular features and the overall morphology of the envelope of L_2 Pup all favor the hypothesis of a compact body. We emphasize, however, that the properties of source B are still uncertain as we do not have a firm lower limit on its mass. The hypothesis that it is a dense clump of dust and gas cannot be formally excluded. Very high angular resolution observations with ALMA at short wavelengths may resolve the putative accretion disk surrounding L_2 Pup B, and allow a more precise measurement of its mass. A schematic view of the configuration we propose for the environment of L_2 Pup is presented in Fig. 3.10.

From its observed properties, L_2 Pup and its companion emerge as a plausible analog of the solar system at an age of approximately 10 Gyr. It provides a view on the complex interactions occurring between a solar-type star entering the planetary nebula phase and its planetary system. The companion could also play an important role in the shaping of the bipolar envelope of L_2 Pup and subsequently of the planetary nebula [142]. Future observations of L_2 Pup with ALMA's highest angular resolutions and the E-ELT, for instance, will provide valuable constraints for the modeling of these interactions (see e.g. [174, 29, 72, 202]).

Chapter 4

ALMA observations of the nearby AGB star L_2 Puppis: II. Gas disk properties derived from ^{12}CO and ^{13}CO J =3–2 emission

(2017A&A...601A..5H)

Ward Homan[1], Anita M. S. Richards[2], Leen Decin[1], Pierre Kervella[3,4], Alex de Koter[1,5], Iain McDonald[2], and Keiichi Ohnaka[7]

[1] Institute of Astronomy, KU Leuven, Celestijnenlaan 200D B2401, 3001 Leuven, Belgium
[2] JBCA, Department Physics and Astronomy, University of Manchester, Manchester M13 9PL, United Kingdom
[3] Unidad Mixta Internacional Franco-Chilena de Astronomía (CNRS UMI 3386), Departamento de Astronomía, Universidad de Chile, Camino El Observatorio 1515, Las Condes, Santiago, Chile
[4] LESIA (UMR 8109), Observatoire de Paris, PSL Research University, CNRS, UPMC, Univ. Paris-Diderot, 5 Place Jules Janssen, 92195 Meudon, France

[5] Sterrenkundig Instituut 'Anton Pannekoek', Science Park 904, 1098 XH Amsterdam, The Netherlands
[6] Universidad Católica del Norte, Instituto de Astronomía, Avenida Angamos 0610, Antofagasta, Chile

Abstract: *The circumstellar environment of the AGB star L_2 Puppis was observed with ALMA in cycle 3, with a resolution of* 15×18 mas*. The molecular emission shows a differentially rotating disk, inclined to a nearly edge-on position. In the first chapter in this series (Chapter 3) the molecular emission has been analysed to accurately deduce the motion of the gas in the equatorial regions of the disk. In this work we model the optically thick ^{12}CO J =3−2 and the optically thin ^{13}CO J =3−2 rotational transition to constrain the physical conditions in the disk. To realise this effort we make use of the 3D NLTE radiative transfer code* `LIME`*. The temperature structure and velocity structure show a high degree of complexity, both radially and vertically. The radial H_2 density profile in the disk plane is characterised by a power law with a slope of* -3.1*. We find a ^{12}CO over ^{13}CO abundance ratio of 10 inside the disk. Finally, estimations of the angular momentum in the disk surpass the expected available angular momentum of the star, strongly supporting the indirect detection of a compact binary companion reported in Chapter 3. We estimate the mass of the companion to be around a few Jupiter mass.*

Contribution to the article: *Save for the data reduction, all work scientific work discussed below, as well as the composition of the article was carried out solitarily, with the exception of regular consulatation with my supervisors and project co-I's.*

4.1 Introduction

In this chapter we continue with the analysis presented in Chapter 3. We model the observed emission of the ^{12}CO and ^{13}CO rotational transition J =3–2 around L_2 Pup, which allows us to make predictions on the (thermo)dynamical and morphological properties of the circumstellar gas. This provides valuable constraints on the possible physical or thermo-chemical formation mechanisms producing such a morphological complexity, as well as insights on the local physics that dominate the inner wind. In addition, revealing and understanding the local inner wind dynamics sheds light on the processes that dictate the further evolution into post-AGB stars and planetary nebulae, whose morphologies have been extensively documented and been found to be highly aspherical. Therefore, an in-depth understanding of the finer physical details governing the inner regions of complexity-harbouring AGB CSEs will aid in the quest to understand the missing morphological link between AGB stars and their progeny.

4.2 ALMA data description

For an extensive description of the ALMA observing set-up as well as an in-depth discussion of the continuum residuals we refer to Chapter 3 [86]. We summarise the most relevant information here.

L_2 Pup was observed on 2015 Nov 5 by ALMA for project code 2015.1.00141.S (PI Kervella), starting at UT 08:39:25 (epoch 2015.8448, MJD = 57 331.361), and ICRS position RA 07:13:32.475914 DEC –44:38:17.91396. 45 antennae were present for all or most of the observations, providing baselines from 0.09 to 16 km. However, the coverage inside 350 m is very sparse, giving a maximum angular scale of about 250 mas for reliable imaging. Standard ALMA observing and data reduction procedures were used, including phase-referencing. The flux scale is accurate to about 7% and the absolute astrometric error is about 7 mas; comparisons within this data set are much more accurate, limited only by the signal-to-noise ratio. The line-free continuum channels of L_2 Pup were used to self calibrate the continuum and the solutions applied to all target data, and then the continuum was subtracted. Image cubes were made for the lines present in the data, adjusted to constant systemic velocity $v_{\rm sys}$ in the target frame.

In this paper, we present the ^{12}CO and ^{13}CO cubes. These have a spectral resolution of $\sim 0.22\,{\rm km\,s^{-1}}$ and a rms noise (off-source) of 2.5 and 2.6 mJy beam^{-1}, respectively. The synthesised beam size is $\sim$ (0.020″ × 0.015″), the exact value depending on frequency. A 2.5 mas pixel size and an image size of 2.56″ was used.

In the following sections we describe the morphological properties of the gas emission,

as deduced from the velocity channel maps, as well as from position-velocity diagrams (PVDs, see Sect. 1.5.2 for more information). We identify the patterns within the inner arcsec as being consistent with emission produced by a rotating disk of gas, and make a detailed description of the fine features present in the data. All descriptions relating to velocity are made relative to $v_{\rm lsr} = 33.3\,{\rm km\,s^{-1}}$, the estimated systemic velocity.

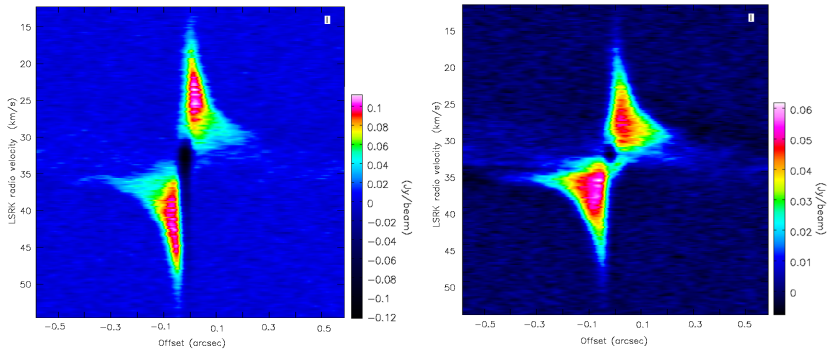

Figure 4.1: Images of the PVD of the continuum subtracted ^{12}CO data, created with a slit parallel to the disk. *Left:* PVD created with a minimal slit width of 15 mas. *Right:* slit width equal to the height of the disk emission, being 280 mas. $v_{\rm sys} = 33.3\,{\rm km\,s^{-1}}$.

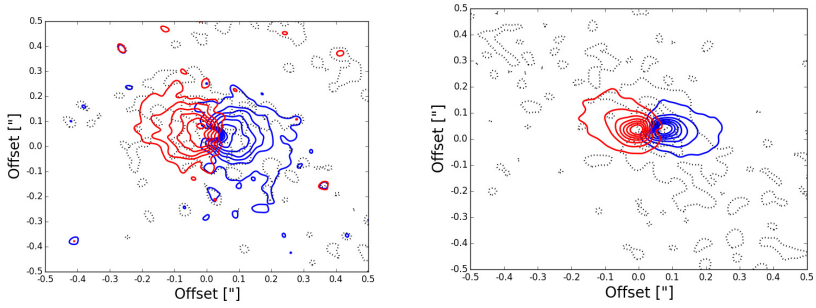

Figure 4.2: Stereogram view of the continuum subtracted ^{12}CO J =3−2 (*left panel*) and ^{13}CO J =3−2 (*right panel*) data. The blue (red) contours correspond to the velocity-averaged emission profile of 98% of the blue-shifted (red-shifted) wing of line. The black dashed contours correspond to the velocity-averaged emission of the central 2% of the emission line. The contours are drawn at every 2.5 times the continuum rms noise value (^{12}CO: 2.5 mJybeam^{-1}, ^{13}CO: 2.6 mJybeam^{-1}). This figure appeared in Chapter 3, and is repeated here to guide the reader.

The intensity maps of the ^{12}CO and ^{13}CO emission as a function of velocity are visually represented in Figs. C.1 and C.3, respectively. The figures are comprised of 49 panels,

selected from the datacubes at even intervals in velocity space. The velocity range of the panels span a domain selected such as to best show the spatial extent of the emission.

4.2.1 ^{12}CO J =3–2 emission

The channel maps (Fig C.1) reveal horizontally elongated emission features, which range up to radial angular distances of 300 mas away from the central star, and vertical heights up to 300-350 mas. These features show a very clear east-west spatial offset separation between blue and red-shifted emission. In addition, the highest (absolute) velocities probe the regions closest to the central star, while the lower (absolute) velocities probe the outer regions. These features clearly point to a compact disk with a global velocity field having the characteristics of differential rotation, seen edge-on. This claim is further supported by making integrated-intensity maps, or stereograms, of the data (Fig. 4.2), where the spatial and spectral separation between both sides of the disk is clearly apparent.

The high-velocity emission of the inner disk probes only a very small vertical region. Shifting to velocities closer to the stellar velocity the extent of this vertical signal increases. This suggests that the disk is flared. However, the emission seems not to support a stereotypical flaring pattern (i.e. an increasing rate at which the scale-height grows with radius). Rather, the ratio of the scale height over distance seems to decrease with respect to distance from the center.

Though expected to be present, the inner rim of the gas disk is not clearly visible in the data. This is mainly due to a combination of the ALMA beam size and the fact that the tilt of the disk obscures a significant portion of the inner rim. Nevertheless, the channel maps show a rather wide initial scale height, indicating that the inner rim of the gas disk may be relatively extended (of the order of a few AU) or even inflated or puffed up [51, 50].

The emission around central velocity appears more diffuse and extended. This emission is probably dominated by the extended CSE of L_2 Pup. However, due to the poor uv-coverage of the smallest baselines of the configuration, length scales above 250 mas have been poorly sampled. In addition, the maximum recoverable scale of the configuration is ~450 mas. Thus, some of the extended emission is probably resolved out and the remaining flux produces low-level artifacts, limiting the dynamic range in these channels. Kerschbaul et al. (1999) [85] detected ^{12}CO J=3–2 with the JCMT (beam size 13"), with a peak of $\approx$ 59 Jy (using S(Jy)/T_{mb}(K) = 15.6), and estimated an expansion velocity of 3 km s^{-1}; their sensitivity was of order 1 Jy and the extreme-velocity wings and disc emission was not detected. Fig. 4.3 shows spectra extracted

from the ALMA data in apertures of the indicated radii. Thus, the JCMT detected almost 10 times as much emission as ALMA from the extended CSE.

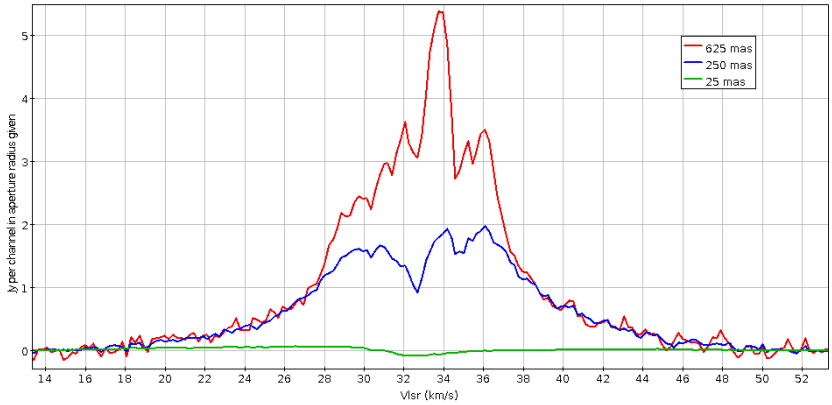

Figure 4.3: Spectral lines of the ^{12}CO J=3−2 emission, labeled by the different apertures used to extract them.

Fig. 4.3 also shows how, using a 250-mas aperture similar to the size of the disc (i.e. all the flux is recovered), there is a drop in intensity close to the systemic velocity, and using an aperture comparable to the size of the star itself shows absorption. This is seen in the corresponding channels of Fig. C.1 where the emission becomes very faint. This is probably due to self-absorption, along the line of sight to the star, by the outer regions of the disc, which must therefore be optically thick and too cool to emit significantly at 345 GHz.

On smaller scales, visible on both the blue- (-4.5 to -3.0 $\mathrm{km\,s^{-1}}$) and the red-shifted (3.0 to 5.0 $\mathrm{km\,s^{-1}}$) sides, the emission is slightly brighter above and below the mid-plane, compared to a narrow horizontal strip passing through the star. These features may be caused by local heating of the inner disk walls directly facing the stellar radiation field. This would also explain the puffed-up inner rim. We discuss this hypothesis in Sect. 4.6.2.

PVDs created by positioning the slit parallel to the disk plane (Fig. 4.1) permit the quantification of the spatial offset increase as a function of velocity. These trends have been extensively analysed in Chapter 3 [86], resulting in a very accurate determination of the central mass of the system (0.659 ± 0.052 $M_\odot$). The PVDs nicely exhibit the lack of compact emission around zero velocity. However, some diffuse emission can be seen around zero velocity up to large spatial offsets. This is the poorly sampled, large-scale emission discussed above. Comparing both diagrams it can be seen that the high-velocity tails do not span the same width in velocity-space. The tail (of significant signal-to-noise) of the narrow slit PVD is longer by about $5\,\mathrm{km\,s^{-1}}$.

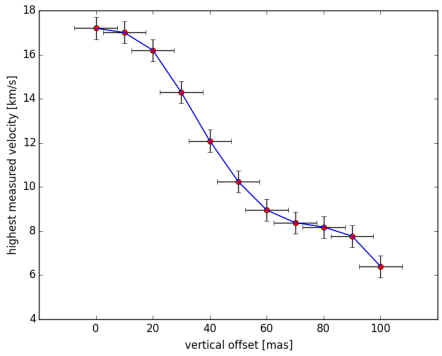

Figure 4.4: The dependence of maximal gas velocity in the disk as function of vertical spatial offset, deduced from the ^{12}CO data. The uncertainty in velocity is 0.5 km s^{-1} (see Sect. 4.4.1), the spatial uncertainty is equal to the beam width.

This suggests that the material of the inner disk has higher tangential velocities close to its equator, compared to the gas at higher vertical offsets. To quantify this velocity gradient, we constructed 11 PVDs, with a vertical separation of 10 mas. We extracted the maximal velocity at each offset by measuring the length of the tails of each PVD, employing the criterion that the signal must be twice the RMS noise value, outside the line. Indeed, this operation permitted us to recover the trend shown in Fig. 4.4. One possible cause for this vertical profile is that one may expect the upper disk regions to strongly interact with the AGB outflow, causing hydrodynamical perturbations that would impact the velocity. We discuss this further in Sect. 4.6.1.

4.2.2 ^{13}CO J =3–2 emission

Morphologically, the qualitative descriptions outlining the ^{13}CO emission patterns (Fig C.3) are in line with the ^{12}CO emission (Fig C.1). In principle no major intrinsic differences are to be expected. The ^{13}C/^{12}C ratio (see e.g. Hinkle et al. (2016) [69] for estimates in AGB stars) is likely to be reflected in the ^{12}CO/^{13}CO ratio (although not necessarily in a one-to-one relation because of isotope-selective photodissociation and chemical fractionation), and hence we expect the ^{13}CO emission to have a lower optical depth than that of the ^{12}CO emission. Hence, the absolute amount of observed emission is substantially lower in the ^{13}CO emission, pushing the emission from the low-density regions of the disk below the sensitivity levels of ALMA. This is best seen in the apparent height of the ^{13}CO disk, which is noticeably smaller than the ^{12}CO disk (see Fig. 4.2). In addition, the ^{13}CO disk is mostly optically thin, as it is still visible around the central velocity, contrary to the ^{12}CO disk (see Fig. C.3). Combined, these effects strongly dilute and blur the finer details present in the ^{12}CO emission maps, resulting in a much smoother emission distribution.

There is, however, a strong asymmetry between the low-velocity blue-shifted side compared to the low-velocity red-shifted side. This asymmetry is best seen by comparing the emission in the -3.5 to -2.0 km s^{-1} channels with the 1.0 to 3.5 km s^{-1} channels. In these channels, the blue-shifted emission is conform with the expected

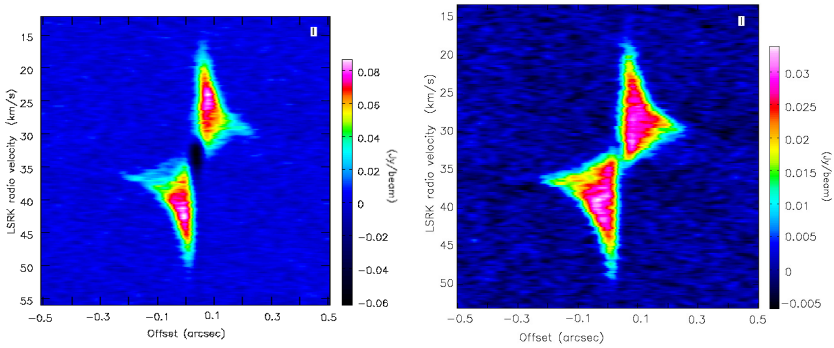

Figure 4.5: Images of the PVD of the continuum subtracted ^{13}CO data, created with a slit parallel to the disk. *Left:* minimal slit width of 15 mas. *Right:* slit width equal to the height of the disk emission, being 190 mas. $v_{\rm sys} = 33.3\,{\rm km\,s^{-1}}$.

patterns of a rotating disk. However, the red-shifted emission seems to be substantially perturbed, causing a deviation from the expected emission morphology. Emission around the equatorial regions seems not to be present, while an emission tendril is seen to reach out to the north-east. This feature subsides beyond 3.5 $\rm km\,s^{-1}$. Although one would expect the presence of a tentative binary companion (see Chapter 3) to generate local perturbations, the projected velocities at which the perturbation is seen are too low to be related to the companion system, which, due to its proximity to the central star, can be expected to only substantially affect the highest velocities. We therefore interpret this feature as a hydrodynamical inhomogeneity in the outer boundaries of the disk.

The ^{13}CO PVDs (Fig. 4.5) show a high degree of similarity with the ^{12}CO diagrams. In fact, the only clear difference is the length of the high-velocity tail, which seems to be identical for both the narrow-slit and the wide-slit PVDs (see Sect. 4.1.4). This can again be attributed to the molecular abundance fraction. The confined vertical extent of the ^{13}CO emission means it probes mainly the Keplerian equatorial regions. The high-velocity tails of the PVDs of the ^{13}CO emission are thus mostly insensitive to the sub-Keplerian velocities at higher vertical spatial offsets.

4.3 Computational methods

In this section we briefly describe the computational methods and strategy used to model the L_2 Pup CO line emission. We perform 3D radiative transfer using the `LIME` code. The result of the radiative transfer calculations are subsequently subjected to the

simulation observation algorithms of CASA to generate 3D synthetic data that can be directly compared to the observed L_2 Pup data.

4.3.1 LIME:

To perform the retrieval of the physical properties of the system, the Non-Local-Thermodynamical-Equilibrium (NLTE) full-3D, submillimeter and infrared (IR) radiative transfer code LIME was used. For a technical overview of the inner workings of the code, see Chapter E in the appendix, or Brinch et al.(2010) [19]. The model is sampled by 10^5 grid points, of which half are distributed logarithmically (gradually refining the grid towards its center), and half are distributed randomly. In addition, the position of the grid points is weighted by relative density, further increasing the mesh refinement in the high-density regions of the model. Another 10^4 grid points are positioned at the edge of the numerical domain, representing the points where the RT calculations are finalised. The spectroscopic CO data of the LAMDA database [165] were used, the collisional rates were taken from Yang et al. (2010) [210]. Because of its low electric dipole moment, the surrounding radiation field is not expected to affect the CO emission much. Nevertheless, both dust and the stellar radiation field were taken into account in the radiative-transfer calculations. The dust composition has been adopted from Kervella et al. (2015) [87], with the dust density distribution following the gas density distribution and a gas to dust mass ratio of 100. The stellar radiation field is approximated by a black body, with a temperature of 3500K and a luminosity of 2500 $L_\odot$.

4.3.2 CASA:

After having retrieved the intrinsic emission distribution from LIME, we have post-processed it with CASA [126] in order to simulate an observation with ALMA. The actual general observation conditions and instrumental set-up have been adopted as input parameters for the simulations, and are shown in Table 6.1. This also implies we used the same antenna locations to give consistent visibility plane coverage between the observations and the simulations.

4.3.3 Modelling strategy

We wish to make it clear that our final models are not achieved via the exploration and statistical analysis of a grid of models covering the 20+ free parameters available to us. Such an analysis can simply not be performed with present-day computational facilities. The final model we have obtained was created by making reasonable assumptions and

Simulation Parameters	
Pixel size of input model	0.0047”
Field size of input model	1.25”
Peak flux	Taken from `LIME` output
Transition 1	^{12}CO J =3−2 (345.765 GHz)
Transition 2	^{13}CO J =3−2 (330.587 GHz)
Pointing	Single
Channel width ^{12}CO	0.12MHz
Channel width ^{13}CO	0.22MHz
PWV	0.42 mm
Thermal noise	standard
Ground temperature	269 K
Integration time	7953 sec on-source

Table 4.1: The ALMA observation simulation specifications, see the ALMA technical handbook.

educated guesses on the general physical properties (based on previous studies and on the nature of the observed emission patterns), and subsequently attempting to converge to the reproduction of the emission characteristics via iterative adjustment of these parameters. Thus, our final model is not a statistically significant result that follows from extensive and detailed post-processing, but rather to the set of parameters for which the simulated emission shows a good visual resemblance to the emission patterns obtained by ALMA.

Due to these computational limitations, we devised a strategy for the determination of the physical disk properties via RT modelling. We decided to start by focusing the analysis on the ^{12}CO emission. The reasons for this choice are listed below, but all stem from the expected lower ^{13}CO molecular abundance compared to the ^{12}CO abundance [69]:

- ^{13}CO over H_2 abundance ratios are not well known, while ^{12}CO over H_2 ratios are better constrained.
- The lower abundance of ^{13}CO results in a flatter and dimmer disk, in which the high degree of complexity in the thermodynamical, kinematical and morphological properties of the disk are less pronounced.
- Photodissociation effects will, if present, have a larger impact on the overall morphology of the ^{13}CO disk. We make no attempt at quantifying the magnitude of photodissociation effects on the gas, so using the ^{12}CO emission as a starting point for the modelling drastically reduces this systematic error.

- We can expect the ^{13}CO emission to be optically thin, causing temperature and absolute density to be fully degenerate. Using the optically thick ^{12}CO emission untangles both by strongly reducing the influence of the absolute density.

After having determined the set of physical conditions that best reproduce the ^{12}CO emission patterns, the model was refined using the ^{13}CO emission, making sure consistency with the ^{12}CO emission is retained.

The extended emission around central velocity (visible in Fig. C.1, discussed in Sect. 4.2.1) is probably not part of the disk-system, and we therefore do not include it in the modelling effort.

4.4 Physical structure of the gas disk

4.4.1 Dominant and turbulent velocity field

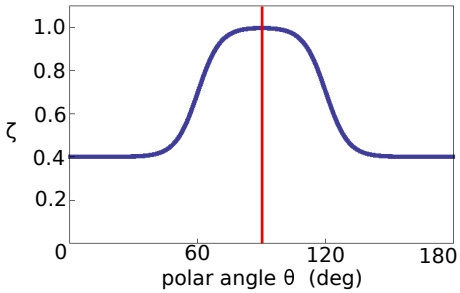

Figure 4.6: The rate, ζ, at which the equatorial tangential velocity decreases as a function of the polar angle θ. The red line indicates the position of the disk equator.

A first analysis of the molecular emission in the ALMA data of L_2 Pup performed in Chapter 3 [86] has shown that the differential rotation of the equatorial regions of the inner gas disk (within a radius of 6 AU) follows Keplerian rotation. This analysis was primarily based on the ^{29}SiO emission, which has the highest signal-to-noise value of the dataset. The tangential velocities of the inner disk could be used to estimate the central mass of the system, which was found to be 0.66 ± 0.05 $M_\odot$. Beyond this Keplerian region (in the outer disk, i.e. for radii greater than 6 AU) the velocity field sharply transitions to a sub-Keplerian regime, where the radial velocity decrease is proportional to $r^{-0.85}$. The radius at which the tangential velocity transitions from Keplerian to sub-Keplerian seems to correspond to the inner rim of the dust disk, as determined by Kervella et al. (2015) [87], indicating that the dust disk may play an important kinematical role in the steady-state hydrodynamical disk system. Following these findings, we have separated our velocity model into two regimes, the inner disk ($r < 6$AU), and the outer disk ($r > 6$AU).

Inner disk:

The tangential gas speeds follow Keplerian rotation:

$$v_{r_{xy},\text{inner}} = \sqrt{\frac{GM_*}{r_{xy}}}, \tag{4.1}$$

where $r_{xy} = \sqrt{x^2 + y^2}$ is the cylindrical radial distance coordinate, G is the universal gravitational constant and M_* is the mass of the central object.

We have approximated the vertical velocity profile (Fig. 4.4) in the inner disk. We define the polar angle as

$$\theta(x, y, z) = \arccos\left(\frac{z}{\sqrt{x^2 + y^2 + z^2}}\right), \tag{4.2}$$

assuming the coordinates (x, y, z) make up an ortho-normal set of axes, and the equatorial plane of the disk coincides with the (x, y) plane. To reproduce the vertical velocity structure of the inner disk (Fig. 4.4), the equatorial tangential velocity field of the inner disk is multiplied with a factor ζ, expressed as

$$\zeta = (1 - f_1) + \left(\frac{f_1}{e^{s_1(\theta-(\pi-\delta))} + 1}\right) - \left(\frac{f_1}{e^{s_1(\theta-\delta)} + 1}\right), \tag{4.3}$$

where f_1 is the factor by which the velocity drops vertically, s_1 is the slope steepness of the drop, and δ is the polar angle at which the drop occurs. The final model parameters are summarised in Table 4.2. This function ζ is visually represented in Fig. 4.6. We hypothesise as to the physical origin for the ζ function in the Sect. 4.6.1.

Table 4.2: Final model vertical velocity profile parameters for the inner disk.

vertical velocity parameters, inner disk	
Parameter	Value
f_1	0.45
s_1	11
δ	$\pi/3$

Outer disk:

A second (sub-Keplerian) velocity field for the equatorial tangential velocities in the outer gas disk ($r > 6$AU) is also based on the preliminary findings of Chapter 3 [86], and is expressed as

$$v_{r_{xy},\text{outer}} = \sqrt{\frac{GM_*}{6\text{AU}}}\left(\frac{6\text{AU}}{r_{xy}}\right)^{0.85}. \tag{4.4}$$

We have found that introducing an additional vertical velocity profile in the outer disk better reproduces the outer edges at high spatial offsets of the wide-slit PVD in Fig. 4.1. Eq. 4 can thus be improved by multiplication with a factor α, expressed as

$$\alpha = (1 - f_2) + f_2 \exp\left(\frac{-z^2}{2s_2^2}\right). \tag{4.5}$$

In this expression f_2 represents the percentage factor by which the equatorial tangential velocity is reduced, and s_2 is a measure for the rate at which the velocity drops to $(1 - f_2)v_{r_{xy},\text{outer}}$. The parameter values that have been found to best reproduce the emission patterns are found in Table 4.3.

Table 4.3: Final model vertical velocity profile parameters for the outer disk.

vertical velocity parameters, outer disk	
Parameter	Value
f_2	0.1
s_2	1.5AU

The α factor simply reduces the tangential velocities of the regions with high vertical offsets by 10%. The continuous transition from the equatorial tangential velocities to the reduced tangential velocities follows a Gaussian trend, with a characteristic width of 1.5 AU. This means that the tangential velocities are fully reduced to 90% of their equatorial values at a vertical distance of around 3 AU from the equator.

Small-scale random motion:

To determine the velocity field of the small-scale random motion (SSRM) the emission gap around the systemic velocity was used. Assuming the gap to indeed be created by the absorption of the ^{12}CO emission by the cold outer regions of the disk, the width of the gap can be used as a proxy for the SSRM. The emission gap spans a width of $1.7\,\mathrm{km\,s^{-1}}$. Assuming such motions to follow a Gaussian distribution, such a gap thus corresponds to a SSRM standard deviation of $v_{\text{ssrm}} = 0.55\,\mathrm{km\,s^{-1}}$. Because we have no means of probing the SSRM for the regions closer to the star, we assume it to be constant throughout space. However, one can expect the SSRM to increase deeper inside the disk. We discuss this further in Sect. 4.6.1.

4.4.2 H_2 density constraints

The morphology of the disk is properly captured by assuming the following expression:

$$\rho(r_{xy}, \phi, z) = \rho_0 \left(\frac{r_{xy}}{r_c} \right)^p \exp \left[\frac{-z^2}{2H(r_{xy})^2} \right], \tag{4.6}$$

with r_c the inner rim of the gas disk (in the equatorial plane), ρ_0 the H_2 gas density at r_c, p the rate with which the density subsides radially, and $H(r_{xy})$ the Gaussian scale height of the disk, expressed as

$$H(r_{xy}) = H_c \left(\frac{r_{xy}}{r_c} \right)^h, \tag{4.7}$$

where H_c is the initial scale height at the location of the inner rim in the midplane of the disk, and h a measure for the rate at which the scale height increases. The radial distance variable r_{xy} is expressed as the cylindrical radial coordinate $\sqrt{x^2 + y^2}$. This density expression follows from the solution of a thin, vertically isothermal, non self-gravitating disk in hydrostatic equilibrium. Although the data indicate that the density profile is more complex, this simplified expression for the profile is sufficiently accurate for the modelling. We reflect upon this in Sect. 4.6.3.

Table 4.4: The model density parameter values of the final model.

Model density parameters	
Parameter	Value
r_c	2.0 AU
H_c	1.5 AU
h	0.20
ρ_0	9.3×10^{-10} kg/m^3
p	−3.1

In Chapter 3 [86], we have shown that the gas in the inner disk (< 6 AU) is undergoing Keplerian rotation. This allows us to make an estimate of the radius of the inner rim using the largest observed velocities in the disk signal. The data shows the faintest beginnings of a disk signal approximately 17 km s^{-1} away from the central velocity. Assuming a central mass of 0.659 $M_\odot$ (deduced in Chapter 3), this tangential velocity translates to the inner rim of the gas being located at approximately r_c = 2.0AU.

The evolution of the height of the gas disk as a function of radial distance in the disk plane could be readily deduced from the shape of the disk emission in the low-velocity channel maps (Fig. C.1). They show that the disk has a degree of flaring. However, contrary to the archetypal appearance of a flaring disk, the rate of flaring of the disk of L_2 Pup decreases as a function of distance from the central star. This trait is reflected in

the value of the parameter h, which has been determined to be less than unity. Finally, combining the location of the inner rim with the flaring rate, the height of the emission in each channel is best reproduced for an initial scale height of 1.5 AU.

The radial behaviour of the density is captured in the parameters ρ_0 and p. The value of ρ_0 is empirically determined by the iterative efforts targeting the convergence of model versus ^{12}CO data emission values in the innermost regions of the disk. The parameter p determines the rate at which the radial density drops, but cannot be determined from modelling the ^{12}CO emission. This is due to the overall optically thick nature of the disk, which results in a substantial insensitivity of the radiative transfer model to the parameter p. The optically thin ^{13}CO emission permits the evaluation of this parameter p. An extensive exploration of the p parameter space has revealed that the data is best modelled by simply assuming a radial power-law drop characterised by $p = -3.1$.

The final model parameters, which follow from the above mentioned considerations, are listed in Table 4.4.

4.4.3 Disk temperature

Being optically thick at its outer edges, the ^{12}CO disk must also be optically thick in its more inner regions. Thus, the ^{12}CO emission patterns are mainly produced on the surface boundary confining the gas emitting at a certain frequency, along the line of sight. The emission produced by the bulk of the gas lies hidden behind this surface. Therefore, the ^{12}CO emission probes the temperature of the gas in this surface layer very accurately, and is mostly insensitive to the distribution of mass. Hence, because of the extremely high spectral resolution of the data, these surfaces are only spatially separated by a small distance, and the temperature can therefore be accurately and sufficiently sampled all throughout the disk, permitting the full temperature profile to be precisely determined from the ^{12}CO emission.

Radial profile:

As seen in Fig. C.1, the ^{12}CO emission close to the central star is brightest, indicating relatively high gas temperatures. The emission drops substantially within the first hundred mas, after which it drops much slower, suddenly plummeting as the outer edge of the emission is reached. This suggests a 3-staged temperature profile.

Analytically, the temperature profile producing the final model model is expressed as

$$T(r) = (T_{\rm z} - T_{\rm p}) \exp\left(-\frac{r_{\rm xy}^2}{2w_1^2}\right) - \left(\frac{T_{\rm p}}{\pi}\right) \arctan\left(\frac{r-D}{w_2} - \frac{\pi}{2}\right), \tag{4.8}$$

where T_z is the temperature at the inner rim of the disk, T_p is the temperature of the plateau, w_1 is a measurement for the rate of the first temperature decrease, D is the distance at which the second major drop in temperature is located, and w_2 is a measure for the rate of the second temperature drop. Table 4.5 lists the parameter values that have been found to produce the best fit of the data. The temperature profile is shown in logarithmic scales in Fig. 4.7. We wish to point out here that the temperature levels-off to a near-constant value of 500 K at a distance of approximately 6 AU, which corresponds with the inner rim of the dust disk observed by Kervella et al. (2015) [87]. This indicates that the dust disk plays an important thermodynamical role in the disk system. The temperature profile of the inner walls of the gas disk (facing the direct radiation of the stellar photosphere) have been determined to be around 2500 K. We discuss this further in Sect. 4.6.2.

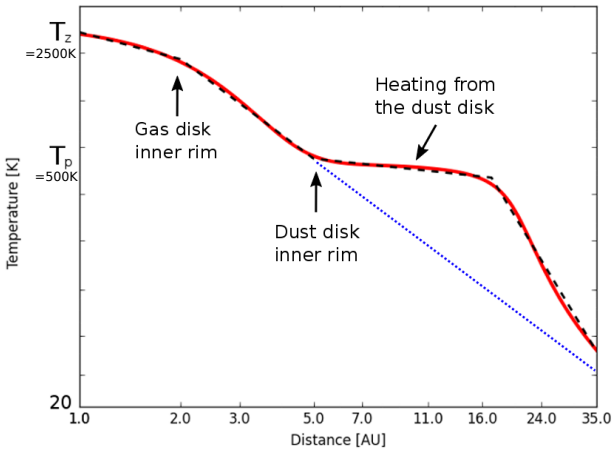

Figure 4.7: Logarithmic plot of the radial temperature profile used to model the ^{12}CO disk surrounding L_2 Pup, as a function of distance from the central star. The red line represents the continuous expression. The black dotted line is the closest approximation of the red curve by a set of subsequent power-laws. The blue dotted line continues the temperature trend of the gas, devoid of dust. The temperature parameter values, and the slopes of the power laws are listed in Table 4.5.

The obtained radial temperature expression can also be approximated by a sequence of power-laws, expressed as $T(r) = T_i(r/r_i)^{\epsilon}$. Here, T_i stands for the temperature at distance r_i, and ϵ is the slope of the power-law. Table 4.5 lists the power-law sequence that best fits the continuous model (shown as the black dotted lines in Fig. 4.7).

Vertical profile:

The high angular resolution of the data allows the identification of some structural complexity in the inner disk. As discussed in Sect. 4.3.2, the channel maps seem to exhibit two patches of increased emission in the inner disk, both on the blue and on the red-shifted side. We have interpreted this signal as the local heating of the walls of the inner disk facing the central star. We modelled this feature as follows:

$$T_{\rm z} = T_{\rm w} - (T_{\rm w} - T_{\rm eq}) \exp\left(\frac{-z^2}{2\sigma_T^2}\right), \tag{4.9}$$

where $T_{\rm w}$ is the temperature of the star-facing disk wall, $T_{\rm eq}$ is the temperature of the equatorial disk plane, and σ_T is the Gaussian one-sigma size of the cool equatorial disk plane. In order to reproduce the correct vertical emission contrast in the inner disk we need the temperature of the central disk plane to be approximately at a temperature of 1000 K. Table 4.5 lists the parameters that have been found to best fit the data.

Table 4.5: The final model model temperature parameter values of the temperature structure.

Radial temp. parameters	
Parameter	Value
$T_{\rm z}$	2500 K
T_p	500.0 K
w_1	1.8 AU
D	20.0 AU
w_2	4.0 AU
Radial temp. power laws	
Zone	Power ϵ
$r \leq 2$ AU	−0.5
2 AU $< r \leq 6$ AU	−1.4
6 AU $< r \leq 17$ AU	−0.2
17 AU $< r$	−2.9
Vertical temp. parameters	
Parameter	Value
$T_{\rm w}$	2500K
$T_{\rm eq}$	1000K
σ_T	0.75AU

4.4.4 ^{12}CO and ^{13}CO molecular abundance

As stated before, molecular abundance and absolute density are degenerate. We have opted not to express the ^{12}CO abundance as a function of the spatial coordinates, but rather as a constant value. No studies which explicitly focus on the molecular abundance of ^{12}CO in L_2 Pup have been found in the literature. Additionally, the handful of studies describing the general parameters of disks around evolved stars indicate the ^{12}CO abundance to be around 10^{-4} [21, 20]. Studies of ^{12}CO abundance values inside protoplanetary disks around young stars also seem to reproduce this value [57]. In addition, due to its high binding energy, carbon monoxide is generally quite chemically unreactive [61].

We have thus chosen to set the $^{12}CO/H_2$ ratio to the constant value of 10^{-4} for this model, a value which lies within the reasonable range of expected ^{12}CO abundance values for AGB stars [40, 36].

Using the values for the physical properties of the inner rim determined from the ^{12}CO analysis as boundary condition, the determination of the ^{13}CO abundance is easily performed. The ^{13}CO molecular abundance has been iteratively adapted until the emission of the inner rim of the ^{13}CO model matched the data. This has resulted in an abundance estimate of 10^{-5}, resulting in a ^{12}CO over ^{13}CO abundance of 10.

4.5 Radiative transfer results

The internal temperature and velocity structure of the disk around L_2 Pup is visually represented by the schematic diagram shown in Fig. 4.8. This physical set-up is propagated through the RT code `LIME`, which produces velocity-dependent maps of intrinsic line emission from the species in question. The `CASA` observation simulation scripts transform the intrinsic maps, by introducing observational and instrumental effects, so they can be compared one-to-one with the ALMA data. We have simulated the observables for an almost edge-on appearance of the disk, at an inclination of 82 degrees. The channel maps of the resulting emission patterns, as well as the data channel maps can be found in Appendix C.

These predicted channel maps are represented visually in Figs. C.2 and C.4. Here one can see that the overall morphology and general features present in the ALMA data have been well reproduced. One must keep in mind that all emission in the ALMA data that is smooth on scales greater than 250 mas has been insufficiently sampled in UV-space, generating the (seemingly) randomly scattered emission patches, most strongly present around zero velocity in the ^{12}CO maps. The bulk of this emission probably makes no part of the disk-system, and it is therefore not present in the model data.

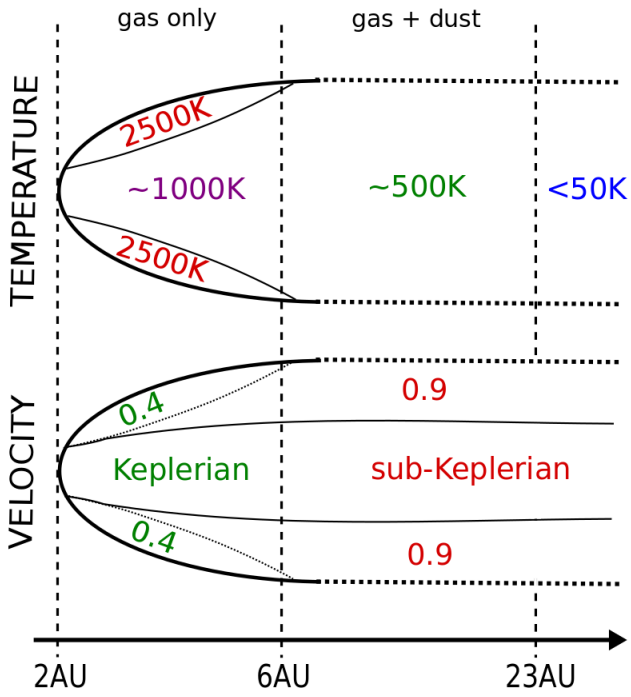

Figure 4.8: Schematic representation of the inner disk velocity and temperature structure, as deduced from the radiative transfer modelling. The global and internal features are not to scale. In the velocity diagram, the numerical values correspond to the multiplication factor with which the equatorial speeds are multiplied to obtain the lowest measured velocities in the regions with high vertical offsets. The colour coding makes the distinction between the inner disk (r < 6 AU) and the outer disk (r > 6 AU). The radial density structure is not represented here, it is simply characterised by a power-law with slope −3.1.

It is quite difficult to compare the model and data channel maps one-to-one. We hence focus the rest of the comparative discussion on the PVDs, which are shown in Figs. 4.9, 4.10 and 4.11. Fig. 4.9 nicely illustrates the quality of the ^{12}CO model along zero spatial offset, which corresponds to the disk midplane. All major and minor features present in the data have been reproduced. We have succeeded in replicating the edges of the emission signal in velocity space, the absolute velocity magnitude of the offset peaks, the width (in velocity space) of the emission gap around the central velocity and the internal emission distribution of the PVD. The curvature of the signal, which characterises how the outer edge of the disk emission varies as a function of velocity has also been properly modelled. Also the absolute emission values have been accurately reproduced. The major difference is found when comparing the signal near the velocities closest to $v_{\rm sys}$. The outer regions of the disk are probably quite turbulent on different length-scales, causing the offset of the lowest velocity regions to decline in a more irregular fashion compared to the analytical model.

The limitations of the model becomes fully apparent in the full disk-width slit PVDs, shown in Fig. 4.10, where important discrepancies between data and model appear. The absolute level of emission around zero spatial offset is slightly overestimated by the model. This is probably caused by the introduction of a vertical temperature dependence to model the temperature difference between the walls of the disk and its equatorial regions. The model most probably overestimates the size of the hottest regions, contributing to the overestimated average emission around zero offset. There is also an emission distribution asymmetry between the east and the west wings of the data, which is of unknown origin, but can perhaps be attributed to the presence of binary companion, as suggested to be possibly present based on iderect evidence presented in Chapter 3 [86]. Close to the central velocities one can clearly identify emission in the data that is not present in the model. We believe this emission to originate completely from the poorly reconstructed large-scale emission, observed by the (poorly covered) shortest baselines of the configuration.

The final PVD comparison we consider is the full disk-width slit PVD of the ^{13}CO data, shown in Fig. 4.11. We do not focus on the narrow-slit PVD of the ^{13}CO emission as it is virtually identical to the discussion on the ^{12}CO narrow-slit diagram. The emission distribution of the wide-slit PVD has been well reproduced by the model, and so has the absolute level of the emission. However, a clear difference is seen in the extent and location of the maximum spatial offset peaks. The peaks of the model are very pointy and long, and are not as widely separated in velocity space as the offset peaks in the data. We believe this difference can be attributed to photodissociation effects, which could affect the outermost regions of the ^{13}CO disk. Accounting for this effect could thus seriously reduce the maximal spatial extent of the offset peaks in the model PVD. In addition, the location of the peaks in velocity space would then also shift to higher projected velocities.

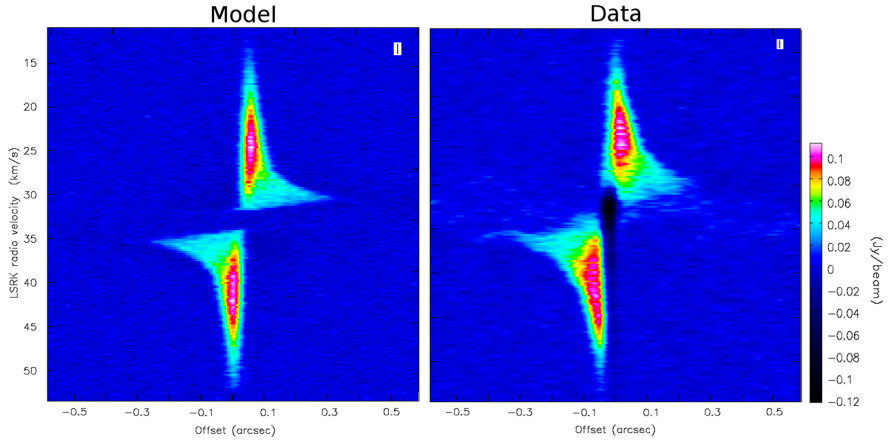

Figure 4.9: Comparison of the ^{12}CO PVD constructed by taking a slit along the disk with a minimal width of 15 mas. The left panel shows the PVD of the radiative transfer model, the right panel shows the PVD of the data. $v_{\rm sys} = 33.3\,{\rm km\,s^{-1}}$.

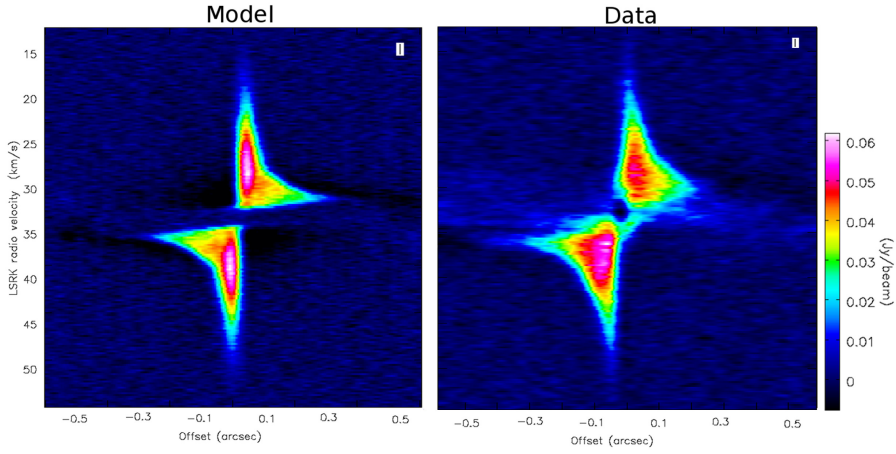

Figure 4.10: Comparison of the ^{12}CO PVD constructed by taking a slit along the disk with a width equal to the with of the disk in the data, being 280 mas. The left panel shows the PVD of the radiative transfer model, the right panel shows the PVD of the data. $v_{\rm sys} = 33.3\,{\rm km\,s^{-1}}$.

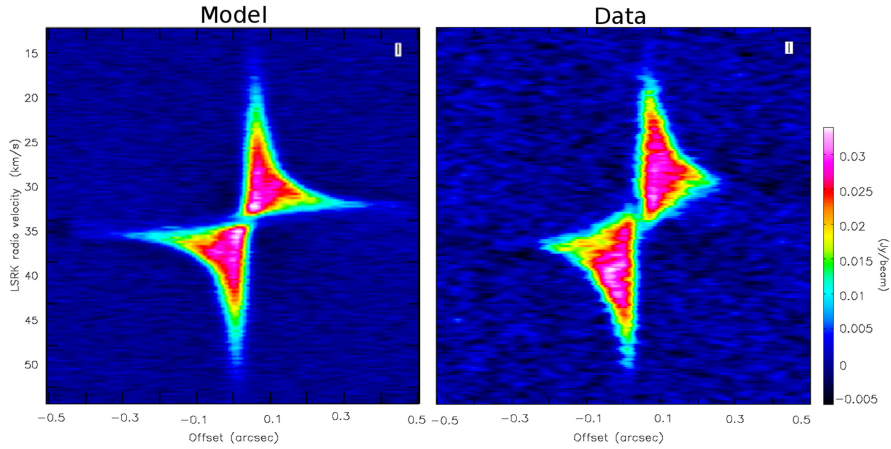

Figure 4.11: Comparison of the ^{13}CO PVD constructed by taking a slit along the disk with a width equal to the with of the disk in the data, being 190 mas. The left panel shows the PVD of the radiative transfer model, the right panel shows the PVD of the data. $v_{\rm sys} = 33.3\,{\rm km\,s^{-1}}$.

4.6 Discussion

4.6.1 Parameter sensitivity

Because we cannot perform an extensive and in-depth exploration of the parameter space available to us (see Sect. 4.3.3), we cannot quantify the quality of the model in terms of statistically significant errors. Hence, we dedicate this section to a discussion of the uncertainties in the estimated parameter values.

The kinematical properties of the disk can be directly measured from the data. We are thus confident that both the equatorial and the vertical velocity profile are accurately constrained, and the parameter values that have directly been deduced from the velocity field can be trusted. Furthermore, the geometrical properties of the system can also be directly extracted from the data. We do not expect major uncertainties here either.

Carbon monoxide has a very low electric dipole moment causing the density, temperature, and molecular fractional abundance (DTA) parameters to be completely degenerate (see Sect. 2.5.1). Fortunately, the modelled data consisted of both optically thick and thin emission. In case of the optically thin ^{13}CO lines, one cannot pin down the exact combination of temperature and density properties of the disk, and the abundance of this molecule. In case of the optically thick ^{12}CO lines the degeneracy of temperature and density profile is mostly lifted, and the temperature profile can be

determined. However, the assumed value for the ^{12}CO molecular abundance remains an uncertainty. The adopted value, from reasonable and justifiable arguments, will directly and linearly affect the disk density. For example, an increase in the molecular abundance by a factor 2 should result in a decrease in density by the same factor. Hence, the largest impact will be on the determined value for ρ_0. But, as argued in Sect. 4.4.4, we do not expect the true abundance fraction to deviate substantially from the assumed one. The radial density power law should not be affected by the abundance estimate, as it is mostly dependent on the assumed temperature profile.

The optical thickness of the ^{12}CO emission, and the high spectral resolution of the data, has permitted us to very accurately constrain the equatorial temperature profile. And assuming the adopted ^{12}CO abundance fraction is correct, then the retrieved equatorial density parameters and ^{13}CO abundance value are also very tightly constrained. However, where the ^{12}CO emission becomes optically thin, the subsequently constrained parameter values likely have much larger uncertainties. In the inner disk, the low density regions of high vertical offset are cut off by the shearing of the stellar outflow. Here the ^{12}CO emission does not become optically thin, and the free parameters are thus expected to be tightly constrained. At the top and bottom edges of the outer disk, the ^{12}CO emission definitely turns optically thin. This locally reinstates the full DTA degeneracy, therefore breaking down the assumption that the temperature can be directly measured from the emission. However, the regions in question are small compared to the full disk size. Thus, increased local uncertainties on the derived parameter values will probably not affect the final result by too great an amount.

4.6.2 Velocity field

Sub-Keplerian regime of the outer disk

The sub-Keplerian regime of the disk has a power law dependence of the tangential velocity that is proportional to $r^{-0.85}$ (see Chapter 3). This suggests the presence of a mechanism that slows down the gas, and whose effectiveness increases with radius. One explanation for such a deviation from Keplerian rotation is a radial force imbalance. However, in this scenario the sub-Keplerian nature of the outer disk should result in the appearance of an inward motion of the gravitationally attracted material. Such an inward velocity component has not been detected in the emission (see Chapter 2 [71] for an overview of the expected emission patterns caused by such an additional inward velocity component). This means that either the projected inward velocity component is negligably small compared to the spectral resolution, or that there exists a mechanism which generates an additional outward force that balances the gravitational pull, yet increases in strength with distance. A possible origin for such a force would be the radial stratification of dust grain sizes within the disk [178]. Such a dependence, with larger grains closer to the star, can produce a radial radiation pressure profile able to

alter the effective gravity felt by the dust grains throughout the disk (science being currently undertaken). Assuming a tight mechanical coupling between the dust and the gas, this scenario should then act as a cumulative reduction of the effective gravity felt by the surrounding gas, as a function of radial distance.

The vertical velocity profile of the inner disk: the ζ and α functions.

We hypothesise that the ζ profile (Fig. 4.6), detailing the vertical distribution of tangential velocities in the inner disk, originates from hydrodynamical boundary instabilities at the disk/radial outflow interface. Media subjected to velocity shear will develop Kelvin-Helmholtz instabilities (KHI) [60], which destroy any original organised velocity field, causing turbulent features of high complexity to arise. For a physical set-up like the inner disk of L_2 Pup, the time scale for KHI to arise is of the order of years [60]. Left to operate for a long time (about $10^3\times$ KHI time scale), the unstable regions of the system will converge to a maximum entropy state via mixing. For the L_2 Pup system this would be of the order of thousands of years, which is much shorter than the AGB lifetime. The resulting velocity field inside this mixed region is an averaged distribution over all velocities that were part of the interaction. Thus, a radial outflow (with no tangential velocity component) shearing against a rotating gas disk will create KHI, which average out to an effective decreased rotation speed. Similarly, one can expect a small radial velocity component to be present in this 'boundary region'. However, because the radial component would be small, and because of the orientation of the radial field with respect to the observer, the effect would potentially only be visible in the channel maps close to central velocity. The emission in these channel maps is hidden behind the optically thick, cold outer disk edge. Thus, we are unable to confirm the presence of this small radial velocity component in the regions with a high vertical offset of the inner disk.

The origins of the α profile, that modifies the vertical profile of the rotational velocity in the outer disk, can be attributed to the same effect. However, because the relative velocities between the disk and the outflow are smaller in the outer disk compared to the inner disk, the magnitude of the effect will be reduced.

Velocity field of the small-scale random motion

We have derived the magnitude of $v_{\rm ssrm}$ from the (lack of) spectral signatures of the gas located in the outermost regions of the disk. We do not possess a complete description of how one can expect the SSRM of a medium to depend on the physical properties of that medium. Therefore, in order to limit the number of assumptions made, we have approximated it as constant throughout the disk. However, this assumption is rather

unlikely. The rms thermal speed of molecules at a certain temperature is given by

$$v_{\mathrm{th,rms}} = \sqrt{\frac{3k_B T}{m}}, \tag{4.10}$$

where k_B is the Boltzmann constant, T is the temperature of the gas, and m is the molecular weight. The rms thermal speed reaches values up to $1.5\,\mathrm{km\,s^{-1}}$ for CO molecules at 2500 K, which is significantly greater than the $v_{\mathrm{ssrm}} = 0.5\,\mathrm{km\,s^{-1}}$ value used in this paper. In addition, as can be inferred from Fig. 4.12, the thermal velocity in the cool outer regions only makes up about 50% of the deduced SSRM. This is a strong indication that the small-scale velocity in the disk consists of additional components besides the thermal rms speed, and that our assumed v_{ssrm} probably underestimates its true physical value inside the disk.

4.6.3 Temperature structure

Vertical temperature profile of the inner disk

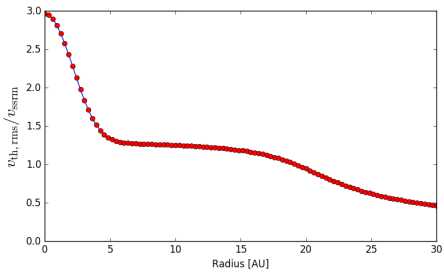

Figure 4.12: Rms thermal velocity (as derived from the temperature profile) relative to the assumed turbulent velocity, as a function of radius.

The modelling strongly suggests the requirement of a vertical temperature profile describing the extent by which the inner disk walls facing the direct stellar radiation field are heated. The maximum temperature of the gas in these regions has been determined to be approximately 2500 K. This can be readily explained by thermal coupling of the gas with the stellar radiation field. The disk walls directly facing the stellar radiation heat up to high temperatures, while shielding the equatorial regions of the disk, keeping them at cooler temperatures.

Radial temperature profile

The shape of the radial temperature profile (Fig. 4.7) strikes as rather peculiar. However, the regime transition between the inner disk and the outer disk seems to strongly indicate that the presence of dust plays an important thermodynamical role. We hypothesise the following explanation. In the inner disk, the temperature profile is simply set by the dissipation of heat, provided by the photospheric resonance photons. From 6

AU onward, dust is prominently present in the disk. Thus, from this radius outward there exists substantial increase in sensitivity to the photospheric continuum emission. Assuming a tight mechanical coupling between the dust and the gas (which the velocity profile suggests), the dust provides a continuous source of heat from inside the disk. This lessens the radial rate of temperature decrease, and acts as a thermal buffer. This happens for as long as there exists interaction between the stellar radiation field and the dust. However, finally, at a specific radius one can expect the dust to become fully optically thick (radially), prohibiting the further propagation of energy via photospheric continuum photons, causing a final temperature drop at large radii.

4.6.4 Density structure

Disk mass

From the density structure of the disk we may calculate its mass. Integrating over an infinite volume the mass of the disk is found to be approximately $2.2 \times 10^{-4}\,M_\odot$, or about 0.23 Jupiter masses. We have analysed the sensitivity of this value to the determined density parameters. Assuming each parameter would have its true physical value between plus and minus 25% of the determined value, then the disk mass would lie between $0.65 \times 10^{-4}\,M_\odot$ and $9.7 \times 10^{-4}\,M_\odot$. The determined disk mass is most sensitive to the exponent of the radial power law. If we assume the same spread on the parameter values as before, but now keep the radial power fixed, the spread on the disk mass diminishes significantly. It would lie between $1.15 \times 10^{-4}\,M_\odot$ and $3.4 \times 10^{-4}\,M_\odot$. These values are in agreement with the estimates of Kervella et al. (2014,2015) [88, 87].

Density profile

As stated in Sect. 4.4.3, the density description is conform with the solution of a thin, vertically isothermal, non-self-gravitating disk in hydrostatic equilibrium. Although on first sight the disk does not seem to be congruent with these assumptions, a deeper consideration of the deduced disk physics can prove otherwise. The channel maps (Figs. C.1 and C.3) exhibit a rather broad disk, with a height of around 300 mas. We find that the observations are well-fitted by a disc with a Gaussian scale height (Sect. 4.4.3), which means that the bulk of the disk is in fact located in a thinner slab around the equator. Around 75% of the total disk material is located in a 5 AU (78 mas) wide slab. The mass of the disk is approximately 1.5% of the central mass, making its self-gravity negligible with respect to the primary gravitational source. The largest part of the disk has been found to be vertically isothermal. Only in the star-facing wall of the inner disk has this property been found to break down. The resultant features, however, are only present in the thin interaction region at the disk-outflow interface. The effect of

this local heating on the overall thermal disk structure is negligible. In fact, this vertical temperature profile of the inner disk could be the cause for the $h = 0.2$ radial scale height growth to be lower than expected (< 1). As for vertical hydrostatic equilibrium (VHE), this is very difficult to deduce from the observations. One can only assume that, if the disk is indeed a stable structure present around the AGB star, then VHE must be satisfied. It therefore seems that the assumptions contained within the analytical density description may very well be satisfied.

The value $p = -3.1$, which characterises the slope of the radial density power law, seems very steep compared to the typical slopes presented in the literature. Typical density slope values for disks around post-AGB stars and planetary nebulae are of the order of $p = -2.0$ [20, 23, 22]. Protoplanetary disks seem to possess even flatter profiles, with $-2.0 \leq p \leq -1.0$ [65, 211, 152, 98]. Rings of asteroids in dynamic resonance with a planet, like the asteroid belt of our Solar System, have an even lower value of $p \sim -0.1$ [161].

4.6.5 Evolutionary considerations

Disk origin

The scenario that the disk is a remnant from an earlier evolutionary phase is improbable as proto-planetary disks disperse fairly early on in the main sequence phase [97]. Therefore, the disk must have been formed during the later evolutionary stages of the star. A scenario for a recent formation of a disk may be that of a latitude dependent mass loss in the AGB phase. However, it seems highly unlikely that such a mechanism produces a disk system that is as vertically compact as observed here. Moreover, it needs a mechanism to prevent the material escaping from the system.

One of the most plausible scenarios for the formation of an equatorial density enhancement in the CSE of an AGB star is by means of a binary companion [179, 172, 119, 92, 135]. Such a companion funnels part of the wind material in its gravitational field, expelling it as a compact stream along the orbital plane. Kervella et al. (2014,2015,2016) [88, 87, 86] have suggested the presence of a binary companion around L_2 Pup, based on precise measurements of continuum asymmetries. The fact that the inner rim of the gas disk (determined in this work) coincides with the location of the observed candidate companion of L_2 Pup in literature supports this hypothesis.

The presence of a binary companion is also supported by angular momentum considerations. From the density distribution and velocity structure we calculate the total angular momentum contained within the gas disk to be

$$L_{\rm tot} = 3.1 \times 10^{42}\ {\rm m^2 kg/s}. \tag{4.11}$$

A first analysis in Chapter 3 [86] suggests that the star L_2 Pup had an initial mass comparable to the mass of the Sun. Recent work has shown the Sun to contain approximately 10^{41} m^2kg/s of angular momentum [75]. In addition, recent astroseismologic analyses of light curves of solar-type stars indicate only minor differences in internal rotation structure [14, 167]. Thus, making the assumption that the total angular momentum of L_2 Pup on the main sequence was comparable to that of the Sun, we find that the disk around L_2 Pup contains approximately 30 times the total amount of available angular momentum inside the star. The presence of a binary companion could easily explain this angular momentum discrepancy. By assuming the companion follows Keplerian rotation, and by assuming an angular momentum transfer efficiency of 30% [142, 143] from the companion to its surroundings, the total angular momentum in the disk could be explained by the presence of a 1 Jupiter mass companion. Extending the 'sensitivity analysis' on the mass of the disk to this discussion (assuming the same uncertainty range of the determined density parameters, and assuming zero uncertainty on the velocity field), the mass of the companion could be expected to lie within the 0.25 to 5.5 Jupiter mass range. This estimation is in agreement with the companion's mass range proposed in Chapter 3 [86]. These estimates are lower limits, as one can expect a portion of the main-sequence angular momentum to have been lost in the stellar wind during previous evolutionary stages.

In Chapter 3 [86], we discuss the likelihood for the candidate planet to have formed inside the disk. After all, the disk does contain enough material to build one or more planets. However, as an additional consideration, Pelupessy et al. (2013) [151] argue that the formation of planets inside evolved disks is rather unlikely. Time scale considerations seem to support this. Miller et al. (2016) [133] claim that thermally pulsing AGB lifetimes are typically less than one Myr, while typical planet formation timescales are orders of magnitude larger [3, 73, 2]. In addition, at present no mechanism can explain the presence and formation of differentially rotating disks around evolved stars, besides binarity. Therefore, the planetary binary companion should probably have been present around the star before the onset of the AGB.

Assuming the candidate companion has been accompanying the star throughout its life, the disk could be either made up of mainly AGB wind material, or contain a substantial portion of evaporated planet material. The evolution of the star to the giant phase will have substantially heated the planet, possibly even causing evaporation and outgassing. Using our determined ^{12}CO over ^{13}CO ratio as a proxy for the ^{12}C / ^{13}C abundance fraction, we find the first scenario more probable. A ^{12}C over ^{13}C ratio of 10 (see Sect. 4.4.4) is typical of oxygen-rich AGB gas. In comparison with typical values in our Sun and solar neighbourhood [9, 100] we would expect a ratio that is an order of magnitude higher were the disk made of substantial amounts of material from planetary origins. This also supports the findings in Chapter 3, where the spectral signatures at the candidate companion location seem to indicate that it is accreting material via wind Roche lobe overflow.

Further evolution

Pelupessy et al. (2013) [151] argue that the formation of planets inside evolved disks is unlikely. Only a very narrow combination of physical parameters permit planet formation. The physical properties of the disk of L_2 Pup lie well outside this range. Although no new planets will be formed in the disk, the question remains whether the ones present can survive. The discovery of planets around a subdwarf-B star [169] shows that planets have survived the tumultuous giant phase. In addition, De Marco et al. (2015) [38] deduce that some PN in the *Kepler* spacecraft field of view may also contain orbiting planets. Evidence thus strongly suggests that planets can persist the final stages, and influence the circumstellar morphology up to the white-dwarf stage.

Detailed studies of post-AGB morphologies [22] show a vast difference in length scale compared to the L_2 Pup system, with disks ranging up to 1000 AU. In addition, their internal density structure is vastly different from the $p = -3.1$ slope found in this work (Sect. 4.6.3). Not many objects have been studied to a high degree of detail so it is difficult to gauge the significance of the difference between the evolutionary stages. We hypothesise nonetheless, and discuss a few scenarios which could explain the difference.

We speculate that the substantial difference in density distribution may be a consequence of the mass-loss rate of the central star. Low mass-loss rate AGB stars do not provide much material for the planet to interact with. This can be expected to result in a compact and low-density disk, with a steep density slope. High mass loss rates would pump more material into the interaction zone, causing wider and denser disks with flatter density slopes. However, as AGB stars evolve towards the post-AGB phase, it is believed that the mass loss rate increases. If the circumstellar disk is not dense and massive enough to fully counter weigh this increased outward force, the disk will be pushed outwards, slowing down its rotation substantially. This could explain the presence of the giant non-rotating tori observed around many post-AGB stars and planetary nebulae [170, 163, 162, 101]. The rotating disks massive enough to survive this 'super wind' phase remain as such [66, 67].

The scale differences between AGB and post-AGB disks could also be explained by morphological constraints. As the star transitions to the AGB, equatorial wind material gets injected into a rotating disk by interaction with an orbiting planet. As more material accumulates, the disk becomes denser. At a certain point in time the density of the disk would reach a point where it would substantially obstruct the movement of the AGB wind along the equator. This would be the current stage of the L_2 Pup system, as there is a clear lack of radial gas flow inside the disk. The outflow material left unchanneled by the potential companion would therefore be forced towards the polar directions (along the path of least resistance), forming a wide bipolar outflow. Akashi et al. (2008) [1] suggest a mechanism via which the disk can accumulate mass expelled

by this outflow, which would cause the disk to grow, and the density slope to flatten.

In any case, the study of the CSE of L_2 Pup strongly suggests that the presence of low mass (planetary) companions may play a vital role in the shaping of the CSE of the AGB star, whose properties dictate the further morphological evolution of the system.

4.7 Summary

The circumstellar environment of L_2 Pup has been imaged by ALMA at 15×18 mas resolution. The ^{12}CO J =3−2 and ^{13}CO J =3−2 emission show a rotating gas disk, in a nearly edge-on orientation. Using the radiative transfer code `LIME` and the `CASA` post-processing tools we have constrained the physical properties of the disk:

- The radial temperature of the disk is characterised by three major regimes. The temperature of the inner disk (< 6AU) is described by a steep drop from around 1000 K to around 500 K. Beyond this radius the temperature levels-off at around 500 K, but drops again steeply to very cold temperatures (< 100 K) at the outer edge of the disk (23 AU). Vertically the temperature of the inner disk is stratified, with cooler (1000 K) equatorial regions and rather hot inner disk walls (2500 K). We attribute this temperature stratification to complex hydrodynamical interactions at the outflow-disk boundary, which will mix dust formed at larger radii back into the innermost regions of the disk.

- The density of the disk is well described by the solution for a thin, vertically isothermal, non-self-gravitating disk in hydrostatic equilibrium. Its radial decay is expressed by a power law, with a power of -3.1. The flaring rate of the inner disk is quantified by a power of 0.2. Its inner rim is located at around 2 AU, which coincides with the location of the candidate binary companion detected in Chapter 3. This inner rim has a height of approximately 1.5 AU, indicating that it may be puffed-up.

- The equatorial velocity has been determined in Chapter 3 [86], showing a sharp transition from Keplerian to sub-Keplerian at a radius of 6 AU. However, there is also an important vertical dependence, which reduces the expected Keplerian velocities of the inner disk gas to approximately 40% of its expected tangential velocity at high vertical offsets. The Gaussian turbulent velocity field component has been deduced to be 0.5 $\mathrm{km\,s^{-1}}$.

- The molecular abundance of ^{12}CO has been assumed to be 10^{-4}. The molecular abundance of ^{13}CO has been deduced to be 10^{-5}, resulting in a ^{12}CO over ^{13}CO abundance ratio of 10. This is in line with values of other oxygen-rich AGB stars

in the literature. This suggests that the bulk of the gas in the disk originates from the star itself.

- The dust in the outer disk (r > 6 AU) seems to play a pivotal role in the thermodynamical and kinematical structure of the disk.

- Constraining the density profile permitted us to deduce the mass of the disk, which has been found to be approximately 2×10^{-4} $M_\odot$. The angular momentum in the disk has been found to be over 30 times the expected angular momentum contained within the star L_2 Pup. We calculate that a binary companion of ~1 Jupiter mass would be sufficient to explain the angular momentum contained in the disk.

Chapter 5

Simplified models of embedded spiral morphologies for interpreting high-resolution data.

(2015A&A...579A.118H)

Ward Homan[1], Leen Decin[1], Alex de Koter[1,2], Allard-Jan Van Marle[1], Robin Lombaert[1], and Wouter Vlemmings[3]

[1] Institute of Astronomy, KU Leuven, Celestijnenlaan 200D B2401, 3001 Leuven, Belgium
[2] Sterrenkundig Instituut 'Anton Pannekoek', Science Park 904, 1098 XH Amsterdam, The Netherlands
[3] Chalmers University of Technology, Onsala Space Observatory, SE-439 92 Onsala, Sweden

Abstract: *Recent high-resolution observations have shown that stellar winds harbour complexities that strongly deviate from spherical symmetry, which generally is assumed as standard wind model. One such morphology is the Archimedean spiral, which is generally believed to be formed by binary interactions, as has been directly observed in multiple sources. We seek to investigate the manifestation in the observables of spiral structures embedded in the spherical outflows of cool stars. We aim to provide an intuitive bedrock with which upcoming ALMA data can be compared and interpreted. By means of an extended parameter study, we modelled rotational CO emission from the stellar outflow of asymptotic giant branch stars. To this end, we developed a simplified analytical parametrised description of a 3D spiral structure. This model is embedded into a spherical wind and fed into the 3D radiative transfer code* `LIME`*, which produces 3D intensity maps throughout velocity space. Subsequently, we investigated the spectral signature of rotational transitions of CO in the models, as well as the spatial aspect of this emission by means of wide-slit position-velocity (PV) diagrams. Additionally, we quantified the potential for misinterpreting the 3D data in a 1D context. Finally, we simulated ALMA observations to explore the effect of interfrometric noise and artefacts on the emission signatures. The spectral signatures of the CO rotational transition v=0 J=3-2 are very efficient at concealing the dual nature of the outflow. Only a select few parameter combinations allow for the spectral lines to disclose the presence of the spiral structure. If the spiral cannot be distinguished from the spherical signal, this might result in an incorrect interpretation in a 1D context. Consequently, erroneous mass-loss rates would be calculated. The magnitude of these errors is mainly confined to a factor of a few, but in extreme cases can exceed an order of magnitude. CO transitions of different rotationally excited levels show a characteristical evolution in their line shape that can be brought about by an embedded spiral structre. However, if spatial information on the source is also available, the use of wide-slit PV diagrams systematically expose the embedded spiral. The PV diagrams also readily provide most of the geometrical and physical properties of the spiral-harbouring wind. Simulations of ALMA observations prove that the choice of antenna configuration is strongly dependent on the geometrical properties of the spiral. We conclude that exploratory endeavours should observe the object of interest with a range of different maximum-baseline configurations.*

Contribution to the article: *All scientific work discussed below, as well as the composition of the article was carried out solitarily, with the exception of regular consulatation with my supervisors and the other co-autors.*

5.1 Introduction

In this chapter we attempt to broaden our understanding of embedded stellar wind morphologies by developing simplified mathematical models of stellar wind structures. Here, we focus on the spiral structure, for which very convincing direct evidence [122, 114], and theoretical background exists [179, 172, 119, 92, 135]. We make no assumptions on the spiral formation mechanism. Instead, we assume its presence, and show how these structures are manifested in the observables by means of 3D radiative transfer calculations. The stellar wind properties are described analytically, and its emission is modelled with `LIME`, a fully three-dimensional non-local-thermodynamical-equilibrium (NLTE) radiative transfer code [19]. Arguably, an exclusively analytical description of the stellar wind properties might not be very physically consistent. However, this approach allows us to calculate a considerable grid of models, which at the present time would be virtually impossible to achieve via consistent radiative-hydrodynamical calculations. We present the results both in spectral form, exhibiting the manifestation of the spiral structure in the molecular emission lines, and in spatial form, providing a reference for high spatial resolution data from telescopes like *ALMA*.

This chapter is organised as follows: In Sect. 5.2 we describe the mathematical structure of the used analytical expression in detail, followed by the computational tools which have been used to produce the results. In Sect. 5.3 we give an overview of the explored parameter space, and of the assumptions we have made in this paper. Section 5.4 presents the results of the radiative transfer, both in spectral and in spatial format. Finally, in Sect. 5.5, we make an effort to relate the emission to intrinsic geometrical properties, and we show the effect of ALMA antenna configurations on the characteristics of the intrinsic emission.

5.2 Numerical procedure

5.2.1 Spiral geometrical model

The following mathematical descriptions are formulated in the spherical coordinate system,

$$r = \sqrt{x^2 + y^2 + z^2} \tag{5.1}$$

$$\theta = \arccos\left(\frac{z}{r}\right) \tag{5.2}$$

$$\phi = \arctan\left(\frac{y}{x}\right), \tag{5.3}$$

representing radial, azimuthal and equatorial distance respectively. The Archimedean spiral is the solution of the equation $r = b\phi$, and is characterised by a constant distance ($d = 2\pi b$) between consecutive turnings. The analytical properties of the assumed spiral model are described by a Gaussian distribution, such that sharp cut-offs of the wind properties described by this geometrical pattern are avoided. In dimensionless units this distribution is given by

$$S(r,\theta,\phi) = \exp\left[-\frac{(r - r_0(r,\theta,\phi))^2}{2\sigma_r(r,\theta,\phi)^2} - \frac{(\theta - \theta_0(r,\theta,\phi))^2}{2\sigma_\theta(r,\theta,\phi)^2}\right], \tag{5.4}$$

where σ_r and σ_θ are Gaussian widths in radial and azimuthal space. In the following subsections, we describe the specific geometrical properties of this model both radially and azimuthally, and provide an in-depth explanation of the functional parameters present in Eq. 5.4. The connection between $S(r,\theta,\phi)$ and the distributions of stellar wind properties (density, temperature) are outlined in Sect. 5.3.

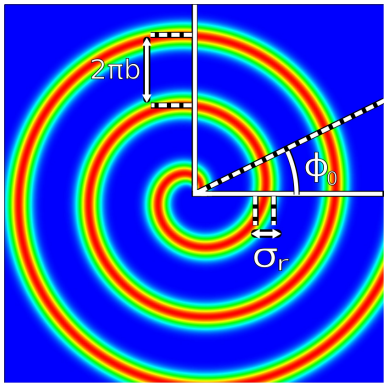

Figure 5.1: Face-on view of the spiral model by taking a slice through the orbital plane, qualitatively depicting the meaning of the geometrical parameters. The colour scheme used is qualitative, and serves to demonstrate the Gaussian nature of the $S(r,\theta,\phi)$ function.

Geometry in the orbital plane

The parameters describing the geometry in the orbital plane are given below and are illustrated in Fig. 5.1:

- $r_0(r,\theta,\phi) = b(\phi - \phi_0)$ describes the exclusive ϕ-dependent outward evolution of the spiral windings. With $\phi > 0$ and $\phi_0 > 0$, ϕ_0 corresponds to the position

angle, that is, the angle with respect to a reference point from which the spiral originates.

- $\sigma_r(r, \theta, \phi) = \sigma_r$ describes the Gaussian width of the spiral arm in the orbital plane.

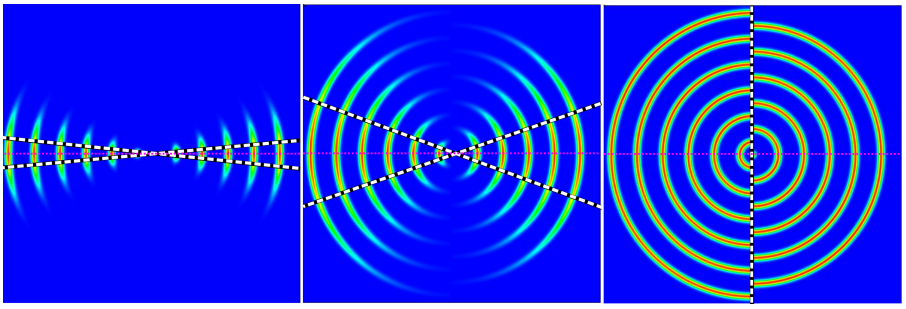

Figure 5.2: Cross-section through the centre of, and perpendicular to the orbital plane. The effect of an increase in α on the edge-on view of the spiral model, with α the angle between the two dashed lines. A narrow spiral with an opening angle of $\alpha = 10°$ (left panel), an intermediate spiral with opening angle $\alpha = 35°$ (middle panel), and a shell spiral with $\alpha = 180°$ (right panel) are shown. The red horizontal dotted line represents the location of the edge-on orbital plane. The colour scheme used is qualitative, and serves to demonstrate the Gaussian nature of the $S(r, \theta, \phi)$ function.

Geometry in the meridional plane

The parameters describing the geometry in the meridional plane, which is perpendicular to the orbital plane, are:

- $\theta_0(r, \theta, \phi) = \pi/2$, chosen such as to keep the Archimedean spiral symmetrical relative to the orbital plane.

- $\sigma_\theta(r, \phi, \theta) = \alpha$ determines the angular height of the spiral, perpendicular to and symmetrical around the orbital plane. It is, in effect, a measure for the extent by which the spiral fans out away from the orbital plane. Its mathematical equivalence to the Gaussian standard deviation in Eq. 5.4 implies that, in case of a density spiral, 68.2% of the total mass in the spiral can be found within the volume bound by α. The choice of an angle as the parameter to quantify the height of the spiral is justified by the geometrical implications of an exclusively radial outflow. If α is small, then the bulk of the material is confined into a narrow spiral close to the orbital plane. If caused by binary interactions, this

would correspond to a case where the spiral is formed by a strong gravitational wake of the companion. For larger α, the spiral windings become more extended shell-like structures. Such a morphology would be a reasonable representation of the effect of a wobbling mass-losing star. In the most extreme case, which is for an opening angle of $\alpha = 180°$, one is left with a dense winding of shells. A visualisation of the effect of α on the edge-on view of the spiral in shown in Fig. 5.2.

Additional considerations

Hydrodynamical simulations by Kim et al. (2011) [92] show the existence of morphological substructures within the overall spiral shape. These models show this substructure to consist of two adjacent spirals. When seen edge-on (as in Fig. 5.2) a frontal (curved) wake, and a rear (flat) wake can be identified. Such details can also be modelled with the previously developed analytical expression. The frontal spiral can be modelled by adopting Eq. 5.4. To model the rear portion of the spiral substructure, Eq. 5.4 needs to be transformed from spherical coordinates to cylindrical coordinates, by substituting the spherical radius ($r = \sqrt{x^2 + y^2 + z^2}$) with the cylindrical radius ($r = \sqrt{x^2 + y^2}$), and the spherical height (θ) with the cylindrical height (z). By subsequently correctly choosing the ratio between the b-parameters of both spiral components, a resulting spiral pattern consistent with hydrodynamical results can be constructed.

We recall the probability of observing the orbital plane of a binary system face-on or edge-on. We define the face-on position to be an orientation for which the normal on the orbital plane deviates by at most ten degrees from the line of sight. Similarly, we define the edge-on position of the orbital plane to be the orientation for which the normal deviates by at most ten degrees from being perpendicular to the line of sight. With these definitions, we find that the probability of a face-on orientation is 1.5%, compared to 17.3% for edge-on. One is thus more than ten times more likely to observe a binary system edge-on than face-on.

We also make a note on our definition of position angle, which, in effect, is a rotation around the z-axis (or a rotation over the angle ϕ). However, the rotational operations over θ and ϕ are not commutative. If the spiral is rotated over ϕ first, then the Archimedean spiral will remain in the x,y-plane. Its effect will be a face-on rotation, revolving the start of the spiral around the origin of the coordinate system. This effect is trivial, and is ignored in this paper. If, on the other hand, the spiral is rotated around θ prior to a manipulation of ϕ, then the inclined spiral will be pivoted around the z-axis. Under such an operation, the normal on the Archimedean spiral plane will precess around the z-axis. We refer to angular manipulation of the latter case as operations on the position angle.

5.2.2 Radiative transfer: LIME

To generate the 3D intensity channel maps of simulated emission of the above models, the Non-Local-Thermodynamical-Equilibrium (NLTE) full-3D, submillimeter and infrared (IR) radiative transfer code `LIME` was used. For a technical overview of the inner workings of the code, see Chapter E in the appendix, or Brinch et al.(2010) [19].

We modelled CO emission, for which the spectroscopic CO data of the LAMDA database [165] were used. The collisional rates were taken from Yang et al. (2010) [210].

5.2.3 Synthetic ALMA simulations: CASA

To produce simulations of *ALMA* observations of the emission of the spiral wind models we used the Common Astronomy Software Applications, `CASA`, post-processing package [126]. It consists of a collection of `C++` tools, managed by a `python` wrapper code.

5.3 Model assumptions

We consider a singular mass-losing system, located in the centre of the model. Though likely to be formed by binary interactions, we attempt to make no assumptions on the formation of the spiral structure in this paper. For all intents and purposes, this singular mass-losing system represents the binary system.

The 3D density field consist of two components. One spherical outflow component, for which mass conservation implies that the density is given by

$$\rho_{\rm HO}(r) = \dot{M}_{\rm HO}/(4\pi r^2 {\rm v}(r)). \tag{5.5}$$

$\dot{M}_{\rm HO}$ is the rate at which mass is lost in the homogeneous outflow. Hydrodynamical models show the outflow velocity of the spiral to be comparable to the intrinsic wind speed [96, 93]. We express the velocity of both the spherical and the spiral wind components by a beta-law,

$$ {\rm v}(r) = {\rm v}_\infty(1 - R_0/r)^\beta, \tag{5.6}$$

where $\rm v_\infty$ is the terminal wind velocity, and R_0 the dust condensation radius. $\rm v(r)$ is thus exclusively radial in nature, and is the key to understanding why the spiral is bound by the opening angle α. In addition to $\rm v(r)$ a constant turbulent velocity field $\rm v_{\mathit{turb}}$ exists throughout the wind.

This homogeneous density field is superimposed by a spiral density enhancement,

$$\rho_{\rm spiral}(r,\theta,\phi) = \dot{M}_{\rm spiral}/(4\pi r^2 {\rm v}(r)) = \rho_0(r,\theta,\phi)\, S(r,\theta,\phi). \tag{5.7}$$

where $S(r,\theta,\phi)$ is described in Eq. 5.4. $\rho_0(r,\theta,\phi) = \rho_{\rm max}(2\pi b/r)^2$ describes the variation of the local Gaussian density peak, where $\rho_{\rm max}$ is a constant, and will be determined later. Supported by mass conservation in a radial outflow, we assumed a radial dependence of ρ_0 proportional to $1/r^2$. The resulting overall density profile of the spiral wind is $\rho_{\rm wind}(r,\theta,\phi) = \rho_{\rm HO}(r) + \rho_{\rm spiral}(r,\theta,\phi)$.

The temperature distribution throughout the wind follows the same twofold format as the density structure. Its main trend is a radial power law,

$$T_{\rm HO}(r) = T_*(R_*/r)^{\epsilon}, \tag{5.8}$$

which describes the temperature of the homogeneous outflow. T_* and R_* are the stellar effective temperature and stellar radius respectively. The temperature of the spiral,

$$T_{\rm spiral}(r,\theta,\phi) = T_0(r,\theta,\phi)\, S(r,\theta,\phi), \tag{5.9}$$

is superposed onto this background, with a chosen distribution maximum of $T_0(r,\theta,\phi) = T_0 = 60$K, corresponding to a value of the same order of magnitude as established from hydrodynamical calculations [96]. The resulting overall temperature profile of the spiral wind is $T_{\rm wind}(r,\theta,\phi) = T_{\rm HO}(r) + T_{\rm spiral}(r,\theta,\phi)$.

Though not expected to affect the CO emission much, dust was taken into account in calculating the radiative-transfer, with the dust density distribution following the gas density distribution. The specific dust input parameters are presented in Table 5.1.

Additional effects such as scattering, magnetic fields, or rotation are not taken into account.

5.3.1 Outflow Parameters

We conducted a parameter study to asses the effect of changes in the free parameters of our model. Here, we present the applied parameter values. The general stellar and dust properties, as well as some overall characteristics of the CSE were taken from De Beck et al. (2012) [36], making the high mass-loss case of the parameter study similar to the carbon-rich CW Leo system. The bias towards C-rich objects reflects that most spirals were observed in such environments [137, 114, 41].

Table 5.1 gives an overview of the fixed parameters of the radiative-transfer models. These are the parameters which are either deemed to have a predictable or even trivial effect on the observables, or which bring about a global influence which is beyond

Stellar Parameters	
T_*	2330 K
L_*	11300 $L_\odot$
Distance	150 pc
Wind Parameters	
v_∞	14.5 km s^{-1}
v_{turb}	1.5 km s^{-1}
β	0.4
R_0	2.0 $R_\star$
ϵ	0.5
CO/H_2	6.0×10^{-4}
Spiral Parameters	
$2\pi b$	270 AU
σ_r	20 AU
T_0	60 K
Dust Parameters	
Amorphous Carbon	53%
Silicon Carbide	25%
Magnesium Sulfide	22%
Gas/Dust	100

Table 5.1: Fixed model parameters.

the scope of this paper. The fixed spiral parameters are chosen such that a spiral with sufficiently contrasting features can be clearly identified in the observables.

The variable parameters are presented in Table 5.2, and the motivation behind their choice is described below.

- The total mass-loss of the system has profound effects on the emission in terms of absolute strength and optical depth effects. Therefore we simulated CSEs for two extreme mass-loss rates, one very high and one very low.
- The contrast between the density of the spiral and the homogeneous outflow brings about changes in relative emission strengths, which can easily be recognised in the observables. We define a mass contrast between both wind elements, using the parameter

$$\Sigma = \frac{\dot{M}_{\text{spiral}}}{\dot{M}_{\text{HO}}} = \frac{M_{\text{spiral}}}{M_{\text{HO}}}, \tag{5.10}$$

with $\dot{M}_{\text{spiral}} + \dot{M}_{\text{HO}} = \dot{M}_{\text{total}}$. $\dot{M}_{\text{spiral}}$ represents the portion of the material confined to the boundaries of the spiral structure, flowing outward per unit time. Σ thus

quantifies the way in which the total mass lost by the star is distributed over the spherical outflow and spiral density enhancement components. $\Sigma \rightarrow 0$ corresponds to $\dot{M}_{\rm HO} \rightarrow \dot{M}_{\rm total}$, $\Sigma \rightarrow \infty$ to $\dot{M}_{\rm spiral} \rightarrow \dot{M}_{\rm total}$. A particular choice of Σ will result in a specific value for $\rho_{\rm max}$. In principle, this parameter should also affect the value of T_0. We have chosen not to let it depend on Σ because the relation between both is not clear to us.

- Two different spiral heights were simulated: one narrow spiral, with a small opening angle, and one spiral having a maximally large opening angle, referred to as a shell spiral.
- The inclination i is defined as the angle that tilts the view of the model between face-on, where the orbital plane lies perpendicular to the line of sight, and edge-on, where the orbital plane lies along the line of sight. Each model is observed under six different inclination angles, evenly spaced between this face-on and edge-on view.

Parameter	Values	Labels
Mass loss $\dot{M}$ $[M_\odot/yr]$	1.5×10^{-5}	H ('High')
	1.5×10^{-7}	L ('Low')
Mass contrast $\Sigma = n/m$	$\forall\ n \in \{1\} : m \in \{2, 5, 10, 100\}$	Sd2,Sd5,Sd10,Sd100
	$\forall\ m \in \{1\} : n \in \{1, 2, 5, 10, 100\}$	S1,S2,S5,S10,S100
Spiral height α	10°	N ('Narrow')
	180°	S ('Shell')
Inclination $\theta = (n/5)(\pi/2)$	$n \in \{0, 1, 2, 3, 4, 5\}$	i=0,18,36,54,72,90

Table 5.2: Variable model parameters. The labels are used throughout the paper to specify the considered models.

5.4 Results

We present the general findings of the parameter study in two parts. First, we exhibit the general trends and effects of the parameters on the spectral lines. Second, we show the effect of identical parameter simulations on the intensity maps. A full overview of the results can be found in Appendix D. In order to investigate these 3D data we make use of the wide-slit position velocity (PV) diagram (see Sect. 1.5.2). The axes along which the asymmetry of the models appears strongest are labelled as X and Y.

All the shown data are of the emission of the ground vibrational CO rotational transition J=3-2, unless otherwise stated. All results are continuum subtracted. In this section, the PV diagrams that best exhibit the asymmetry of the data (along X and Y) are referred

to as PV1 and PV2 respectively. The spectral data are modelled as seen with a 20 arcsecond beam. (The quality of most images shown below is strongly enhanced when viewed on screen.)

5.4.1 Reference model

Fig. 5.3 shows both the spectral line and the PV diagrams of an optically thin narrow spiral, with a total mass-loss = 1.5×10^{-7} $M_{\odot}$ yr^{-1} and $\Sigma = 1$. This is considered the reference model, and will be referred to as such. Every model below shows the effect of the change of a singular parameter with respect to this model.

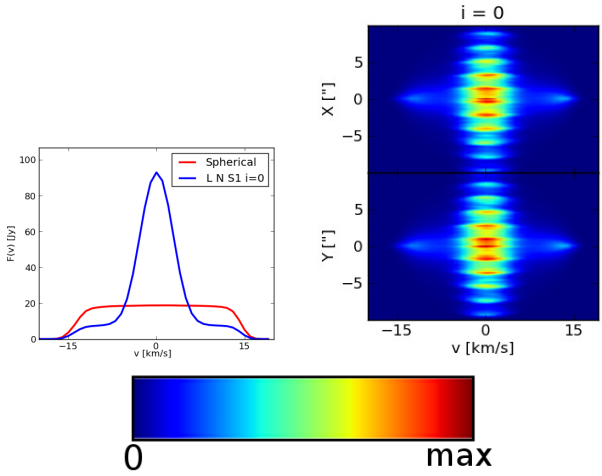

Figure 5.3: *Top Left:* The spectral line of the reference model (blue), seen from an inclination angle of 0 degrees (face-on). Overplotted is the spectral line of an exclusively homogeneous spherical outflow with identical global characteristics. *Top Right:* The wide-slit PV diagram of the reference model. The linear colour map at the bottom provides a reference to the colour coding. Every coloured diagram is constructed using this map. MAX represents the maximum emission in the PV diagram.

5.4.2 Spectral aspect

Narrow spiral

Inclination: Fig. 5.4 shows the effect of the inclination angle under which the spiral is seen. The appearance of the narrow spiral is very dependent on its orientation with respect to the observer. We therefore expect the inclination to have a strong effect on the observables. The homogeneous background wind is indifferent to these same transformations. The face-on view (i = 0) of the spectral line clearly shows the dual nature of the CSE. The spiral wind produces a sharp and narrow peak in velocity space. The width of this peak depends strongly on the height of the spiral. It is much narrower than the terminal velocity of the wind. This is because the spiral only hardly extends away from the $v = 0\,\mathrm{km\,s^{-1}}$ Doppler plane. Because the wind is optically thin, higher local densities generate more emission, which is why the peak extends above the lower plateau, generated by the spherical wind. As the inclination angle increases, the contribution of the spiral decreases and widens, whilst the contribution of the homogeneous background wind remains unchanged, as expected. This evolution of the central peak is explained by the fact that the total emission is smeared out over a wider velocity range. At the highest inclinations, a double-peaked profile emerges in the spiral wind feature. Additionally, its width becomes comparable to the width of the spherical outflow, ultimately concealing the dual nature of the system. As a side note, the position angle has no effect on the spectral lines.

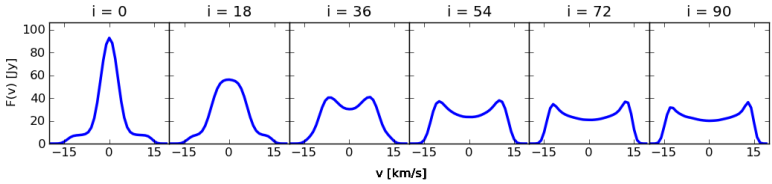

Figure 5.4: Spectral lines of a narrow spiral in a low mass-loss wind, in which the total amount of outstreaming mass is equally divided between both wind components, as seen from a range of different inclination angles.

Mass contrast: The main effect of the mass contrast is on the relative heigths of the spectral features generated by the spiral and spherical winds, as seen in Fig. 5.5. For $\Sigma > 1$, the contribution of the spherical wind rapidly diminishes and disappears from the resultant profile, and only the spectral feature generated by the spiral wind remains. For $\Sigma \sim 1$ we find that the relative sizes of both contributions are comparable. When Σ becomes very small, the spherical wind dominates the spectal feature.

Figure 5.5 shows a model with $\Sigma = 1/5$. The face-on case shows both a decreased contribution of the spiral wind and an increased contribution of the spherical wind

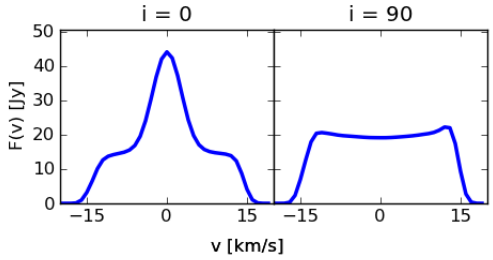

Figure 5.5: Spectral lines of a narrow spiral in the low mass-loss wind, in which the total amount of mass contained in the homogeneous outflow is five times the amount in the spiral ($\Sigma = 1/5$), seen face-on (left panel) and edge-on (right panel).

relative to the reference model. Viewed edge-on, the spiral wind's double-peak characteristics (visible in the $\Sigma = 1$ case) are reduced, leaving a flat-topped resultant spectral profile.

Total mass-loss: The first and most important effect of an increase in the total mass-loss is an increase in flux, visible in Fig. 5.6. For low-inclination angles the peak due to the contribution of the spiral wind broadens with respect to the face-on reference model. This is due to the increased emission in the Gaussian tails of the density distribution of the narrow spiral. For high inclinations (nearing an edge-on view) the double-peaked aspect of the spectral line is less pronounced as the spiral becomes optically thick and relative brightening due to its long column depths in the line of sight direction (at maximum and minimum velocity) is suppressed.

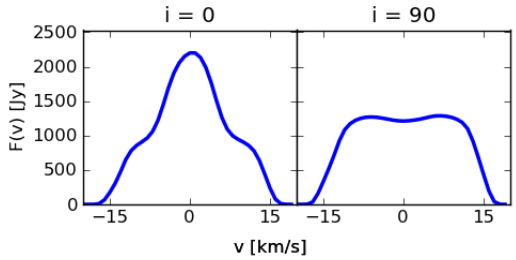

Figure 5.6: Spectral lines of a narrow spiral in the high mass-loss wind, in which the total amount of outstreaming mass is equally divided between both wind components, seen face-on (left panel) and edge-on (right panel).

Shell spiral

In the case of the shell spiral, the spiral and spherical wind components possess virtually identical widths in velocity space, which makes both components essentially indistinguishable from one-another. This is due to the broadening effect of the opening angle α on the emission feature of the spiral wind. For high values of α both wind components will be of comparable width. For this reason we refrain from showing this in figures. In Sect. 5.4.3 we discuss the integrated line fluxes for various combinations of mass-loss in spiral and spherical outflow to assess the potential for erroneous estimates of the total mass-loss rate if assuming a spherical wind only.

Other CO lines

Different rotational transitions of CO (besides CO J=3-2) can provide additional information. In Fig. 5.7 the effect of rotational CO transitions ranging from J=3-2 to J=38-37 (probing the inner parts of the wind) on the line shapes of the reference model is shown. Hydrodynamical simulations of the regions close to the mass-losing star show that the sphericity of the outflow is completely destroyed locally by the binary interactions. The effect of a well-behaved analytical spherical outflow close to the centre of the spiral is thus unrealistic. The spiral shape, however, is recognisable on this scale. Therefore, to properly show how the spectral lines are affected by the spiral, we omitted the contribution of the spherical wind.

In the case of the face-on narrow spiral, the spectral lines show no recognisable changes in the overall characteristics. However, other viewing angles show a very characteristic evolution in the line shapes of the narrow spiral, with a progressively receding red or blue wing. This is explained as follows. For the higher CO transitions the emitting region, probing the most central regions of the spiral, will merely contain an incomplete portion of the first revolution of the spiral. Depending on whether the part of the spiral contibuting to the line flux is predominantly approaching or receding, emission is more concentrated in the blue or the red wing. It is likely that the most central regions of the binary system will show additional complexities, as this region harbours all the mechanics that form the spiral. These effects are not taken into account, and may cause additional effects on the overall shape of the high CO transition lines. The shell spiral shows an evolution towards a triangular line shape. However, this is not dissimilar from the expected evolution of a homogeneous outflow, as the higher CO transitions probe the acceleration region of the wind.

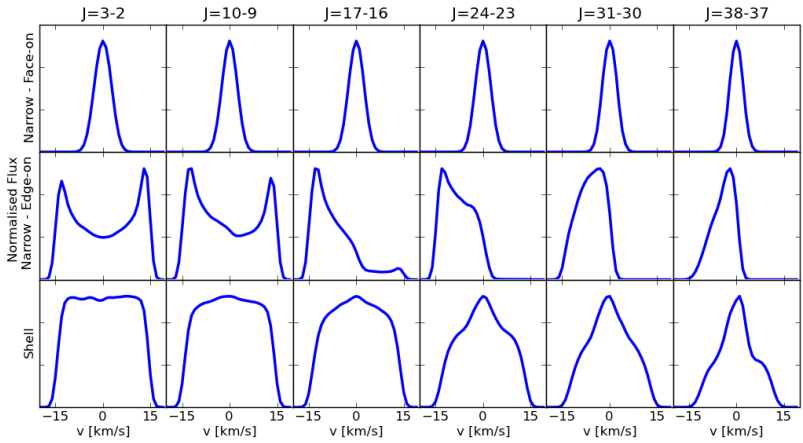

Figure 5.7: The effect on the shape of the spectral lines as a function of CO transition. The first row shows the line shapes for a face-on narrow spiral, the second row for an edge-on narrow spiral, and the third row for a shell spiral. To focus the attention on the shapes of the emission lines, the peak strengths have been normalised, and the spherical wind contributions have been omitted.

5.4.3 Spatial aspect

In this section we present the spatial counterpart of the above results. Generally, the two-fold nature of the wind is clearly recognisable in the PV diagrams. The spiral is manifested as a sequence of emission bands, whilst the contribution of the spherical wind is a large circular shape with a strongly enhanced central bar, representing the warm and dense regions near the star. This elongated feature approximately reaches up to the terminal velocity of the wind, and is visible in most PV diagrams below.

Narrow spiral

Inclination: The appearance of the narrow spiral is dependent on its orientation with respect to the observer, thus the velocity channel maps will be sensitive to global angular transformations. We recognise the central bar generated by the spherical wind in Fig. 5.8. The main feature, however, is the strongly periodic pattern seen in both

PV1 and PV2, generated by the spiral. The face-on view of the narrow spiral generates two identical PV diagrams, with a narrow column of periodic emission bands. The bands decrease in brightness for increased distance to the orbital plane (positioned at an angular deviation of 0 arcsec), as a result of the combined $1/r^2$ density dependence and local temperature. As the inclination increases, the primary contribution to PV1 gradually twists into an S-shaped feature, tightening around the central contribution, until it becomes a narrow, horizontal dumbell-like feature. In PV2 the evolution is different, because of the strong asymmetry of the edge-on narrow spiral. Its evolution stretches the initial shape sideways, ultimately forming an ellipsoidal pattern of periodic emission bands for the highest inclination values.

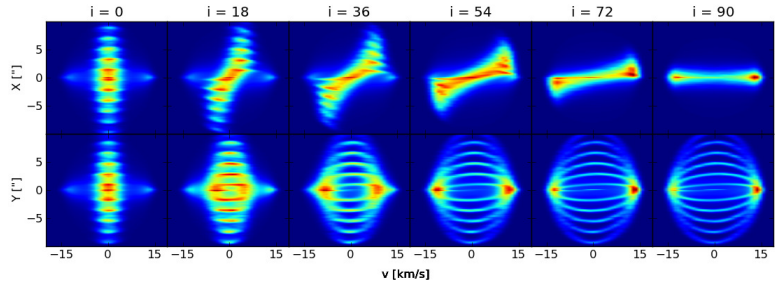

Figure 5.8: Position-velocity diagrams of a narrow spiral in a low mass-loss wind, in which the total amount of outstreaming mass is equally divided between both wind components, as seen from a range of different inclination angles. The top row shows PV1, the bottom row PV2.

Mass contrast: As the mass contrast varies the emission contribution between the spiral and spherical winds changes accordingly. In the case of $\Sigma = 1/5$, as seen in Fig. 5.9, the contribution of the spherical wind is strongly enhanced, with a decreased relative emission of the spiral wind. However, the general structure of the PV diagrams remains unchanged.

Total mass-loss: In the high mass-loss regime the PV diagrams show an overall increase in emission compared to the low mass-loss regime, as seen when comparing Fig. 5.10 with Fig. 5.8. The apparent widening of the features of the spiral wind is due to non-negligible emission coming from the tails of the Gaussian density profile; emission which, in the low mass-loss case, barely contributed to the PV features. Optical depth effects keep the emission peak from increasing by the same factor as the wing emission.

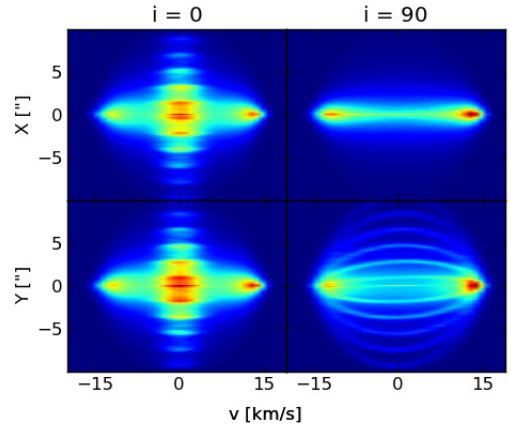

Figure 5.9: Position-velocity diagrams of a narrow spiral in the low mass-loss wind, in which the total amount of mass contained in the homogeneous outflow is five times the amount in the spiral, seen face-on and edge-on. The top row shows PV1, the bottom row PV2.

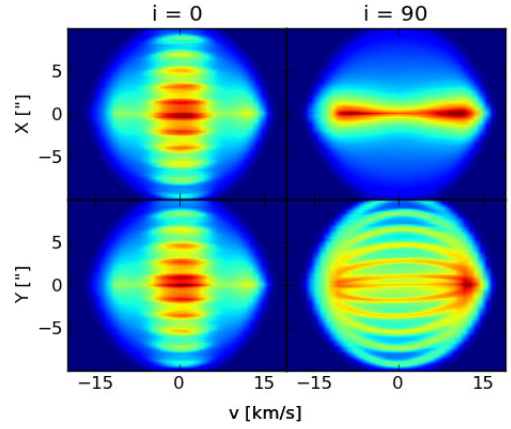

Figure 5.10: Position-velocity diagrams of a narrow spiral in a high mass-loss wind for $\Sigma = 1/5$, seen face-on (left panels) and edge-on (right panels). The top row shows PV1, the bottom row PV2.

Shell spiral

The primary and spherical wind components possess identical spectral widths, and their general tendency to invariance under angular transformations translates into

particularly similar PV1 and PV2 diagrams. This strong characteristic is a reliable diagnostic, assisting with the differentiation between the shell and narrow spiral.

Inclination: Unlike for the spectral lines, the PV diagrams do reveal information on the inclination of the shell spiral, be it only for higher inclinations. Fig. 5.11 shows that for low inclinations both PV1 and PV2 are virtually indistinguishable. Higher inclinations show the appearance of gaps in the emission bands of PV1. The gaps appear at i=54 around + and - 12 km/s and follow these bands as i increases, before reaching a vertical position at i=90. Under an inclination of $i = 0°$, any chosen PV slit (or axis along the plane of the sky) will be parallel to the orbital plane of the system. This means that the resulting PV diagram will be invariant to the particular choice of axis along which to construct the PV diagram. This explains why PV1 and PV2 are identical. However, at an inclination of $i = 90°$, and when the axes are chosen to best show the asymmetry of the system, the orbital plane of the model will be perpendicular to one, whilst remaining parallel to the other axis. The axis parallel to the orbital plane thus again produces an identical PV diagram as before, whilst the other will enhance the features along the dimension perpendicular to the orbital plane, which, in case of the shell spiral, contains the gaps.

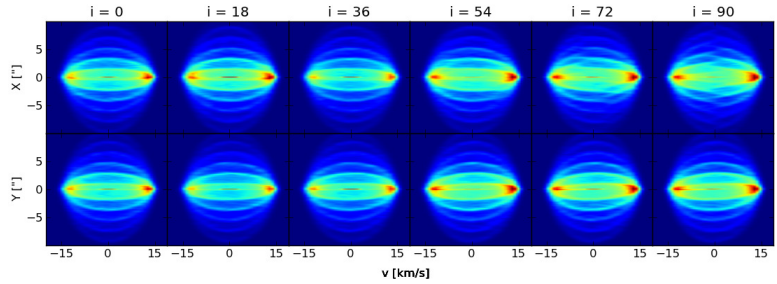

Figure 5.11: Position-velocity diagrams of a shell spiral in a low mass-loss wind for $\Sigma = 1$, as seen from a range of different inclination angles. The top row shows PV1, the bottom row PV2

Mass contrast: The $\Sigma = 1/5$ case is displayed in Fig. 5.12, and shows how the relative contribution of the spherical wind intensifies as the contribution of the spiral wind fades. The general structure of the PV diagrams remains unchanged.

Total mass-loss: A strong overall increase in emission, as seen when comparing Fig. 5.13 with Fig. 5.11. The general structure of the PV diagrams remains unchanged.

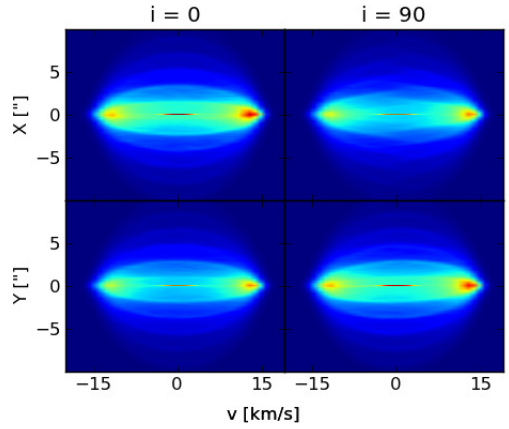

Figure 5.12: Position-velocity diagrams of a shell spiral in a low mass-loss wind for $\Sigma = 1/5$, seen face-on (left panels) and edge-on (right panels). The top row shows PV1, the bottom row PV2.

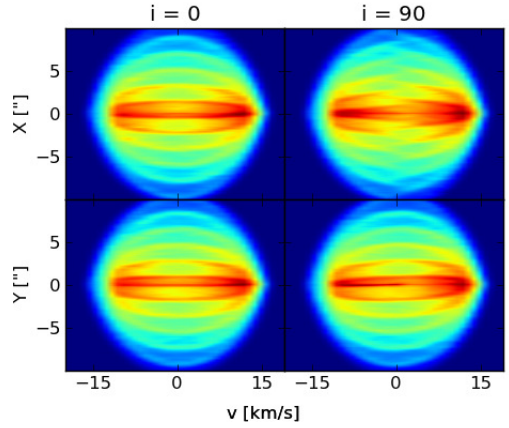

Figure 5.13: Position-velocity diagrams of a shell spiral in a high mass-loss wind for $\Sigma = 1$, seen face-on (left panels) and edge-on (right panels). The top row shows PV1, the bottom row PV2.

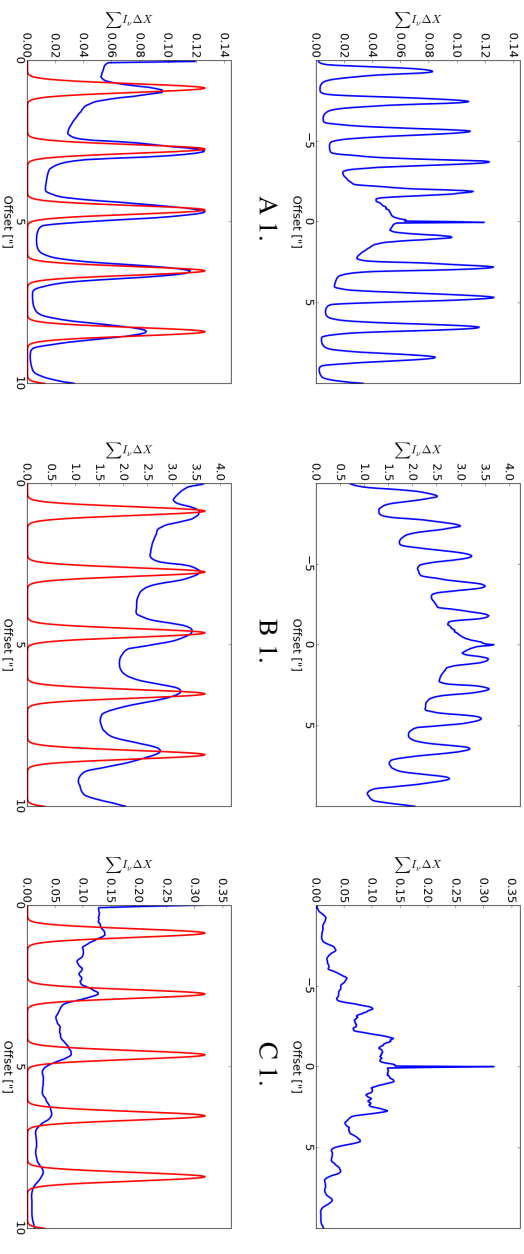

Figure 5.14: A selection of SP for a $\Sigma = 1$ edge-on narrow spiral (A) in the low mass-loss regime, and (B) in the high mass-loss regime. (C) shows an SP with an identically parametrised shell spiral to (A).

5.5 Discussion

5.5.1 Constraining the geometry

For our specific model parameters and our specific choice of PV axes, we find that PV2 readily provides the angular width and size of the gap between the emission bands, and thus the value of b. A slice through $v = 0$ km s^{-1} of PV2 allows to constrain the geometrical parameters in the orbital plane of the spiral. We refer to these diagrams as Slice Profiles (SPs) below. A number of such SPs are shown in Fig. 5.14. The top row exhibits the SP as they are, the bottom row shows the right half of the SP, overplotted with the geometrical model. We find as a general rule that the emission peaks systematically coincide with the density peaks. The angular distance between the spiral windings is thus readily available from the SPs of the PV diagrams. This distance can, if caused by binary interactions, directly be related to local physics according to Kim et al. (2012) [96] via the relation

$$\Delta r_{\mathrm{arm}} = \left(\langle V_w \rangle + \frac{2}{3} V_p \right) \times \frac{2\pi r_p}{V_p}, \tag{5.11}$$

with $\langle V_w \rangle$ the wind velocity, V_p the orbital velocity, and r_p the orbital radius of the primary. The orbital period T_p is given by the last term.

The angular width of the emission bands, however, does not relate one-on-one to the spiral geometry and is thus more difficult to deduce from actual observations.

The plots labelled A in Fig. 5.14 present the SP for a low mass-loss wind harbouring a narrow spiral seen edge-on, with $\Sigma = 1$. As expected, the spiral geometry tightly fits the emission characteristics. Additionally, a smooth bell-shaped background feature is visible, which is generated by the homogeneous component of the wind. Finally, the peak strength of the spiral-induced emission spikes clearly changes as a function of offset. This is due to a combination of the model specific radial dependence of the spiral density and of the temperature law, as the latter defines the line-contribution regions.

For more complex SPs, such as those for the shell spiral (labelled C), the emission peaks are not as narrow and smooth because the emission is smeared out over the offset dimension. Nevertheless, the presence of the spiral is still unmistakable. In this case, only the top portion of the peak, which ranges from approximately the emission plateau strictly to the left of the spiral peak to the plateau strictly to its right, should be used to determine the geometry. Additionally, the bell-shaped background curve is still recognisable, but as a result of the nature of the shell spiral, the smeared-out emission somewhat conceals its shape.

In the case of high mass-loss, the Gaussian tails of the density distribution contribute considerably to the SPs, while optical depth effects prevent the highest density regions from augmenting their emission by as much. This results in a decreased peak to background emission contrast. The emission from the tails broadens the emission zones significantly, which therefore no longer directly traces the width of the spiral arms. This effect is inherent to the mathematical properties of the Gaussian density distribution. Sharp cut-offs of the spiral density would not result in such a broadening. The bell-shaped emission feature of the smooth background of the A models has become much more prominent compared to the emission peaks generated by the spiral. Its shape has also changed to triangular. These two differences can be assigned to optical depth effects, which suppress emission from high-density regions.

It is necessary to note that these SPs should not be overinterpreted as their overall and absolute morphology is extremely sensitive to the specificities of the geometrical and radiative transfer model. Additionally, superimposed noise and diffraction effects will blur the small features in the SP.

Constraining the inclination

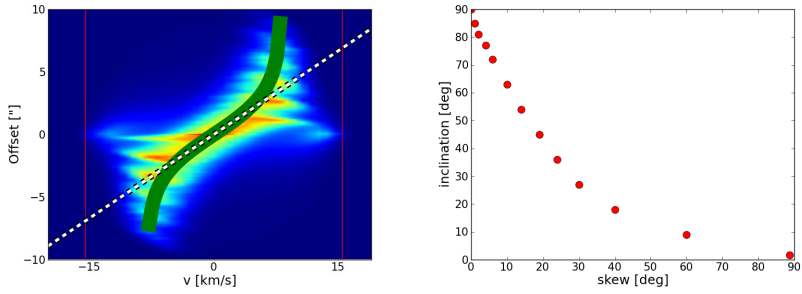

Figure 5.15: *Left panel:* A visual representation of the analytical model (green curve, Eq. 5.12) used to fit the emission features of the PV diagrams, applied to the reference model at an inclination of 36°. The slope of the curve around $v = 0\,\mathrm{km\,s^{-1}}$ (white dashed line) determines the characteristical skew of the diagram. *Right panel:* The relation between the measured skew of the PV diagram and the inclination angle.

The dependence of the emission signature on the inclination is characterised by the formation of an S-shaped feature in PV1 as inclination increases. For a narrow spiral the S-shape is unmistakable. The shell spiral exhibits this S-shape in the form of gaps in the emission bands. We constructed an analytical expression that fits the overall morphological trend of the inclination dependence of the PV1 diagram. This relation is

given by

$$S(v) = -Aln\left[\frac{B}{v + \left(\frac{B}{2}\right)} - 1\right]. \tag{5.12}$$

Exhibited as the wide green curve in Fig. 5.15, left panel, this expression allows for the determination of the angle that the emission feature makes with the velocity axis, around $v = 0\,\mathrm{km\,s^{-1}}$, by using

$$\frac{dS(v=0)}{dv} = \frac{4A}{B}. \tag{5.13}$$

This is referred to as the skew of the diagram, and was determined for a range of inclinations. We related the measured skew to the actual inclination angle to determine how they are related. The resulting curve (Fig. 5.15, right panel) shows a clear trend.

5.5.2 Impact of the spiral structure on the total line strengths

The signature of a spiral can quite easily be discerned in PV diagrams. However, the effect on the CO spectral lines is much less outspoken particularly so for extended (large α) spirals and high mass-loss rate systems. Here, we investigate the effect of a spiral structure on the frequency-integrated line strength of CO transitions. We discuss this integrated line strength relative to the case in which all of the gas is in a spherical outflow to assess the error we would make in constraining the mass-loss if we applied a model for a spherical wind to a system in which part (or all) of the material leaves the star in a spiraling outflow.

Figure 5.16 presents the total line flux normalised to the case of a spherical flow for six different CO transitions, from J=2-3 to 38-37. The total flux ratio is plotted versus Σ. Models for a range of inclinations are presented at each value of Σ. The four basic configurations are labelled with different colours (blue for the shell spiral and red for the narrow spiral) and symbols (triangles for the low-$\dot{M}_{\rm total}$ model and squares for the high-$\dot{M}_{\rm total}$ model). The green horizontal bar represents a typical error margin of line-data calibrations, approximately 20 percent.

For low values of Σ the bulk of the matter is in the spherical outflow and all ratios tend towards unity, as expected. The seeming failure of convergence to unity for high J levels originates in the fact that the elevated temperature of the spiral is not present in the spherical reference models. For the J=3-2 transition, optical depth effects do not play a dominant role, safe for the high-$\dot{M}_{\rm total}$ narrow spiral models. For these models the flux ratio drops because of the high opacity. Note that, generally, the low-$\dot{M}_{\rm total}$ models tend to have an increased flux ratio and the high-$\dot{M}_{\rm total}$ models a decreased flux ratio. The former is an effect of density. If the material is concentrated in a spiral structure collisional excitations are more important causing the upper level of the

transition to become overpopulated. This may increase the flux ratio by up to a factor of three. However, densities never reach values that strongly affect the populations of very high levels, with $J \gtrsim 30$. Note also that the effect of inclination is not that important (compared to calibration uncertainties) for the low mass-loss case as the medium remains optically thin (in the line of sight). In the high-$\dot{M}_{\rm total}$ case the line ratio drops, the more so if most of the material is in a narrow spiral structure (high Σ) and the inclination is high (approaching an edge-on view). In that case the flux may drop by up to a factor of ten. If the spiral fans out to well above the plane of symmetry (i.e. high α) the drop in flux is not that dramatic, simply because of less pronounced optical depth effects compared to the narrow spiral.

The models discussed here present a wide range in Σ, that may not all be realistic. The blue line in Fig. 5.16 represents the mass ratio Σ that was derived for the wind structure of the binary AGB system AFGL 3068 by Kim et al. (2012) [96]. It shows that for this particular system one would not derive a significantly different total mass-loss rate if one would have applied a spherical outflow model.

We used the analytical expression derived by De Beck et al. (2010) [35], relating integrated line flux to mass-loss, to estimate the error on derived mass-loss rates provided prior knowledge on flux ratios. They showed that the analytically derived mass-loss scales as the integrated line flux to a certain exponent, $\dot{M} \sim [\int F_\nu dv]^\gamma$, where γ depends on the specific CO transition, and on the optical thickness of the spectral line. For the CO J=3-2 transition they found values for γ to be 1.14 in the optically thin regime, and 0.61 in the optically thick regime. This translates, in the optically thin regime, into an uncertainty on the mass loss which is approximately a factor 1.3 greater than the uncertainty on the line flux (a flux uncertainty of a factor ten translates into an uncertainty in deduced mass loss of a factor thirteen). For optically thick spectral lines, the uncertainty on the mass-loss is approximately a factor of 2.5 smaller than the uncertainty on the line flux (a flux uncertainty of a factor ten translates to an uncertainty in deduced mass loss of a factor four). Note that the results of De Beck et al. (2010) [35] were derived by explicitly calculating the energy balance throughout the parameter study, as opposed to assuming a fixed temperature structure as in our models.

It is worth noting that difficulties with the 1D modelling of an abundance of spectral lines, like for example a combination of ground-based and unresolved PACS lines, are usually solved by forcing the model to have a peculiar and possibly somewhat misshapen temperature profile. The need for such actions might indicate the presence of a complex geometrical structure in the observed stellar wind.

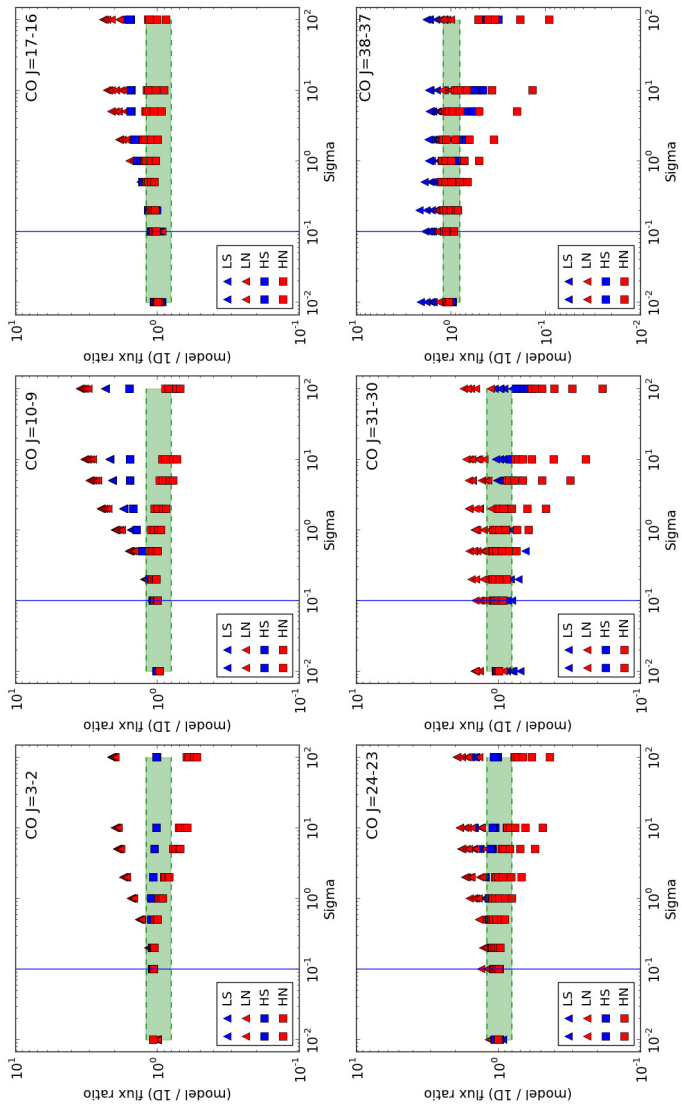

Figure 5.16: The ratio between the integrated flux of the spiral models, and the integrated flux of its 1D equivalent, in which all material is located in a homogeneous outflow. In principle this figure should exhibit identical amounts of red and blue markers, but a major overlap of both has resulted in an artificial bias favouring the red-labelled models. The green zone represents the instrumental calibration errors. The blue vertical line respresents the Σ value found in the hydrodynamical simulations of Kim et al. (2012) [96].

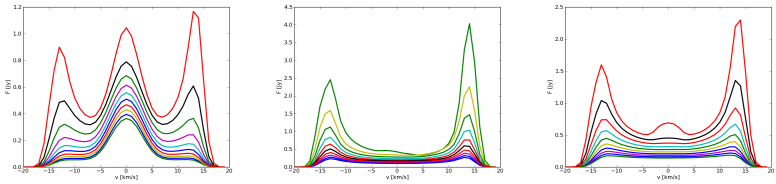

Figure 5.17: The effect of single-dish telescope beam size on the spectral lines of three models is shown. The telescope beam size is simulated by a normalised Gaussian filter. The total flux of the spectral lines is therefore scaled by the normalisation factor $1/(\sigma\sqrt{2\pi})$, with $FWHM = 2\sqrt{2ln(2\sigma)}$. In effect, this means that the peak flux of the line (in the plot) scales with beam resolution. This is done to emphasise the evolution of the line shape. *Left panel:* shows the effect of a decreasing beam size on the face-on reference model, which creates a trident shaped profile. *Middle panel:* shows the effect on the edge-on reference model, which forms a very explicit double-peaked profile. *Right panel:* exhibits the beam-size effect on a low mass-loss, $\Sigma = 1$, face-on shell spiral. Here the double-peaked character of the spectral line is preserved.

5.5.3 Single-dish simulations

Spectral features of single-dish observations can be heavily influenced by the telescope beam profile. To simulate how the intrinsic spectral lines of our models are affected by a beam profile, we covered our specific intensity images with a Gaussian filter, centered onto the location of the central source. In Fig. 5.17 the effect of Gaussian filters with different full-width at half-maximum (FWHM) values on the overall shape of the spectral lines is shown. The adopted values for the FWHM are $n/20$ for $n \in \{1, 2, 3, ..., 10\}$ of the total image size, which is 20 arcsec. It is important to note that, for the clarity of the figures, the Gaussian filter was normalised. This operation scales the flux by the normalisation factor, allowing us to properly demonstrate the effect on the line shape without overlapping the lines. Plot A shows the effect of an ever narrower beam on a face-on narrow spiral. The prominent central feature remains, but as the beam size diminishes, a double-peaked profile forms around this central peak, created by the strongly resolved spherical wind. Plot B presents the effect of beam size on an edge-on narrow spiral. When fully resolved, the spectral line shows a very pronounced double-peak, which could be incorrectly identified as a detached shell. Finally, plot C shows the same effect for a face-on shell spiral. As a result of its similarity to a homogeneous outflow, the gradual evolution to a double-peaked profile is expected. However, for an extremely resolved shell spiral, a small bump appears in the centre of the spectral line, which is some remaining numerical artifacts.

5.5.4 ALMA simulations

The functions simobserve and the clean of `CASA` generated these synthetical *ALMA* observations.

Simulation Parameters	
Pixel size	0.04”
Field size	20”
Peak flux	Taken from `LIME` output
Transition	CO 3-2 (345.76599 GHz)
Antenna configurations	All available in cycle2
Pointing	Single
Channel width	1.15MHz, centred on rest freq.
PWV	0.913 mm
Thermal noise	standard
Temperature	269 K
Integration time	10 min on-source

Table 5.3: The *ALMA* observation simulation specifications.

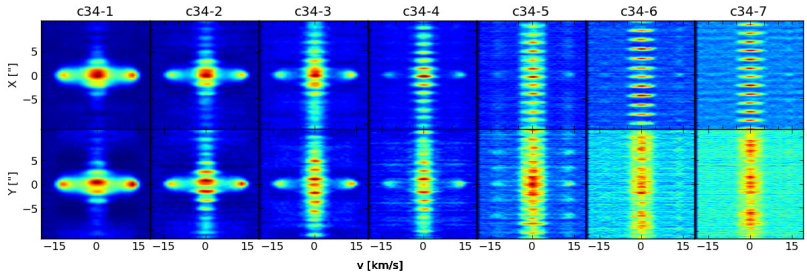

Figure 5.18: A simulation of ALMA observations of the face-on reference model, with all the different extended antenna configurations offered during ALMA cycle two. The scaled colour bar used for the production of these images is identical to the one used to produce the intrinsic signatures, and is found in Fig. 5.3.

In Fig. 5.18, we present the effect of the seven different antenna configurations offered in ALMA Cycle 2[1] on the face-on reference model, for which the fixed geometrical parameters can be found in Table 5.1. For these model-specific geometrical parameters (combined with a fixed distance of 150 pc), we find that the resolution of the C34-1 configuration is too coarse. It only poorly samples the spiral structure. Additionally, the largest recoverable scale for the C34-1 configuration is large enough to nicely see

[1] http://almascience.eso.org/documents-and-tools/cycle-2/alma-technical-handbook

the spherical wind. Combined, these effects show a strong bias towards the spherical wind. The C34-7 configuration has the opposite effect, with a resolution high enough to detect the spiral structure, but a largest recoverable scale that is too small for a proper sampling of the spherical wind. Its flux contribution is completely lost. The C34-3 and C34-4 antenna configurations combine the advantages of both extremes, making them the optimal setup with which to simulate observations of this spiral model. A direct consequence of using this best-fit configuration is that, as a general tendency, the overall structure of the PV diagrams remains relatively unaffected by the observation. We thus conclude that for this specific model, an extended configuration with a maximum baseline of about 500m and a minimum baseline about 20m produces images of the highest quality. These baselines correspond to angular resolutions of approximately 0.32-0.4 arcseconds, which, as expected, is similar to the angular size of the minimal length-scale of our models (the spiral arm thickness) of approximately 0.26 arcseconds. We would like to emphasise that these results are very model dependent, with the angular width of the smallest scale of the object being the most influential on the quality of the observations. The angular resolution $\Delta\theta$ of a configuration with a maximum baseline L_{max} can be estimated with the following relation

$$\Delta\theta \simeq \frac{61800}{L_{max}\nu}, \tag{5.14}$$

with ν the observing frequency in GHz. Keeping the value of $\Delta\theta$ close to, but lower than the smallest expected angular size of the observed features of interest (in the case of the spiral structure the value σ_r/distance) should ensure a good quality observation.

The compact array simulations are not shown. The resolution of the compact array is too low to be able to discern any useful features in the PV diagrams.

Fig. 5.19 presents the effect of the C34-1,4 and 7 antenna configurations on the PV diagrams of the face-on high and low mass-loss narrow spiral models (labelled by HN and LN respectively), and the high and low mass-loss shell spiral models (labelled by HS and LS respectively). An immediate conclusion from a preliminary inspection of the figures is that the lower resolution configuration provides considerably more information on the object than configurations with resolutions which are too high. The longest baseline configurations resolve out all the large-scale information, leaving only an exceptionally biased focus on the smallest scale, largest emission features.

From these simulations we conclude that it is impossible, without any prior knowledge on the geometrical parameters of the spiral structure, to determine the optimal antenna configuration with which to observe the object. This being said, two scenarios can be thought of that can facilitate the configuration determination. Either hydrodynamical simulations predict a preferred spiral arm thickness, inter-spiral-winding-distance, or relation between both, in which case an optimal (longest) interferometry baseline can be calculated. Or theoretical models provide no such information, in which case it is advised to observe with a combination of configurations.To determine the best-fit

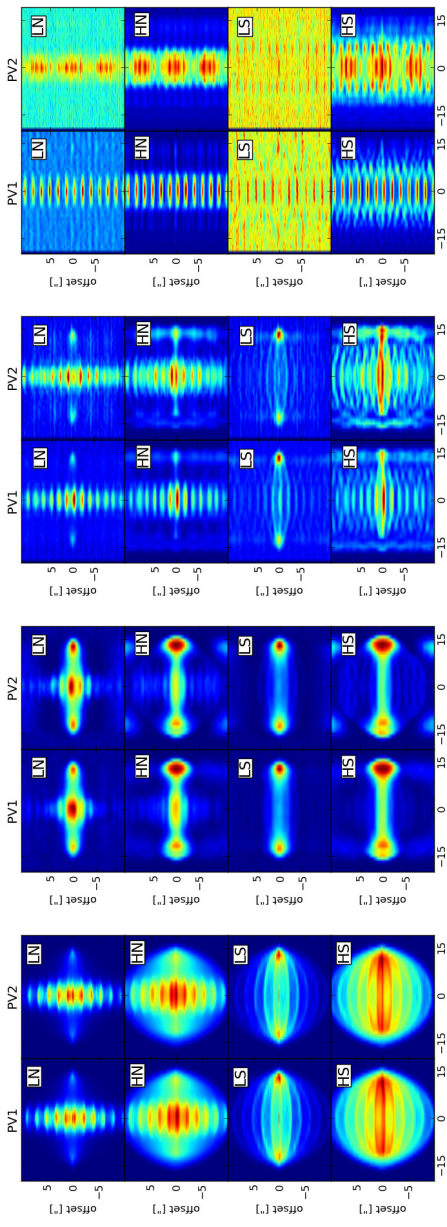

Figure 5.19: The effect of three cycle 2 extended antenna configurations on the intrinsic emission of a number of face-on wind models, presented in *panel A*. *Panel B* shows the effect of the C34-1 configuration, with a minimum baseline of 14.2m, a maximum baseline of 165.6m, and an angular resolution of 1.08 arcseconds. In *panel C*, the effect of the C34-4 configuration is shown. It is characterised by a minimum baseline of 20.6m, a maximum baseline of 558.2m, and a resolution of 0.32 arcseconds. Finally, shown in *panel D* is the influence of the C34-7 configuration, with a minimum baseline of 40.6m, a maximum baseline of 1507.9m, and a resolution of 0.12 arcseconds.

antenna configuration the observed wind needs to be probed with at least the two most extreme maximum baselines.

5.6 Conclusions

Using the 3D radiative transfer code LIME, we have conducted a large-scale parameter study to investigate the effect of geometrical and global wind properties of AGB outflows containing spiral structures that are embedded in a spherical outflow. Considering the CO v=0 J=3-2 transition, a singular spectral line generally conceals the dual nature of the wind. Only for limited combinations of parameters (inclination and spiral width) is its dual nature recognisable. However, when comparing different rotational transitions of CO, a characteristical evolution of the line shape is perceived as one progresses to higher transitions for the non-face-on narrow spiral models. The peculiarity of the (evolution of the) resulting line shapes shows strong evidence for the presence of an embedded spiral.

The LIME output also allowed us to investigate the 3D emission of the CO v=0 J=3-2 transition throughout velocity space. We found that the best tools for analysing these images are the wide-slit PV diagrams, which intensify the correlated structural trends in the emission. Using these PV diagrams, we consistently found a strong signature of the spiral in the data, from which most of the geometrical properties can be recovered. It seems that one specific parameter, the mass- or density contrast, cannot be deduced by only analysing the emission, that is without resorting to detailed radiative transfer efforts. We compared the integrated flux of the 3D emission with an equivalent 1D model (where all the material resides in the spherical outflow component) to explore the uncertainties such a 1D misinterpretation brings about. We found that generally the errors on derived mass-loss do not exceed a factor of a few. Only in extreme cases can the difference between the embedded spiral flux and the exclusively spherical flux reach factors of up to ten, translating into uncertainties on derived mass losses exceeding an order of magnitude (for optically thin lines), or up to a factor of four (for optically thick lines).

Finally, we have simulated cycle 2 *ALMA* observations of the model emission with CASA. In addition to the importance of recognising interferometric artifacts, we conclude that no preferred antenna configuration exists, since the required resolutions depend strongly on the spiral geometry. To promote spiral detection the source of interest should be observed with a range of different maximum-baseline configurations.

Chapter 6

Detailed model of the spiral structure in the inner wind of CW Leonis.

This chapter is based on a pilot study, and has not yet been subjected to the peer-reviewing process.

Ward Homan[1], Leen Decin[1], and Alex de Koter[1,2]

[1] Institute of Astronomy, KU Leuven, Celestijnenlaan 200D B2401, 3001 Leuven, Belgium
[2] Sterrenkundig Instituut 'Anton Pannekoek', Science Park 904, 1098 XH Amsterdam, The Netherlands

Abstract: *High resolution ALMA observations of the inner wind of the carbon-rich AGB star CW Leonis suggest that it harbours a spiral morphology. We seek to further constrain the properties of the spiral in order to better understand the physics governing the inner wind of mass losing AGB stars. We model the emission distribution of the* ^{13}CO *rotational transition J =6−5, acquired with ALMA (cycle 0), first presented and analysed by Decin et al. (2015), using the full 3D NLTE code* `LIME`*. We compare the model of best resemblance to the ALMA data directly via the channel maps, but also through the wide-slit position-velocity diagrams and the spectral line shape. The data is very well modelled with a spiral embedded in a smooth spherical outflow. The spiral extends up to 25 degrees above and below the equatorial plane, and its density decays radially as a power of -1.5. The vertical extent of the spiral suggests that the spiral-inducing binary companion and CW Leo has a mass that is of the same order, as suggested in the first analysis. The smooth outflow is best reproduced assuming a current mass-loss rate of* 4×10^{-5} $M_{\odot}$ yr^{-1}*. The spiral morphology fits the data very well, but cannot explain all the detail in the spatial emission distribution. We attribute these unexplained features to vigorous and chaotic convective stellar pulsations that cause highly anisotropic mass loss and shock waves.*

Contribution to the article: *All scientific work discussed below, as well as the composition of the article was carried out solitarily, with the exception of regular consulatation with my supervisors.*

6.1 Introduction

At a distance of merely 130 pc [62], the asymptotic giant branch (AGB) star CW Leonis (IRC+10216) is the closest carbon-rich AGB star. It has a surface temperature of ∼2800 K [128] and has a radial velocity relative to the Local Standard of Rest (lsr) of $v_{\rm lsr} = 26.5\,{\rm km\,s^{-1}}$. It is a Mira-type pulsator with a period of 630 days [207]. These pulsations are believed to be the primary cause for circumstellar dust formation, and hence the wind-driving process. The luminosity of the central star (8300 $L_\odot$, [129]) efficiently couples to the opaque carbon-rich dust and rapidly accelerates the dust outwards [41]. Collisions of the dust particles with the surrounding gas result in an intense stellar wind with a terminal velocity of 14.5 $\rm km\,s^{-1}$ [36] and a mass loss rate of 2×10^{-5} $M_\odot\ yr^{-1}$ [156], and hence in a vast circumstellar environment (CSE).

Because of its proximity, CW Leo has been the subject of intense scientific scrutiny over the past few decades. Hence, the star has become one of the, if not the best studied AGB star in the night sky in terms of circumstellar dynamics and chemistry. Early resolved observations have shown it to be surrounded by multiple concentric dusty and gaseous shells and arcs [120, 56, 103, 42]. The presence of these density inhomogeneities strongly suggests that the star is not undergoing isotropic mass loss, but that the outflow is instead strongly perturbed in the wind formation region. Indeed, high-resolution observations of the inner wind of CW Leo by e.g. Kim et al. (2015) and Stewart et al. (2016) [94, 177] show a chaotic clumpy inner wind structure, with no apparent well-defined morphology. And yet, continuum observations by Jeffers et al. (2014) [80] surprisingly show that the CSE of CW Leo possesses an equatorial high density dust band, strongly suggesting that the mass lost by the central star is focused along a preferential direction. The ALMA data studied in this chapter support this hypothesis.

In December 2012, CW Leo was observed during ALMA's cycle 0 (2011.0.00277.S, PI Decin), yielding spatially resolved band 9 observations of the CSE using the extended antenna configuration. The longest baselines permitted observations at an angular resolution of ∼ 0.2". This has allowed the inner wind of CW Leo to be studied in unprecedented detail. An extensive primary analysis of the full dataset by Decin et al. (2015) [41] has yielded new constraints on e.g. the gas velocity of the inner wind, and the spatial distribution of this gas. Surprisingly, the spatial distribution of the ^{13}CO rotational transition J =6−5 showed a large amount of structure, which suggested the possible presence of a spiral morphology. This was strongly supported by the unmistakable detection of a cylindrically symmetrical mass distribution comprised of shell-like structures in the orthogonal wide-slit position-velocity diagrams (PVDs, see Sect. 1.5.2).

In this chapter we refine the preliminary study of the morphology observed in the ^{13}CO J =6−5 emission by Decin et al. (2015) [41], which allows us to better constrain

the morphological properties of the circumstellar gas. This permits a more detailed study of the emission distribution. In particular, it enables to distinguish between the spiral structure, and the other (seemingly spiral unrelated) structures. Exposing the local dynamics prevailing in the inner winds of AGB stars helps pave the road towards understanding the processes which dictate subsequent evolution into the AGB progeny: the post-AGB stars and planetary nebulae (PN), whose morphological characteristics deviate substantially from that of the mostly spherically symmetric AGB predecessors.

6.2 ALMA data description

6.2.1 Data acquisition and reduction

For an extensive description of the ALMA observing set-up as well as an in-depth discussion of the continuum residuals we refer to Decin et al. (2015) [41]. We summarise the most relevant information here. CW Leonis was observed on 1st of Dec 2012 by ALMA for project code 2011.0.00277.S (Cycle 0, PI Decin), at ICRS position 09:47:57.4553 +13:16:43.749 (J2000), epoch 2012.92. All 18 antennae were present for the observations, providing baselines from 25 to 340 m. The shortest baselines in the observations impose a limit of ∼3" on the size of any structure that can be imaged accurately. Emission on scales 3"−6" is imperfectly sampled due to the poor uv coverage of the smallest baselines, and emission that is smooth over spatial extents larger than 6" is undetectable. The total observing time on IRC+10216 was 17.5 minutes. Standard ALMA observing and data reduction procedures were used, including phase-referencing. The flux scale is accurate to about 20% and the absolute astrometric error is less than 6 mas. The line-free continuum channels were used to self calibrate the continuum and the solutions applied to all target data, and then the continuum was subtracted. Image cubes were made for the lines present in the data, adjusted to constant $v_{\rm lsr}$ in the target frame.

6.2.2 ^{13}CO J =6−5 emission

The full dataset, including the ^{13}CO J =6−5 emission have been extensively discussed by Decin et al. (2015) [41]. We briefly summarise the most important points relevant to this work. The molecular emission in the full dataset shows no structure, except for the ^{13}CO emission, which exhibits clumpy and arc-like emission clumps and filaments. The channel maps are shown in Fig. 6.1. Though likely also present in the other molecules of the dataset, this complexity is not observed due to the extremely low abundances, pushing the signal in the density inhomogeneities below detection limits. Especially apparent in the channel map at -37.4 km s^{-1} is the appearance of a hook-like feature,

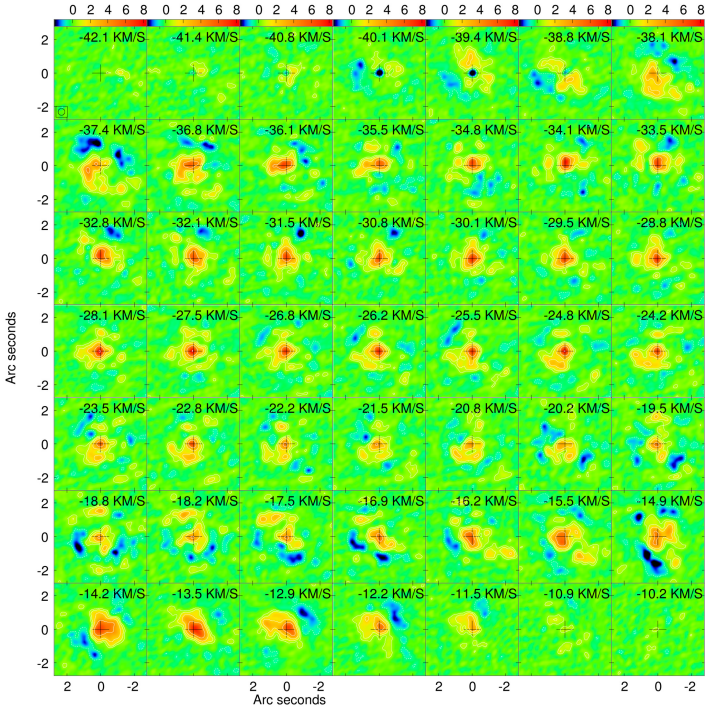

Figure 6.1: Tile plot of the channel maps of the ^{13}CO J =6−5 emission. The velocity bin is marked in the top right corner of each panel. Different arc-like features can be discerned. Flux density units are in Jy/beam. The contrast in the figure is best seen on screen. Figure adopted from Decin et al. (2015) [41].

which is the only prominently recognisable feature in the data. The seeming chaotic nature of the observed emission structures makes direct interpretation from the channel maps extremely difficult. Indeed, this property seems to also manifest in the spectral line, shown in Fig. 6.3. It shows no recognisable trends yet exhibits a surprising amount of structure.

As has been shown by Homan et al. (2015,2016) [72, 71], underlying correlated structures in the emission can be brought to surface by making use of wide-slit position-velocity diagrams (PVDs). This method was applied by Decin et al. (2015) [41], resulting in the emergence of unmistakable structural trends in the emission distribution. These correlated structures are shown through the PVD in Fig. 6.2, and strongly suggest the presence of an almost edge-on spiral pattern. A preliminary morphological analysis by Decin et al. (2015) [41] has yielded some first geometric constraints on the spiral

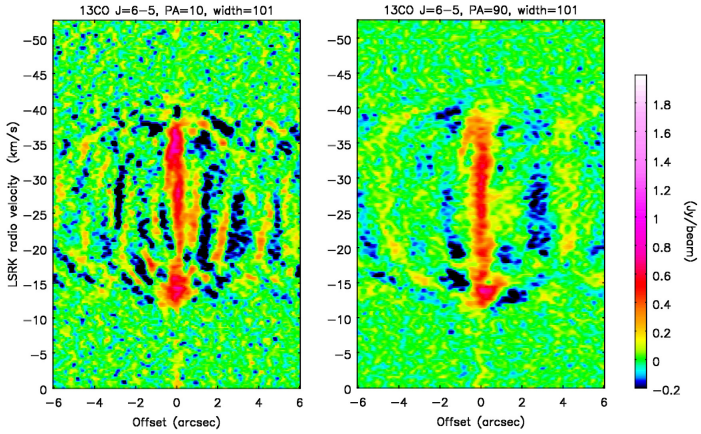

Figure 6.2: Wide-slit position velocity diagrams of the ^{13}CO J =6−5 emission, for different position angles. The slit has a width of 101 resolution element widths. The position angle is indicated in the title of each panel, and is defined to be the angular offset to the west. Figure adopted from Decin et al. (2015) [41].

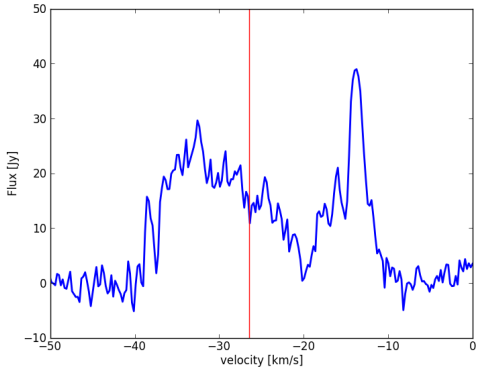

Figure 6.3: Spectral line of the ^{13}CO J =6−5 transition. The flux has been collected from a square aperture of 21", centered on the continuum peak [41]. The red vertical line indicates the velocity of CW Leo with respect to the local standard of rest.

shape. We discuss and use these constraints later in our fully 3D NLTE radiative transfer modelling efforts.

6.3 Computational methods

In this section we briefly describe the computational methods and strategy used to model the extended ^{13}CO J =6−5 emission. The method is identical to the methods used by Homan et al. (submitted) in the radiative transfer study of the CSE of the star L_2 Puppis.

We perform 3D radiative transfer using the `LIME` code [19]. For a technical overview of the inner workings of the code, see Chapter E in the appendix, or Brinch et al.(2010) [19]. The output is subsequently subjected to the simulation observation algorithms of `CASA` to generate 3D synthetic data that can be directly compared to the observed CW Leo data.

6.3.1 LIME:

For the radiation transport calculations the full 3D, non-local-thermodynamical-equilibrium (NLTE), infrared (IR) and submillimeter radiative transfer (RT) code `LIME` was used. For a technical overview of the inner workings of the code, see Sect. E in the appendix, or Brinch et al.(2010) [19]. The physical model is sampled by 10^5 grid points, of which half are distributed logarithmically (gradually refining the grid towards its center) and half are distributed randomly. In addition, the position of the grid points is weighted by relative density, further increasing the mesh refinement in the high-density regions of the model. Another 3×10^4 grid points are positioned at the edge of the numerical domain, representing the points where the RT calculations are finalised. This total of 13×10^5 grid points are Delaunay-triangulated to form approximately 7×10^5 tetrahedral cells, which are subsequently Voronoi-tesselated and inside which the physical conditions are assumed to be constant. The physical set-up is described in terms of density, temperature, molecular abundance, and macro- and micro-scale velocity fields. In order to determine the mean intensity field, the RT equations are solved along the Delaunay lines connecting the neighbouring grid points, up to the edge of the numerical domain. Once the RT calculations are finalised, and the level populations have converged, the simulation is ray-traced from a specific vantage-point. The radiative CO data of the LAMDA database [165] were used, the collisional rates were taken from Yang et al. (2010) [210]. Because of its low electric dipole moment, the surrounding radiation field is not expected to affect the CO emission much. Nevertheless, both dust and the stellar radiation field were taken into account in the radiative-transfer calculations. The dust composition has been adopted from De Beck et

al. (2012) [36], with the dust density distribution following the gas density distribution and a gas to dust mass ratio of 100. The stellar radiation field is approximated by a black body, with a temperature of 2800K and a luminosity of 8300 $L_{\odot}$.

6.3.2 CASA:

After having retrieved the intrinsic emission distribution from `LIME`, we have post-processed it with `CASA` [126] in order to simulate an observation with ALMA. The actual general observation conditions and instrumental set-up have been adopted as input parameters for the simulations, and are given in Table 6.1. In these simulations we have used the same antenna locations as for the observation, to ensure consistent visibility plane coverage.

Simulation Parameters	
Pixel size of input model	0.038”
Field size of input model	12.0”
Peak flux	Taken from `LIME` output
Molecule	^{13}CO
Transition	J =6−5 (661.1255 GHz)
Pointing	Single
Channel width	220 m/s
Precipitable water vapor	0.55 mm
Thermal noise	standard
Temperature	269 K
Integration time	1020 sec on-source

Table 6.1: The ALMA observation simulation specifications.

6.3.3 Modelling strategy

We perform this analysis based on a singular spectral line of carbon monoxide, observed in the ALMA cycle 0. This has some important consequences. Because carbon monoxide is mostly collisionally excited, temperature, density, and molecular abundance are fully degenerate (see Sect. 2.5.1). To cope with this, we have based the physical properties of our radiative transfer model of the inner wind of CW Leo on all the available relevant literature, on the star CW Leo itself, as well as on the general properties of spiral patterns. Furthermore, our final model is not produced via the extensive exploration and statistical analysis of a grid of models covering the vast number of free parameters. Such an effort can simply not be done with present-day computational facilities. The final model we present here was created by visual

reproduction of the emission patterns via iterative adjustment of the model parameters. Thus, our final model reflects the set of physical and gemoetrical conditions whose simulated emission best visually resembles the ALMA emission patterns, instead of a statistically sound product which derives from extensive and detailed post-processing.

6.4 Physical structure of inner wind of CW Leo

6.4.1 Dominant and turbulent velocity field

Because of the obvious spread on the measured inner wind (radii < 50 AU) velocities by Decin et al. (2015) [41], we believe the actual local velocity field is very complex, and most likely dominated by intense surface pulsations of the mass losing star [58], combined with the perturbations caused by the binary companion [92]. Nevertheless, the velocity field of CW Leo can be adequately approximated by assuming a rudimentary fitting of the measured wind velocities of the lines in the original ALMA dataset. We assume that the wind velocity field v_w can be sufficiently approximated with a standard beta law

$$v_w = v_0 + (v_\infty - v_0)\left(1 - \frac{R_c}{r}\right)^\beta, \tag{6.1}$$

where R_c is the dust condensation radius, v_0 is the unaccelerated wind prior to dust condensation, v_∞ is the terminal velocity of the wind, β is a measure for the efficiency of the acceleration of the wind, and r is the radial coordinate. The final model parameter values are found in Table 6.2. For the small-scale random motions of the gas in the wind $v_{\rm sto}$, we use the value found by De Beck et al. (2012) [36]. This value can also be found in Table 6.2.

Table 6.2: Velocity profile parameters for the inner wind.

Radial velocity parameters	
v_0	$5\,\mathrm{km\,s^{-1}}$
v_∞	$14.5\,\mathrm{km\,s^{-1}}$
R_c	15AU
β	0.1
Small-scale random motions	
$v_{\rm sto}$	$1.5\,\mathrm{km\,s^{-1}}$

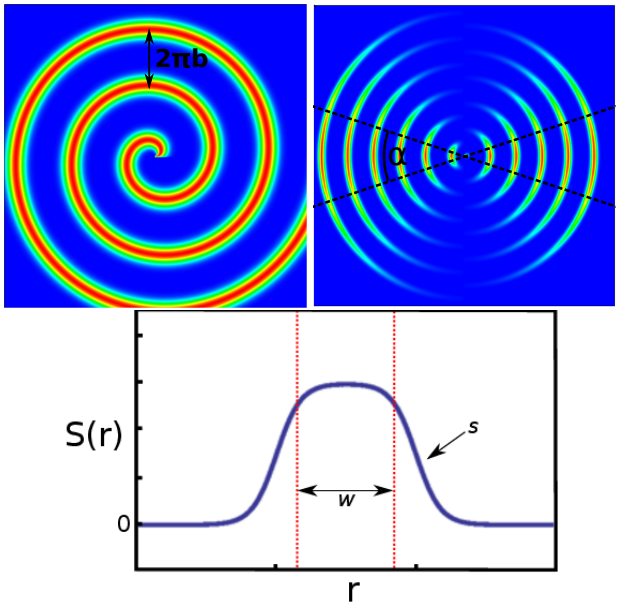

Figure 6.4: Visualisation of the geometrical parameters. *Left panel:* A slice through the equatorial plane of the spiral morphology. The parameter b is related to the spacing between the spiral arms. *Right panel:* A slice through a meridional plane of the same spiral model, where the opening angle α has been indicated. *Middle panel:* Radial plot of a portion of the equatorial spiral pattern $S(r, \phi)$, at constant ϕ.

6.4.2 H_2 density constraints

To properly reproduce the emission features presented by Decin et al. (2015) [41], the wind density must be partitioned into two distinct contributions. The first is the smooth outflow, for which the density $\rho_{\rm so}$ is given by

$$\rho_{\rm so} = \frac{\dot{M}_{\rm so}}{4\pi r^2 v_w}, \tag{6.2}$$

where $\dot{M}_{\rm so}$ is the mass loss rate through the smooth outflow. Superposed onto this density profile is a spiral pattern, with a density $\rho_{\rm sp}$ comprised of three major parts

$$\rho_{\rm sp} = \rho_r(r)\, S(r, \phi)\, T(\theta). \tag{6.3}$$

Here, ρ_r is the radial density trend of the peak density values in the spiral arms, $S(r, \phi)$ is the equatorial spiral pattern (with $\phi = \arctan(y/x)$ the equatorial angle), and $T(\theta)$ is the vertical spiral pattern (with $\theta = \arccos(z/r)$ the vertical angle). Analytically, these

components are expressed as

$$\rho_r(r) = \rho_0 \left(\frac{R_0}{r}\right)^p , \tag{6.4}$$

where ρ_0 is the density value at radius R_0, and p is the slope of the radial density power law;

$$S(r,\phi) = \frac{1}{e^{s(r-b\phi-w/2)}+1} - \frac{1}{e^{s(r-b\phi+w/2)}+1}, \tag{6.5}$$

where $2\pi b$ is the radial separation between the spiral arms, w is a measure for the width of the spiral arms, and s is a measure for the radial steepness of the spiral arm edges;

$$T(\theta) = \exp\left(-\frac{(\theta-\frac{\pi}{2})^2}{2\alpha^2}\right), \tag{6.6}$$

where α equals the one-standard-deviation Gaussian opening angle of the vertical spiral pattern. The total density ρ_w of the wind is then given by $\rho_w = \rho_{so} + \rho_{sp}$. The equatorial geometrical parameters (w, s, b) have been directly deduced from the ^{13}CO datacube. Because the spiral has such a large vertical extent, it must be created primarily due to the rotation of CW Leo around the center of mass of the binary system. The inner boundary of the spiral has been placed at the stellar surface, at a radius R_0 of 3 AU [129]. The remaining parameters have been completely newly constrained. The final model parameters are found in Table 6.3.

Table 6.3: Density parameters for the inner wind.

Density parameters	
ρ_0	1×10^{-10}kg/m^3
$\dot{M}_{so}$	4×10^{-5} M$_\odot$ yr^{-1}
R_0	3AU
p	1.5
s	1/(3AU)
$2\pi b$	200AU
w	20AU
α	25°

6.4.3 Spiral temperature

As for the density, the temperature also consists of two components. One temperature profile $T_{so}(r)$ for the smooth outflow, and one profile T_{sp} following the spiral density enhancements. The radial temperature distribution of the smooth outflow has been

adopted from De Beck et al. (2012) [36]. The temperature of the spiral pattern exactly follows the spiralling density distribution. It has the following form

$$T_{\rm sp} = T_r(r)S(r,\phi)T(\theta), \tag{6.7}$$

where $T_r(r)$ is the rate at which the temperature drops radially. In order to mitigate the difficulties arising from the degeneracy described in Sect. 6.3.3, we have chosen to fix the value of $T_r(r)$ based on the results by Kim et al. (2012) [96]. They found that the temperature in the spiral arms is well approximated by the temperature of the smooth outflow at the location of the spiral arm, multiplied by a universal scaling factor γ. Hence, we express $T_r(r)$ as

$$T_r(r) = \gamma T_{\rm so}(r). \tag{6.8}$$

The value for γ has been set to 10 in these simulations, following the findings of Kim et al. (2012) [96].

6.4.4 ^{13}CO molecular abundance

Decin et al. (2010) [40] and De Beck et al. (2012) [36] found that the fractional abundance of ^{12}CO with respect to H_2 is around 6×10^{-4}, and that the carbon monoxide isotopologue ratio ^{12}CO over ^{13}CO is around 30. Hence, the assumed ^{13}CO abundance with respect to H_2 has been assumed to be 2×10^{-5}.

6.5 Radiative transfer results

We have simulated the observables for an almost edge-on appearance of the spiral, at an inclination of 70 degrees. This inclination angle has been deduced by comparing the PVDs of the data with the PVDs of the synthetic embedded spiral models presented in Homan et al. (2015) [72].

The predicted channel maps of the radiative transfer calculation are shown in Fig. 6.5. Comparing with the real data (Fig. 6.1), one can see that some important features have been reproduced. The hook-like feature around -37 km s^{-1} is present both in the synthetic and in the real data, strongly suggesting that it is spiral-related. In addition, the two distinct emission patches to the north-east and to the south-west of the center, visible in most of the channel maps, are also present both in the real as in the synthetic data. These correspond with the emission of the innermost spiral windings, taking into account the position angle of the ALMA data. Finally, the large emission patches at high red- and blue-shifted velocities have also been properly reproduced. However, much of the smaller scale emission structure has not been reproduced by the spiral

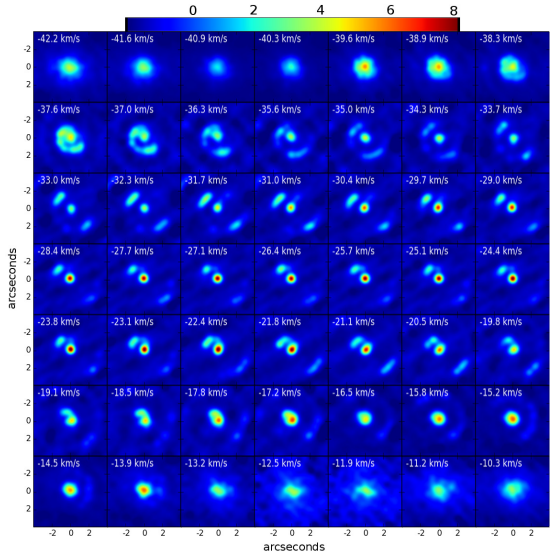

Figure 6.5: Tile plot of the channel maps of the synthetic emission. The contrast in the figure is best seen on screen. Flux density units are in Jy/beam.

model. We conclude that the source of these clumpy features is probably not related to the spiral, but instead caused by other, more localised phenomena.

The PVDs presented in Fig. 6.6 show a remarkable resemblance to the real data. Indeed, as for the channel maps, much of the smaller-scale detail is not present in the synthetic PVDs, but the correlated structures first identified by Decin et al. (2015) [41] are prominently recognisable. For the PVD constructed by placing the slit perpendicular to the equatorial plane of the spiral (the top panels in Fig. 6.6), the most important features have been reproduced, as well as the absolute strength of the emission. The central bar along zero spatial offset in the data is also prominently present in the simulation, with an increased emission patch around $-15\,\mathrm{km\,s^{-1}}$. In addition, the small hooks at maximal velocity are also present in the synthetic data, albeit not as pronounced. The PVDs constructed by placing the slit along the spiral equator (the bottom panels in Fig. 6.6) show more structure. The weak central bar around zero spatial offset has been accurately reproduced, as well as the relative strength of this bar with respect to the stronger emission patches at high velocity. Furthermore, the manifestation of the spiral arms in the PVD are also well reproduced. The arms in the data are more broken-up, suggesting that whatever dynamics caused the unreproduced emission structure in the channel maps is also likely responsible for perturbing the otherwise smooth spiral pattern.

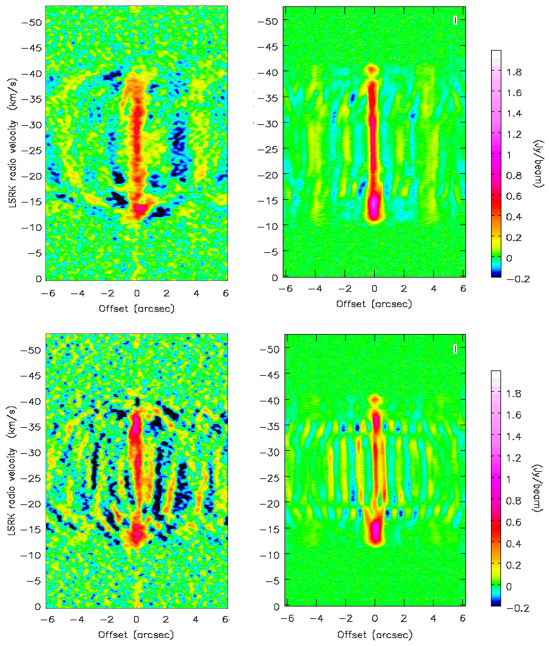

Figure 6.6: Comparison of the wide-slit PVDs of the ^{13}CO J =6−5 emission from the data (*left panels*), with the equivalent wide-slit PVDs of the radiative transfer model (*right panels*), for two position angles, 90° (*top*) and 10° (*bottom*).

We compare the spectral line of the synthetic model emission with the real data in Fig. 6.7. In this figure, both spectral lines are plotted together. This supports the claims made when comparing the channel maps. A fraction of the emission present in the data does not originate form the spiral pattern, but should be attributed to a different source. What is very interesting is that the spectral lines show that most of this extra (non-spiral-related) emission is localised in velocity-space. The most important difference is seen in the red shifted part of the spectrum. Here, almost half of the emission in the data cannot be reproduced by the spiral. On the blue shifted side the agreement is much better. Though a distinct emission spike is observed around -14 km s^{-1} which is also not explained by the spiral model. Finally, the signal in the synthetic emission seems to be slightly stretched beyond the velocity domain confined by the real data. This suggests that we may have overestimated $v_{\rm sto}$. This is possible seeing as the value used in this work was adopted from De Beck et al. (2012) [36], for whom the constraint on the magnitude of the small-scale random motions came primarily from emission from the outer wind of CW Leo. In addition, the value of $v_{\rm sto}$ is probably not contant throughout the whole wind.

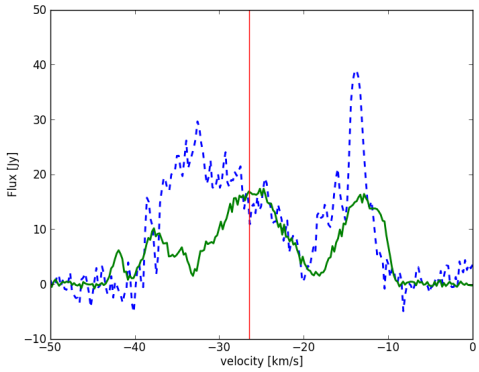

Figure 6.7: Spectral line of the ^{13}CO J =6−5 transition (*blue dashed line*), overlayed with the spectral line of the synthetic model (*green line*). Specifics are the same as in Fig. 6.3.

6.6 Discussion

6.6.1 Sensitivity of parameters

Because we cannot perform an extensive and in-depth exploration of the parameter space available to us, we cannot quantify the quality of the model in terms of statistically significant errors. Hence, we dedicate a section in the discussion to the sensitivity of the introduced parameters, and how well we can expect these parameters to be constrained by the work presented here.

To repeat the point made in Sect. 6.3.3, the modelling of a singular carbon monoxide transition implies that density, temperature and molecular abundance are completely degenerate. Therefore, because the density distribution is the primary focus, we have had to make important and well considered assumptions on the molecular abundance fraction and the temperature of the inner wind. The molecular abundance value has been carefully estimated in a detailed analysis by De Beck et al. (2010) [35], and is in agreement with the findings of Hinkle et al. (2016) [69]. The temperature profile of the smooth outflow has been retrieved by De Beck et al. (2012) [36] through one-dimensional radiative transfer efforts, for both low and high rotational transitions of CO. However, the simplification of performing the analysis in 1D may have yielded erroneous estimations on the inner wind temperature structure, especially considering that the contribution of the spiral pattern is implicitly contained within the analysed spectral line properties. Hence, if the temperature of the smooth outflow deviates

substantially from the results of De Beck et al. (2012) [36] (and thus the profile used here), then the absolute density constraints obtained here will be inaccurate. The results adopted from Kim et al. (2012) [96] for the spiral arm temperature are based on a specific case study of the AGB star AFGL 3068, from which we have adopted the value for γ. Again, we have no way to gauge whether their value for γ can be simply transferred to CW Leo. Any uncertainties there will also translate in uncertainties in the derived density properties.

We do not expect that our simplified expression for the velocity field introduces major uncertainties into the derived system properties. Though the acceleration of the gas can be directionally dependent due to the random convective agitation of the stellar surface [58], on average the gas accelerates from the dust condensation radius outwards. This is also seen in the general velocity trend obtained by Decin et al. (2015) [41]. Because this is an extreme carbon-rich environment, the acceleration happens so intensely that any non-radial or otherwise deviating acceleration contributions will most likely be comparatively negligible.

If we now assume that the temperature, molecular abundance and wind velocity field have been adequately constrained, then this permits the deduction of the physical and morphological properties of the density distribution. The equatorial morphological parameters (s, b and w) have been estimated from the emission distribution in the channel maps and in the PVDs. The physical density parameters (ρ_0, $\dot{M}_{\rm so}$) have been retrieved by delicately tweaking their values in the code to best reproduce the absolute and relative emission values observed in the data. And finally, the parameters p and α have been determined by reproducing the intensities and spatial extent of the spiral features in the data channel maps.

6.6.2 H_2 density considerations

Spiral Geometry

From the retrieval efforts in this chapter we deduce an opening angle α of 25 degrees. This means that around 95% of the mass of the spiral is contained within a wedge with an opening angle of 50°, around the equatorial plane. This suggests that, besides the formation of an equatorial spiral pattern by the gravitational funneling of the companion, the spiral shape is substantially influenced by the wobbling of the mass losing star around the center of mass of the system [92]. And this, in turn, implies that the companion mass must be quite substantial. From the retrieved geometrical values, it is impossible to accurately estimate the mass of the companion, but the relatively high mass of 1.1 $M_\odot$ derived by Decin et al. (2015) [41] appears to be in agreement with our findings here. Similarly, the findings of Cernicharo et al. (2015) [26] also deduce the need for the presence of relatively massive companion.

Both the inclination angle and the spacing of the spiral arms obtained here are in agreement with the first analysis. However, analysis of the large-scale gaseous shells [26] measure a spacing of the order of 750 AU. This strongly suggests that there are important shaping mechanisms which most probably compress the spiral shells as they travel outwards. The strong interplay between the stellar wobbling, the pulsational shocks and the gravitational funneling of the circumstellar gas into the spiral can be expected to generate unpredictable hydrodynamical outcomes, like the morphological discrepancy between the small and the larger scale structures.

The deduced width of the spiral arms (20 AU) is exactly two orders of magnitude larger than the ones obtained by Decin et al. (2015) [41]. The tested models with an arm thickness of 0.2 AU show almost no spiral pattern in the synthetic emission. We hence suspect that the value presented by Decin et al. (2015) [41] was mistakenly submitted, but that the correct value of 20 AU was used in their modelling with SHAPE [175].

Mass loss rate

The derived mass loss rate of 4×10^{-5} $M_{\odot}$ yr^{-1} is necessary to properly model the innermost emission of the channel maps, and especially the central bar in the bottom panels in Fig. 6.6. However, it is a value which is at least twice as high as the typically derived total mass loss rate of CW Leo. This can mean either of two things. Either our derived mass loss rate is erroneous, which would then most likely imply that the used temperature power-law is invalid in these innermost regions. Or, it is an accurate estimation of the current mass loss rate of the star. It is generally accepted that TP-AGB stars have a monotonically increasing mass loss rate with time [158, 188]. The mass loss rate derivations in the literature are mostly all based on analyses of low excitation spectral lines, which are primarily formed in the outermost regions of the stellar outflow, which have been expelled by the star a long time ago. Furthermore, most previous spectral analyses of CW Leo were performed under the assumption that the wind is smooth and spherically symmetrical, which is not the case [42, 26]. Recent models of the gaseous shells observed at angular scales of ~100" by Cernicharo et al. (2015) [26] finds mass loss rates in agreement with the value found in here.

Spiral mass

The slope of the spiral density power-law $p = 1.5$ is less shallow than the expected value of $p = 2.0$ if mass-conservation is assumed. We expect this deviation to be a consequence of the wobbling of CW Leo around the center of mass of the binary system and the chaotic stellar surface pulsation. Because of this shallow slope, the spiral contains a substantial amount of mass. The mass dynamically forced into the spiral shape amounts to around 1.2×10^{-5} $M_{\odot}$ yr^{-1}, or approximately 25% of the total

mass lost by the central star. This is an important fraction of the total mass budget, and seems somewhat implausible. Yet this can be readily explained by the fact that the resultant spiral shape observed in the ALMA data is not only caused by the gravitational funneling of the companion, but also by the wobbling of the mass losing star. This would cause global compression and stretching of the wind material, resulting in much higher spiral mass fractions [92]. However, this can only be the case if the mass of the secondary is comparable to the mass of CW Leo, because otherwise the wobbling would be too weak to form a detectable spiral with a wide opening angle. The multiple arcs which are almost universally seen in the CSE of CW Leo at larger spatial scales can hence be the final remnants of the spiral arms, which can only remain detectable at such spatial scales if the spiral contained a substantial amount of mass to begin with.

Residual unmodelled emission

The residual emission left unmodelled by the spiral pattern is localised in velocity-space. Fig. 6.7 shows that the large difference between the data and the model emission are located primarily in the region between -27 km s^{-1} and -37 km s^{-1}, and around -14 km s^{-1}. This exceptionally localised, asymmetrical emission indicates that besides the spiral-shaping mechanism (which is most likely binary related), other morphology inducing processes co-dominate the inner wind. The most plausible scenario is probably the random convective agitation of the stellar surface layers [58], causing directional mass loss. If the convective cells are large enough, then the random directional mass loss can be quite substantial. A large burst of backwardly propagated material could have generated the excess red shifted emission, while a smaller frontward burst could have produced the blue shifted peak. The presence of such a chaotic wind shaping mechanism is supported by the vast difference in observed emission structure between the data channel maps and the synthetic ones. The data shows much more fine structure in the emission close to the central star, with no seeming directional preference, both spatially or spectrally. In addition, the PV diagrams show a highly 'chopped-up' spiral, with interrupted features, and seemingly scattered sections of spiral arms. The larger scale arcs discussed in the literature can hence be the remnants of this disintegrating spiral.

6.7 Summary

The contents of this chapter are based on data first presented by Decin et al. (2015) [41], who have performed a first rudimentary analysis of the morphological features present in the ^{13}CO J =6−5 spatial emission distribution. We have refined the spiral model used to first fit the data, by doing a rigorous three-dimensional NLTE radiative transfer analysis of the morphological and spectral aspects of the data. Our analysis supports

that, as claimed by Decin et al. (2015) [41], the inner wind harbours an embedded spiral morphology. The spiral has an arm width of 20 AU, an inter-spiral arm distance of 200 AU, a radially decaying density power of −1.5, and a vertical extent of 25° below and above the equatorial plane. The magnitude of the vertical extent of the spiral strongly suggests that the primary spiral-shaping mechanism is not the gravitational funneling of the wind material by the companion, but rather the wobbling of the mass losing star around its center of mass. This implies that the mass of the companion must be of comparable magnitude to the current mass of CW Leo, strengthening the hypothesis first made by Decin et al. (2015) [41]. The current mass loss rate of CW Leo has been estimated to be 4×10^{-5} $M_{\odot}$ yr^{-1}, which is approximately twice as much as previously estimated mass loss rate in the literature. The mass calculated to be contained within the spiral amounts up to 25% of the total mass bugdet. This seems excessive, but can be explained by the global compression of the wind material as the mass losing star wobbles around the center of mass of the binary system. Finally, much of the smaller scale emission present in the data is not explained by the spiral. We hypothesise that these structures are caused by convective stellar surface pulsations which result in highly anisotropic mass loss and shock waves.

Chapter 7

Summary and conclusion

This PhD thesis focused primarily on the observational challenges associated with the complex morphologies harboured by the stellar winds of AGB stars, and specifically addressed embedded spiral structures and equatorial density enhancements. The work presented in this manuscript can be divided up into two major categories: (1) theoretical pattern production and recognition, and (2) observational pattern recognition and retrieval.

In the theoretical studies, we compiled a database of expected emission patterns of the two above mentioned morphologies through extensive radiative transfer parameter studies. This is timely because with the onset of exceptionally high spatial resolution submm telescopes, the detail with which these circumstellar environments can be imaged to superceed previous imaging attempts, showing structure and features which are typically very difficult to interpret by visual inspection. This difficulty arises from the fact that the acquired images are two-dimensional projections of three-dimensional (velocity dependent) surfaces on which the emission is probed, per frequency. Hence, the combination of these projection effects can substantially alter the appearance of an otherwise easily identified morphology. We compiled a directory of expected emission patterns for embedded spiral morphologies and equatorial density enhancements. To achieve this, we have produced approximate analytical models of the morphologies of interest, and parametrised these expressions in terms of their most important geometrical and physical properties. These have been obtained from the literature. Subsequently, the effect of each parameter on the resulting observables (channel maps, position-velocity diagrams and spectral lines) has been carefully probed. The resulting synthetic emission patterns can now be used by astronomers to help with the identification of prominently present, or potentially hidden morphologies in the stellar winds of evolved stars. The most important conclusions can be found at the end

of Chapters 2 and 5. Specifically, we find that orthogonal wide-slit position-velocity diagrams are the ideal tool to identify AGB CSE morphologies, and to make first-order estimations on the local conditions.

Subsequently, we show the importance and use of this theoretical bedrock by performing extensive radiative transfer retrieval efforts on ALMA data, both for a disk-harbouring CSE (L_2 Puppis, Chapters 3 and 4), and for an embedded spiral structure (CW Leonis, Chapter 6). The first notable achievement is the ability to immediately identify the morphology in question by comparison with the previously obtained theoretical results, by making use of the abovementioned position-velocity diagrams. Once the observed morphology had been unambiguously identified, we proceed to extract all geometrical and physical properties of the systems by delicate iterative procedures attempting to best reproduce the emission patterns through 3D radiative transfer. This has yielded some surprising results. For example, in Chapter 3 we identify a possible planetary companion in the vicinity of the mass losing star L_2 Puppis, and in Chapter 4 we determine that the inner rim of the modelled disk is situated at the estimated location of this tentative planetary companion, indicating that its presence may be related to the formation of the disk. The modelling of spiral structure embedded in the outflow surrounding the AGB star CW Leonis suggests the presence of a massive companion, with a mass of the order of a few Solar masses, via two distinctly different geometrical properties of the spiral.

The power of the pattern recognition procedures developed in this thesis lies in the fact that they are a means by which high-resolution data can be more easily interpreted, paving the way to deeper understanding of the physical mechanisms responsible for the asymmetric structures.

Bipolar post-AGB stars and PNe almost always exhibit disk-like structures, often interpreted as caused by a binary companion, suggesting their presence influences the global morphology of the system. Studies of stellar companions travelling through the inner AGB wind show that the CSEs can be potentially distorted to such a degree that the resulting morphologies become strongly directionally dependent, disk-like structures. And now, with our study of the L_2 Puppis system, we find important clues that even low mass companions may contribute to global wind shaping. Indeed, if planets have the power to influence CSE morphology to this degree, then we may find wind-binary interactions to be a leading cause of asphericity in AGB CSEs, hence possibly even explaining the first steps of the shaping mechanism of highly complex PNe, as has been suggested before [173]. Future studies of AGB wind morphologies may reveal the importance of planetary companions on (post-) AGB evolution, and will undoubtedly yield surprising results.

Appendix A

Appendix to chapter 2: Channel maps of the calculated models

In this section we show the channel maps of the radiative transfer models which have been discussed in the paper above. To this end, we have respresented the synthetic 3D data by means of a 4 by 4 tile plot, showing slices throughout velocity space. The used colour coding is dictated by the linear colourbar shown in Fig. 2.5.

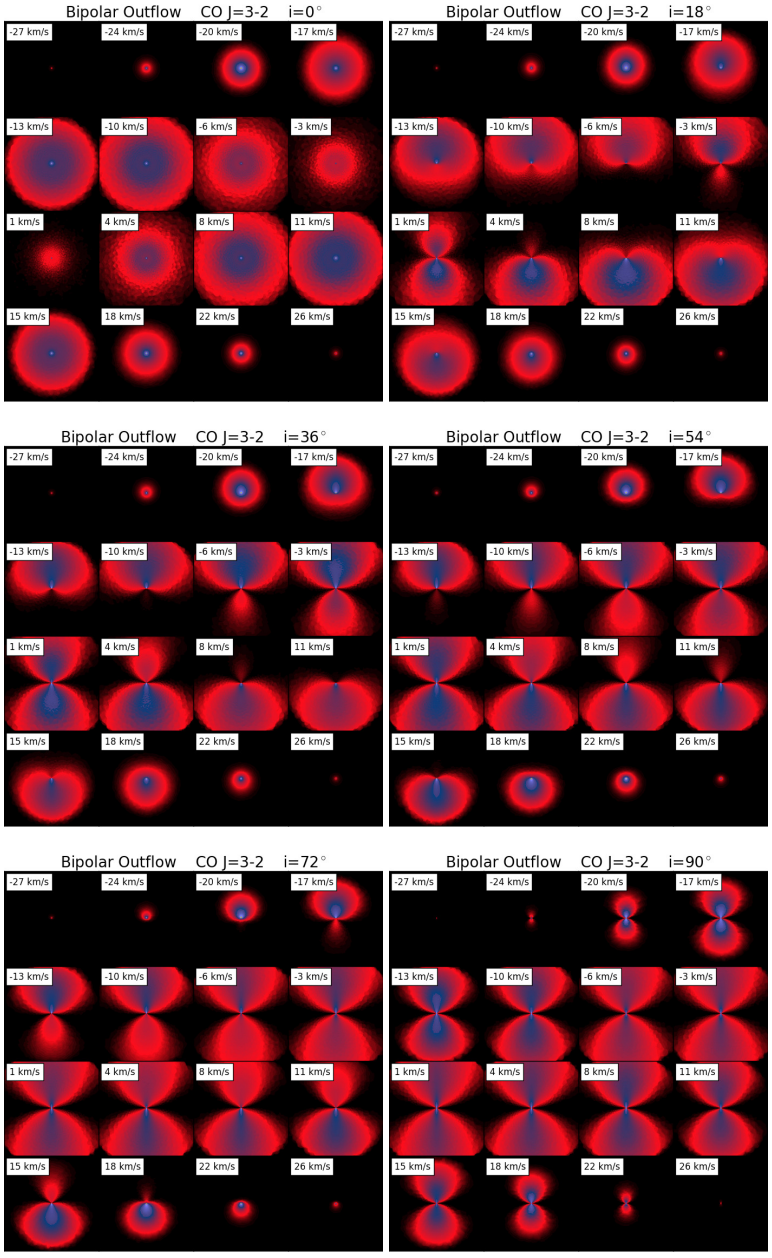

Figure A.1: Channel maps of the bipolar outflow model, as a function of inclination.

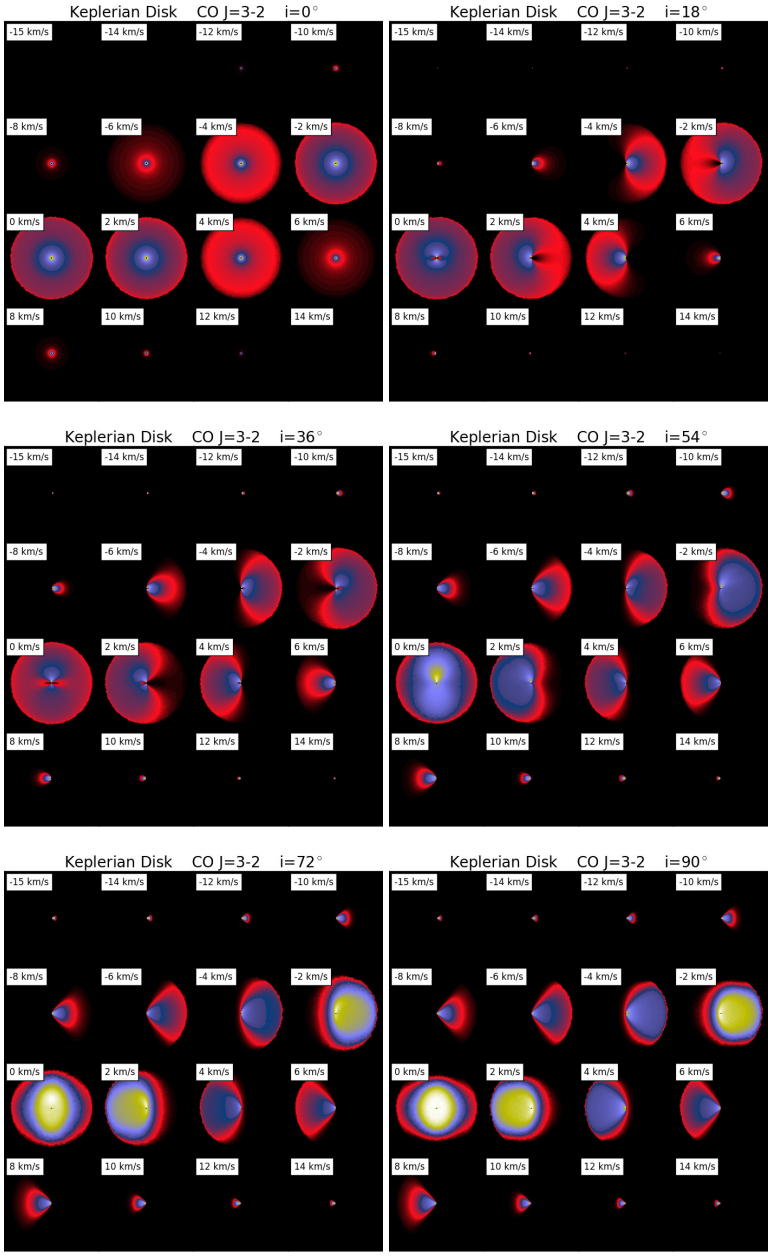

Figure A.2: Channel maps of the Keplerian disk model, as a function of inclination.

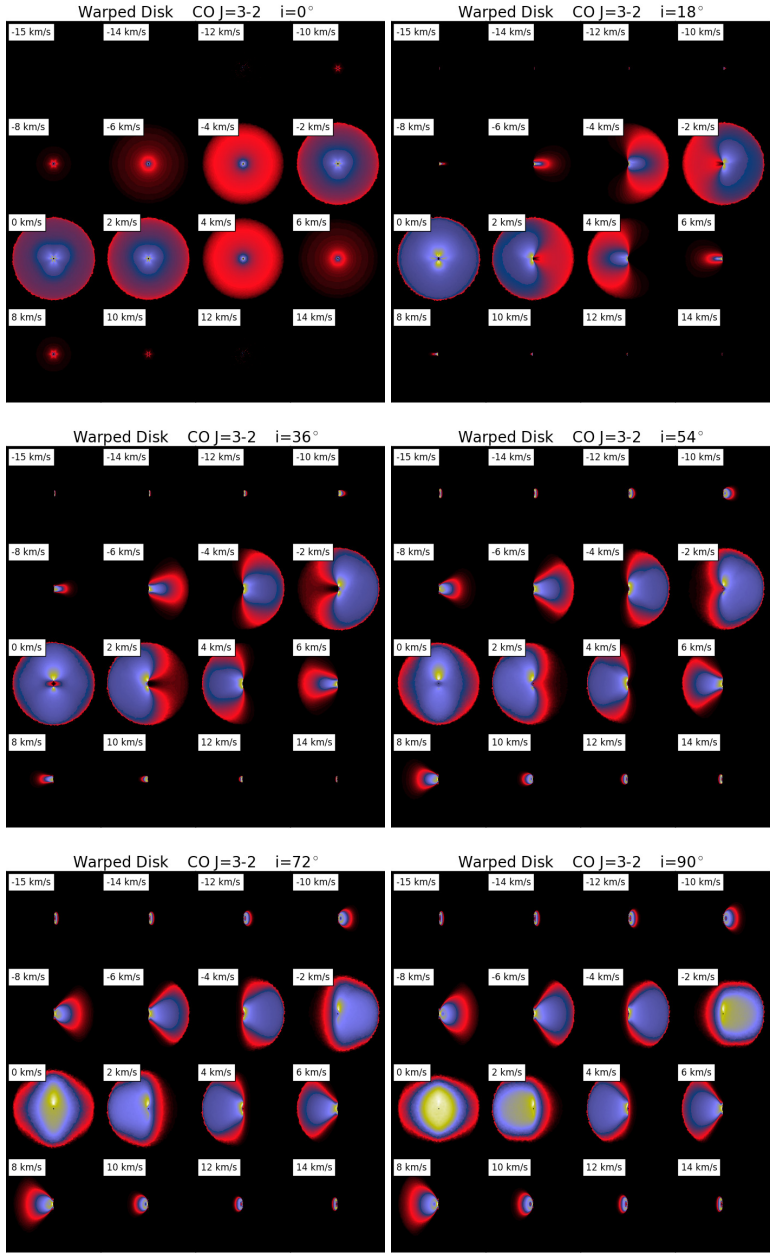

Figure A.3: Channel maps of the warped Keplerian disk model, as a function of inclination.

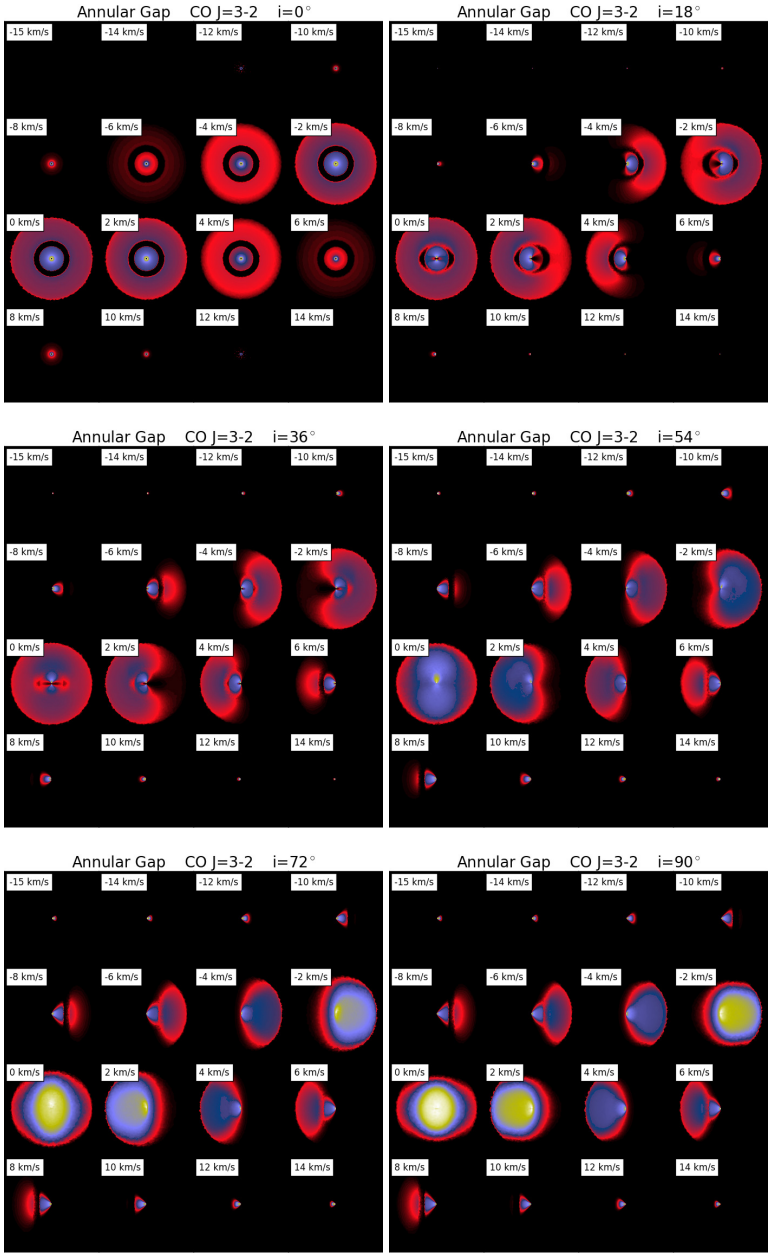

Figure A.4: Channel maps of the Keplerian disk with an annular gap, as a function of inclination.

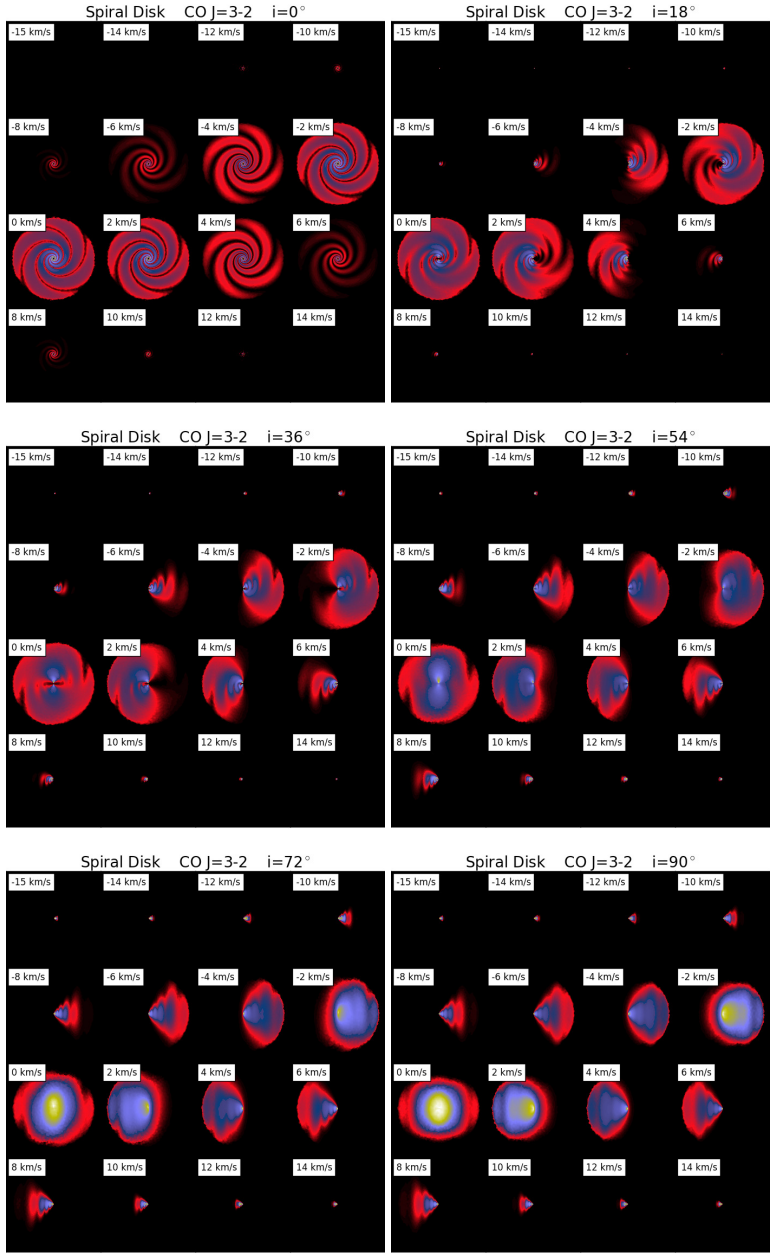

Figure A.5: Channel maps of the Keplerian disk model, with spiral instabilities, as a function of inclination.

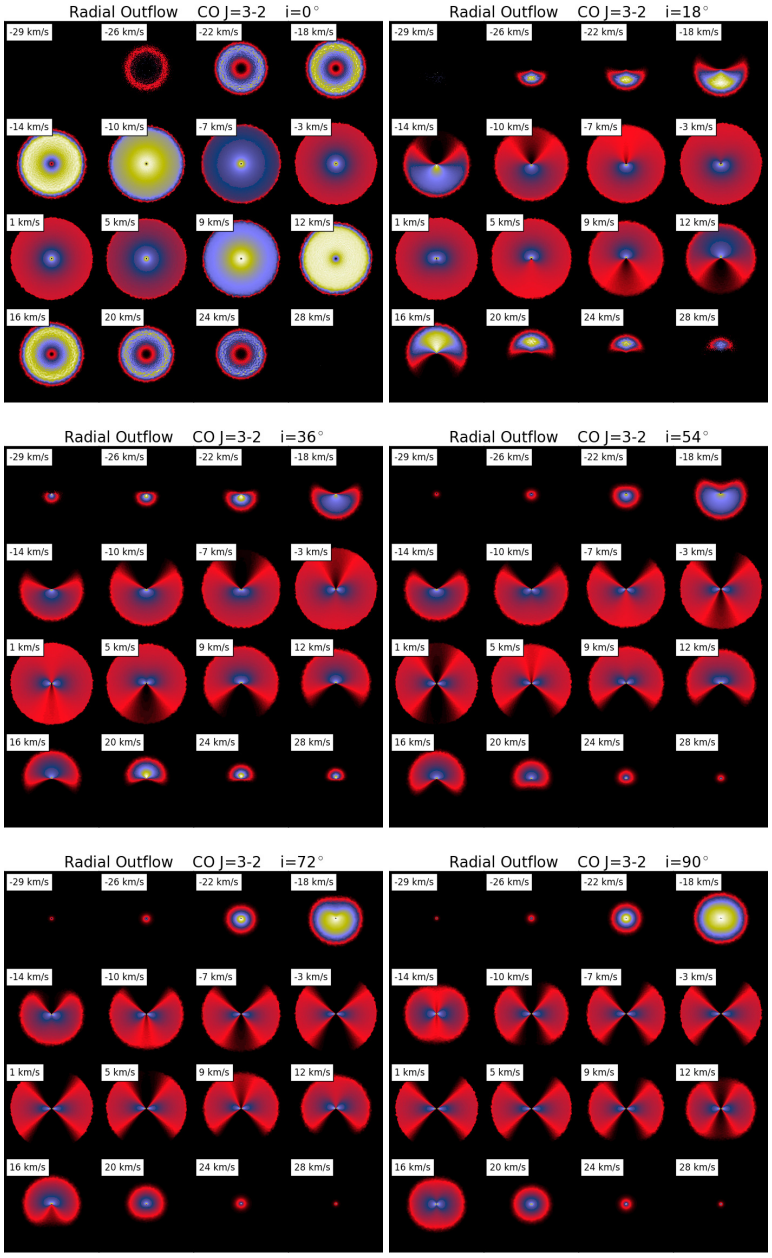

Figure A.6: Channel maps of the torus model with a radial velocity field, as a function of inclination.

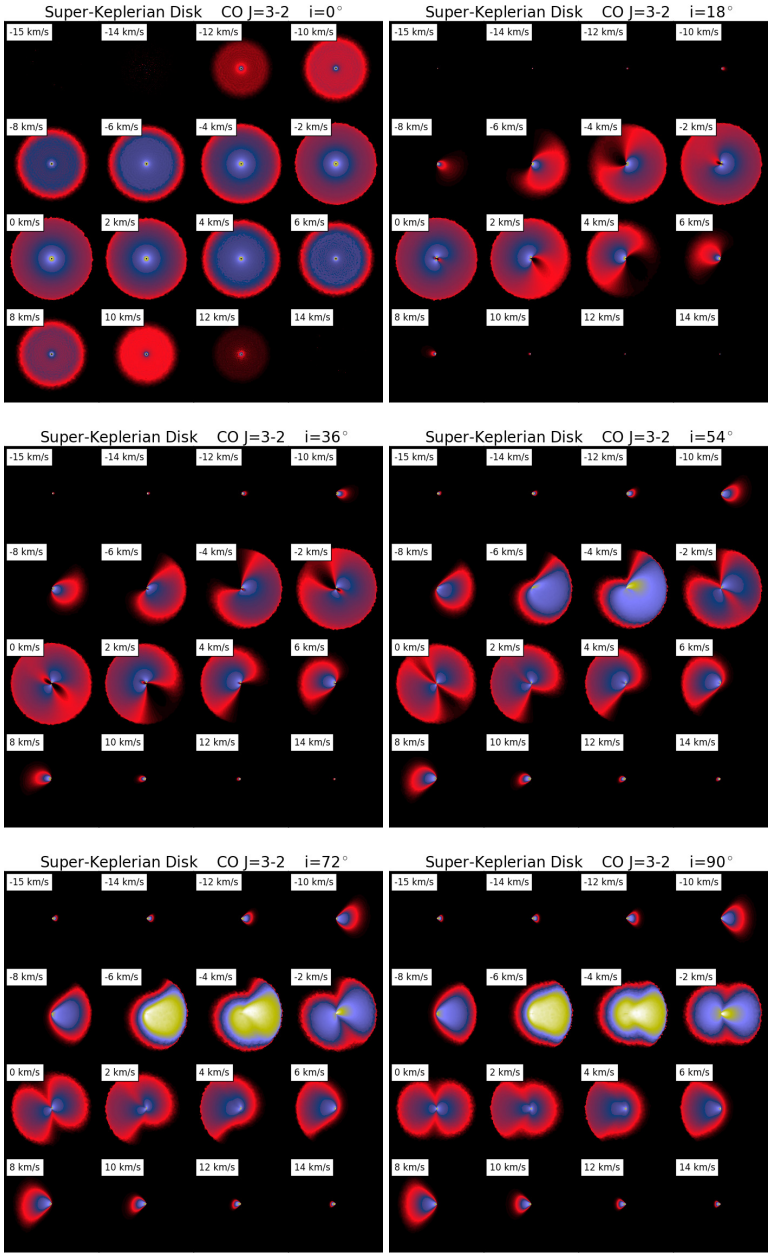

Figure A.7: Channel maps of the super-Keplerian disk model, as a function of inclination.

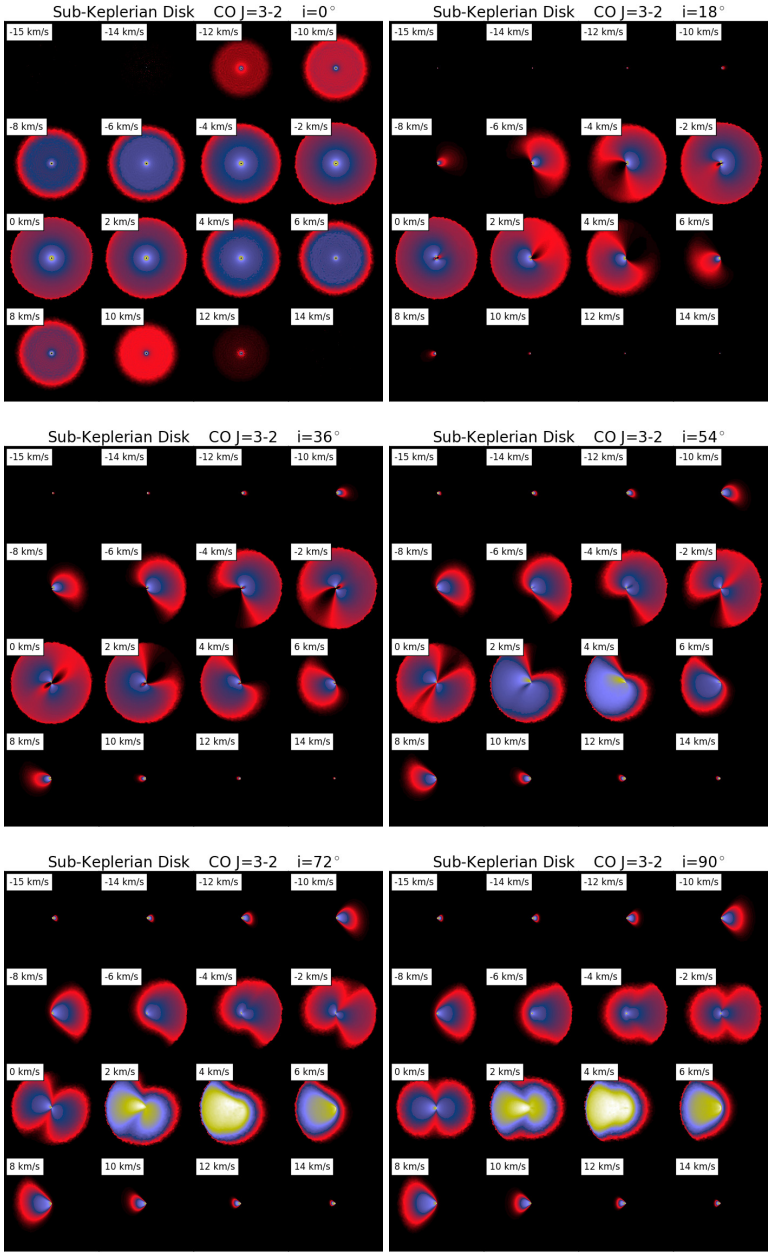

Figure A.8: Channel maps of the sub-Keplerian disk model, as a function of inclination.

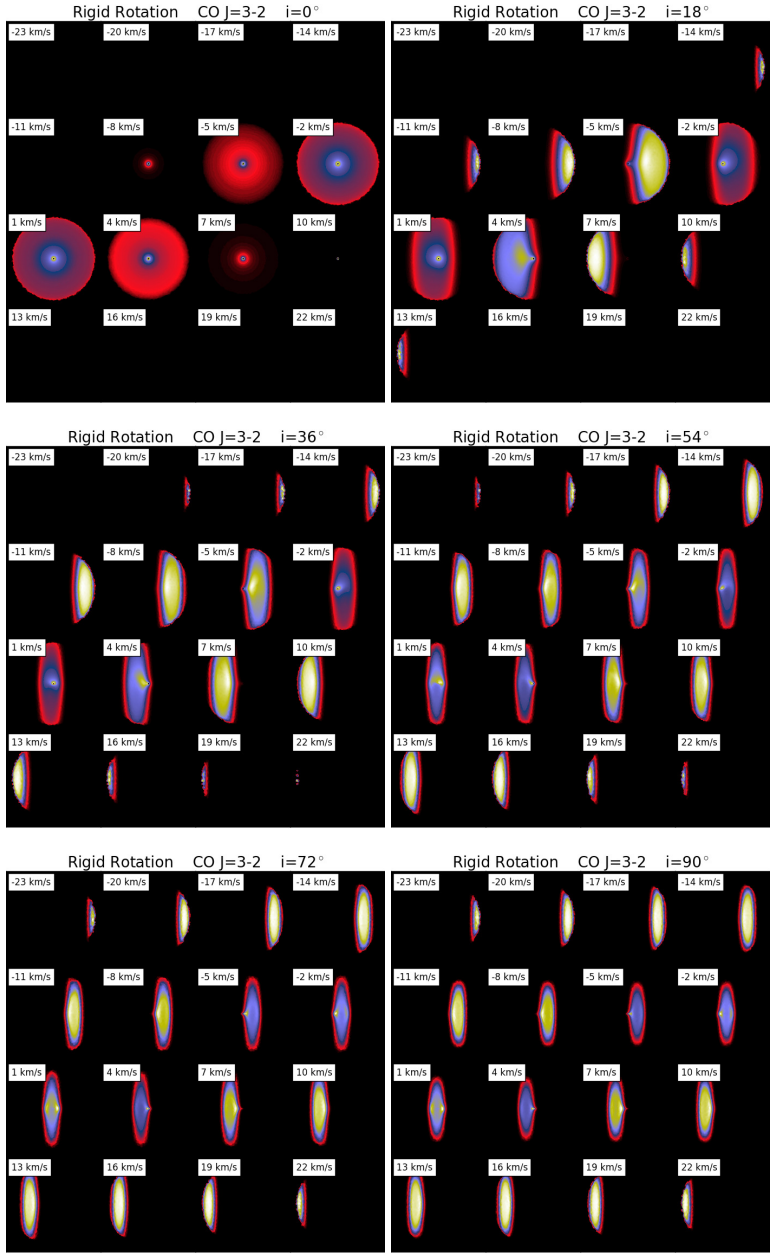

Figure A.9: Channel maps of the rigidly rotating disk model, as a function of inclination.

Appendix B

Appendix to chapter 3: molecular emission of L_2 Puppis ALMA cycle 3 dataset.

B.1 ^{12}CO($\Delta v = 0, J = 3 - 2$) line

The emission of L_2 Pup in the ^{12}CO line is presented in Fig. B.1 (top panel). The total peak intensity is 0.35 to 0.40 Jy beam^{-1} km s^{-1} and the maximum emission is located at a radius of approximately 2 AU. The degree of asymmetry is small, although the position angles of the emission peaks are slightly tilted with respect the position angle of the plane of the disk. We detect ^{12}CO($v = 0, J = 3 - 2$) emission between -20 and +20 km s^{-1} relative to the mean velocity of L_2 Pup (+33.0 km s^{-1}). Within a 0.63 arcsecond aperture, we measure an emission peak of 5.4 Jy, centered close to the stellar velocity. Single-dish observations by Kerschbaum et al. (1999)[85] showed spectral peaks that are several times higher than ALMA in the same transition of CO but only close to the stellar velocity. This suggests that in addition to the high-velocity CO detected by ALMA close to the star, there exists an extended, slowly expanding, diffuse envelope that is resolved out by the long baselines of the interferometer.

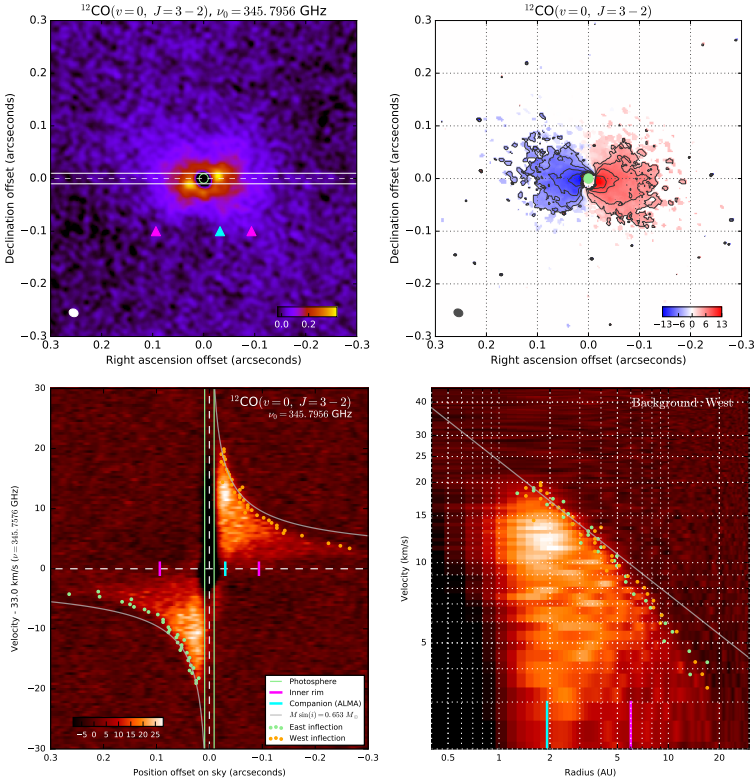

Figure B.1: *Top left panel:* Map of the emission from L_2 Pup in the ^{12}CO($\Delta v = 0, J = 3 - 2$) line. *Top right panel:* First moment of velocity map (color scale in km s^{-1}). The contours are drawn between 4 and 10 km s^{-1} with a 2 km s^{-1} step, and the size of the photosphere is shown with a light green disk. *Bottom panels:* Position-velocity diagram of the ^{12}CO($\Delta v = 0, J = 3 - 2$) emission line. The Keplerian velocity profile corresponding to a central mass of $M \sin(i) = 0.653\ M_\odot$ (determined from the ^{29}SiO line fit) is shown with gray curves in the two panels.

B.2 ^{13}CO($\Delta v = 0, J = 3 - 2$) line

The ^{13}CO emission of L_2 Pup (Fig. B.2, top panel) has a similar radial extension to the ^{12}CO line but the ^{13}CO isotopologue appears significantly more confined in the plane of the disk. The total peak intensity is comparable to ^{12}CO (0.35 to 0.40 Jy beam^{-1} km s^{-1}) and the maximum emission is also located at a radius of approximately 2 AU. The position angles of the emission peaks is less tilted than ^{12}CO with respect the east-west

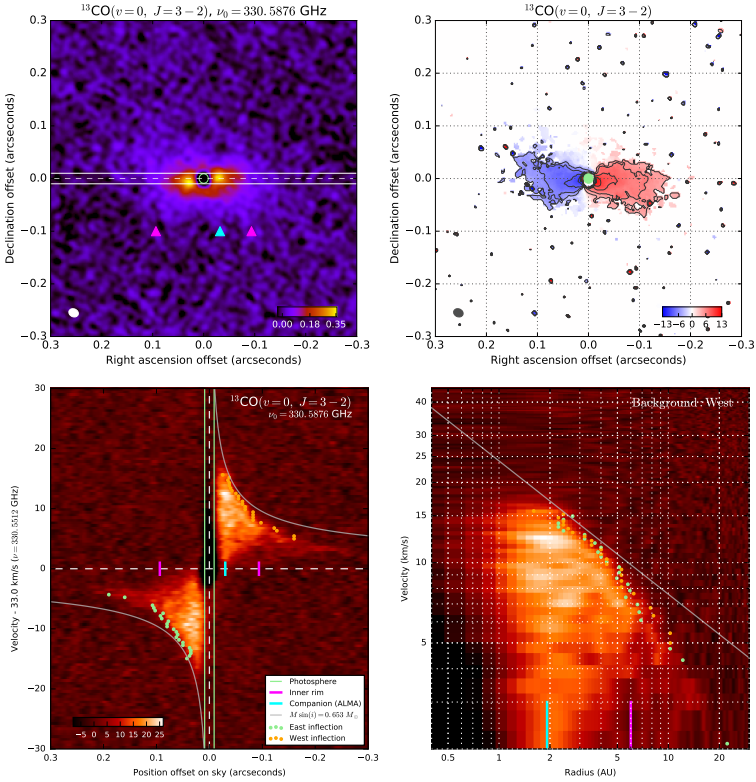

Figure B.2: *Top left panel:* Map of the emission from L_2 Pup in the ^{13}CO($\Delta v = 0, J = 3 - 2$) line. *Top right panel:* First moment of velocity map (color scale in km s^{-1}). *Bottom panels:* Position-velocity diagrams.

axis of the disk.

B.3 $SO_2(\Delta v = 0, 34(3,31) - 34(2,32))$ line

As shown in Fig. B.3 (top panel), the sulfur dioxide emission is spread over a large vertical extension of approximately ± 0.1" with respect to the disk plane. The PVD is incomplete as the line was located close to the edge of the spectral window. In the flux image, the emission appears stronger on the east side of the disk, but this is an artifact due to the incompleteness of the coverage of the frequencies showing Doppler shifted emission. The velocity profile is sub-Keplerian over the full extent of the detected

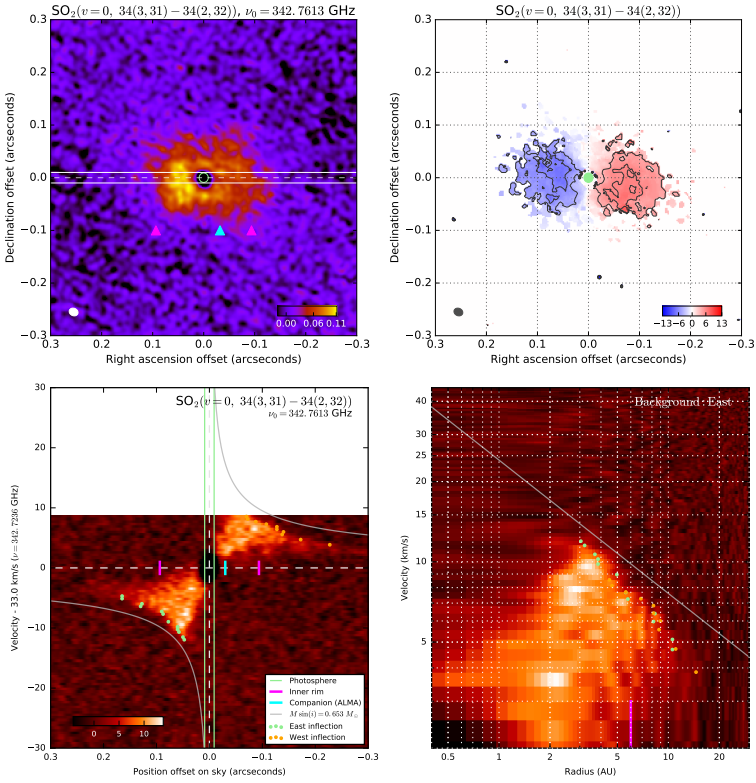

Figure B.3: Emission map (*top left panel*), first moment of velocity map (*top right panel*) and position-velocity diagram (*bottom panels*) of the $SO_2(\Delta v = 0, 34(3,31) - 34(2,32))$ emission line.

emission, but the deviation is smaller as the radius decreases. At a radius of 3 AU, the deviation from the Keplerian velocity is approximately $\Delta v = -2\,\mathrm{km\,s^{-1}}$.

B.4 SO 3Σ ($\Delta v = 0, 8(8) - 7(7)$) line

The SO 3Σ ($\Delta v = 0, 8(8) - 7(7)$) emission map (Fig. B.4) exhibits a strong emission reaching 0.18 Jy beam^{-1} km s^{-1} on the west side of the disk, close to the position of the L_2 Pup B source (Sect. 3.4.2). As for the SO_2 line (Appendix B.3), the PVD is incomplete as the line was located close to the edge of the spectral window, and this explains the apparent east-west asymmetry of the flux distribution. The western part of

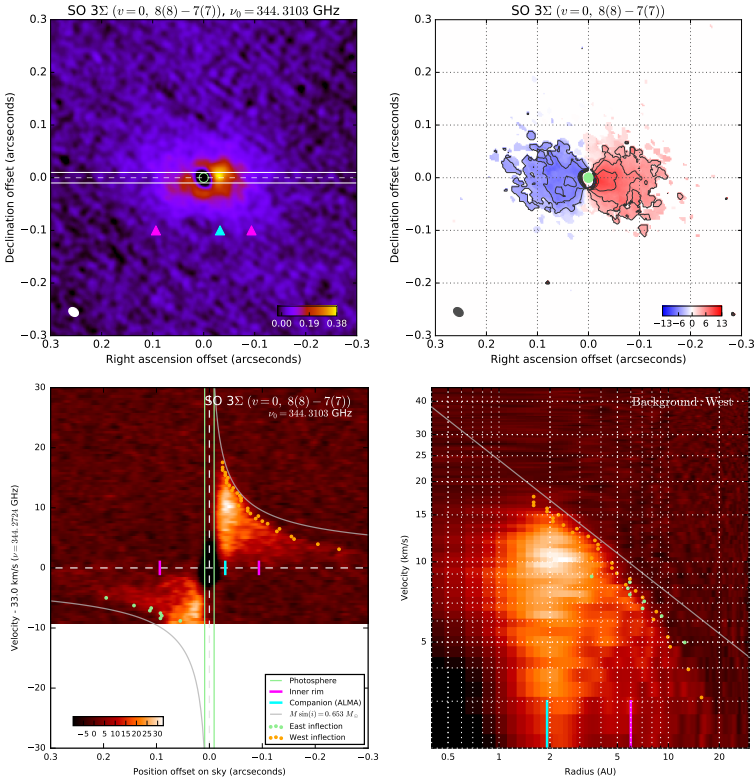

Figure B.4: Emission map (*top left panel*), first moment of velocity map (*top right panel*) and position-velocity diagram (*bottom panels*) of the SO 3Σ (Δv = 0, 8(8) − 7(7)) emission line.

the PVD represented in the bottom right panel of Fig. B.4 shows a rotation velocity close to Keplerian between 2 and 4 AU from the central star.

B.5 SiS(Δv = 1, J = 19 − 18) line

The emission map in the SiS(Δv = 1, J = 19 − 18) (Fig. B.5) shows that this line is narrowly contained within the plane of the dust disk and has a very restricted vertical extension. The PVD indicates that the emission is confined to a thin ring located around the inner rim of the dust disk (6 AU), and that its radial extension is mostly limited to between 4 and 7 AU. No significant emission is detected beyond a radius

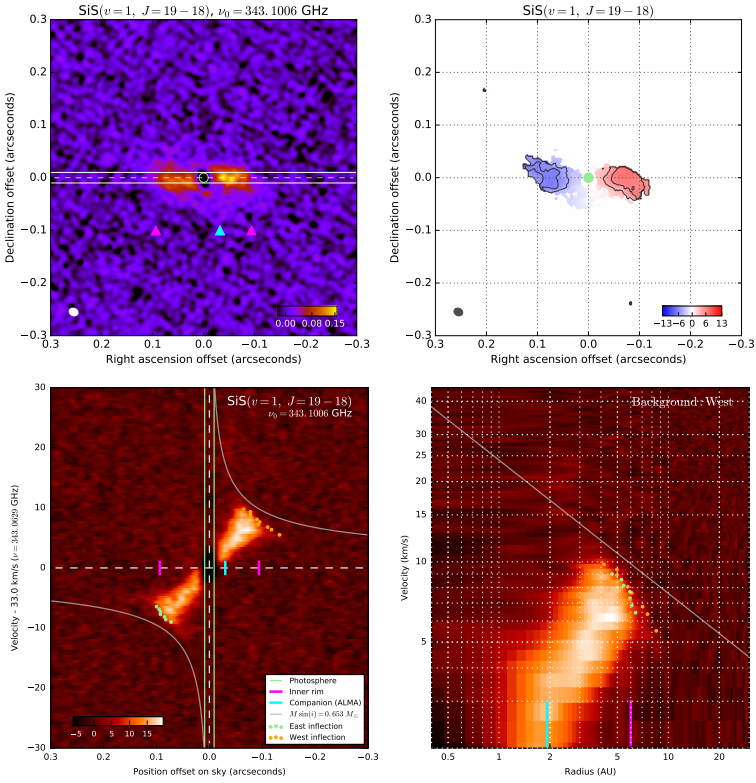

Figure B.5: Emission map (*top left panel*), first moment of velocity map (*top right panel*) and position velocity diagram (*bottom panels*) of the SiS($\Delta v = 1, J = 19 - 18$) emission line.

of approximately 10 AU. The PVD shows that the rotational velocity is always sub-Keplerian, with an increasing deviation from the $M\sin(i) = 0.653\,M_\odot$ velocity profile with increasing radius. The emission is asymmetric between the east and west parts of the disk, with a significantly stronger emission on the west side.

Appendix C

Appendix to chapter 4: Channel maps of L_2 Puppis disk, and synthetic model emission.

C.1 ^{12}CO channel maps - ALMA data

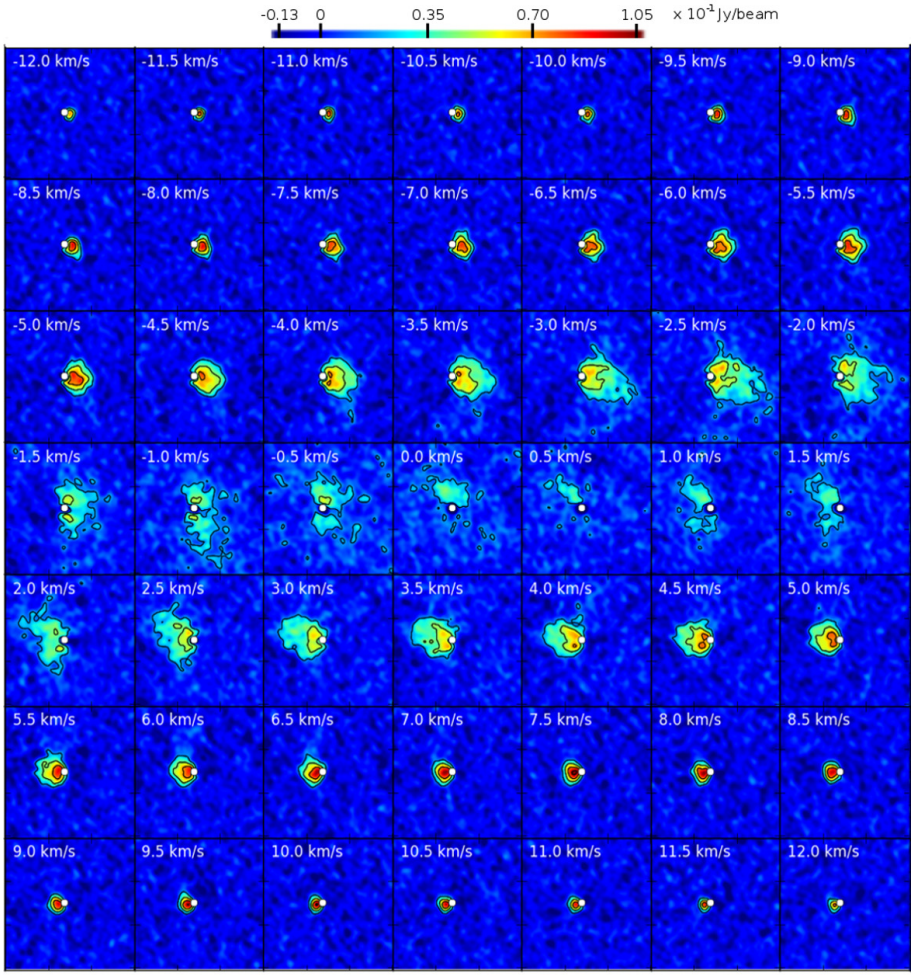

Figure C.1: Visualisation of the velocity channel maps of the ^{12}CO J =3−2 emission of the circumstellar environment of L_2 Pup, with the continuum subtracted. Each panel has a dimension of 1" by 1". The velocity channel is indicated in the top left corner of each panel. The black contour levels are drawn every 7 times the rms noise value outside the line. The white dot represents the location of the center of mass.

C.2 ^{12}CO channel maps - radiative transfer model

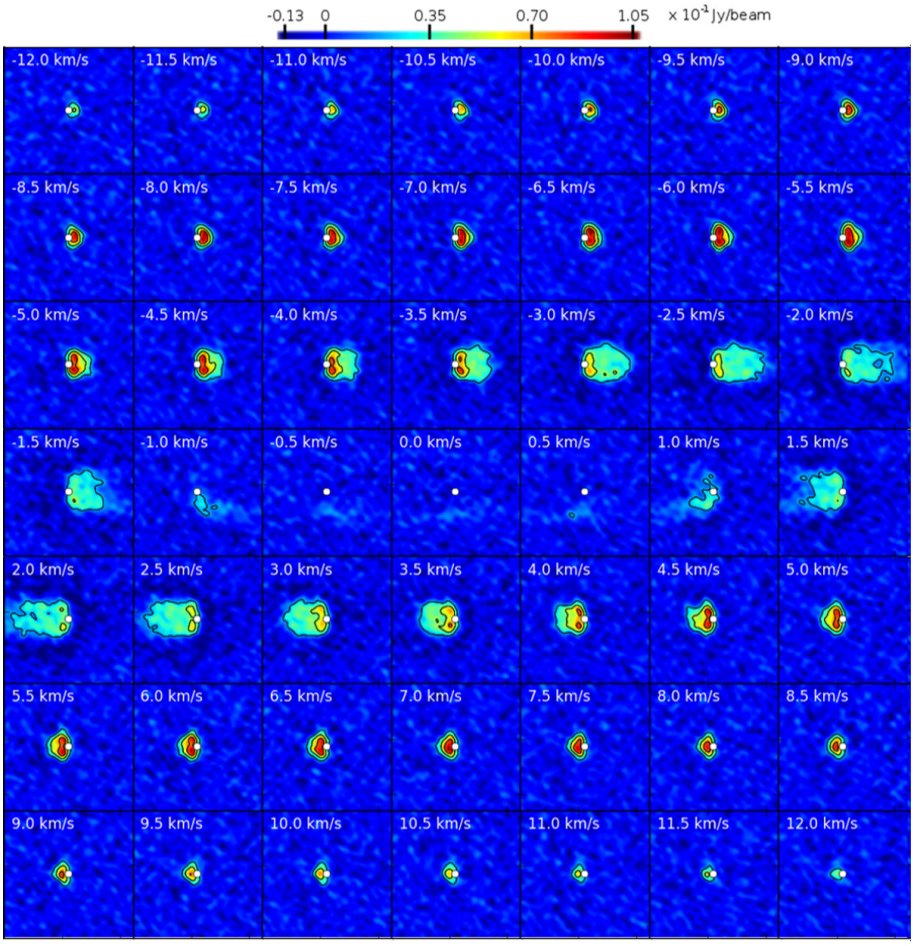

Figure C.2: Same as Fig. C.1, but now showing the synthetic emission of the rotating disk model.

C.3 ^{13}CO channel maps - ALMA data

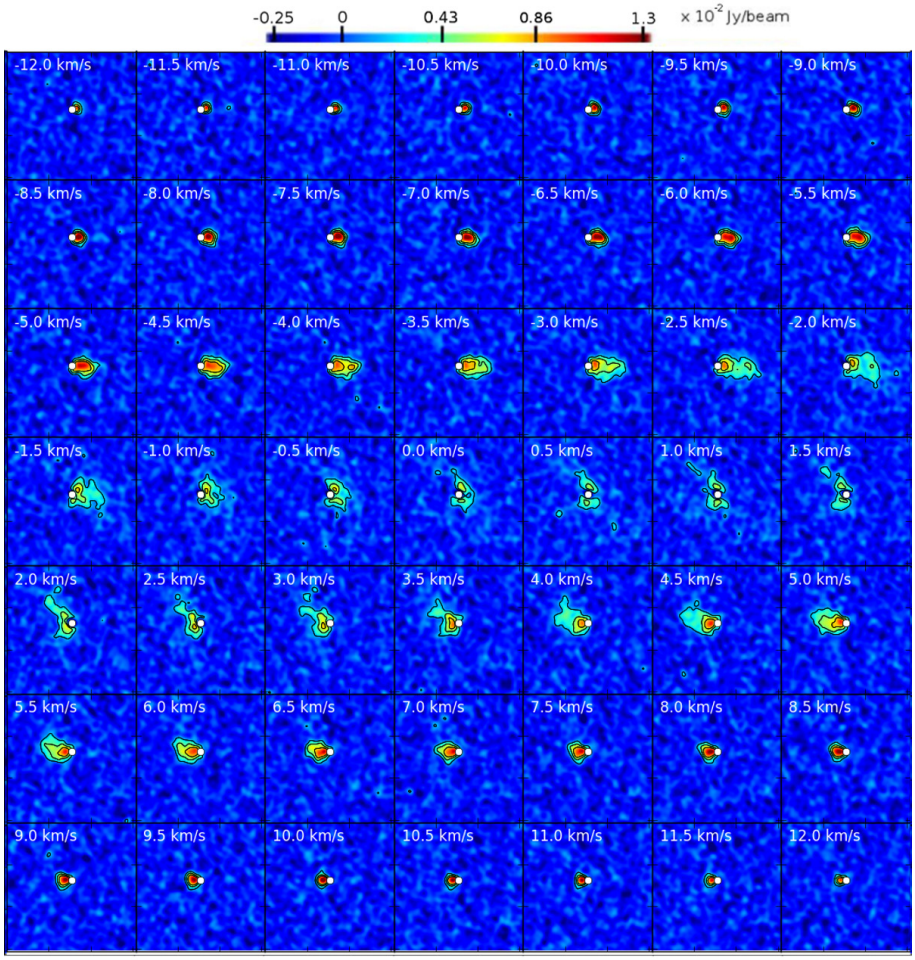

Figure C.3: Visualisation of the velocity channel maps of the ^{13}CO J =3−2 emission of the circumstellar environment of L_2 Pup, with the continuum subtracted. Each panel has a dimension of 1" by 1". The velocity channel is indicated in the top left corner of each panel. The black contour levels are drawn every 4 times the rms noise value outside the line. The white dot represents the location of the center of mass.

C.4 ^{13}CO channel maps - radiative transfer model

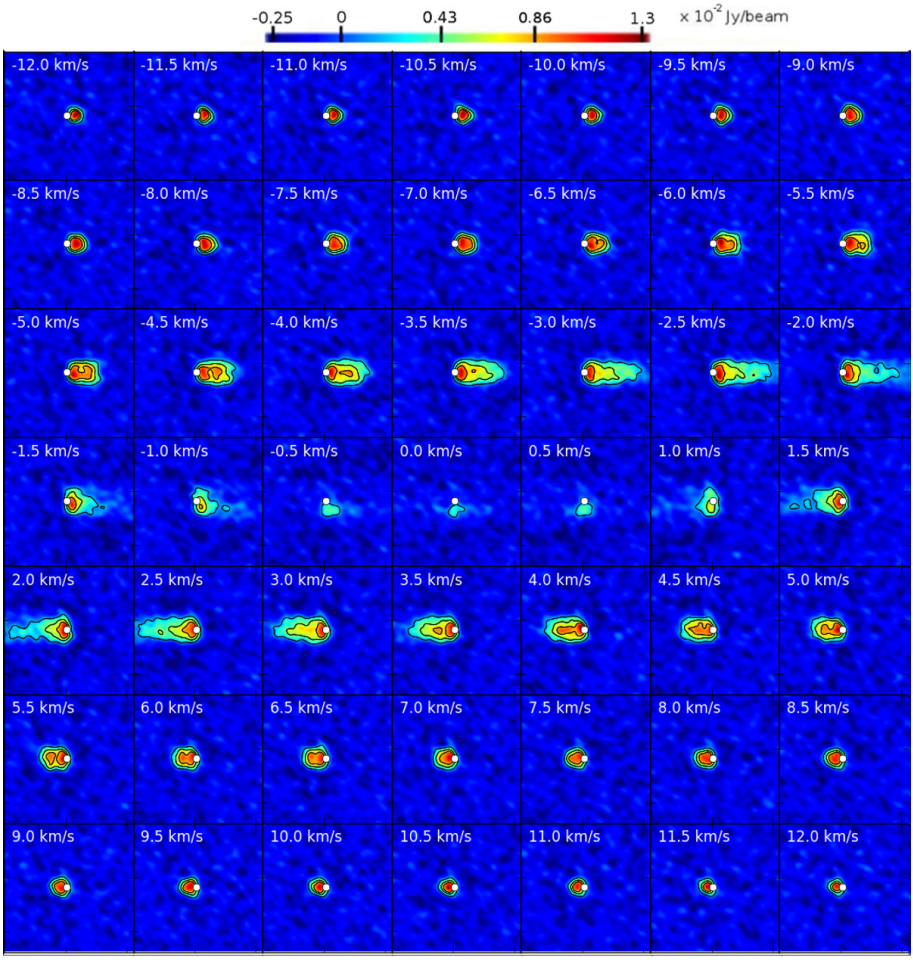

Figure C.4: Same as Fig. C.3, but now showing the synthetic emission of the rotating disk model.

Appendix D

Appendix to chapter 5: Position-velocity diagrams of spiral morphology parameter study.

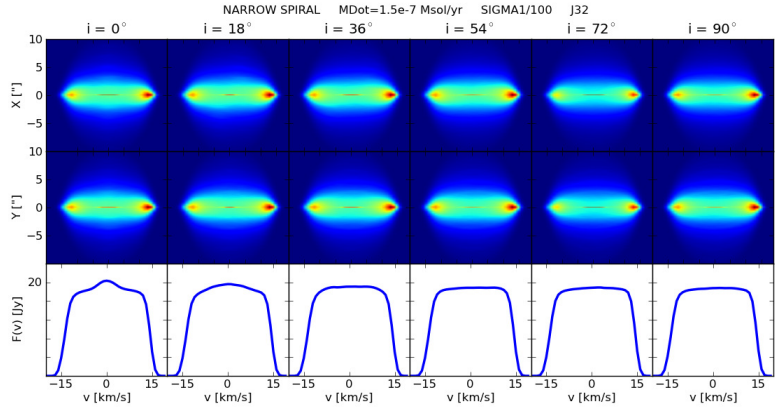

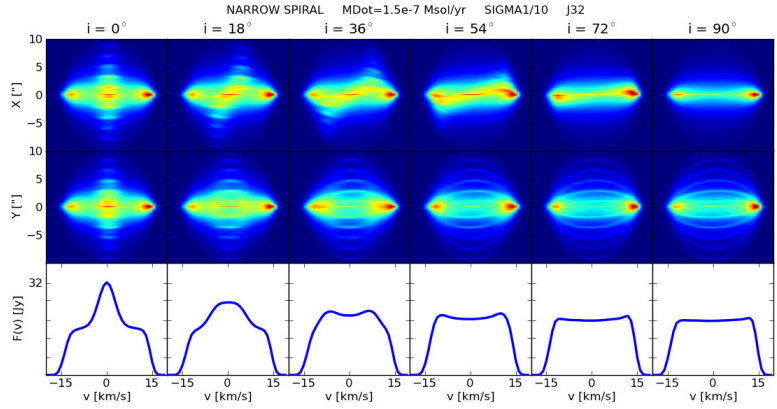
NARROW SPIRAL MDot=1.5e-7 Msol/yr SIGMA1/10 J32
i = 0°
i = 18°
i = 36°
i = 54°
i = 72°
i = 90°
X ["]
Y ["]
F(v) [Jy]
32
v [km/s]

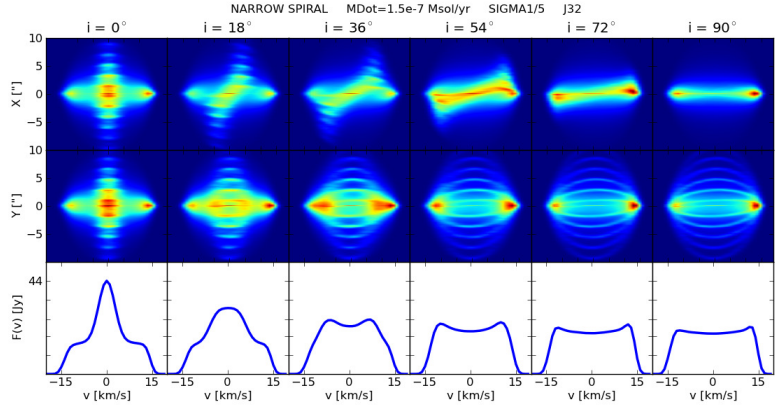
NARROW SPIRAL MDot=1.5e-7 Msol/yr SIGMA1/5 J32
i = 0°
i = 18°
i = 36°
i = 54°
i = 72°
i = 90°
X ["]
Y ["]
F(v) [Jy]
44
v [km/s]

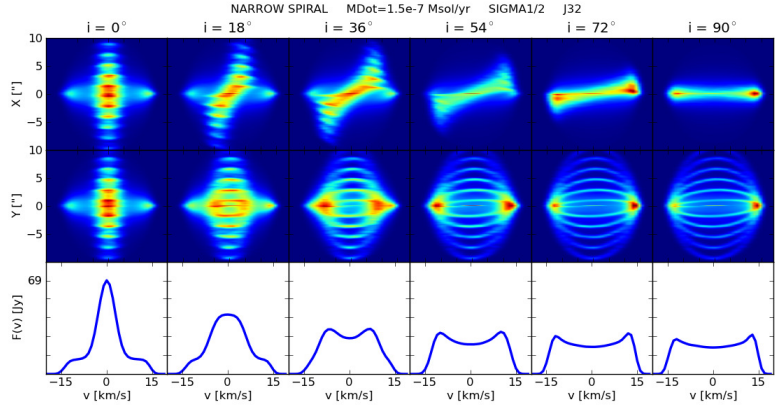
NARROW SPIRAL MDot=1.5e-7 Msol/yr SIGMA1/2 J32
i = 0°
i = 18°
i = 36°
i = 54°
i = 72°
i = 90°
X ["]
Y ["]
F(v) [Jy]
69
v [km/s]

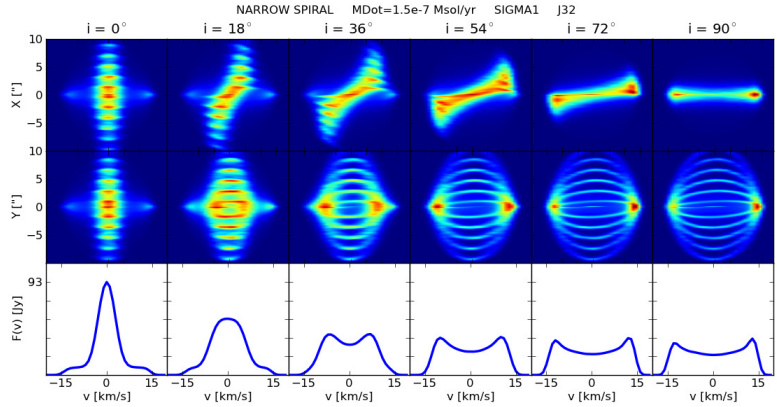
NARROW SPIRAL MDot=1.5e-7 Msol/yr SIGMA1 J32
i = 0°
i = 18°
i = 36°
i = 54°
i = 72°
i = 90°
X ["]
Y ["]
F(v) [Jy]
93
v [km/s]

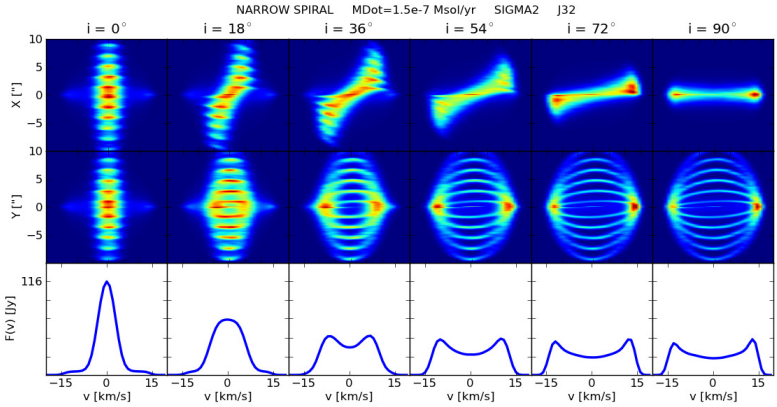
NARROW SPIRAL MDot=1.5e-7 Msol/yr SIGMA2 J32
i = 0°
i = 18°
i = 36°
i = 54°
i = 72°
i = 90°
X ["]
Y ["]
F(v) [Jy]
116
v [km/s]

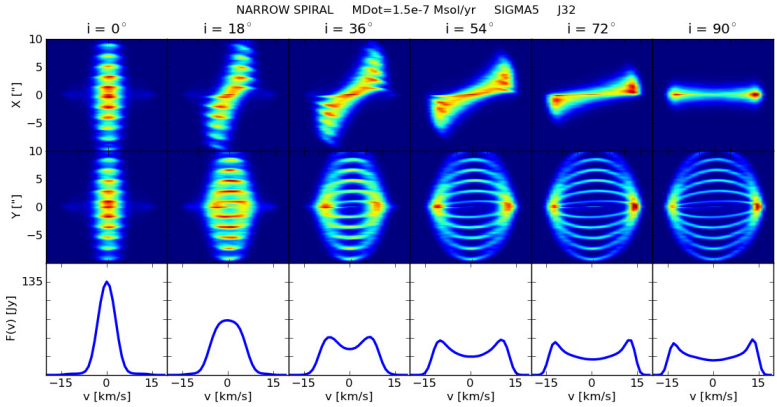
NARROW SPIRAL MDot=1.5e-7 Msol/yr SIGMA5 J32
i = 0°
i = 18°
i = 36°
i = 54°
i = 72°
i = 90°
X ["]
Y ["]
F(v) [Jy]
135
v [km/s]

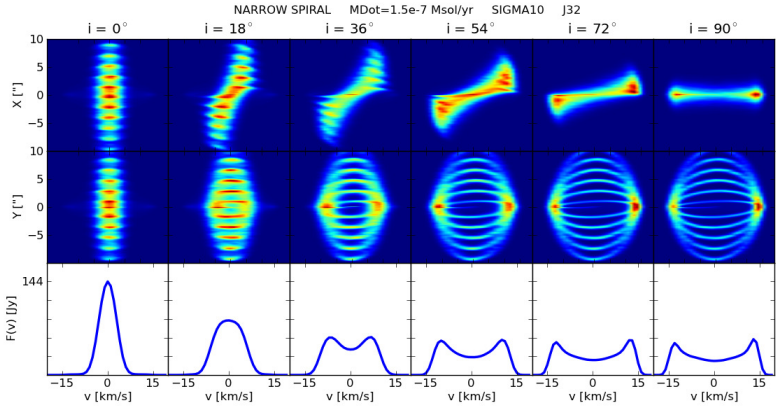
NARROW SPIRAL MDot=1.5e-7 Msol/yr SIGMA10 J32
i = 0°
i = 18°
i = 36°
i = 54°
i = 72°
i = 90°
X ["]
Y ["]
F(v) [Jy]
144
v [km/s]

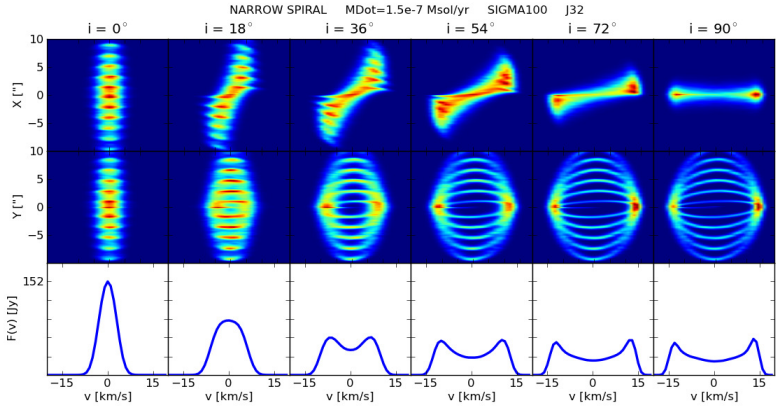
NARROW SPIRAL MDot=1.5e-7 Msol/yr SIGMA100 J32
i = 0°
i = 18°
i = 36°
i = 54°
i = 72°
i = 90°
X ["]
Y ["]
F(v) [Jy]
152
v [km/s]

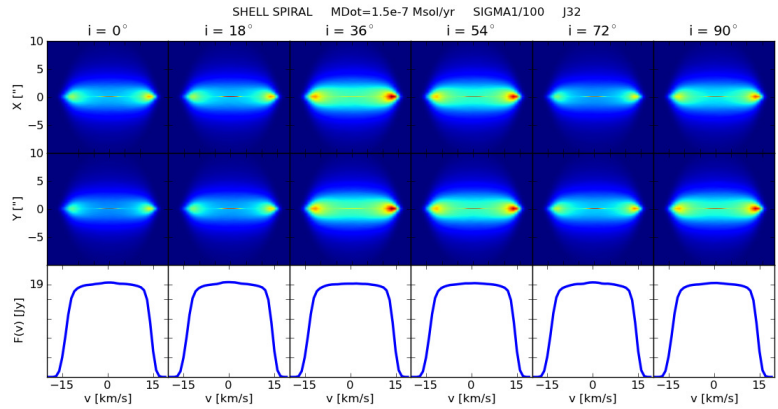
SHELL SPIRAL MDot=1.5e-7 Msol/yr SIGMA1/100 J32
i = 0°
i = 18°
i = 36°
i = 54°
i = 72°
i = 90°
X ["]
Y ["]
F(v) [Jy]
19
v [km/s]

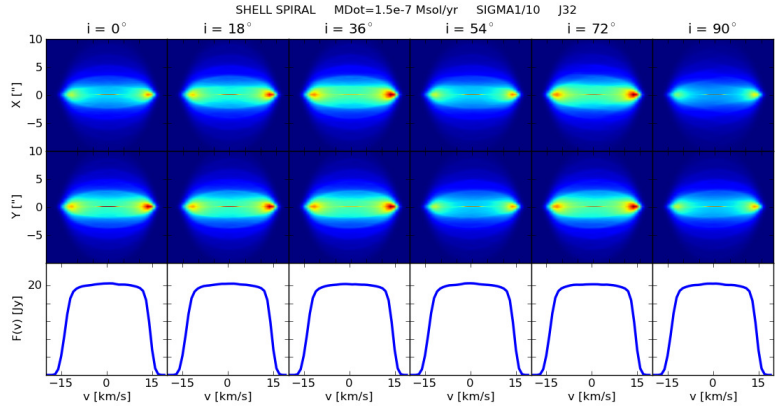
SHELL SPIRAL MDot=1.5e-7 Msol/yr SIGMA1/10 J32
i = 0°
i = 18°
i = 36°
i = 54°
i = 72°
i = 90°
X ["]
Y ["]
F(v) [Jy]
v [km/s]

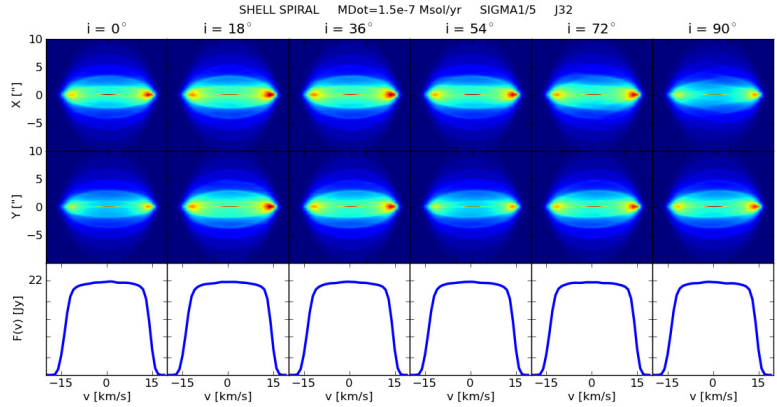
SHELL SPIRAL MDot=1.5e-7 Msol/yr SIGMA1/5 J32
i = 0°
i = 18°
i = 36°
i = 54°
i = 72°
i = 90°
X ["]
Y ["]
F(v) [Jy]
v [km/s]

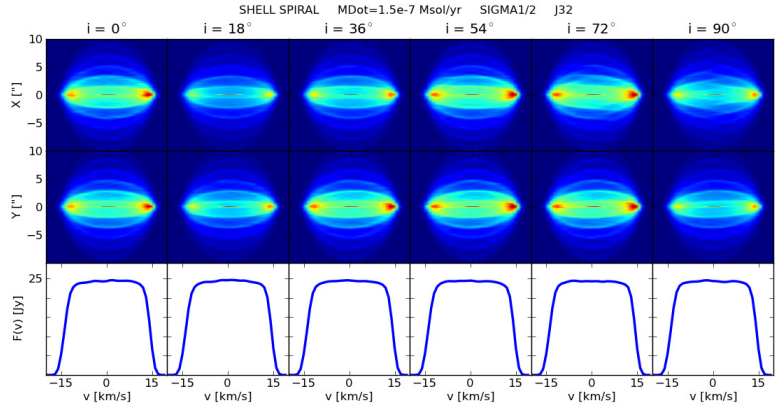
SHELL SPIRAL MDot=1.5e-7 Msol/yr SIGMA1/2 J32
i = 0°
i = 18°
i = 36°
i = 54°
i = 72°
i = 90°
X ["]
Y ["]
F(v) [Jy]
v [km/s]

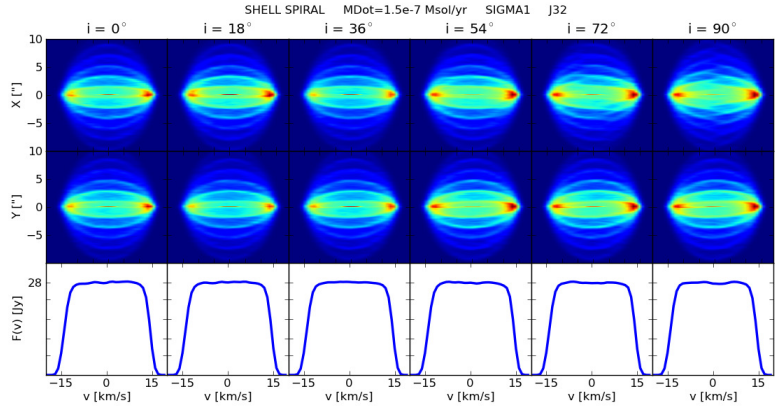
SHELL SPIRAL MDot=1.5e-7 Msol/yr SIGMA1 J32
i = 0°
i = 18°
i = 36°
i = 54°
i = 72°
i = 90°
X ["]
Y ["]
F(v) [Jy]
v [km/s]

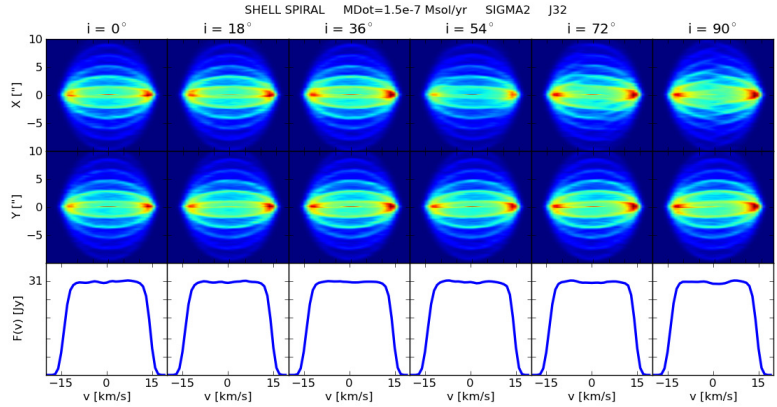
SHELL SPIRAL MDot=1.5e-7 Msol/yr SIGMA2 J32
i = 0°
i = 18°
i = 36°
i = 54°
i = 72°
i = 90°
X ["]
Y ["]
F(v) [Jy]
v [km/s]

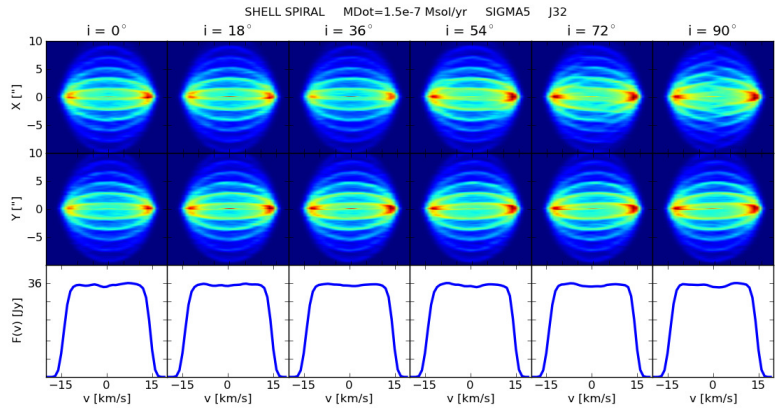
SHELL SPIRAL MDot=1.5e-7 Msol/yr SIGMA5 J32
i = 0°
i = 18°
i = 36°
i = 54°
i = 72°
i = 90°
X ["]
Y ["]
F(v) [Jy]
v [km/s]

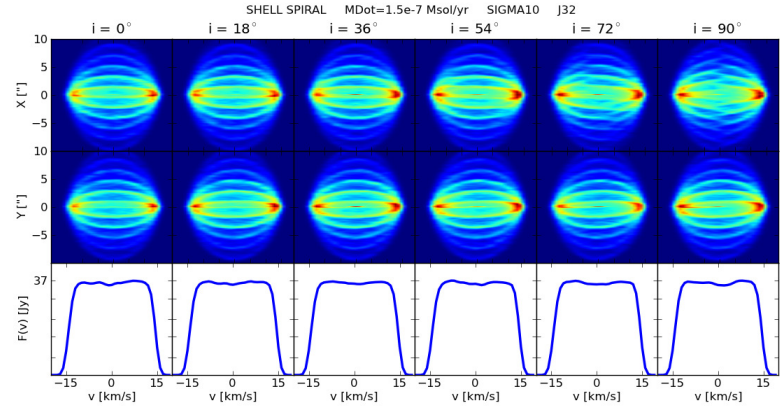
SHELL SPIRAL MDot=1.5e-7 Msol/yr SIGMA10 J32
i = 0°
i = 18°
i = 36°
i = 54°
i = 72°
i = 90°
X ["]
Y ["]
F(v) [Jy]
37
v [km/s]

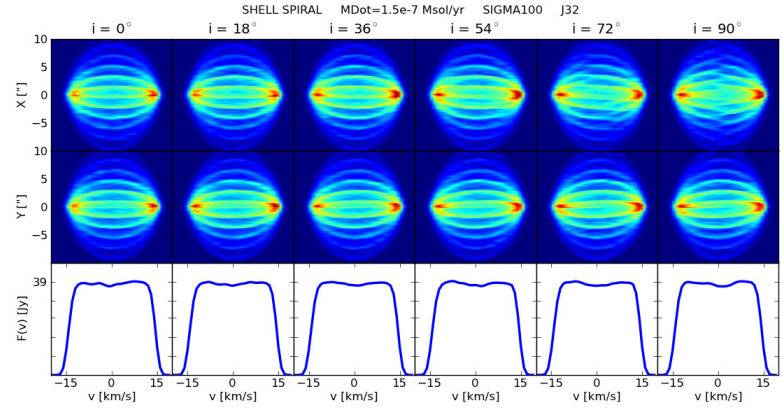
SHELL SPIRAL MDot=1.5e-7 Msol/yr SIGMA100 J32
i = 0°
i = 18°
i = 36°
i = 54°
i = 72°
i = 90°
X ["]
Y ["]
F(v) [Jy]
39
v [km/s]

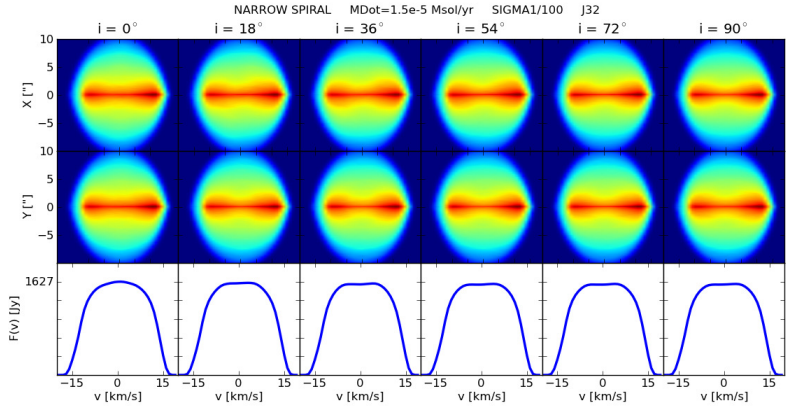
NARROW SPIRAL MDot=1.5e-5 Msol/yr SIGMA1/100 J32
i = 0°
i = 18°
i = 36°
i = 54°
i = 72°
i = 90°
X ["]
Y ["]
F(v) [Jy]
1627
v [km/s]

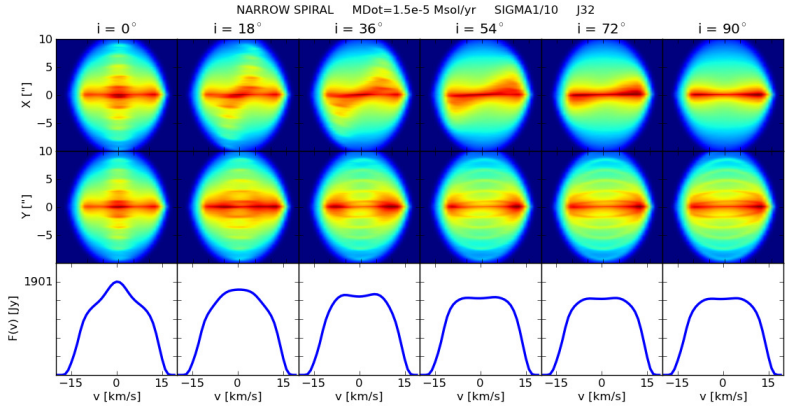
NARROW SPIRAL MDot=1.5e-5 Msol/yr SIGMA1/10 J32
i = 0°
i = 18°
i = 36°
i = 54°
i = 72°
i = 90°
X ["]
Y ["]
F(v) [Jy]
1901
v [km/s]

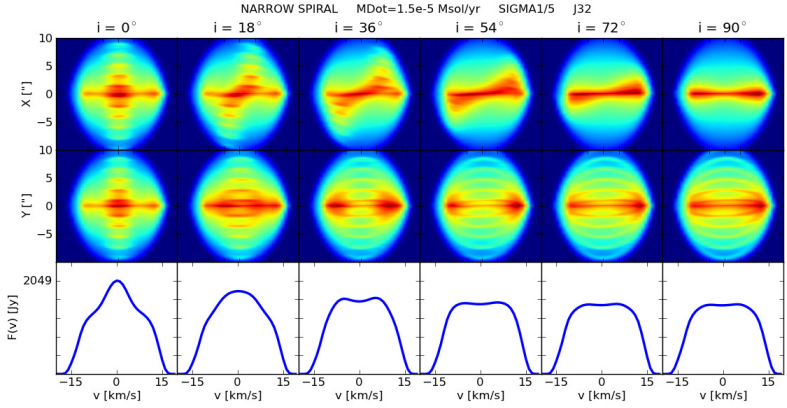
NARROW SPIRAL MDot=1.5e-5 Msol/yr SIGMA1/5 J32
i = 0°
i = 18°
i = 36°
i = 54°
i = 72°
i = 90°
X ["]
Y ["]
F(v) [Jy]
2049
v [km/s]

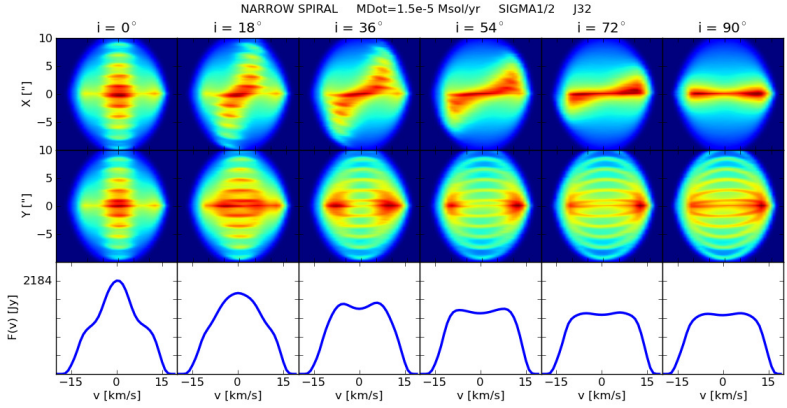
NARROW SPIRAL MDot=1.5e-5 Msol/yr SIGMA1/2 J32
i = 0°
i = 18°
i = 36°
i = 54°
i = 72°
i = 90°
X ["]
Y ["]
F(v) [Jy]
2184
v [km/s]

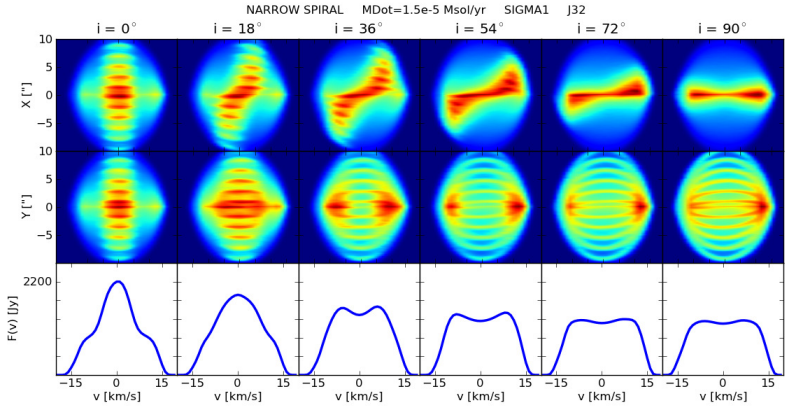
NARROW SPIRAL MDot=1.5e-5 Msol/yr SIGMA1 J32
i = 0°
i = 18°
i = 36°
i = 54°
i = 72°
i = 90°
X ["]
Y ["]
F(v) [Jy]
2200
v [km/s]

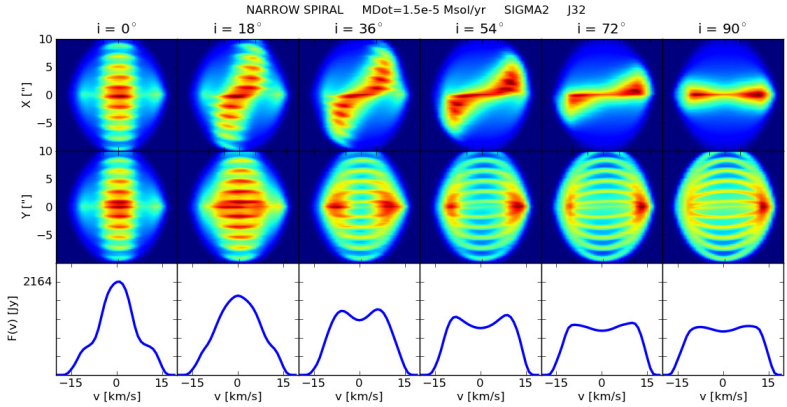
NARROW SPIRAL MDot=1.5e-5 Msol/yr SIGMA2 J32
i = 0°
i = 18°
i = 36°
i = 54°
i = 72°
i = 90°
X ["]
Y ["]
F(v) [Jy]
2164
v [km/s]

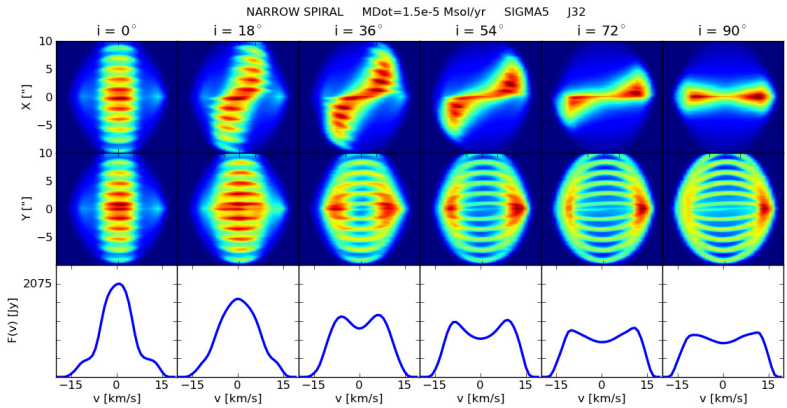
NARROW SPIRAL MDot=1.5e-5 Msol/yr SIGMA5 J32
i = 0°
i = 18°
i = 36°
i = 54°
i = 72°
i = 90°
X ["]
Y ["]
F(v) [Jy]
2075
v [km/s]

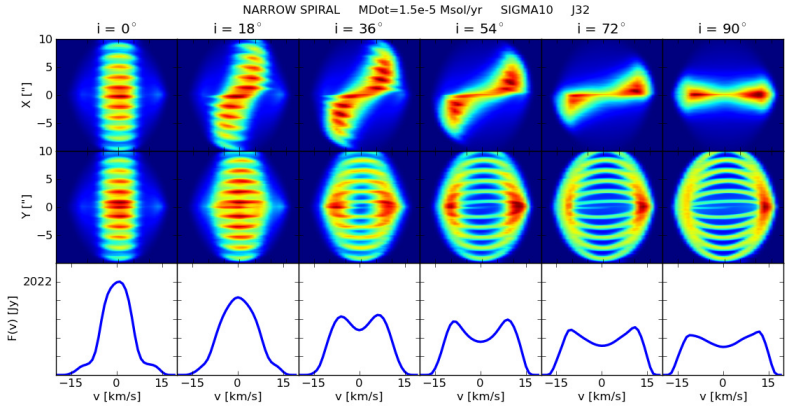
NARROW SPIRAL MDot=1.5e-5 Msol/yr SIGMA10 J32
i = 0°
i = 18°
i = 36°
i = 54°
i = 72°
i = 90°
X ["]
Y ["]
F(v) [Jy]
2022
v [km/s]

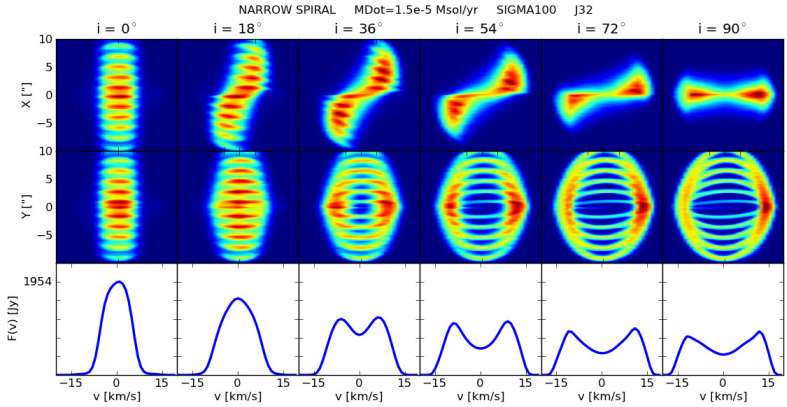
NARROW SPIRAL MDot=1.5e-5 Msol/yr SIGMA100 J32
i = 0°
i = 18°
i = 36°
i = 54°
i = 72°
i = 90°
X ["]
Y ["]
F(v) [Jy]
1954
v [km/s]

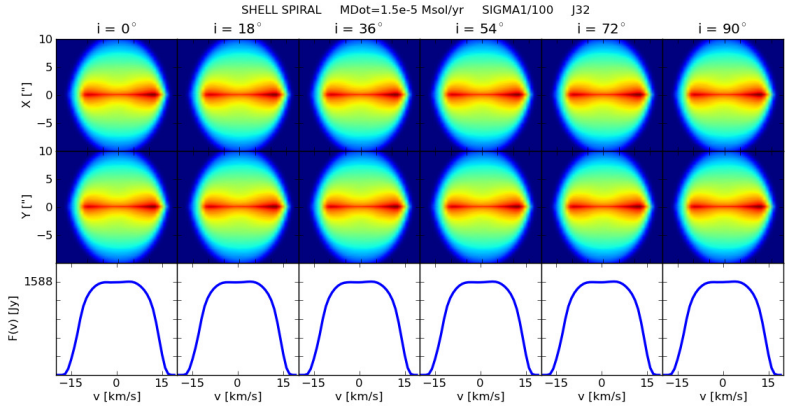
SHELL SPIRAL MDot=1.5e-5 Msol/yr SIGMA1/100 J32
i = 0°
i = 18°
i = 36°
i = 54°
i = 72°
i = 90°
X ["]
Y ["]
F(v) [Jy]
1588
v [km/s]

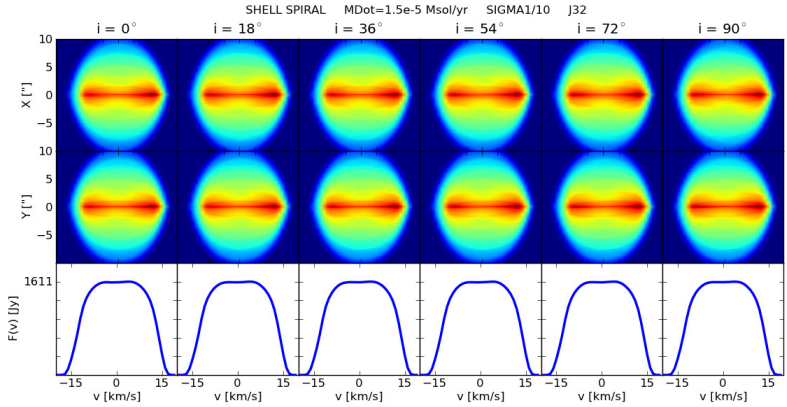
SHELL SPIRAL MDot=1.5e-5 Msol/yr SIGMA1/10 J32
i = 0°
i = 18°
i = 36°
i = 54°
i = 72°
i = 90°
X ["]
Y ["]
F(v) [Jy]
1611
v [km/s]

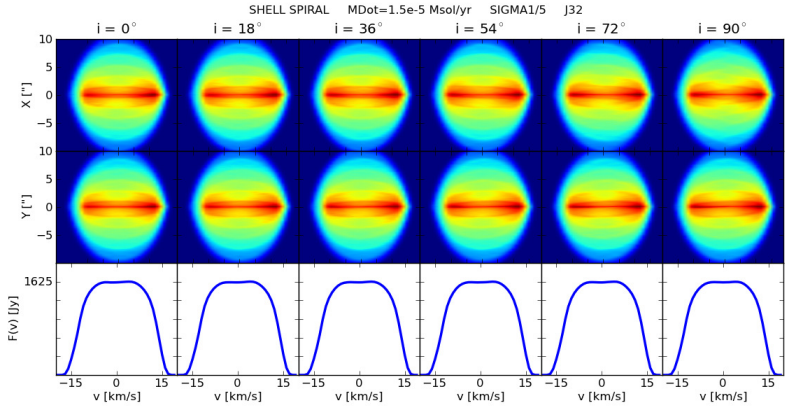
SHELL SPIRAL MDot=1.5e-5 Msol/yr SIGMA1/5 J32
i = 0°
i = 18°
i = 36°
i = 54°
i = 72°
i = 90°
X ["]
Y ["]
F(v) [Jy]
1625
v [km/s]

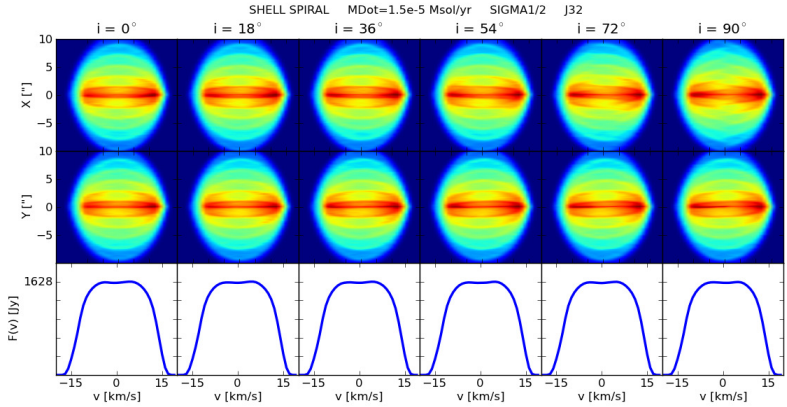
SHELL SPIRAL MDot=1.5e-5 Msol/yr SIGMA1/2 J32
i = 0°
i = 18°
i = 36°
i = 54°
i = 72°
i = 90°
X ["]
Y ["]
F(v) [Jy]
1628
v [km/s]

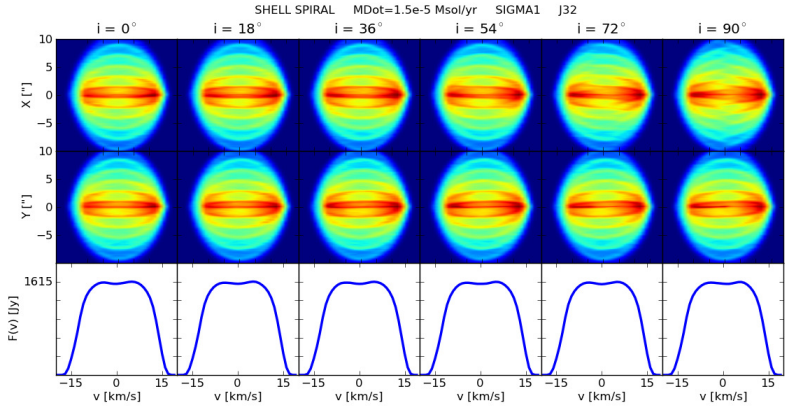
SHELL SPIRAL MDot=1.5e-5 Msol/yr SIGMA1 J32
i = 0°
i = 18°
i = 36°
i = 54°
i = 72°
i = 90°
X ["]
Y ["]
F(v) [Jy]
1615
v [km/s]

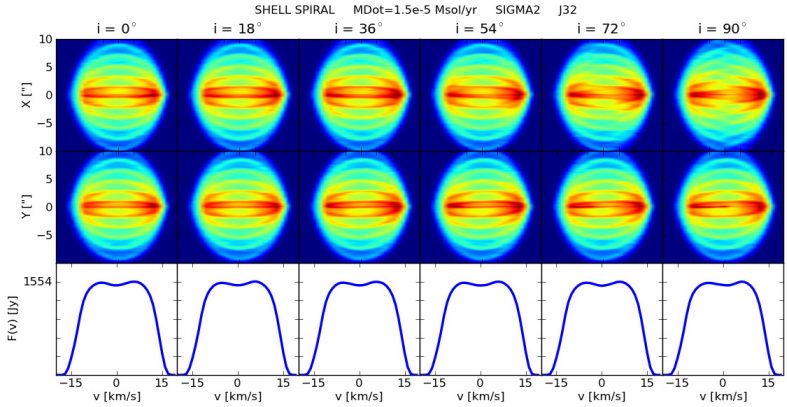
SHELL SPIRAL MDot=1.5e-5 Msol/yr SIGMA2 J32
i = 0°
i = 18°
i = 36°
i = 54°
i = 72°
i = 90°
X ["]
Y ["]
F(v) [Jy]
1554
v [km/s]

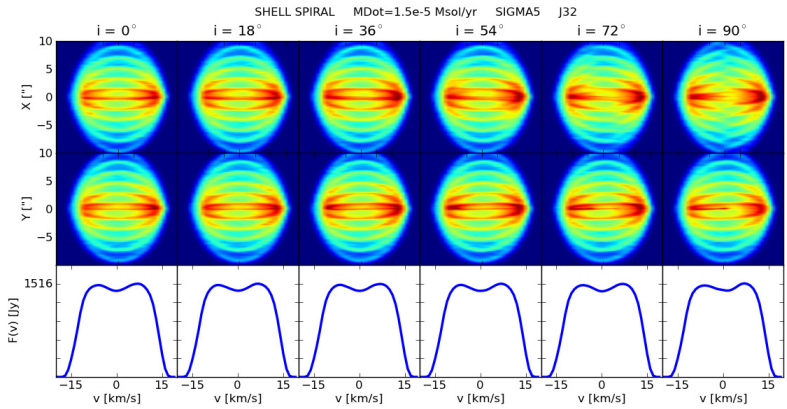
SHELL SPIRAL MDot=1.5e-5 Msol/yr SIGMA5 J32
i = 0°
i = 18°
i = 36°
i = 54°
i = 72°
i = 90°
X ["]
Y ["]
F(v) [Jy]
1516
v [km/s]

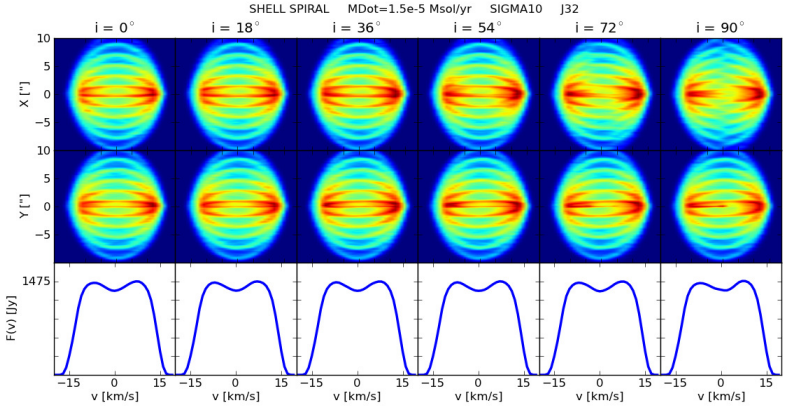
SHELL SPIRAL MDot=1.5e-5 Msol/yr SIGMA10 J32
i = 0°
i = 18°
i = 36°
i = 54°
i = 72°
i = 90°
X ["]
Y ["]
F(v) [Jy]
1475
v [km/s]

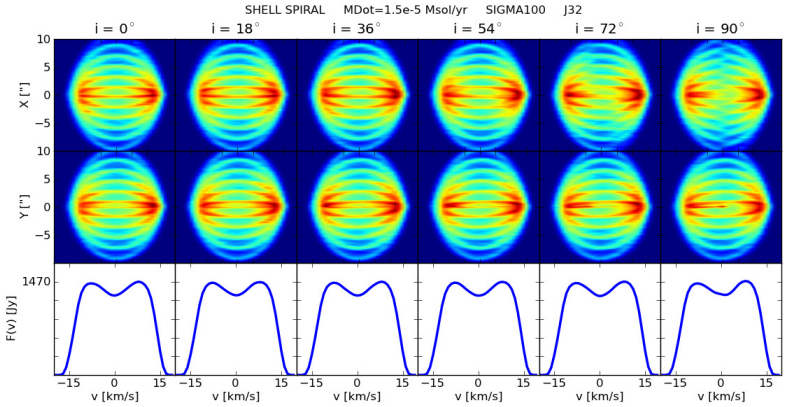
SHELL SPIRAL MDot=1.5e-5 Msol/yr SIGMA100 J32
i = 0°
i = 18°
i = 36°
i = 54°
i = 72°
i = 90°
X ["]
Y ["]
F(v) [Jy]
1470
v [km/s]

Appendix E

Solving the radiative transfer equation - LIME

Both to compile repositories of synthetic emission and for validating of the developed methods by application to real data we have opted to make use of the NLTE full-3D radiative transfer (RT) code `LIME` [19]. The important advantage this code has over others is that it solves the equations of radiation transport fully under the assumption of NLTE for an arbitrary three-dimensional physical morphology. Furthermore, our main interest lies with gas emission, which the code had been specially designed for.

The numerical procedure which `LIME` follows to produce synthetic spectra of molecular emission can be divided into two major phases. Consider the calculations of a spectrum of carbon monoxide emitted by a disk around an AGB star, as performed in Chapter 4, for which the physical properties [1] have been estimated. Then as a first step, the populations of the energy levels of the molecules of interest must be determined, in order to gauge how much energy is emitted per frequency. These level populations depend on three majorly important contributions: (1) the radiative Einstein coefficients of the allowed transitions between every available energy level in the molecule, (2) the contribution to the energy supply and removal via inter-molecular collisions, and (3) the mean radiation field experienced by each molecule. It is the calculation of the mean intensity field that requires such an elaborate code. `LIME` calculates the radiation field according to the following steps.

The code first samples the model via randomly placed grid points, weighted in a specific way to allow for flexible sampling. A primary weighting samples the wind for its overall radial density trend. For centrally condensed models a logarithmic

[1] like temperature, absolute density, molecular abundance, gas velocity field, etc...

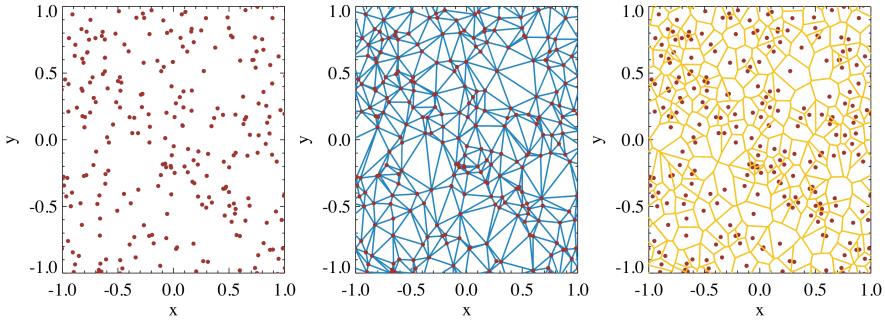

Figure E.1: *From left to right:* (1) Sampling of numerical space via random placement of grid points. (2) The Delaunay triangulation algorithm connects each grid point to its neighbours. These Delaunay paths are the tracks along which the radiative transfer equation is calculated. (3) Finally, the grid is subdivided into Voronoi cells. Figure adopted from Brinch et al (2010) [19].

sampling is typically used, which places more gridpoints near the center of the model. Non-centrally condensed models might benefit more from purely random sampling. A secondary weighting, using a Markov-Chain monte carlo-type algorithm [171], enables the additional sampling of model-specific properties (as a function of absolute or relative density, density gradients, temperature, ...). After placing the gridpoints throughout the numerical domain, they are connected according to the Delaunay triangulation algorithm [43]. This will connect 4 neighbouring gridpoints to form a tetrahedron. Subsequently, a Voronoi tesselation algorithm [198] defines the grid cells around each grid point. These cells are characterised by the fact that any mathematical point inside the cell will be closer to its defining gridpoint than to any other gridpoint. This whole procedure is visually shown in Fig. E.1. Finally, the application of Lloyd's algorithm [111] will smoothen the grid by slightly moving each gridpoint towards the geometrical centroid of its Voronoi cell, as is shown in Fig. E.2. This last step is necessary due to the probabilistic nature of the original gridding algorithm, which, after triangulation, is likely to have generated unnecessarily disproportionate tetrahedra. The smoothing will ensure each tetrahedron to be relatively 'tidy', and thus each Voronoi cell to properly represent the closest region around the grid point in question. Additionally, a number of sink points are added to the edge of the numerical domain, and they represent the physical edge beyond which the conditions are excluded from the RT calculation. All physical parameters are evaluated in the grid points, with each Voronoi cell representing the physical region around the grid point where conditions are identical to the grid point parameters. This substantially simplifies the mathematics, because now each cell can be considered a homogeneous medium, and so the analytic solution of the transport equation for a homogeneous medium can be used in the

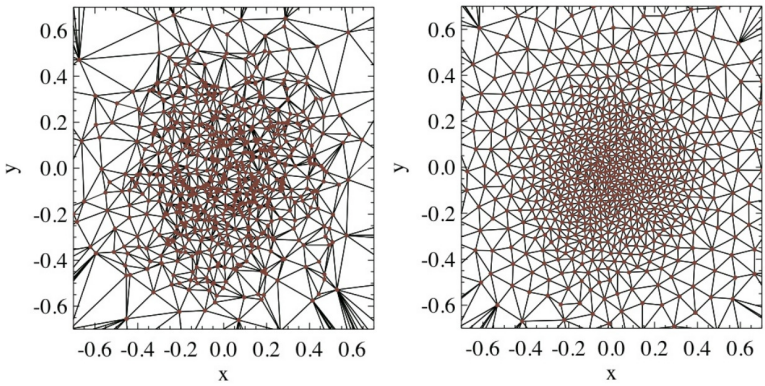

Figure E.2: *Left panel:* Delaunay triangulated grid before smoothing. *Right Panel:* Delaunay triangulated grid after smoothing. Figure adopted from Brinch et al (2010) [19].

subsequent calculations. However, for this assumption to hold one must take care to sample the physical model with enough grid points. This can be ensured by weighting the placement of the grid points with the steepness of the gradients which make up the physical description of the synthetic CSE.

In order to estimate the mean radiation field

$$J_\nu = \frac{1}{4\pi} \int I_\nu \, d\Omega \tag{E.1}$$

to which each grid cell is subjected, the code selects a gridpoint at random, and divides the full solid-angle sphere as seen from the vantage point of this particular grid point into a number of directions. Along each of these directions, outward paths are traced along the Delaunay lines, taking care to preserve the original direction by weighting the choice at each path intersection with the path that makes the smallest angle with the original direction. Per direction, a multitude of such paths are traced outwards, up to when a sinkpoint is struck. The resulting path structure for a single such direction is shown in Fig. E.3. The equation of radiation transport is then calculated inwards along these paths, each path adding up to the cone's contribution to the mean radiation field. When the contributions from the cones for each individual initial direction have all been calculated, then their mean is assumed to be an estimate of the mean radiation field as seen by the gridpoint. This mean field affects the level populations in that particular cell. The level populations are updated when this procedure has been iterated over all gridpoints. Then, the whole sequence is repeated, until the level populations converge. Due to the complexity of defining a universal criterion for convergence through a whole 3D numerical domain, the `LIME` code instead provides its user with

the option to adjust the number of iterations. The user himself must then perform the testing to verify whether or not the level populations have indeed converged.

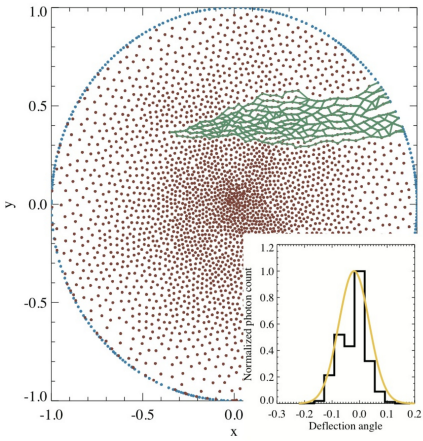

Figure E.3: Paths (in green) traced from the grid point outwards. The intensity arriving from that direction is calculated along the paths contained by this cone. Figure adopted from Brinch et al (2010) [19].

Once the level populations have indeed been found to be consistent with the physical input model, the code can transition to the *ray tracing* phase. This is the stage when the spectrum, and corresponding high-resolution emission distribution image is made. The procedure is comparable with the placement of a virtual CCD chip of a digital camera at a user-determined location and orientation with respect to the physical model. Parallel rays are traced from each pixel on the chip through the physical model. The equation of radiation transport is solved along these lines, effectively adding up the intensity contribution of each penetrated Voronoi cell up to an optical depth of τ =30. The final intensity along that particular ray is then stored on the corresponding pixel. This is done for every pixel, at every user-selected frequency, creating an image cube of Doppler-shifted intrinsic intensity maps as function of coordinates in the plane of the sky, to be readily used as one would real data.

The code also has a few shortcomings. The code was originally designed for modelling cool molecular clouds. For the modelling of stellar winds, however, the central mass-losing star is the most important source of energy. In collaboration with Wouter Vlemmings we implemented the possibility to position an arbitrary number of 'stars' on the locations of choice. The stars emit as black bodies with an arbitrary temperature, luminosity and density. Another shortcoming is that the code only possesses a very rudimentary implementation of thermal dust contributions to the total emission. This limitation can not be underestimated, as the continuum emission of the dust may contribute significantly to the excitation of certain molecular energy levels. Currently, the code can only take into consideration one singular dust opacity table, which would then correspond to either the most important dust species, or an averaged opacity of all the contributing dust species combined. And as a final important constraint, the code is completely non-dynamical, meaning that the code solves the RT equations exclusively

in order to determine the energy level populations of the molecules of interest for a given initial physical set-up. This user-defined physical set-up is thus not modified as the level populations converge. This, in turn, means that self-consistency of the physical model is only guaranteed if it was verified prior to the application of `LIME`.

Bibliography

[1] Akashi, M., and Soker, N. A model for the formation of large circumbinary disks around post AGB stars. *New Astronomy 13* (Apr. 2008), 157–162.

[2] Alibert, Y., Carron, F., Fortier, A., Pfyffer, S., Benz, W., Mordasini, C., and Swoboda, D. Theoretical models of planetary system formation: mass vs. semi-major axis. *A&A558* (Oct. 2013), A109.

[3] Alibert, Y., Mordasini, C., Benz, W., and Winisdoerffer, C. Models of giant planet formation with migration and disc evolution. *A&A434* (Apr. 2005), 343–353.

[4] ALMA Partnership, Brogan, C. L., Pérez, L. M., Hunter, T. R., Dent, W. R. F., Hales, A. S., Hills, R. E., Corder, S., Fomalont, E. B., Vlahakis, C., Asaki, Y., Barkats, D., Hirota, A., Hodge, J. A., Impellizzeri, C. M. V., Kneissl, R., Liuzzo, E., Lucas, R., Marcelino, N., Matsushita, S., Nakanishi, K., Phillips, N., Richards, A. M. S., Toledo, I., Aladro, R., Broguiere, D., Cortes, J. R., Cortes, P. C., Espada, D., Galarza, F., Garcia-Appadoo, D., Guzman-Ramirez, L., Humphreys, E. M., Jung, T., Kameno, S., Laing, R. A., Leon, S., Marconi, G., Mignano, A., Nikolic, B., Nyman, L.-A., Radiszcz, M., Remijan, A., Rodón, J. A., Sawada, T., Takahashi, S., Tilanus, R. P. J., Vila Vilaro, B., Watson, L. C., Wiklind, T., Akiyama, E., Chapillon, E., de Gregorio-Monsalvo, I., Di Francesco, J., Gueth, F., Kawamura, A., Lee, C.-F., Nguyen Luong, Q., Mangum, J., Pietu, V., Sanhueza, P., Saigo, K., Takakuwa, S., Ubach, C., van Kempen, T., Wootten, A., Castro-Carrizo, A., Francke, H., Gallardo, J., Garcia, J., Gonzalez, S., Hill, T., Kaminski, T., Kurono, Y., Liu, H.-Y., Lopez, C., Morales, F., Plarre, K., Schieven, G., Testi, L., Videla, L., Villard, E., Andreani, P., Hibbard, J. E., and Tatematsu, K. The 2014 ALMA Long Baseline Campaign: First Results from High Angular Resolution Observations toward the HL Tau Region. *ApJ808* (July 2015), L3.

[5] Andrews, S. M., and Williams, J. P. High-Resolution Submillimeter Constraints on Circumstellar Disk Structure. *ApJ659* (Apr. 2007), 705–728.

[6] Andrews, S. M., Wilner, D. J., Hughes, A. M., Qi, C., and Dullemond, C. P. Protoplanetary Disk Structures in Ophiuchus. *ApJ700* (Aug. 2009), 1502–1523.

[7] Andrews, S. M., Wilner, D. J., Hughes, A. M., Qi, C., and Dullemond, C. P. Protoplanetary Disk Structures in Ophiuchus. II. Extension to Fainter Sources. *ApJ723* (Nov. 2010), 1241–1254.

[8] Ansdell, M., Williams, J. P., van der Marel, N., Carpenter, J. M., Guidi, G., Hogerheijde, M., Mathews, G. S., Manara, C. F., Miotello, A., Natta, A., Oliveira, I., Tazzari, M., Testi, L., van Dishoeck, E. F., and van Terwisga, S. E. ALMA Survey of Lupus Protoplanetary Disks. I. Dust and Gas Masses. *ApJ828* (Sept. 2016), 46.

[9] Asplund, M., Grevesse, N., Sauval, A. J., and Scott, P. The Chemical Composition of the Sun. *ARA&A47* (Sept. 2009), 481–522.

[10] Balick, B., and Frank, A. Shapes and Shaping of Planetary Nebulae. *ARA&A40* (2002), 439–486.

[11] Balick, B., Huarte-Espinosa, M., Frank, A., Gomez, T., Alcolea, J., Corradi, R. L. M., and Vinković, D. Outflows from Evolved Stars: The Rapidly Changing Fingers of CRL 618. *ApJ772* (July 2013), 20.

[12] Bedding, T. R., Kiss, L. L., Kjeldsen, H., Brewer, B. J., Dind, Z. E., Kawaler, S. D., and Zijlstra, A. A. The light curve of the semiregular variable L_2 Puppis - II. Evidence for solar-like excitation of the oscillations. *MNRAS361* (Aug. 2005), 1375–1381.

[13] Bedding, T. R., Zijlstra, A. A., Jones, A., Marang, F., Matsuura, M., Retter, A., Whitelock, P. A., and Yamamura, I. The light curve of the semiregular variable L_2 Puppis - I. A recent dimming event from dust. *MNRAS337* (Nov. 2002), 79–86.

[14] Benomar, O., Takata, M., Shibahashi, H., Ceillier, T., and García, R. A. Nearly uniform internal rotation of solar-like main-sequence stars revealed by space-based asteroseismology and spectroscopic measurements. *MNRAS452* (Sept. 2015), 2654–2674.

[15] Boccaletti, A., Thalmann, C., Lagrange, A.-M., Janson, M., Augereau, J.-C., Schneider, G., Milli, J., Grady, C., Debes, J., Langlois, M., Mouillet, D., Henning, T., Dominik, C., Maire, A.-L., Beuzit, J.-L., Carson, J., Dohlen, K., Engler, N., Feldt, M., Fusco, T., Ginski, C., Girard, J. H., Hines, D., Kasper, M., Mawet, D., Ménard, F., Meyer, M. R., Moutou, C., Olofsson, J., Rodigas, T., Sauvage, J.-F., Schlieder, J., Schmid, H. M., Turatto, M., Udry, S., Vakili, F., Vigan, A., Wahhaj, Z., and Wisniewski, J. Fast-moving features in the debris disk around AU Microscopii. *Nature526* (Oct. 2015), 230–232.

[16] Bonsor, A., Kennedy, G. M., Crepp, J. R., Johnson, J. A., Wyatt, M. C., Sibthorpe, B., and Su, K. Y. L. Spatially resolved images of dust belt(s) around the planet-hosting subgiant κ CrB. *MNRAS431* (June 2013), 3025–3035.

[17] Bonsor, A., Kennedy, G. M., Wyatt, M. C., Johnson, J. A., and Sibthorpe, B. Herschel observations of debris discs orbiting planet-hosting subgiants. *MNRAS437* (Feb. 2014), 3288–3297.

[18] Bowers, P. F., and Johnston, K. J. Sensitive VLA observations of OH 127.8 - 0.0 and OH 26.5 + 0.6. *ApJ354* (May 1990), 676–686.

[19] Brinch, C., and Hogerheijde, M. R. LIME - a flexible, non-LTE line excitation and radiation transfer method for millimeter and far-infrared wavelengths. *A&A523* (Nov. 2010), A25.

[20] Bujarrabal, V., and Alcolea, J. Warm gas in the rotating disk of the Red Rectangle: accurate models of molecular line emission. *A&A552* (Apr. 2013), A116.

[21] Bujarrabal, V., Alcolea, J., Van Winckel, H., Santander-García, M., and Castro-Carrizo, A. Extended rotating disks around post-AGB stars. *A&A557* (Sept. 2013), A104.

[22] Bujarrabal, V., Castro-Carrizo, A., Alcolea, J., Santander-García, M., van Winckel, H., and Sánchez Contreras, C. Further ALMA observations and detailed modeling of the Red Rectangle. *A&A593* (Sept. 2016), A92.

[23] Bujarrabal, V., Castro-Carrizo, A., Alcolea, J., and Van Winckel, H. Detection of Keplerian dynamics in a disk around the post-AGB star AC Herculis. *A&A575* (Mar. 2015), L7.

[24] Casassus, S., Marino, S., Pérez, S., Roman, P., Dunhill, A., Armitage, P. J., Cuadra, J., Wootten, A., van der Plas, G., Cieza, L., Moral, V., Christiaens, V., and Montesinos, M. Accretion Kinematics through the Warped Transition Disk in HD142527 from Resolved CO(6-5) Observations. *ApJ811* (Oct. 2015), 92.

[25] Cassen, P., and Moosman, A. On the formation of protostellar disks. *Icarus 48* (Dec. 1981), 353–376.

[26] Cernicharo, J., Marcelino, N., Agúndez, M., and Guélin, M. Molecular shells in IRC+10216: tracing the mass loss history. *A&A575* (Mar. 2015), A91.

[27] Cernicharo, J., Waters, L. B. F. M., Decin, L., Encrenaz, P., Tielens, A. G. G. M., Agúndez, M., De Beck, E., Müller, H. S. P., Goicoechea, J. R., Barlow, M. J., Benz, A., Crimier, N., Daniel, F., di Giorgio, A. M.,

Fich, M., Gaier, T., García-Lario, P., de Koter, A., Khouri, T., Liseau, R., Lombaert, R., Erickson, N., Pardo, J. R., Pearson, J. C., Shipman, R., Sánchez Contreras, C., and Teyssier, D. A high-resolution line survey of IRC +10216 with Herschel/HIFI. First results: Detection of warm silicon dicarbide (SiC{_2}). *A&A521* (Oct. 2010), L8.

[28] Chen, Y., Bressan, A., Girardi, L., Marigo, P., Kong, X., and Lanza, A. PARSEC evolutionary tracks of massive stars up to 350 Msol at metallicities 0.0001 < Z < 0.04. *MNRAS452* (Sept. 2015), 1068–1080.

[29] Chen, Z., Nordhaus, J., Frank, A., Blackman, E. G., and Balick, B. Three-dimensional hydrodynamic simulations of L2 Puppis. *ArXiv e-prints* (Feb. 2016).

[30] Chiang, E. I., and Goldreich, P. Spectral Energy Distributions of T Tauri Stars with Passive Circumstellar Disks. *ApJ490* (Nov. 1997), 368–376.

[31] Chiu, P.-J., Hoang, C.-T., Dinh-V-Trung, Lim, J., Kwok, S., Hirano, N., and Muthu, C. A Slowly Expanding Disk and Fast Bipolar Outflow from the S Star π^1 Gruis. *ApJ645* (July 2006), 605–612.

[32] Christiaens, V., Casassus, S., Perez, S., van der Plas, G., and Ménard, F. Spiral Arms in the Disk of HD 142527 from CO Emission Lines with ALMA. *ApJ785* (Apr. 2014), L12.

[33] Cox, N. L. J., Kerschbaum, F., van Marle, A.-J., Decin, L., Ladjal, D., Mayer, A., Groenewegen, M. A. T., van Eck, S., Royer, P., Ottensamer, R., Ueta, T., Jorissen, A., Mecina, M., Meliani, Z., Luntzer, A., Blommaert, J. A. D. L., Posch, T., Vandenbussche, B., and Waelkens, C. A far-infrared survey of bow shocks and detached shells around AGB stars and red supergiants. *A&A537* (Jan. 2012), A35.

[34] David, T. J., Hillenbrand, L. A., Petigura, E. A., Carpenter, J. M., Crossfield, I. J. M., Hinkley, S., Ciardi, D. R., Howard, A. W., Isaacson, H. T., Cody, A. M., Schlieder, J. E., Beichman, C. A., and Barenfeld, S. A. A neptune-sized transiting planet closely orbiting a 5–10-million-year-old star. *Nature 534*, 7609 (06 2016), 658–661.

[35] De Beck, E., Decin, L., de Koter, A., Justtanont, K., Verhoelst, T., Kemper, F., and Menten, K. M. Probing the mass-loss history of AGB and red supergiant stars from CO rotational line profiles. II. CO line survey of evolved stars: derivation of mass-loss rate formulae. *A&A523* (Nov. 2010), A18.

[36] De Beck, E., Lombaert, R., Agúndez, M., Daniel, F., Decin, L., Cernicharo, J., Müller, H. S. P., Min, M., Royer, P., Vandenbussche, B., de Koter, A., Waters, L. B. F. M., Groenewegen, M. A. T., Barlow, M. J., Guélin, M., Kahane, C.,

Pearson, J. C., Encrenaz, P., Szczerba, R., and Schmidt, M. R. On the physical structure of IRC +10216. Ground-based and Herschel observations of CO and C_2H. *A&A539* (Mar. 2012), A108.

[37] De Marco, O. The Origin and Shaping of Planetary Nebulae: Putting the Binary Hypothesis to the Test. *PASP121* (Apr. 2009), 316–342.

[38] De Marco, O., Long, J., Jacoby, G. H., Hillwig, T., Kronberger, M., Howell, S. B., Reindl, N., and Margheim, S. Identifying close binary central stars of PN with Kepler. *MNRAS448* (Apr. 2015), 3587–3602.

[39] Decin, L., Cox, N. L. J., Royer, P., Van Marle, A. J., Vandenbussche, B., Ladjal, D., Kerschbaum, F., Ottensamer, R., Barlow, M. J., Blommaert, J. A. D. L., Gomez, H. L., Groenewegen, M. A. T., Lim, T., Swinyard, B. M., Waelkens, C., and Tielens, A. G. G. M. The enigmatic nature of the circumstellar envelope and bow shock surrounding Betelgeuse as revealed by Herschel. I. Evidence of clumps, multiple arcs, and a linear bar-like structure. *A&A548* (Dec. 2012), A113.

[40] Decin, L., De Beck, E., Brünken, S., Müller, H. S. P., Menten, K. M., Kim, H., Willacy, K., de Koter, A., and Wyrowski, F. Circumstellar molecular composition of the oxygen-rich AGB star IK Tauri. II. In-depth non-LTE chemical abundance analysis. *A&A516* (June 2010), A69.

[41] Decin, L., Richards, A. M. S., Neufeld, D., Steffen, W., Melnick, G., and Lombaert, R. ALMA data suggest the presence of spiral structure in the inner wind of CW Leonis. *A&A574* (Feb. 2015), A5.

[42] Decin, L., Royer, P., Cox, N. L. J., Vandenbussche, B., Ottensamer, R., Blommaert, J. A. D. L., Groenewegen, M. A. T., Barlow, M. J., Lim, T., Kerschbaum, F., Posch, T., and Waelkens, C. Discovery of multiple dust shells beyond 1 arcmin in the circumstellar envelope of IRC +10216 using Herschel/PACS. *A&A534* (Oct. 2011), A1.

[43] Delaunay, B. Sur la sphère vide. A la mémoire de Georges Voronoï. *Bulletin de l'Académie des Sciences de l'URSS*, 6 (1934), 793–800.

[44] Dipierro, G., Lodato, G., Testi, L., and de Gregorio Monsalvo, I. How to detect the signatures of self-gravitating circumstellar discs with the Atacama Large Millimeter/sub-millimeter Array. *MNRAS444* (Oct. 2014), 1919–1929.

[45] Dipierro, G., Pinilla, P., Lodato, G., and Testi, L. Dust trapping by spiral arms in gravitationally unstable protostellar discs. *MNRAS451* (July 2015), 974–986.

[46] Doeleman, S. S., Fish, V. L., Schenck, D. E., Beaudoin, C., Blundell, R., Bower, G. C., Broderick, A. E., Chamberlin, R., Freund, R., Friberg, P., Gurwell,

M. A., Ho, P. T. P., Honma, M., Inoue, M., Krichbaum, T. P., Lamb, J., Loeb, A., Lonsdale, C., Marrone, D. P., Moran, J. M., Oyama, T., Plambeck, R., Primiani, R. A., Rogers, A. E. E., Smythe, D. L., SooHoo, J., Strittmatter, P., Tilanus, R. P. J., Titus, M., Weintroub, J., Wright, M., Young, K. H., and Ziurys, L. M. Jet-launching structure resolved near the supermassive black hole in m87. *Science 338*, 6105 (2012), 355–358.

[47] Dong, R., Zhu, Z., and Whitney, B. Observational Signatures of Planets in Protoplanetary Disks I. Gaps Opened by Single and Multiple Young Planets in Disks. *ApJ809* (Aug. 2015), 93.

[48] Dreyer, C., Hegmann, M., and Sedlmayr, E. Circumstellar dust shells around long-period variables. IX. Dynamics of C-rich AGB star shells dominated by the exterior κ-mechanism. *A&A499* (June 2009), 765–771.

[49] Duchêne, G., Bouvier, J., Moraux, E., Bouy, H., Konopacky, Q., and Ghez, A. M. Substellar multiplicity in the Hyades cluster. *A&A555* (July 2013), A137.

[50] Dullemond, C. P., and Dominik, C. The effect of dust settling on the appearance of protoplanetary disks. *A&A421* (July 2004), 1075–1086.

[51] Dullemond, C. P., Dominik, C., and Natta, A. Passive Irradiated Circumstellar Disks with an Inner Hole. *ApJ560* (Oct. 2001), 957–969.

[52] Dumm, T., and Schild, H. Stellar radii of M giants. *New Astronomy 3* (Apr. 1998), 137–156.

[53] Eistrup, C., Walsh, C., and van Dishoeck, E. F. Setting the volatile composition of (exo)planet-building material. Does chemical evolution in disk midplanes matter? *A&A595* (Nov. 2016), A83.

[54] Fadeyev, Y. A. Nonlinear pulsations of stars with initial mass 3 Msun on the asymptotic giant branch. *Astronomy Letters 42* (Oct. 2016), 665–673.

[55] Flock, M., Ruge, J. P., Dzyurkevich, N., Henning, T., Klahr, H., and Wolf, S. Gaps, rings, and non-axisymmetric structures in protoplanetary disks. From simulations to ALMA observations. *A&A574* (Feb. 2015), A68.

[56] Fong, D., Meixner, M., Sutton, E. C., Zalucha, A., and Welch, W. J. Evolution of the Circumstellar Molecular Envelope. I. A BIMA CO Survey of Evolved Stars. *ApJ652* (Dec. 2006), 1626–1653.

[57] France, K., Herczeg, G. J., McJunkin, M., and Penton, S. V. CO to H2 Abundance Ratio = 10^{-4} in a Protoplanetary Disk. *ApJ794* (Oct. 2014), 160.

[58] Freytag, B., and Höfner, S. Three-dimensional simulations of the atmosphere of an AGB star. *A&A483* (May 2008), 571–583.

[59] Freytag, B., Liljegren, S., and Höfner, S. Global 3D radiation-hydrodynamics models of AGB stars. Effects of convection and radial pulsations on atmospheric structures. *A&A600* (Apr. 2017), A137.

[60] Funada, T., and Joseph, D. D. Viscous potential flow analysis of kelvin–helmholtz instability in a channel. *Journal of Fluid Mechanics 445* (10 2001), 263–283.

[61] Gobrecht, D., Cherchneff, I., Sarangi, A., Plane, J. M. C., and Bromley, S. T. Dust formation in the oxygen-rich AGB star IK Tauri. *A&A585* (Jan. 2016), A6.

[62] Groenewegen, M. A. T., Barlow, M. J., Blommaert, J. A. D. L., Cernicharo, J., Decin, L., Gomez, H. L., Hargrave, P. C., Kerschbaum, F., Ladjal, D., Lim, T. L., Matsuura, M., Olofsson, G., Sibthorpe, B., Swinyard, B. M., Ueta, T., and Yates, J. An independent distance estimate to CW Leonis. *A&A543* (July 2012), L8.

[63] Grunblatt, S. K., Huber, D., Gaidos, E. J., Lopez, E. D., Fulton, B. J., Vanderburg, A., Barclay, T., Fortney, J. J., Howard, A. W., Isaacson, H. T., Mann, A. W., Petigura, E., Silva Aguirre, V., and Sinukoff, E. J. EPIC 211351816.01: A (Re-?)Inflated Planet Orbiting a Red Giant Star. *ArXiv e-prints* (June 2016).

[64] Hardy, A., Schreiber, M. R., Parsons, S. G., Caceres, C., Brinkworth, C., Veras, D., Gänsicke, B. T., Marsh, T. R., and Cieza, L. The detection of dust around NN Ser. *MNRAS459* (July 2016), 4518–4526.

[65] Hartmann, L., Calvet, N., Gullbring, E., and D'Alessio, P. Accretion and the Evolution of T Tauri Disks. *ApJ495* (Mar. 1998), 385–400.

[66] Hillen, M. An N Band Interferometric Survey of The Disks Around Post-AGB Binary Stars. In *EAS Publications Series* (Dec. 2015), vol. 71 of *EAS Publications Series*, pp. 223–228.

[67] Hillen, M., Kluska, J., Le Bouquin, J.-B., Van Winckel, H., Berger, J.-P., Kamath, D., and Bujarrabal, V. Imaging the dust sublimation front of a circumbinary disk. *A&A588* (Apr. 2016), L1.

[68] Hinkle, K. H., Hall, D. N. B., and Ridgway, S. T. Time series infrared spectroscopy of the Mira variable Chi Cygni. *ApJ252* (Jan. 1982), 697–714.

[69] Hinkle, K. H., Lebzelter, T., and Straniero, O. Carbon and Oxygen Isotopic Ratios for Nearby Miras. *ApJ825* (July 2016), 38.

[70] Hirano, N., Shinnaga, H., Dinh-V-Trung, Fong, D., Keto, E., Patel, N., Qi, C., Young, K., Zhang, Q., and Zhao, J. High-Velocity Bipolar Outflow and Disklike Envelope in the Carbon Star V Hydrae. *ApJ616* (Nov. 2004), L43–L46.

[71] Homan, W., Boulangier, J., Decin, L., and de Koter, A. Simplified models of circumstellar morphologies for interpreting high-resolution data. Analytical approach to the equatorial density enhancement. *A&A596* (Dec. 2016), A91.

[72] Homan, W., Decin, L., de Koter, A., van Marle, A. J., Lombaert, R., and Vlemmings, W. Simplified models of stellar wind anatomy for interpreting high-resolution data. Analytical approach to embedded spiral geometries. *A&A579* (July 2015), A118.

[73] Hori, Y., and Ikoma, M. Gas giant formation with small cores triggered by envelope pollution by icy planetesimals. *MNRAS416* (Sept. 2011), 1419–1429.

[74] Huggins, P. J. Jets and Tori in Proto-Planetary Nebulae. *ApJ663* (July 2007), 342–349.

[75] Iorio, L. Constraining the Angular Momentum of the Sun with Planetary Orbital Motions and General Relativity. *Solar Phys.281* (Dec. 2012), 815–826.

[76] Ireland, M. J., Monnier, J. D., Tuthill, P. G., Cohen, R. W., De Buizer, J. M., Packham, C., Ciardi, D., Hayward, T., and Lloyd, J. P. Born-Again Protoplanetary Disk around Mira B. *ApJ662* (June 2007), 651–657.

[77] Ireland, M. J., Tuthill, P. G., Bedding, T. R., Robertson, J. G., and Jacob, A. P. Multiwavelength diameters of nearby Miras and semiregular variables. *MNRAS350* (May 2004), 365–374.

[78] Izumiura, H., Ueta, T., Yamamura, I., Matsunaga, N., Ita, Y., Matsuura, M., Nakada, Y., Fukushi, H., Mito, H., Tanabé, T., and Hashimoto, O. Extended dust shell of the carbon star U Hydrae observed with AKARI. *A&A528* (Apr. 2011), A29.

[79] Izzard, R. G. *Nucleosynthesis In Binary Stars*. PhD thesis, University of Cambridge, 2004.

[80] Jeffers, S. V., Min, M., Waters, L. B. F. M., Canovas, H., Pols, O. R., Rodenhuis, M., de Juan Ovelar, M., Keller, C. U., and Decin, L. Surprising detection of an equatorial dust lane on the AGB star IRC+10216. *A&A572* (Dec. 2014), A3.

[81] Juhász, A., Benisty, M., Pohl, A., Dullemond, C. P., Dominik, C., and Paardekooper, S.-J. Spiral arms in scattered light images of protoplanetary discs: are they the signposts of planets? *MNRAS451* (Aug. 2015), 1147–1157.

[82] Jura, M., Chen, C., and Plavchan, P. The Very Slow Wind from the Pulsating Semiregular Red Giant, L_2 Puppis. *ApJ569* (Apr. 2002), 964–974.

[83] Kato, M. T., Nakamura, K., Tandokoro, R., Fujimoto, M., and Ida, S. Modification of Angular Velocity by Inhomogeneous Magnetorotational Instability Growth in Protoplanetary Disks. *ApJ691* (Feb. 2009), 1697–1706.

[84] Kenyon, S. J., and Hartmann, L. Spectral energy distributions of T Tauri stars - Disk flaring and limits on accretion. *ApJ323* (Dec. 1987), 714–733.

[85] Kerschbaum, F., and Olofsson, H. Oxygen-rich semiregular and irregular variables. A catalogue of circumstellar CO observations. *A&AS138* (Aug. 1999), 299–322.

[86] Kervella, P., Homan, W., Richards, A. M. S., Decin, L., McDonald, I., Montargès, M., and Ohnaka, K. ALMA observations of the nearby AGB star L_2 Puppis. I. Mass of the central star and detection of a candidate planet. *A&A596* (Dec. 2016), A92.

[87] Kervella, P., Montargès, M., Lagadec, E., Ridgway, S. T., Haubois, X., Girard, J. H., Ohnaka, K., Perrin, G., and Gallenne, A. The dust disk and companion of the nearby AGB star L_2 Puppis. SPHERE/ZIMPOL polarimetric imaging at visible wavelengths. *A&A578* (June 2015), A77.

[88] Kervella, P., Montargès, M., Ridgway, S. T., Perrin, G., Chesneau, O., Lacour, S., Chiavassa, A., Haubois, X., and Gallenne, A. An edge-on translucent dust disk around the nearest AGB star, L_2 Puppis. VLT/NACO spectro-imaging from 1.04 to 4.05 μm and VLTI interferometry. *A&A564* (Apr. 2014), A88.

[89] Kholopov, P. N., Samus, N. N., Kazarovets, E. V., and Perova, N. B. The 67th Name-List of Variable Stars. *Information Bulletin on Variable Stars 2681* (Mar. 1985), 1.

[90] Khouri, T., Maercker, M., Waters, L. B. F. M., Vlemmings, W. H. T., Kervella, P., de Koter, A., Ginski, C., De Beck, E., Decin, L., Min, M., Dominik, C., O'Gorman, E., Schmid, H.-M., Lombaert, R., and Lagadec, E. Study of the inner dust envelope and stellar photosphere of the AGB star R Doradus using SPHERE/ZIMPOL. *A&A591* (June 2016), A70.

[91] Khouri, T., Waters, L. B. F. M., de Koter, A., Decin, L., Min, M., de Vries, B. L., Lombaert, R., and Cox, N. L. J. Dusty wind of W Hydrae. Multi-wavelength modelling of the present-day and recent mass loss. *A&A577* (May 2015), A114.

[92] Kim, H. Gravitationally Induced Density Wake of a Circularly Orbiting Object as an Interpretative Framework of Ubiquitous Spirals and Arcs. *ApJ739* (Oct. 2011), 102.

[93] Kim, H., Hsieh, I.-T., Liu, S.-Y., and Taam, R. E. Evidence of a Binary-induced Spiral from an Incomplete Ring Pattern of CIT 6. *ApJ776* (Oct. 2013), 86.

[94] Kim, H., Lee, H.-G., Mauron, N., and Chu, Y.-H. HST Images Reveal Dramatic Changes in the Core of IRC+10216. *ApJ804* (May 2015), L10.

[95] Kim, H., Liu, S.-Y., Hirano, N., Zhao-Geisler, R., Trejo, A., Yen, H.-W., Taam, R. E., Kemper, F., Kim, J., Byun, D.-Y., and Liu, T. High-resolution CO Observation of the Carbon Star CIT 6 Revealing the Spiral Structure and a Nascent Bipolar Outflow. *ApJ814* (Nov. 2015), 61.

[96] Kim, H., and Taam, R. E. A New Method of Determining the Characteristics of Evolved Binary Systems Revealed in the Observed Circumstellar Patterns: Application to AFGL 3068. *ApJ759* (Nov. 2012), L22.

[97] Kimura, S. S., Kunitomo, M., and Takahashi, S. Z. From birth to death of protoplanetary discs: modelling their formation, evolution and dispersal. *MNRAS461* (Sept. 2016), 2257–2265.

[98] Kirchschlager, F., Wolf, S., and Madlener, D. The circumstellar disc of FS Tau B - a self-consistent model based on observations in the mid-infrared with NACO. *MNRAS462* (Oct. 2016), 858–866.

[99] Kitamura, Y., Momose, M., Yokogawa, S., Kawabe, R., Tamura, M., and Ida, S. Investigation of the Physical Properties of Protoplanetary Disks around T Tauri Stars by a 1 Arcsecond Imaging Survey: Evolution and Diversity of the Disks in Their Accretion Stage. *ApJ581* (Dec. 2002), 357–380.

[100] Kobayashi, C., Karakas, A. I., and Umeda, H. The evolution of isotope ratios in the Milky Way Galaxy. *MNRAS414* (July 2011), 3231–3250.

[101] Lagadec, E., Verhoelst, T., Mékarnia, D., Suáeez, O., Zijlstra, A. A., Bendjoya, P., Szczerba, R., Chesneau, O., van Winckel, H., Barlow, M. J., Matsuura, M., Bowey, J. E., Lorenz-Martins, S., and Gledhill, T. A mid-infrared imaging catalogue of post-asymptotic giant branch stars. *MNRAS417* (Oct. 2011), 32–92.

[102] Lambrechts, M., Johansen, A., Capelo, H. L., Blum, J., and Bodenschatz, E. Spontaneous concentrations of solids through two-way drag forces between gas and sedimenting particles. *A&A591* (June 2016), A133.

[103] Leão, I. C., de Laverny, P., Mékarnia, D., de Medeiros, J. R., and Vandame, B. The circumstellar envelope of IRC+10216 from milli-arcsecond to arcmin scales. *A&A455* (Aug. 2006), 187–194.

[104] Lee, U. Viscous Decretion Discs around Rapidly Rotating Stars. *PASJ65* (Dec. 2013), 122.

[105] Les, R., and Lin, M.-K. Gap formation and stability in non-isothermal protoplanetary discs. *MNRAS450* (June 2015), 1503–1513.

[106] Li, X., Millar, T. J., Heays, A. N., Walsh, C., van Dishoeck, E. F., and Cherchneff, I. Chemistry and distribution of daughter species in the circumstellar envelopes of O-rich AGB stars. *A&A588* (Mar. 2016), A4.

[107] Li, X., Millar, T. J., Walsh, C., Heays, A. N., and van Dishoeck, E. F. Photodissociation and chemistry of N_2 in the circumstellar envelope of carbon-rich AGB stars. *A&A568* (Aug. 2014), A111.

[108] Lieman-Sifry, J., Hughes, A. M., Carpenter, J. M., Gorti, U., Hales, A., and Flaherty, K. M. Debris Disks in the Scorpius-Centaurus OB Association Resolved by ALMA. *ApJ828* (Sept. 2016), 25.

[109] Lin, D. N. C., Bodenheimer, P., and Richardson, D. C. Orbital migration of the planetary companion of 51 Pegasi to its present location. *Nature380* (Apr. 1996), 606–607.

[110] Lin, M.-K. One-armed spirals in locally isothermal, radially structured self-gravitating discs. *MNRAS448* (Apr. 2015), 3806–3819.

[111] Lloyd, S. Least squares quantization in pcm. *IEEE Trans. Inf. Theor. 28*, 2 (Sept. 2006), 129–137.

[112] Louvet, F., Dougados, C., Cabrit, S., Hales, A., Pinte, C., Menard, F., Bacciotti, F., Coffey, D., Mardones, D., Bronfman, L., and Gueth, F. ALMA observations of the Th 28 protostellar disk - A new exemple of counter-rotation between disk and optical jet. *ArXiv e-prints* (July 2016).

[113] Lykou, F., Klotz, D., Paladini, C., Hron, J., Zijlstra, A. A., Kluska, J., Norris, B. R. M., Tuthill, P. G., Ramstedt, S., Lagadec, E., Wittkowski, M., Maercker, M., and Mayer, A. Dissecting the AGB star L_2 Puppis: a torus in the making. *A&A576* (Apr. 2015), A46.

[114] Maercker, M., Mohamed, S., Vlemmings, W. H. T., Ramstedt, S., Groenewegen, M. A. T., Humphreys, E., Kerschbaum, F., Lindqvist, M., Olofsson, H., Paladini, C., Wittkowski, M., de Gregorio-Monsalvo, I., and Nyman, L.-A. Unexpectedly large mass loss during the thermal pulse cycle of the red giant star R Sculptoris. *Nature490* (Oct. 2012), 232–234.

[115] Maercker, M., Vlemmings, W. H. T., Brunner, M., De Beck, E., Humphreys, E. M., Kerschbaum, F., Lindqvist, M., Olofsson, H., and Ramstedt, S. A detailed view of the gas shell around R Sculptoris with ALMA. *A&A586* (Feb. 2016), A5.

[116] Mamon, G. A., Glassgold, A. E., and Huggins, P. J. The photodissociation of CO in circumstellar envelopes. *ApJ328* (May 1988), 797–808.

[117] Marigo, P., Bressan, A., Nanni, A., Girardi, L., and Pumo, M. L. Evolution of thermally pulsing asymptotic giant branch stars - I. The COLIBRI code. *MNRAS434* (Sept. 2013), 488–526.

[118] Marigo, P., Girardi, L., Bressan, A., Groenewegen, M. A. T., Silva, L., and Granato, G. L. Evolution of asymptotic giant branch stars. II. Optical to far-infrared isochrones with improved TP-AGB models. *A&A482* (May 2008), 883–905.

[119] Mastrodemos, N., and Morris, M. Bipolar Pre-Planetary Nebulae: Hydrodynamics of Dusty Winds in Binary Systems. II. Morphology of the Circumstellar Envelopes. *ApJ523* (Sept. 1999), 357–380.

[120] Mauron, N., and Huggins, P. J. Multiple shells in the circumstellar envelope of IRC+10216. *A&A349* (Sept. 1999), 203–208.

[121] Mauron, N., and Huggins, P. J. Multiple shells in IRC+10216: shell properties. *A&A359* (July 2000), 707–715.

[122] Mauron, N., and Huggins, P. J. Imaging the circumstellar envelopes of AGB stars. *A&A452* (June 2006), 257–268.

[123] Mayer, A., Jorissen, A., Kerschbaum, F., Mohamed, S., van Eck, S., Ottensamer, R., Blommaert, J. A. D. L., Decin, L., Groenewegen, M. A. T., Posch, T., Vandenbussche, B., and Waelkens, C. Herschel's view into Mira's head. *A&A531* (July 2011), L4.

[124] Mayor, M., and Queloz, D. A Jupiter-mass companion to a solar-type star. *Nature378* (Nov. 1995), 355–359.

[125] McDonald, I., Kerins, E., Penny, M., Beaulieu, J.-P., Batista, V., Calchi Novati, S., Cassan, A., Fouqué, P., Mao, S., Marquette, J. B., Rattenbury, N., Robin, A. C., Tisserand, P., and Zapatero Osorio, M. R. ExELS: an exoplanet legacy science proposal for the ESA Euclid mission - II. Hot exoplanets and sub-stellar systems. *MNRAS445* (Dec. 2014), 4137–4154.

[126] McMullin, J. P., Waters, B., Schiebel, D., Young, W., and Golap, K. CASA Architecture and Applications. In *Astronomical Data Analysis Software and Systems XVI* (Oct. 2007), R. A. Shaw, F. Hill, and D. J. Bell, Eds., vol. 376 of *Astronomical Society of the Pacific Conference Series*, p. 127.

[127] Meibom, S., Mathieu, R. D., and Stassun, K. G. Stellar Rotation in M35: Mass-Period Relations, Spin-Down Rates, and Gyrochronology. *ApJ695* (Apr. 2009), 679–694.

[128] Men'shchikov, A. B., Balega, Y., Blöcker, T., Osterbart, R., and Weigelt, G. Structure and physical properties of the rapidly evolving dusty envelope of <ASTROBJ>IRC +10 216</ASTROBJ> reconstructed by detailed two-dimensional radiative transfer modeling. *A&A368* (Mar. 2001), 497–526.

[129] Menten, K. M., Reid, M. J., Kamiński, T., and Claussen, M. J. The size, luminosity, and motion of the extreme carbon star IRC+10216 (CW Leonis). *A&A543* (July 2012), A73.

[130] Menut, J.-L., Gendron, E., Schartmann, M., Tuthill, P., Lopez, B., Danchi, W. C., Wolf, S., Lagrange, A.-M., Flament, S., Rouan, D., Clénet, Y., and Berruyer, N. The carbon star IRC+10216: linking the complex inner region with its spherical large-scale structures. *MNRAS376* (Mar. 2007), L6–L10.

[131] Mečina, M., Kerschbaum, F., Groenewegen, M. A. T., Ottensamer, R., Blommaert, J. A. D. L., Mayer, A., Decin, L., Luntzer, A., Vandenbussche, B., Posch, T., and Waelkens, C. Dusty shells surrounding the carbon variables S Scuti and RT Capricorni. *A&A566* (June 2014), A69.

[132] Millar, T. J. Astrochemistry. *Plasma Sources Science Technology 24*, 4 (Aug. 2015), 043001.

[133] Miller Bertolami, M. M. New models for the evolution of post-asymptotic giant branch stars and central stars of planetary nebulae. *A&A588* (Apr. 2016), A25.

[134] Miotello, A., van Dishoeck, E. F., Kama, M., and Bruderer, S. Determining protoplanetary disk gas masses from CO isotopologues line observations. *A&A594* (Oct. 2016), A85.

[135] Mohamed, S., and Podsiadlowski, P. Mass Transfer in Mira-type Binaries. *Baltic Astronomy 21* (2012), 88–96.

[136] Montgomery, M. M. Tilt, Warp, and Simultaneous Precessions in Disks. *ApJ753* (July 2012), L27.

[137] Morris, M., Sahai, R., Matthews, K., Cheng, J., Lu, J., Claussen, M., and Sánchez-Contreras, C. A Binary-Induced Pinwheel Outflow from the Extreme Carbon Star, AFGL 3068. In *Planetary Nebulae in our Galaxy and Beyond* (2006), M. J. Barlow and R. H. Méndez, Eds., vol. 234 of *IAU Symposium*, pp. 469–470.

[138] Murillo, N. M., Lai, S.-P., Bruderer, S., Harsono, D., and van Dishoeck, E. F. A Keplerian disk around a Class 0 source: ALMA observations of VLA1623A. *A&A560* (Dec. 2013), A103.

[139] Mustill, A. J., and Villaver, E. Foretellings of Ragnarök: World-engulfing Asymptotic Giants and the Inheritance of White Dwarfs. *ApJ761* (Dec. 2012), 121.

[140] Nixon, C. Accretion disc viscosity: a limit on the anisotropy. *MNRAS450* (July 2015), 2459–2465.

[141] Nixon, C., and King, A. Warp propagation in astrophysical discs. *ArXiv e-prints* (May 2015).

[142] Nordhaus, J., and Blackman, E. G. Low-mass binary-induced outflows from asymptotic giant branch stars. *MNRAS370* (Aug. 2006), 2004–2012.

[143] Nordhaus, J., Blackman, E. G., and Frank, A. Isolated versus common envelope dynamos in planetary nebula progenitors. *MNRAS376* (Apr. 2007), 599–608.

[144] Nordhaus, J., Spiegel, D. S., Ibgui, L., Goodman, J., and Burrows, A. Tides and tidal engulfment in post-main-sequence binaries: period gaps for planets and brown dwarfs around white dwarfs. *MNRAS408* (Oct. 2010), 631–641.

[145] Ogilvie, G. I., and Latter, H. N. Local and global dynamics of warped astrophysical discs. *MNRAS433* (Aug. 2013), 2403–2419.

[146] Ohnaka, K. High spectral resolution spectroscopy of the SiO fundamental lines in red giants and red supergiants with VLT/VISIR. *A&A561* (Jan. 2014), A47.

[147] Ohnaka, K., Schertl, D., Hofmann, K.-H., and Weigelt, G. AMBER-NACO aperture-synthesis imaging of the half-obscured central star and the edge-on disk of the red giant L_2 Puppis. *A&A581* (Sept. 2015), A127.

[148] Olofsson, H., Eriksson, K., Gustafsson, B., and Carlstrom, U. A study of circumstellar envelopes around bright carbon stars. I - Structure, kinematics, and mass-loss rate. *ApJS87* (July 1993), 267–304.

[149] Paczyński, B. Evolutionary Processes in Close Binary Systems. *ARA&A9* (1971), 183.

[150] Pavlyuchenkov, Y., Semenov, D., Henning, T., Guilloteau, S., Piétu, V., Launhardt, R., and Dutrey, A. Molecular Line Radiative Transfer in Protoplanetary Disks: Monte Carlo Simulations versus Approximate Methods. *ApJ669* (Nov. 2007), 1262–1278.

[151] Pelupessy, F. I., and Portegies Zwart, S. The formation of planets in circumbinary discs. *MNRAS429* (Feb. 2013), 895–902.

[152] Podio, L., Kamp, I., Codella, C., Nisini, B., Aresu, G., Brittain, S., Cabrit, S., Dougados, C., Grady, C., Meijerink, R., Sandell, G., Spaans, M., Thi, W.-F., White, G. J., and Woitke, P. Probing the Gaseous Disk of T Tau N with CN 5-4 Lines. *ApJ783* (Mar. 2014), L26.

[153] Poelarends, A. J. T., Herwig, F., Langer, N., and Heger, A. The Supernova Channel of Super-AGB Stars. *ApJ675* (Mar. 2008), 614–625.

[154] Raghavan, D., McAlister, H. A., Henry, T. J., Latham, D. W., Marcy, G. W., Mason, B. D., Gies, D. R., White, R. J., and ten Brummelaar, T. A. A Survey of Stellar Families: Multiplicity of Solar-type Stars. *ApJS190* (Sept. 2010), 1–42.

[155] Ramstedt, S., Mohamed, S., Vlemmings, W. H. T., Maercker, M., Montez, R., Baudry, A., De Beck, E., Lindqvist, M., Olofsson, H., Humphreys, E. M. L., Jorissen, A., Kerschbaum, F., Mayer, A., Wittkowski, M., Cox, N. L. J., Lagadec, E., Leal-Ferreira, M. L., Paladini, C., Pérez-Sánchez, A., and Sacuto, S. The wonderful complexity of the Mira AB system. *A&A570* (Oct. 2014), L14.

[156] Ramstedt, S., Schöier, F. L., Olofsson, H., and Lundgren, A. A. On the reliability of mass-loss-rate estimates for AGB stars. *A&A487* (Aug. 2008), 645–657.

[157] Ray, T., Dougados, C., Bacciotti, F., Eislöffel, J., and Chrysostomou, A. Toward Resolving the Outflow Engine: An Observational Perspective. *Protostars and Planets V* (2007), 231–244.

[158] Reimers, D. Circumstellar absorption lines and mass loss from red giants. *Memoires of the Societe Royale des Sciences de Liege 8* (1975), 369–382.

[159] Rosenfield, P., Marigo, P., Girardi, L., Dalcanton, J. J., Bressan, A., Gullieuszik, M., Weisz, D., Williams, B. F., Dolphin, A., and Aringer, B. Evolution of Thermally Pulsing Asymptotic Giant Branch Stars. IV. Constraining Mass loss and Lifetimes of Low Mass, Low Metallicity AGB Stars. *ApJ790* (July 2014), 22.

[160] Rosenfield, P., Marigo, P., Girardi, L., Dalcanton, J. J., Bressan, A., Williams, B. F., and Dolphin, A. Evolution of Thermally Pulsing Asymptotic Giant Branch Stars. V. Constraining the Mass Loss and Lifetimes of Intermediate-mass, Low-metallicity AGB Stars. *ApJ822* (May 2016), 73.

[161] Ryan, E. L., Woodward, C. E., Dipaolo, A., Farinato, J., Giallongo, E., Gredel, R., Hill, J., Pedichini, F., Pogge, R., and Ragazzoni, R. The Asteroid Distribution in the Ecliptic. *AJ137* (June 2009), 5134–5145.

[162] Sahai, R., Morris, M. R., and Villar, G. G. Young Planetary Nebulae: Hubble Space Telescope Imaging and a New Morphological Classification System. *AJ141* (Apr. 2011), 134.

[163] Sahai, R., Young, K., Patel, N. A., Sánchez Contreras, C., and Morris, M. A Massive Bipolar Outflow and a Dusty Torus with Large Grains in the Preplanetary Nebula IRAS 22036+5306. *ApJ653* (Dec. 2006), 1241–1252.

[164] Schnee, S. L., Brogan, C., Espada, D., Humphreys, E., Komugi, S., Petry, D., Vila-Vilaro, B., and Villard, E. The human pipeline: distributed data reduction for ALMA. In *Observatory Operations: Strategies, Processes, and Systems V* (Aug. 2014), vol. 9149 of *Proc. SPIE*, p. 91490Z.

[165] Schöier, F. L., van der Tak, F. F. S., van Dishoeck, E. F., and Black, J. H. An atomic and molecular database for analysis of submillimetre line observations. *A&A432* (Mar. 2005), 369–379.

[166] Schröder, K.-P., and Connon Smith, R. Distant future of the Sun and Earth revisited. *MNRAS386* (May 2008), 155–163.

[167] Schunker, H., Schou, J., Ball, W. H., Nielsen, M. B., and Gizon, L. Asteroseismic inversions for radial differential rotation of Sun-like stars: ensemble fits. *A&A586* (Feb. 2016), A79.

[168] Seifried, D., Sánchez-Monge, Á., Walch, S., and Banerjee, R. Revealing the dynamics of Class 0 protostellar discs with ALMA. *MNRAS459* (June 2016), 1892–1906.

[169] Silvotti, R., Charpinet, S., Green, E., Fontaine, G., Telting, J. H., Østensen, R. H., Van Grootel, V., Baran, A. S., Schuh, S., and Fox Machado, L. Kepler detection of a new extreme planetary system orbiting the subdwarf-B pulsator KIC 10001893. *A&A570* (Oct. 2014), A130.

[170] Skinner, C. J., Meixner, M., and Bobrowsky, M. The birth of a planetary nebula around the carbon star IRC+10216. *MNRAS300* (Nov. 1998), L29–L33.

[171] Smith, R. L. Efficient monte carlo procedures for generating points uniformly distributed over bounded regions. *Operations Research 32*, 6 (1984), pp. 1296–1308.

[172] Soker, N. Influences of Wide Binaries on the Structures of Planetary Nebulae. *MNRAS270* (Oct. 1994), 774.

[173] Soker, N. Shaping Planetary Nebulae and Related Objects. In *Asymmetrical Planetary Nebulae III: Winds, Structure and the Thunderbird* (July 2004), M. Meixner, J. H. Kastner, B. Balick, and N. Soker, Eds., vol. 313 of *Astronomical Society of the Pacific Conference Series*, p. 562.

[174] Staff, J. E., De Marco, O., Wood, P., Galaviz, P., and Passy, J.-C. Hydrodynamic simulations of the interaction between giant stars and planets. *MNRAS458* (May 2016), 832–844.

[175] Steffen, W., and López, J. A. Morpho-Kinematic Modeling of Gaseous Nebulae with SHAPE. *Revista Mexicana de Astronomía y Astrofisica 42* (Apr. 2006), 99–105.

[176] Stevens, I. R., Blondin, J. M., and Pollock, A. M. T. Colliding winds from early-type stars in binary systems. *ApJ386* (Feb. 1992), 265–287.

[177] Stewart, P. N., Tuthill, P. G., Monnier, J. D., Ireland, M. J., Hedman, M. M., Nicholson, P. D., and Lacour, S. The weather report from IRC+10216: evolving irregular clouds envelop carbon star. *MNRAS455* (Jan. 2016), 3102–3109.

[178] Thebault, P., Kral, Q., and Augereau, J.-C. Grain size segregation in debris discs. *A&A561* (Jan. 2014), A16.

[179] Theuns, T., and Jorissen, A. Wind Accretion in Binary Stars - Part One - Intricacies of the Flow Structure. *MNRAS265* (Dec. 1993), 946.

[180] Toomre, A. On the gravitational stability of a disk of stars. *ApJ139* (May 1964), 1217–1238.

[181] Ud-Doula, A., Owocki, S. P., and Townsend, R. H. D. Dynamical simulations of magnetically channelled line-driven stellar winds - II. The effects of field-aligned rotation. *MNRAS385* (Mar. 2008), 97–108.

[182] Ueta, T. Spitzer MIPS Imaging of NGC 650: Probing the History of Mass Loss on the Asymptotic Giant Branch. *ApJ650* (Oct. 2006), 228–236.

[183] van Buren, D. Stellar Wind Bow Shocks. In *Massive Stars: Their Lives in the Interstellar Medium* (Jan. 1993), J. P. Cassinelli and E. B. Churchwell, Eds., vol. 35 of *Astronomical Society of the Pacific Conference Series*, p. 315.

[184] van Leeuwen, F. Validation of the new Hipparcos reduction. *A&A474* (Nov. 2007), 653–664.

[185] van Marle, A. J., Keppens, R., and Meliani, Z. Thin shell morphology in the circumstellar medium of massive binaries. *A&A527* (Mar. 2011), A3.

[186] van Winckel, H. Post-AGB Stars. *ARA&A41* (2003), 391–427.

[187] Van Winckel, H., Lloyd Evans, T., Reyniers, M., Deroo, P., and Gielen, C. Binary post-AGB stars and their Keplerian discs . 943.

[188] Vassiliadis, E., and Wood, P. R. Evolution of low- and intermediate-mass stars to the end of the asymptotic giant branch with mass loss. *ApJ413* (Aug. 1993), 641–657.

[189] Veras, D. Post-main-sequence planetary system evolution. *Royal Society Open Science 3* (Feb. 2016), 150571.

[190] Veras, D. The fates of Solar system analogues with one additional distant planet. *MNRAS463* (Dec. 2016), 2958–2971.

[191] Veras, D., Hadjidemetriou, J. D., and Tout, C. A. An exoplanet's response to anisotropic stellar mass loss during birth and death. *MNRAS435* (Nov. 2013), 2416–2430.

[192] Veras, D., and Wyatt, M. C. The Solar system's post-main-sequence escape boundary. *MNRAS421* (Apr. 2012), 2969–2981.

[193] Veras, D., Wyatt, M. C., Mustill, A. J., Bonsor, A., and Eldridge, J. J. The great escape: how exoplanets and smaller bodies desert dying stars. *MNRAS417* (Nov. 2011), 2104–2123.

[194] Villaver, E., and Livio, M. Can Planets Survive Stellar Evolution? *ApJ661* (June 2007), 1192–1201.

[195] Villaver, E., and Livio, M. The Orbital Evolution of Gas Giant Planets Around Giant Stars. *ApJ705* (Nov. 2009), L81–L85.

[196] Visser, R., and Dullemond, C. P. Sub-Keplerian accretion onto circumstellar disks. *A&A519* (Sept. 2010), A28.

[197] Vorobyov, E. I., and Basu, S. Variable Protostellar Accretion with Episodic Bursts. *ApJ805* (June 2015), 115.

[198] Voronoi, G. Nouvelles applications des paramètres continus à la théorie des formes quadratiques. deuxième mémoire. recherches sur les paralléllo èdres primitifs. *Journal für die reine und angewandte Mathematik 134* (1908), 198–287.

[199] Walder, R., and Folini, D. 3D-hydrodynamics of colliding winds in massive binaries. In *A Massive Star Odyssey: From Main Sequence to Supernova* (2003), K. van der Hucht, A. Herrero, and C. Esteban, Eds., vol. 212 of *IAU Symposium*, p. 139.

[200] Walsh, C., Juhász, A., Meeus, G., Dent, W. R. F., Maud, L. T., Aikawa, Y., Millar, T. J., and Nomura, H. ALMA Reveals the Anatomy of the mm-sized Dust and Molecular Gas in the HD 97048 Disk. *ApJ831* (Nov. 2016), 200.

[201] Wang, Q., and Willson, L. A. Multiple Spiral Branches on Late Asymptotic Giant Branch Stars. *ApJ755* (Aug. 2012), 136.

[202] Wang, Q., and Willson, L. A. Spirals from Interaction of a Small Body with a Pulsating AGB-Star Wind. In *Resolving The Future Of Astronomy With Long-Baseline Interferometry* (Sept. 2014), M. J. Creech-Eakman, J. A. Guzik, and R. E. Stencel, Eds., vol. 487 of *Astronomical Society of the Pacific Conference Series*, p. 401.

[203] Wiesemeyer, H., Thum, C., Baudry, A., and Herpin, F. Precessing planetary magnetospheres in SiO stars?. First detection of quasi-periodic polarization fluctuations in R Leonis and V Camelopardalis. *A&A498* (May 2009), 801–810.

[204] Williams, J. P., and McPartland, C. Measuring Protoplanetary Disk Gas Surface Density Profiles with ALMA. *ApJ830* (Oct. 2016), 32.

[205] Wilner, D. J., and Lay, O. P. Subarcsecond Millimeter and Submillimeter Observations of Circumstellar Disks. *Protostars and Planets IV* (May 2000), 509.

[206] Winters, J. M., Le Bertre, T., Nyman, L.-Å., Omont, A., and Jeong, K. S. The hydrodynamical structure of circumstellar envelopes around low mass-loss rate, low outflow velocity AGB stars. *A&A388* (June 2002), 609–614.

[207] Witteborn, F. C., Strecker, D. W., Erickson, E. F., Smith, S. M., Goebel, J. H., and Taylor, B. J. The spectrum of IRC + 10216 from 2.0 to 8.5 microns. *ApJ238* (June 1980), 577–584.

[208] Woitke, P. Dust-driven Winds Beyond Spherical Symmetry. In *The Art of Modeling Stars in the 21st Century* (Oct. 2008), L. Deng and K. L. Chan, Eds., vol. 252 of *IAU Symposium*, pp. 229–234.

[209] Wolszczan, A. Confirmation of Earth-Mass Planets Orbiting the Millisecond Pulsar PSR B1257+12. *Science 264* (Apr. 1994), 538–542.

[210] Yang, B., Stancil, P. C., Balakrishnan, N., and Forrey, R. C. Rotational Quenching of CO due to H_2 Collisions. *ApJ718* (Aug. 2010), 1062–1069.

[211] Zhang, K., Isella, A., Carpenter, J. M., and Blake, G. A. Comparison of the Dust and Gas Radial Structure in the Transition Disk [PZ99] J160421.7-213028. *ApJ791* (Aug. 2014), 42.

[212] Zhu, Z., Dong, R., Stone, J. M., and Rafikov, R. R. The Structure of Spiral Shocks Excited by Planetary-mass Companions. *ArXiv e-prints* (July 2015).

FACULTY OF SCIENCE
DEPARTMENT OF PHYSICS AND ASTRONOMY
INSITUUT VOOR STERRENKUNDE (IVS)
Celestijnenlaan 200D box 2401
B-3001 Leuven
ward.homan@ster.kuleuven.be
http://fys.kuleuven.be/ster/